

AD-A252 209



1

Office of Naval Research

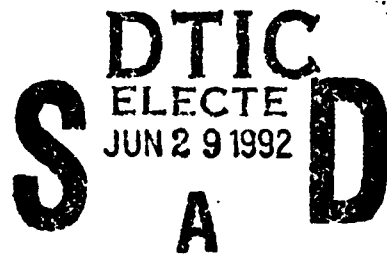
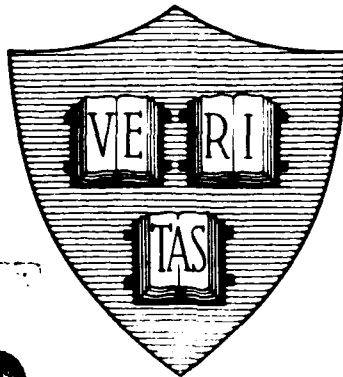
Grant N00014-89-J-1023

Grant N00014-89-J-1565

National Sciences Foundation Grant DMR-89-12927

National Sciences Foundation Grant DMR-89-20490

**GEOMETRICAL EFFECTS IN TWO-DIMENSIONAL
ARRAYS OF JOSEPHSON JUNCTIONS**



By

Lydia Lee Sohn

May 1992

Technical Report No. 33

This document has been approved for public release and sale; its distribution is unlimited. Reproduction in whole or in part is permitted by the U.S. Government.

**Division of Applied Sciences
Harvard University · Cambridge, Massachusetts**

92 6 20 050

92-16945



REPORT DOCUMENTATION PAGE

Form Approved
OMB No. 0704-0188

1a. REPORT SECURITY CLASSIFICATION Unclassified			1b. RESTRICTIVE MARKINGS		
2a. SECURITY CLASSIFICATION AUTHORITY N/A			3. DISTRIBUTION/AVAILABILITY OF REPORT Unclassified/Unlimited		
2b. DECLASSIFICATION/DOWNGRADING SCHEDULE					
4. PERFORMING ORGANIZATION REPORT NUMBER(S) Technical Report No. 33			5. MONITORING ORGANIZATION REPORT NUMBER(S)		
6a. NAME OF PERFORMING ORGANIZATION Harvard University		6b. OFFICE SYMBOL (if applicable)	7a. NAME OF MONITORING ORGANIZATION Office of Naval Research		
6c. ADDRESS (City, State, and ZIP Code) Division of Applied Sciences Harvard University Cambridge, MA 02138			7b. ADDRESS (City, State, and ZIP Code) 800 N. Quincy Street Arlington, VA 22217		
8a. NAME OF FUNDING/SPONSORING ORGANIZATION Office of Naval Research		8b. OFFICE SYMBOL (if applicable)	9. PROCUREMENT INSTRUMENT IDENTIFICATION NUMBER N00014-89-J-1023		
8c. ADDRESS (City, State, and ZIP Code) 800 N. Quincy Street Arlington, Va 22217			10. SOURCE OF FUNDING NUMBERS		
			PROGRAM ELEMENT NO.	PROJECT NO.	TASK NO.
					WORK UNIT ACCESSION NO.
11. TITLE (Include Security Classification) Geometrical Effects in Two-Dimensional Arrays of Josephson Junctions					
12. PERSONAL AUTHOR(S) Lydia Lee Sohn					
13a. TYPE OF REPORT Interim (Technical)		13b. TIME COVERED FROM _____ TO _____		14. DATE OF REPORT (Year, Month, Day) May-92	
15. PAGE COUNT					
16. SUPPLEMENTARY NOTATION					
17. COSATI CODES			18. SUBJECT TERMS (Continue on reverse if necessary and identify by block number)		
FIELD	GROUP	SUB-GROUP			
19. ABSTRACT (Continue on reverse if necessary and identify by block number)					
<p>We present an extensive experimental and theoretical study of Josephson-junction arrays with both short- and long-range interaction. We first investigate the effects of current direction on the dynamical properties of rf and dc current-biased overdamped Josephson-junction arrays with short-range interaction in the presence of magnetic flux. We show that if the Lorentz force, produced by the transport current, acting on vortices is directed towards the island barrier, the array will behave like a set of coupled one-dimensional arrays and produce <i>only</i> integer giant Shapiro steps. If, however, the Lorentz force is directed towards any other direction, the array will produce <i>both</i> integer giant and fractional giant Shapiro steps. A moving vortex model and a pendulum model are used to describe our experimental and computational results.</p>					
20. DISTRIBUTION/AVAILABILITY OF ABSTRACT <input type="checkbox"/> UNCLASSIFIED/UNLIMITED <input type="checkbox"/> SAME AS RPT. <input type="checkbox"/> DTIC USERS			21. ABSTRACT SECURITY CLASSIFICATION		
22a. NAME OF RESPONSIBLE INDIVIDUAL			22b. TELEPHONE (Include Area Code)		22c. OFFICE SYMBOL

We then investigate underdamped Josephson-junction arrays with long-range interaction. These arrays consist of N horizontal and N vertical superconducting filaments arranged in two parallel planes separated by an oxide layer; consequently, every wire is Josephson-coupled to every other wire as nearest- or next-nearest-neighbors. Using Monte-Carlo simulations and a mean field approximation, we show that these novel arrays undergo a phase transition to a macroscopically phase-coherent state at $T_C = NE_J/2k_B$ in the zero field case. When a magnetic field, corresponding to a strongly commensurate number of flux quanta per unit cell, $f = p/q$, is present, $T_C = NE_J/2k_B \sqrt{q}$ for ordered arrays. For disordered arrays, T_C is defined for four different regimes of f . For $f < 1/N^2$, $T_C = NE_J/2k_B$. For $1/N^2 < f < 1/N$, $T_C = E_J/2k_B \sqrt{f}$, and for $1/N < f < 1$, T_C rises with f , although the exact form is presently unknown. For $f > 1$, T_C asymptotically approaches $-0.75E_J\sqrt{N}/k_B$.

Our ac measurements performed on these arrays show that they undergo the above phase transition at temperatures ranging from 3-5 K. We experimentally find that T_C is field-sensitive in ordered arrays but field-insensitive in disordered arrays. DC transport measurements reveal, among many things, that the arrays are *hysteretic* despite their consisting of *nonhysteretic* junctions. We show that the finite ratio of the wire inductance to the Josephson inductance limits the effective number of junctions along a given wire to $N_{eff} \ll N$.

Office of Naval Research

Grant N00014-89-J-1023

Grant N00014-89-J-1565

National Sciences Foundation Grant DMR-89-12927

National Sciences Foundation Grant DMR-89-20490

GEOMETRICAL EFFECTS IN TWO-DIMENSIONAL
ARRAYS OF JOSEPHSON JUNCTIONS



by

Lydia Lee Sohn

Technical Report No. 33

Accession For	
NTIS CRA&I	<input checked="checked" type="checkbox"/>
DTIC TAB	<input type="checkbox"/>
Unannounced	<input type="checkbox"/>
Justification	
By	
Distribution /	
Availability Codes	
Dist	Avail. and/or Special
A-1	

Reproduction in whole or in part is permitted for any purpose of the United States Government. Approved for public release; distribution unlimited.

May 1992

The research reported in this document was made possible through support extended the Division of Applied Sciences, Harvard University, by the Office of Naval Research, under Grants N00014-89-J-1023, N00014-89-J-1565 and by the National Sciences Foundation Grants DMR-89-12927 and DMR-89-20490.

Division of Applied Sciences
Harvard University · Cambridge, Massachusetts

© 1992 by Lydia Lee Sohn
All rights reserved.

ABSTRACT

We present an extensive experimental and theoretical study of Josephson-junction arrays with both short- and long-range interaction. We first investigate the effects of current direction on the dynamical properties of rf and dc current-biased overdamped Josephson-junction arrays with short-range interaction in the presence of magnetic flux. We show that if the Lorentz force, produced by the transport current, acting on vortices is directed towards the island barrier, the array will behave like a set of coupled one dimensional arrays and produce *only* integer giant Shapiro steps. If, however, the Lorentz force is directed towards any other direction, the array will produce *both* integer giant and fractional giant Shapiro steps. A moving vortex model and a pendulum model are used to describe our experimental and computational results.

We then investigate underdamped Josephson-junction arrays with long-range interaction. These arrays consist of N horizontal and N vertical superconducting filaments arranged in two parallel planes separated by an oxide layer; consequently, every wire is Josephson-coupled to every other wire as nearest- or next-nearest-neighbors. Using Monte-Carlo simulations and a mean field approximation, we show that these novel arrays undergo a phase transition to a macroscopically phase-coherent state at $T_C = NE_J/2k_B$ in the zero field case. When a magnetic field, corresponding to a strongly commensurate number of flux quanta per unit cell, $f = p/q$, is present, $T_C = NE_J/2k_B \sqrt{q}$ for ordered arrays. For disordered arrays, T_C is defined for four different regimes of f . For $f < 1/N^2$, $T_C \sim NE_J/2k_B$. For $1/N^2 < f < 1/N$, $T_C = E_J/2k_B \sqrt{f}$, and for $1/N < f < 1$, T_C rises with f , although the exact form is presently unknown. For $f > 1$, T_C asymptotically approaches $\sim 0.75 E_J \sqrt{N}/k_B$.

Our ac measurements performed on these arrays show that they undergo the above phase transition at temperatures ranging from 3-5 K. We experimentally find that T_C is field-sensitive in ordered arrays but field-insensitive in disordered arrays. DC transport

measurements reveal, among many things, that the arrays are *hysteretic* despite their consisting of *nonhysteretic* junctions. We show that the finite ratio of the wire inductance to the Josephson inductance limits the effective number of junctions along a given wire to $N_{eff} \ll N$.

TABLE OF CONTENTS

	page
ABSTRACT	iii
LIST OF FIGURES	ix
LIST OF TABLES	xii
CHAPTER I. INTRODUCTION	
1.1 Single Josephson Junctions	2
1.1.1 The RCSJ model	2
1.1.2 I - V characteristics	6
1.2 Josephson-Junction Arrays with Short-Range Interaction	8
1.2.1 Kosterlitz-Thouless phase transition	10
1.2.2 Frustration	12
1.2.3 Collective effects	15
1.3 Josephson-Junction Arrays with Long-Range Interaction	20
<i>PART A: THE EFFECTS OF CURRENT DIRECTION ON THE DYNAMICAL PROPERTIES OF JOSEPHSON-JUNCTION ARRAYS</i>	
CHAPTER II. EXPERIMENTAL DETAILS ON SNS ARRAYS	
2.1 Introduction	21
2.2 Fabrication	25
2.2.1 History	25
2.2.2 Array fabrication	26
2.3 Measurement Apparatus	33
2.4 Experiment	37

CHAPTER III. EXPERIMENTAL RESULTS

3.1	Introduction	39
3.2	Experimental Results	40
	3.2.1 Magnetoresistance	40
	3.2.2 Giant Shapiro steps	42
3.3	Summary of Results	51

CHAPTER IV. NUMERICAL SIMULATIONS

4.1	Introduction	52
4.2	Large Scale Simulations of [11] SNS Arrays	53
	4.2.1 Algorithm	53
	4.2.2 The results	56
	4.2.3 Possible evidence of spatial period doubling	61
4.3	Microscopic Model	66
	4.3.1 The 2 x 2 unit cell of the [11]-oriented square-lattice array	66
	4.3.2 $[10\bar{1}]$ -oriented triangular-lattice array	69
	4.3.3 $[2\bar{1}\bar{1}]$ -oriented triangular-lattice array	71
4.4	Conclusion	75

CHAPTER V. DISCUSSION

5.1	Introduction	76
5.2	The Moving Vortex Model	77
5.3	The Pendulum Model	84
5.4	Conclusion	90

PART B: ARRAYS WITH LONG-RANGE INTERACTION

CHAPTER VI. MEAN FIELD THEORY

6.1	Introduction	92
6.2	Mean Field Theory	96
	6.2.1 Ordered arrays	96

6.2.2	Disordered arrays	107
6.3	Discussion	109

CHAPTER VII. MONTE CARLO SIMULATIONS

7.1	Introduction	111
7.2	Metropolis Algorithm	111
7.3	Implementation of Metropolis Algorithm	114
7.4	Monte Carlo Results	116
7.4.1	Heat capacity	116
7.4.2	Phase-coherence modulus	123
7.5	Summary	125

CHAPTER VIII. EXPERIMENTAL DETAILS

8.1	Introduction	126
8.2	Fabrication	126
8.2.1	Array parameters	126
8.2.2	Mask design	127
8.2.3	Sample fabrication	129
8.3	Measurement Techniques	134
8.3.1	DC measurements	134
8.3.2	AC measurements	139
8.4	Results	142
8.4.1	DC measurements	142
8.4.2	AC measurements	151
8.5	Summary	157

CHAPTER IX. DISCUSSION

9.1	Introduction	158
9.2	DC Measurements	159
9.2.1	Model for critical currents	159
9.2.2	Voltage steps	166
9.2.3	Hysteresis	167
9.3	AC Measurements	168
9.4	Summary	169

CHAPTER X. SUMMARY AND SUGGESTIONS FOR FUTURE WORK

10.1	Summary	170
10.2	Future Research	172
REFERENCES		174
APPENDIX I	Fabrication of SNS Niobium-Copper-Niobium Arrays	178
APPENDIX II	Fabrication of SIS Niobium-Aluminum Oxide-Niobium Arrays	183
APPENDIX III	Fabrication of Niobium-Aluminum Oxide-Niobium Junctions	186
APPENDIX IV	Microfabrication Protocols	188
ACKNOWLEDGEMENTS		191

LIST OF FIGURES

	page
Fig. 1.1	Current-biased SIS Josephson junction 3
Fig. 1.2	RCSJ model schematic 5
Fig. 1.3	(a) I - V curve of an overdamped junction 7
	(b) I - V curve of an underdamped junction
Fig. 1.4	Square-lattice array schematic 9
Fig. 1.5	Resistive transition for a 1414×141 square-lattice array 11
Fig. 1.6	(a) $f=1/2$ superlattice 13
	(b) $f=1/3$ superlattice
Fig. 1.7	Vortex potential energy vs. position for one array unit cell 14
Fig. 1.8	Theoretical estimates for I_C vs. f and T_C vs. f 16
Fig. 1.9	Current vs. voltage curves for commensurate fields 18
Fig. 1.10	Array with long-range interaction schematic 19
Fig. 2.1	(a) $[10]$ -oriented square-lattice array schematic 22
	(b) 15° square-lattice array schematic
	(c) $[11]$ -oriented square-lattice array schematic
Fig. 2.2	(a) $[10\bar{1}]$ -oriented triangular-lattice array schematic 24
	(b) $[2\bar{1}\bar{1}]$ -oriented triangular-lattice array schematic
Fig. 2.3	Outline of the Nb-Cu bilayer fabrication process 27
Fig. 2.4	Outline of the array patterning and processing 29
Fig. 2.5	3- d schematic diagram of a portion of a square-lattice array 30
Fig. 2.6	SEM photograph of a square-lattice array 31
Fig. 2.7	3- d schematic diagram of a portion of a triangular-lattice array 32
Fig. 2.8	SEM photograph of a triangular-lattice array 34
Fig. 2.9	Measurement leads and circuit for array sample 35
Fig. 3.1	(a) Dynamic resistance vs. flux quanta for a square-lattice array 41
	(b) Dynamic resistance vs. flux quanta for a triangular-lattice array
Fig. 3.2	dV/dI vs. V for a $[10]$ -oriented square-lattice array in the presence of commensurate fields 43
Fig. 3.3	dV/dI vs. V for a $[11]$ -oriented square-lattice array in the presence of commensurate fields 45

Fig. 3.4	dV/dI vs. V for a 15° square-lattice array in the presence of commensurate fields	47
Fig. 3.5	dV/dI vs. V for a $[10\bar{1}]$ -oriented triangular-lattice array in the presence of fields	48
Fig. 3.6	dV/dI vs. V for a $[2\bar{1}\bar{1}]$ -oriented triangular-lattice array in the presence of commensurate fields	49
Fig. 4.1	Schematic of a 6×6 junction array with periodic boundaries	55
Fig. 4.2	Current vs. voltage curves for $f=0$ and $1/2$	57
Fig. 4.3	(a) Time evolution of supercurrents in a $[11]$ -oriented square-lattice array at the beginning of an rf cycle (b) Time evolution of supercurrents in a $[11]$ -oriented square-lattice array in the middle of an rf cycle (c) Time evolution of supercurrents in a $[11]$ -oriented square-lattice array at the end of an rf cycle	58
Fig. 4.4	Voltage wave forms for $f=1/2$ at low frequency	60
Fig. 4.5	Voltage wave forms for $f=1/2$ at high frequency	62
Fig. 4.6	(a) Supercurrent flow pattern of an array at $f=1/2$ and low frequency (b) Supercurrent flow pattern of an array at $f=1/2$ and high frequency	63
Fig. 4.7	2×2 unit cell of the $[11]$ -oriented square-lattice array	68
Fig. 4.8	Unit cell of the $[10\bar{1}]$ -oriented triangular-lattice array	70
Fig. 4.9	Stepwidth vs. rf power for the $[10\bar{1}]$ -oriented triangular-lattice array at $f=1/2$	72
Fig. 4.10	Unit cell of the $[2\bar{1}\bar{1}]$ -oriented triangular-lattice array	73
Fig. 4.11	Stepwidth vs. rf power for the $[2\bar{1}\bar{1}]$ -oriented triangular-lattice array at $f=0$	74
Fig. 5.1	Vortex configuration in the $[10]$ -oriented square-lattice array at $f=1/2$	78
Fig. 5.2	Vortex configuration in the $[11]$ -oriented square-lattice array at $f=1/2$	80
Fig. 5.3	Vortex configuration in the $[10\bar{1}]$ -oriented triangular-lattice array at $f=1/2$	81
Fig. 5.4	Vortex configuration in the $[2\bar{1}\bar{1}]$ -oriented triangular-lattice array at $f=1/2$	82
Fig. 5.5	(a) Gauge-invariant phase differences in a $[10]$ -oriented square-lattice array at $f=1/2$ and at the beginning of an rf cycle (b) Gauge-invariant phase differences in a $[10]$ -oriented square-lattice array at $f=1/2$ and at the end of an rf cycle (c) Pendulum diagram	86

Fig. 5.6	(a) Gauge-invariant phase differences in a $[11]$ -oriented square-lattice array at $f=1/2$	87
	(b) Pendulum diagram	
Fig. 5.7	(a) Gauge-invariant phase differences in a $[2\bar{1}\bar{1}]$ -oriented triangular-lattice array at $f=1/2$	89
	(b) Pendulum diagram	
Fig. 6.1	(a) Ordered array with long-range interaction schematic	93
	(b) Disordered array with long-range interaction schematic	
Fig. 6.2	Numerical solution of the ordered parameter	98
Fig. 6.3	Mean field prediction of heat capacity vs. temperature	101
Fig. 6.4	(a) Ground state configuration at $f=1/2$	102
	(b) Ground state configuration at $f=1/3$	
Fig. 6.5	Transition temperature vs. flux quanta in an infinite-sized ordered array	105
Fig. 6.6	Transition temperature vs. flux quanta in a finite-sized ordered array	106
Fig. 6.7	Transition temperature vs. flux quanta in a finite-sized disordered array	108
Fig. 7.1	Monte-Carlo results of heat capacity per wire vs. temperature for an ordered array	118
Fig. 7.2	Heat capacity per wire vs. temperature for an ordered array in the presence of commensurate fields	120
Fig. 7.3	Transition temperature vs. field, where $0 < f < 10$, for a 10% disordered array	121
Fig. 7.4	Transition temperature vs. field for a 50% disordered array	122
Fig. 7.5	Phase-coherence modulus vs. temperature	124
Fig. 8.1	(a) Mask I schematic	128
	(b) Mask II schematic	
Fig. 8.2	Outline of chlorobenzene process	132
Fig. 8.3	Completed array schematic	135
Fig. 8.4	SEM picture of an ordered array	136
Fig. 8.5	SEM picture of a disordered array	137
Fig. 8.6	(a) Current-feed orientation A	138
	(b) Current-feed orientation B	
Fig. 8.7	Two-coil mutual inductance apparatus schematic	140

Fig. 8.8	Set-up of experiment	141
Fig. 8.9	I - V curve of fabricated single tunnel junction	144
Fig. 8.10	I - V curves for differently fabricated single tunnel junctions	145
Fig. 8.11	(a) I - V curve of array with current-feed orientation A (b) I - V curve of array with current-feed orientation B	147
Fig. 8.12	Critical current vs. field for an ordered array	150
Fig. 8.13	(a) AC response vs. temperature of a 1000 x 1000 ordered array (b) AC response vs. temperature of a 600 x 600 disordered array	152
Fig. 8.13	T_c vs. f of an ordered array	153
Fig. 8.14	(a) Complex ac response vs. field of an ordered array at $T=4.25$ K (b) Complex ac response vs. field of an ordered array at $T=3.75$ K (c) Complex ac response vs. field of an ordered array at $T=3.5$ K	155
Fig. 8.15	Complex ac response vs. field of a disordered array	156
Fig. 9.1	Schematic drawing of a section of an array	161
Fig. 9.2	Comparison between data and theory for I_c	165

LIST OF TABLES

Table 3.1	Strengths of fractional giant Shapiro steps produced by the various array geometries	50
Table AIII.1	Critical current densities of differently fabricated Nb-Al ₂ O ₃ -Nb junctions	187

CHAPTER I

INTRODUCTION

Two-dimensional arrays of Josephson junctions are excellent realizations of a rich variety of 2- d systems in statistical physics. For example, in zero magnetic field, they model pure XY magnets; in finite fields, uniformly frustrated XY magnets. Since they can be fabricated in a controlled way with relative ease, Josephson-junction arrays are often used to study various problems associated with the phase transitions predicted for 2- d systems. Such problems include the Kosterlitz-Thouless vortex-unbinding transition, the effects of frustration on this phase transition, commensurate-incommensurate transitions, and the effects of disorder.¹

This work is both a theoretical and experimental study of arrays of classical Josephson junctions.² We examine the arrays not as models of any particular 2- d system; rather, we examine them *solely* as *arrays* of junctions. In particular, we concentrate on how the overall array geometry affects the collective behavior of the junctions. In one study, we inject the macroscopic transport current in different directions with respect to the array unit cell in arrays with *short-range* interaction, i.e. those arrays whose superconducting elements are *islands* which are Josephson-coupled to four or six nearest-neighbors. As we will show, this change in macroscopic current direction dramatically affects the phase-locking ability of the junctions when they are rf current-biased. In another study, we completely alter the physical configuration of our arrays such that they have *long-range* interaction, i.e. the arrays have superconducting elements which are now

¹See for instance, Kosterlitz and Thouless (1973); Lobb et al. (1983); Lobb (1984); and Mooij (1983b).

²We say *classical* in a sense that the junction area is large enough for the Josephson energy, $E_J = \hbar i_c / 2e$ to be much greater than the charging energy of a single electron transfer, $E_C = e^2 / 2C$. Here, i_c is the critical current of a single junction and C is the capacitance of that particular junction. For a thorough study of arrays in which $E_J < E_C$, see van der Zant, thesis (1991).

wires, all of which are Josephson-coupled to each other as nearest- or next-nearest neighbors. We find that the properties of these arrays are vastly different from those with short-range interaction.

This thesis is organized as follows. In this chapter, we provide the necessary foundation and motivation upon which much of this thesis is built. We then divide the thesis into two major parts with each part consisting of chapters on experiments/results, numerical analyses, and discussion. In part A, we examine the effect of current direction on the dynamical properties of arrays with *short-range* interaction. In part B, we investigate the ac and dc properties of arrays with *long-range* interaction. We conclude our work with a summary and suggestions for possible future work.

1.1 Single Josephson Junctions

1.1.1 The RCSJ model

As shown schematically in Fig. 1.1, a Josephson junction consists of two superconducting electrodes which are coupled together through a “weak” link. If the weak link is an insulator, the junction is referred to as SIS (superconductor-insulator-superconductor); if it is a normal metal, the junction is referred to as SNS (superconductor-normal-superconductor). Both SNS and SIS junctions have unique properties, one of which is that a zero-voltage supercurrent given by

$$i = i_c \sin(\phi_i - \phi_j - \psi_{ij}) \quad (1.1.1)$$

can flow through them [Josephson, 1962]. Here, i_c is the maximum supercurrent that can flow through the junction, and ϕ_i and ϕ_j are the phases of the Ginzburg-Landau wave functions describing the two superconducting electrodes, i and j . ψ_{ij} is the magnetic field

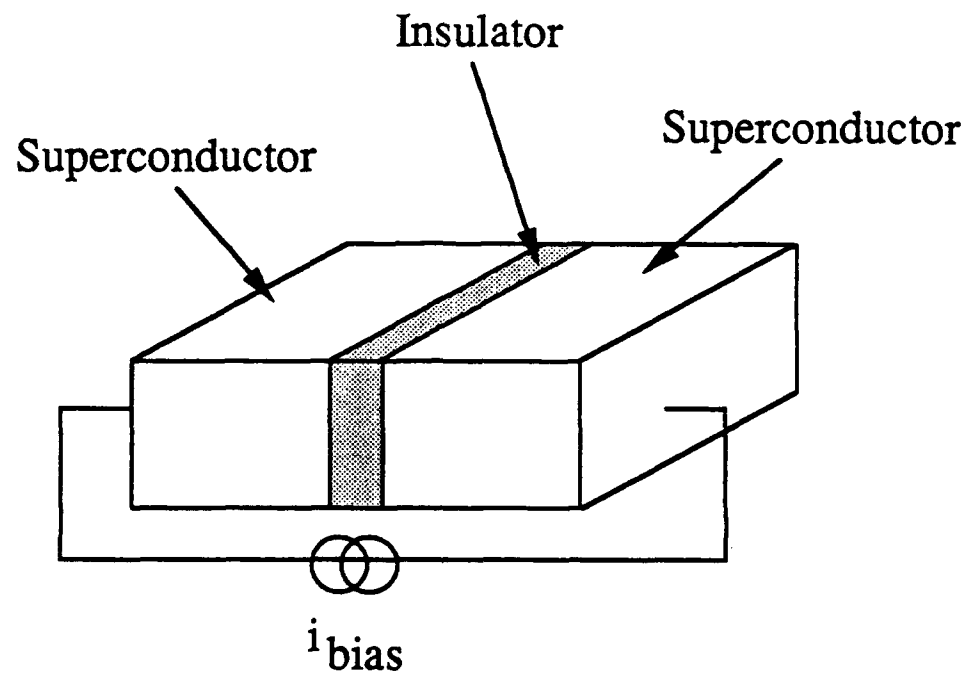


Fig. 1.1. Current-biased SIS Josephson junction.

contribution to the phase difference and is given by $(2\pi/\Phi_0)\int_i^j \vec{A} \cdot d\vec{\ell}$, where \vec{A} is the vector potential (arising from an applied magnetic field) and Φ_0 is the superconducting flux quantum. The strength of the energetic coupling between islands i and j is related to i_c by

$$E = -E_J \cos(\varphi_i - \varphi_j - \psi_{ij}) \quad (1.1.2)$$

where $E_J = \hbar i_c / 2e$. If the gauge-invariant phase difference, $\gamma_{ij} = \varphi_i - \varphi_j - \psi_{ij}$, changes with respect to time, a voltage difference across the junction develops

$$V = \frac{\hbar}{2e} \frac{d\gamma_{ij}}{dt} \quad (1.1.3)$$

[Josephson, 1962].

Single Josephson junctions have been extensively studied both theoretically and experimentally,³ and several models have been developed which accurately predict their behavior.⁴ One model in particular which will be used throughout this thesis is the resistively-capacitively-shunted-junction (RCSJ) model, developed independently by Stuart (1968) and McCumber (1968). As shown in Fig. 1.2, this model treats a junction as a nonlinear Josephson element with critical current, i_c , in parallel with a resistor r_n (representing the quasiparticles found in the system), and a capacitor C (reflecting the junction's parallel plate structure). If we current-bias this circuit as we would do to a junction, we obtain the equation,

$$i_{bias} = \frac{\hbar C}{2e} \frac{d^2\gamma}{dt^2} + \frac{\hbar}{2er_n} \frac{d\gamma}{dt} + i_c \sin \gamma \quad (1.1.4)$$

³See for example, Barone and Paterno (1982).

⁴See van Duzer (1981), p. 175 and the references therein.

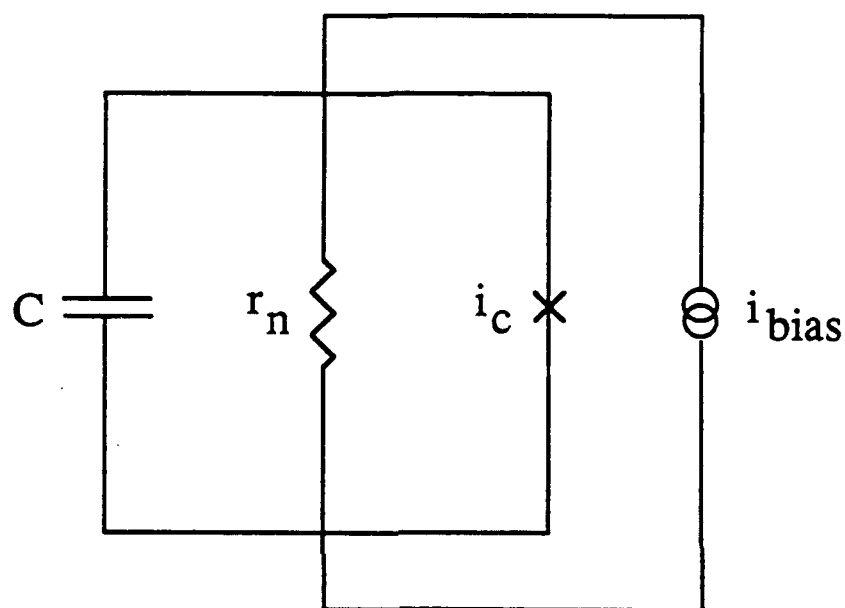


Fig. 1.2. Schematic diagram of the RCSJ model. The Josephson junction is modeled as a resistance, r_n , and a capacitance, C , in parallel with the supercurrent channel with critical current, i_c . The bias current, i_{bias} , is driving the junction.

This equation is completely analogous to the equation of motion of a particle with mass $\propto C$, moving in a cosinusoidal potential and subject to a viscous damping force which scales as $1/r_n$.⁵ Using Eq. (1.1.3), we can reduce the variables in Eq. (1.1.4) to dimensionless units, obtaining

$$\frac{ibias}{i_c} = \sin \gamma + \frac{d\gamma}{d\tau} + \beta_c \frac{d^2\gamma}{d\tau^2} \quad (1.1.5)$$

Here, $\tau = 2\pi\nu_c t$, where ν_c is defined as the junction's characteristic frequency, $\nu_c = 2e i_c r_n / \hbar$, and $\beta_c = 2e i_c r_n^2 C / \hbar$ is the McCumber parameter. When $\beta_c < 1$, the junction is considered *overdamped*; when $\beta_c > 1$, the junction is considered *underdamped*.

1.1.2 I-V characteristics

In SNS junctions, C is so small that $\beta_c \sim 0$. Consequently, Eq. (1.1.5) reduces to the first-order differential equation,

$$\frac{ibias}{i_c} = \frac{d\gamma}{d\tau} + \sin \gamma \quad (1.1.6)$$

To find the average value of voltage $V = \langle \hbar/2e \rangle d\gamma/d\tau$ for the system, we directly integrate Eq. (1.1.6) using $d\tau = 2\pi\nu_c dt$. If $ibias < i_c$, $V = 0$. If $ibias > i_c$, $V = i_c r_n \sqrt{(ibias/i_c)^2 - 1}$. Plotting this, we find the resulting I - V curve, as shown in Fig. 1.3a, is *non-hysteretic*.

In SIS junctions, C is *not* negligible and consequently, the resulting I - V curves are more complex than those of SNS junctions. As shown in Fig. 1.3b, if $\beta_c > 1$ the overall I - V curve is hysteretic. At i_c , V jumps discontinuously up to a finite voltage,

⁵This analogy has further been developed into what is called the "tilted-washboard" model. See Tinkham (1991), p. 8 and van Duzer (1981), p. 179.

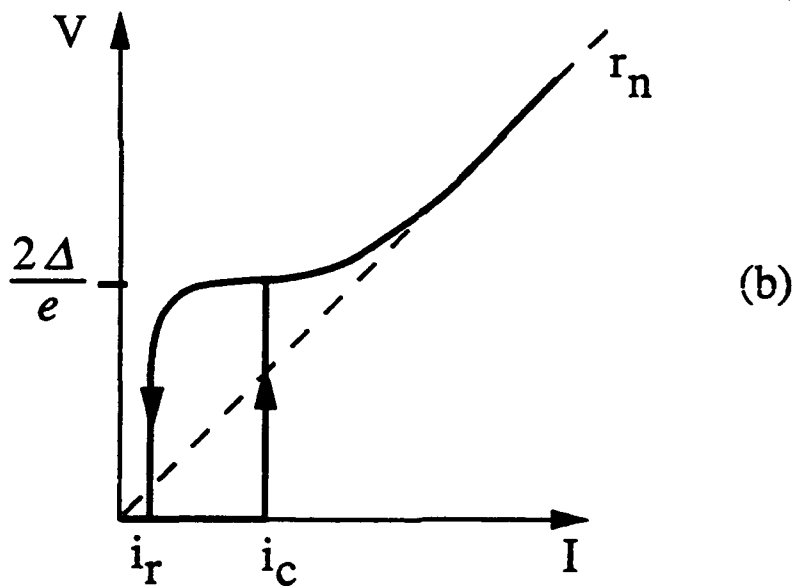
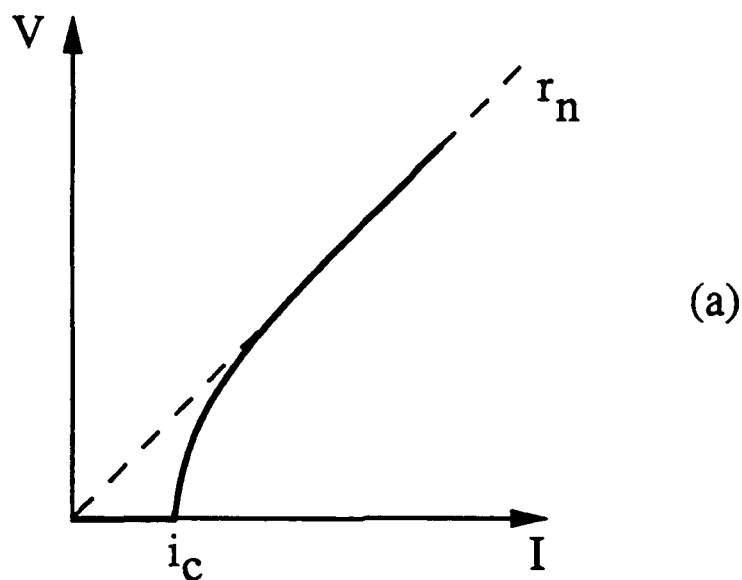


Fig. 1.3. Schematic drawings of the I - V curves for two different types of Josephson junctions. (a) For SNS junctions, the curve is clearly non-hysteretic. The dashed line represents r_n , the normal state resistance of the junction, and illustrates how the junction I - V curve approaches r_n at higher currents. (b) For SIS junctions, the curve is hysteretic. The voltage jumps discontinuously to near the value $V_g = 2\Delta/e$ at i_c , plateaus, and then smoothly increases, approaching the ohmic law, $V = ir_n$. The dashed line, again, represents r_n . When i is reduced, V does not drop back to zero until the retrapping current, i_r , is reached.

approximately equal to $V_g = 2\Delta/e = i_c r_n$ where Δ is the energy gap. It then smoothly increases, approaching the ohmic law, $V = i_{bias} r_n$. If i_{bias} is reduced below i_c , V does not drop back to zero until a retrapping current, $i_r = 4i_c/\pi Q$ where $Q = \sqrt{\beta_c}$, is reached.

1.2 Josephson Junction Arrays with Short-Range Interaction

Josephson-junction arrays with short-range interaction usually consist of superconducting islands that are arranged in a regular lattice and are coupled to their nearest neighbors by Josephson junctions (see Fig. 1.4). The Hamiltonian of the system is merely the sum of the coupling energies of the individual junctions [Eq. (1.1.2)] which make up the array,

$$H = - \sum_{\langle ij \rangle} E_J \cos(\varphi_i - \varphi_j - \psi_{ij}) \quad (1.2.1)$$

where the sum is over nearest-neighbor pairs of islands.⁶ Here, ψ_{ij} is constrained by

$$\sum \psi_{ij} = 2\pi(n + f) \quad n = 0, \pm 1, \pm 2, \dots \quad (1.2.2)$$

where the sum is around a single plaquette in the array and $f = Ha^2/\Phi_0$ (defined for a square-lattice array) is the number of flux quanta per plaquette and a is the lattice constant of the array. If no flux is applied and if that generated by the current is negligible, the upper bound of the array's critical current, I_c , is Ni_c where N is the number of junctions in parallel along the direction of the injected current. At $T=0$ and zero field, all the phases are equal and the array has long-range order. However, when $T>0$ or $H>0$, this long-range order is destroyed by two types of excitations, spin waves and vortices of positive (vortex)

⁶This Hamiltonian is completely analogous to that of XY magnet systems.

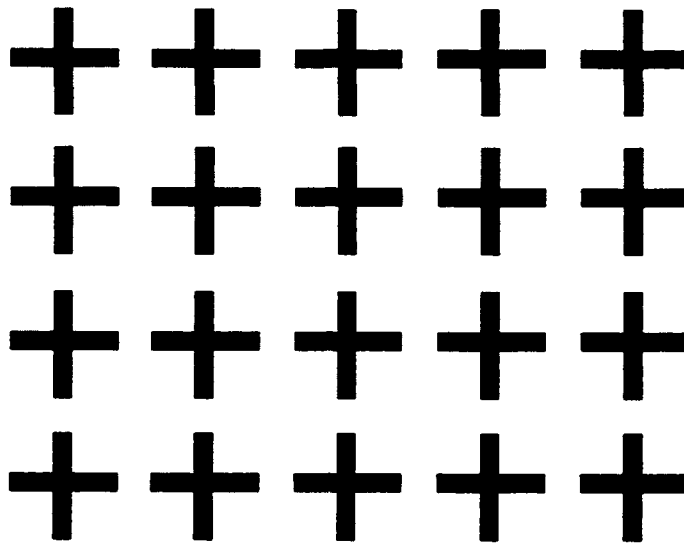


Fig. 1.4. Schematic drawing of a square-lattice array of Josephson junctions. The black crosses represent the superconducting islands, and the spaces between the legs of the crosses are the junctions. Each island, i , has a phase, ϕ_i , associated with it.

and negative (anti-vortex) circulating supercurrents. The importance of thermally-nucleated and field-induced vortices will become apparent in the following sections.

1.2.1 Kosterlitz-Thouless phase transition⁷

An important aspect of Josephson-junction arrays is that they can undergo a Kosterlitz-Thouless (K - T) phase transition [Kosterlitz and Thouless, 1973] at a temperature, T_{KT} . This phase transition occurs when thermally-nucleated vortex-antivortex pairs become bound in the arrays. To be more specific, when $T < T_{KT}$, all vortices are bound to each other as vortex-antivortex pairs. When a small bias current is applied to the system, the pairs will feel no Lorentz force and hence not drift across the sample since each pair has no *net* circulation. Thus, the array will have zero resistance. When $T > T_{KT}$, thermal excitations unbind some of the vortex-antivortex pairs, creating single vortices which are free to move when the bias current is now applied to the array. This movement contributes to the linear resistance of the array. The temperature, T_{KT} , at which the K - T transition occurs is determined by

$$k_B T_{KT} = \frac{\pi}{2} E_J^*(T_{KT}) \quad (1.2.3)$$

where $E_J^*(T_{KT})$ is the renormalized coupling energy that includes the effects of fluctuations from spin waves and vortices [Lobb et al., 1983 and Mooij, 1983b].

Fig. 1.5 shows the resistive transition of one of our fabricated arrays in zero field. As can be seen, a sharp decrease in resistance occurs at $T=8.75$ K, signifying the superconducting transition of the niobium (Nb) islands. The resistance reaches a plateau

⁷This section contains only a brief overview of the K - T transition in arrays. For a more complete discussion, see for example, Abraham, thesis (1983); Lobb et al. (1983); Mooij (1983b), Forrester, thesis (1988); and van der Zant, thesis (1991).

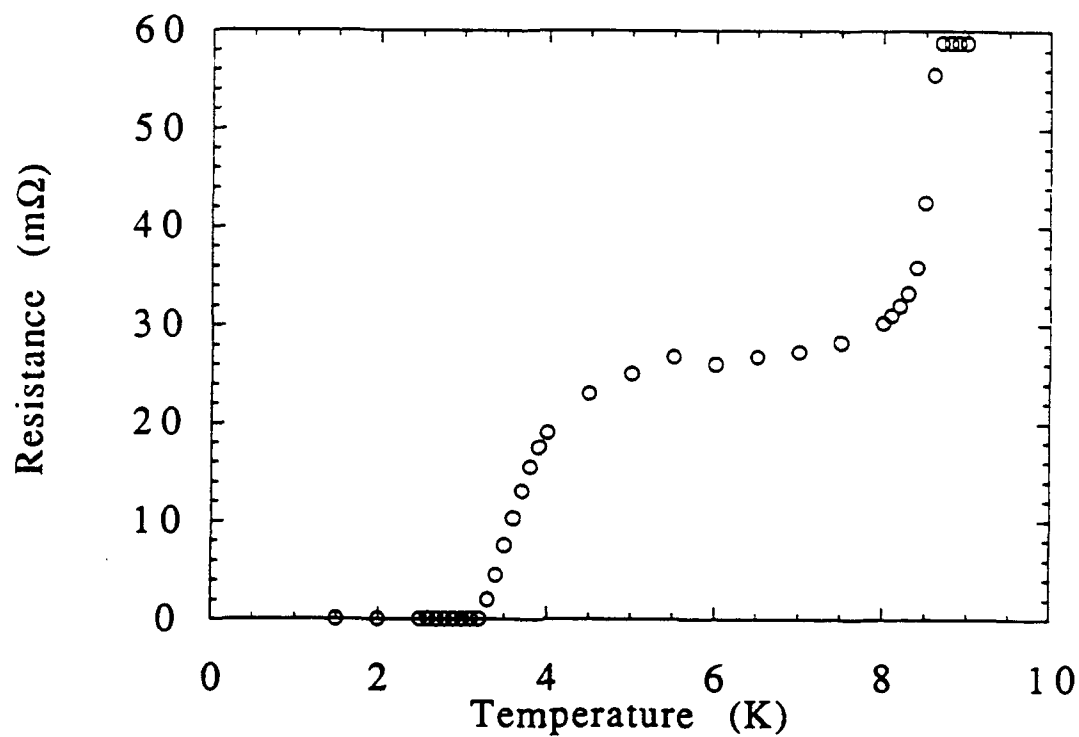


Fig. 1.5. The resistive transition of a 1414×141 square-lattice array of Josephson junctions in zero field. The sharp decrease in resistance at $T=8.75$ K is due to the Nb islands becoming superconducting. The drop to zero resistance at $T=3.5$ K is due to the Kosterlitz-Thouless phase transition.

between the temperatures 8 K and 4 K, which is essentially the resistance of the normal metal between the superconducting islands. It then undergoes another sharp decrease to zero at $T=3.5$ K, signalling the K - T transition. Below this temperature, only bound vortex-antivortex pairs are present in the array.⁸

1.2.2 Frustration

We can introduce frustration into the array by applying a transverse magnetic field, H , to the array. When this is done, field-induced vortices appear in the system and their motion is constrained by the array geometry and flux quantization. Ideally, when the average number of flux quanta per unit cell, $f=Ha^2/\Phi_0$ where a is the array-lattice constant (of a square array), is a ratio of two small integers, i.e. $f=p/q$, the field-induced vortices arrange themselves in a spatially periodic lattice which is *commensurate* with the underlying array lattice (see Fig. 1.6).

Teitel and Jayaprakash (1983b) have shown that the vortex superlattices for general fields, $f=p/q$, consist of $q \times q$ unit cells (see Fig. 1.6, again, for an illustration of two different vortex superlattices). The field-induced vortices arrange themselves in this superlattice because of their mutually repulsive interactions and their own interaction with the underlying array lattice. To a vortex, the array lattice is a periodic two-dimensional energy potential, and as shown in Fig. 1.7, this energy potential looks very much like an egg-carton [Rzchowski et al., 1990], with the peaks representing the four superconducting islands, the saddle points at the actual junctions, and the well at the center of the four nearest-neighbor junctions. When the vortex is centered in the well, it is in a stable state; therefore, the well is a pinning center for the vortex. Vortices can move from one well to

⁸Actually, nucleation of free vortices occur at *all* temperatures, $T>0$, due to the *finite* size of the fabricated arrays. However, because the number of free vortices in a finite-sized array is so small (one, on average at T_{KT}), the resistance caused by them is negligible compared to the effects studied in this research. See Abraham, thesis (1983) and Kadin et al. (1983).

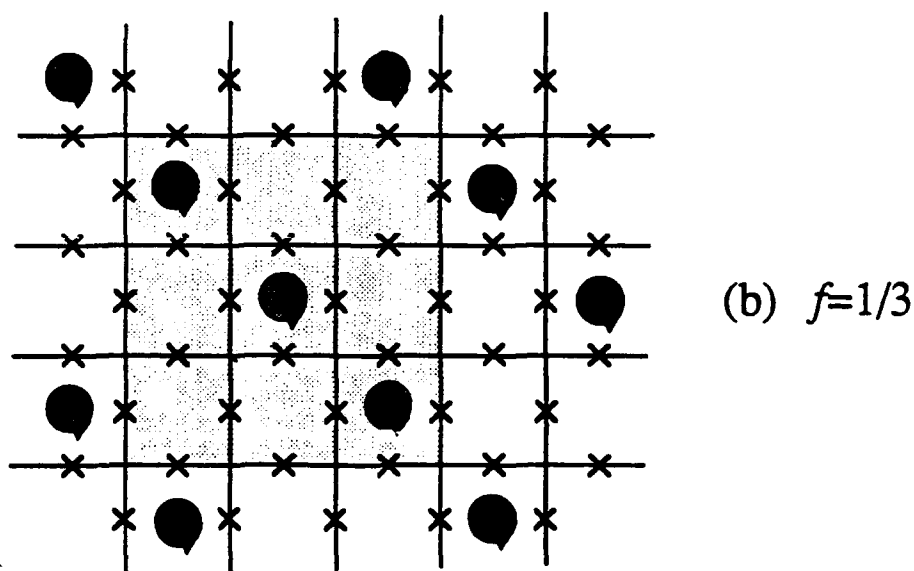
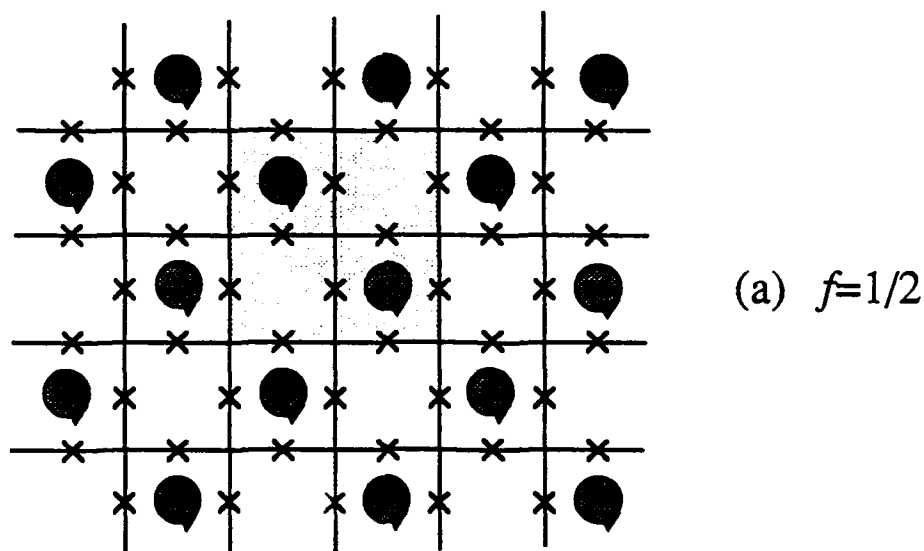


Fig. 1.6. Schematic diagram of a square-lattice array of Josephson junctions in the presence of a commensurate magnetic field, where the average number of flux quanta per unit array cell, f , is (a) $1/2$ and (b) $1/3$. The "x"s represent the positions of the junctions and the direction of the applied field is out of the page. The darkened circles with arrows represent the field-induced vortices, and they are arranged in a *superlattice* which is commensurate with the underlying array lattice. A unit cell of the superlattice is shown shaded in each of the diagrams.

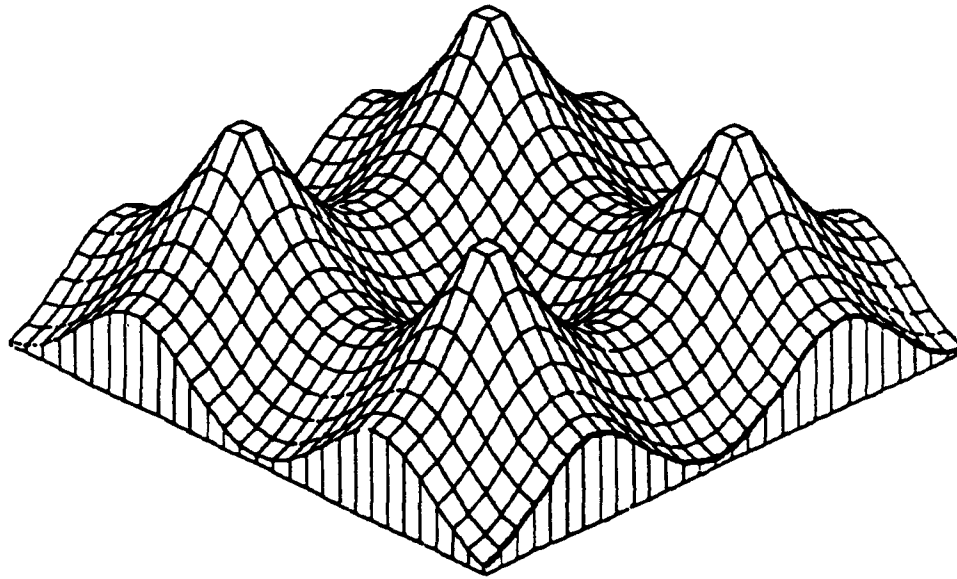


Fig. 1.7. The 2-d periodic vortex potential energy as a function of vortex position for a representative single unit cell in a square-lattice array [Rzchowski et al., 1990]. The four peaks corresponds to the junction islands and the saddle points, to the junctions themselves. The well corresponds to the center of the four nearest-neighbor junctions and is the position where the vortex rests in a unit cell. The energy barrier from the well to the saddle points on the junctions is $0.2E_J$ [Lobb et al., 1983].

the next only by crossing the low energy barrier of the egg-carton potential, calculated to be $0.2E_J$ [Lobb et al., 1983].

For all *integer* f , the vortex superlattice consist of vortices in every array unit cell. This results in no net field-induced currents through the junction, causing the array to behave as though it were in zero field. Fields in the range $1/2 < f < 1$ give currents identical to those for fields below $f' = (1-f)$ in the range $0 < f' < 1/2$, with the exception that all the current directions are reversed.⁹ For example, the superlattice for $f=2/3$ is identical to that for $f=1/3$ except that the current flow is in the opposite direction. Because of this symmetry about $f=1/2$ in addition to the symmetry between f and $-f$, or between f and $f+1$, we only need to investigate our arrays in fields where $0 \leq f \leq 1/2$.

The effects of different commensurate magnetic fields on both the array's critical current, I_C , and the temperature at which the array undergoes a resistive transition, T_C , have been theoretically and experimentally studied.¹⁰ Fig. 1.8 shows a theoretical calculation of I_C , as a function of f . Values of $T_C(f)$, where $k_B T_C(f) \leq (\hbar/2e) i_C(f)$, obtained from Monte Carlo simulations [Teitel and Jayaprakash, 1983b] are also plotted in this figure. Note that I_C and T_C are both periodic in f .

1.2.3 Collective effects

When a single overdamped Josephson junction is both dc and rf current-biased, the junction can phase-lock to the rf current at voltages

$$V_n = n \frac{\hbar v}{2e} \quad n = 0, 1, 2, \dots \quad (1.2.4)$$

⁹ $f=1/2$ is considered to be the fully-frustrated case in arrays because the vortices are most closely packed.

¹⁰See for instance, Teitel and Jayaprakash (1983a); Shih and Stroud (1983 and 1985); and Brown and Garland (1986).

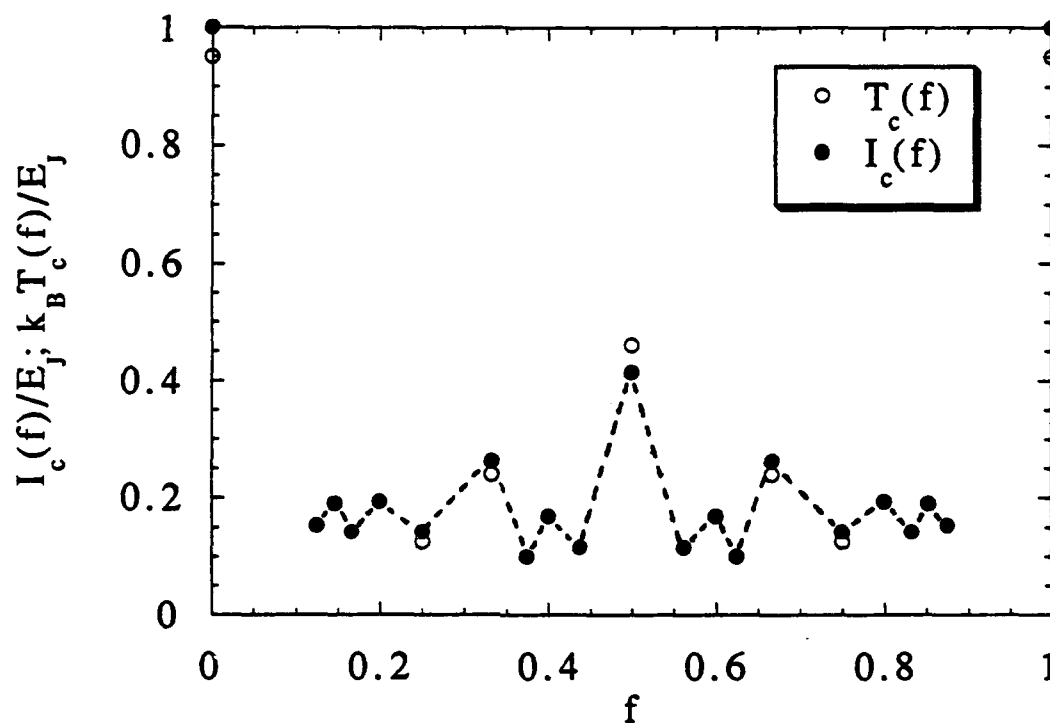


Fig. 1.8. Theoretical calculation of the zero-temperature critical current, $I_c(f)$, for different commensurate magnetic fields [Teitel and Jayaprakash, 1983b]. The zero-current critical temperature, $T_c(f)$, obtained from Monte Carlo simulations for fields, $f=0, 1/2, 1/3$, and $1/4$, is also plotted [Teitel and Jayaprakash, 1983b]. The dashed line is a guide to the eye only.

where ν is the rf frequency [Shapiro, 1963]. When this phase-locking occurs, we say that the junction is on its n th Shapiro step. Josephson junctions arranged in an $N \times M$ square-lattice array (where N is the number of junctions in the direction of the current flow) can also phase-lock with the rf current at voltages

$$V_n = n \left[\frac{N\hbar\nu}{2e} \right], \quad n = 0, 1, 2, \dots \quad (1.2.5)$$

[Clark, 1973 and Leeman et al., 1984]. When this collective effect occurs, i.e. when all the junctions are simultaneously on the n th Shapiro step, we say that the array is on its n th *giant* Shapiro step (see Fig. 1.9). In the presence of a transverse magnetic field which corresponds to a strongly commensurate number of flux quanta per plaquette, $f=p/q$, the array can again phase-lock to the rf current but at voltages

$$V_n = n \left[\frac{N\hbar\nu}{q2e} \right], \quad n = 0, 1, 2, \dots \text{ and } q = 1, 2, 3, \dots \quad (1.2.6)$$

[Benz et al., 1990; Free et al., 1990; K. H. Lee et al.; 1990; and H. C. Lee et al., 1990]. For $q>1$, these particular steps are named *fractional* giant Shapiro steps (again, see Fig. 1.9) and have been attributed to the driven motion (caused by a current-induced Lorentz force) of a superlattice of *field-induced* vortices commensurate with the underlying array lattice.

The collective effects in rf current-biased arrays we have just introduced all occur when the macroscopic transport current is injected along the $[10]$ direction of the array unit cell. The Lorentz force, caused by this current, directs the field-induced vortices across the *low* energy barrier of the array's egg-carton potential. The synchronized motion of these vortices with an applied rf current is what allows for fractional giant Shapiro steps to occur in the array. Using an analytical approach, Halsey (1990) has argued that arrays in which

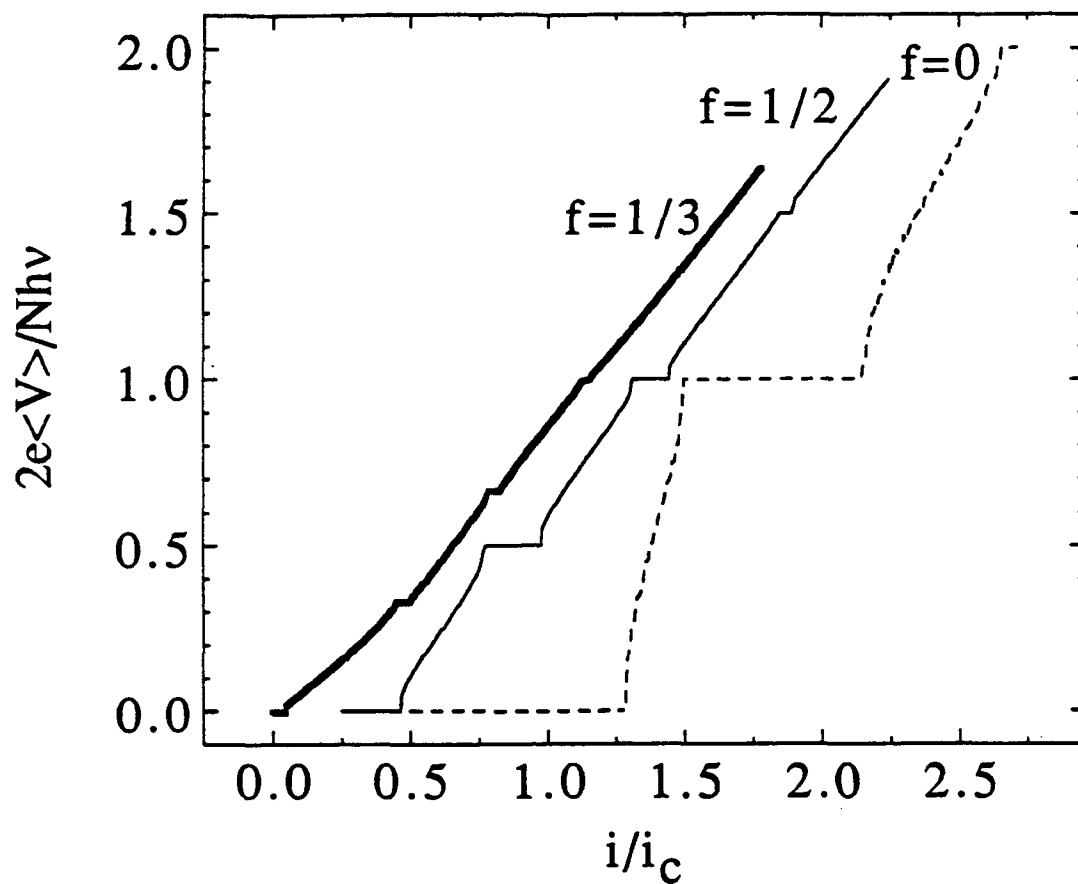


Fig. 1.9. Normalized voltage vs. normalized current per junction for an $N \times M$ array. Steps at integer values are integer giant Shapiro steps; steps at fractional values are fractional giant Shapiro steps [Free et al., 1990]. Curves $f=1/2$ and $f=0$ are shifted from the origin along the current axis by successive 0.25 increments.

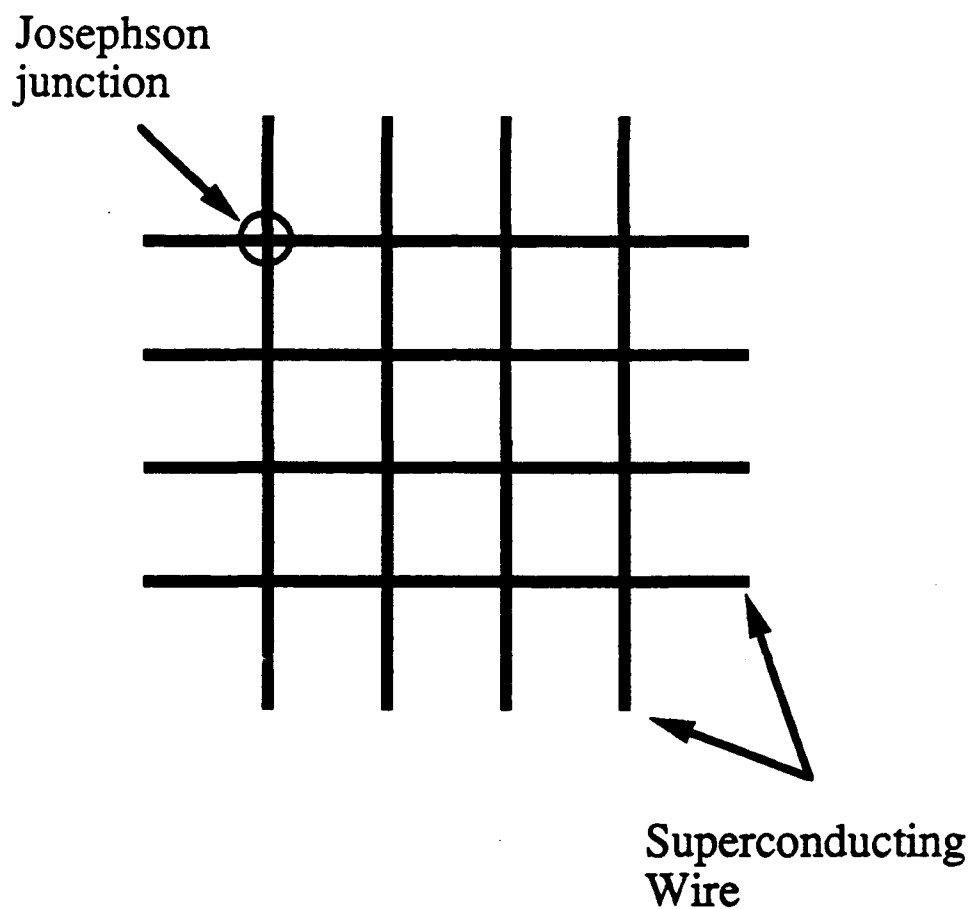


Fig. 1.10. 4 x 4 array with long-range interaction. Each black line represents a superconducting wire. Note that unlike the conventional arrays with short-range interaction (Fig. 1.4), all the wires in this array are Josephson-coupled together as nearest- or next-nearest neighbors.

current flows along the [11] direction of the array unit cell should also exhibit fractional giant Shapiro steps. Since the Lorentz force in these arrays directs the vortices against the *high* energy barrier of the egg-carton potential, and since the vortices, themselves, *cannot* cross over this barrier, two questions are immediately raised. What exactly is the vortex-superlattice motion and how does it allow fractional giant Shapiro steps to occur in the arrays? These intriguing questions are the motivation behind our work in part A.

1.3 Josephson-Junction Arrays with Long-Range Interaction

Although they have been *theoretically* studied in the disordered limit by Vinokur et al. (1987), arrays with long-range interaction have *not* been physically realized, and therefore experimentally studied, until now. In part B of this thesis, we will examine these novel arrays which consist entirely of N horizontal and N vertical superconducting filaments arranged in two parallel planes separated by an oxide layer. This configuration results in every wire being Josephson-coupled to every other wire in the array as nearest- or next-nearest neighbors (see Fig. 1.10). In the disordered limit, where every wire is randomly spaced from its neighbors, arrays with long-range interaction are predicted to behave like a spin glass, undergoing a phase transition to a macroscopically phase-coherent state at a temperature, T_C (Vinokur et al., 1987). Experimentally, we find that both the ordered and disordered arrays produce a strong diamagnetic response to an ac magnetic field at T_C , indicating that they have undergone the transition to their phase-coherent state. Our additional findings, reported in part B, show that these arrays are far *less* simple than early theoretical work [Vinokur et al., 1987 and Sohn et al., 1992b] had suggested.

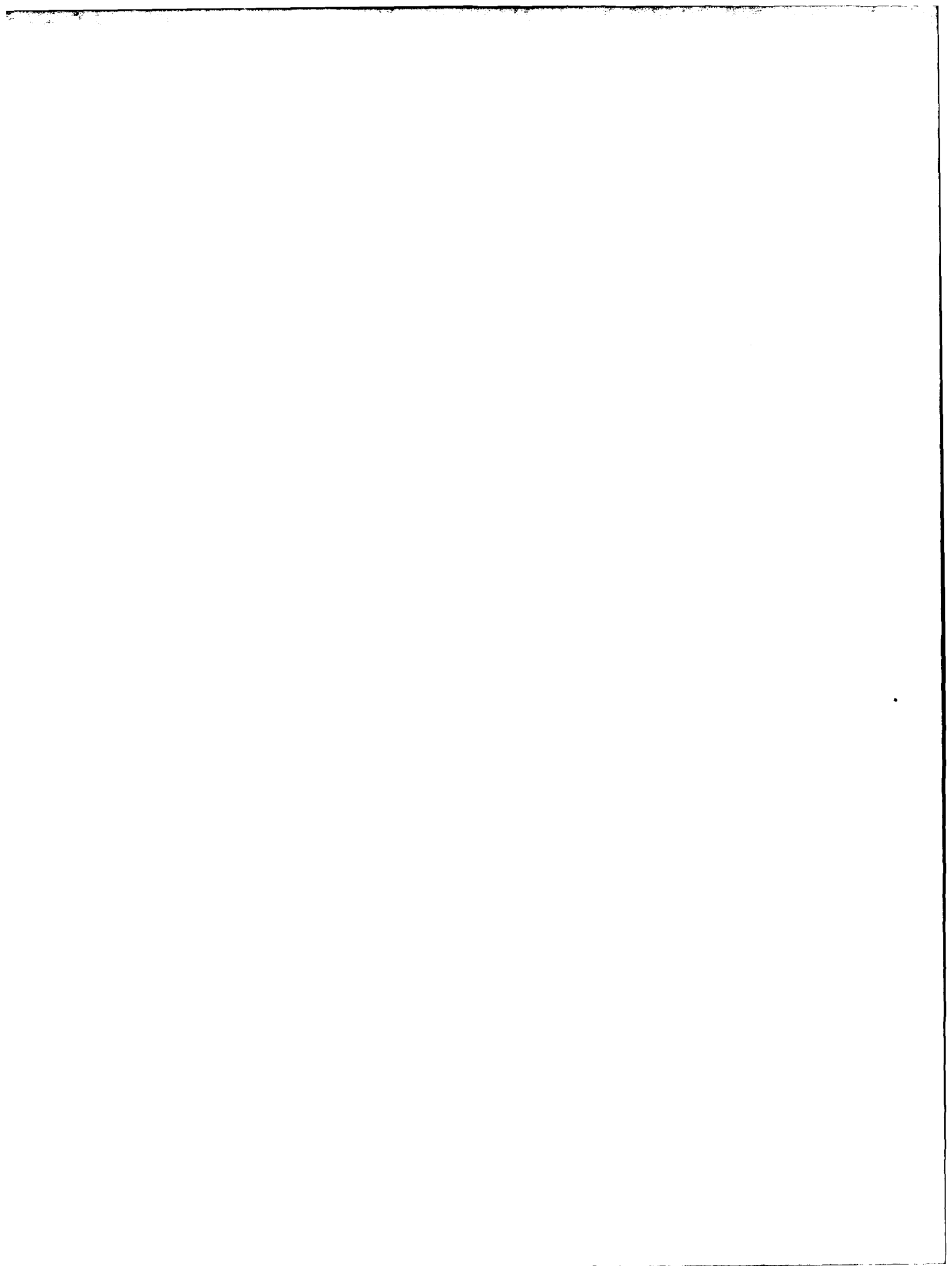
**PART A: THE EFFECTS OF CURRENT DIRECTION
ON THE DYNAMICAL PROPERTIES OF
JOSEPHSON-JUNCTION ARRAYS**

**CHAPTER II
EXPERIMENTAL DETAILS ON SNS ARRAYS**

2.1 Introduction

We first focus our attention to our discovery that changing the direction of the applied macroscopic current with respect to the array unit cell can greatly affect the dynamical properties of proximity-effect Josephson-junction arrays [Sohn et al., 1991 and 1992a]. We have found that square-lattice arrays in which the transport current is injected along the $[11]$ direction of the array (Fig. 2.1c) exhibit *only* integer giant and *not* fractional giant Shapiro steps. This surprising result is in stark contrast to the usual case in which the transport current is injected along the $[10]$ direction of the array (Fig. 2.1a). Arrays of this sort exhibit *both* integer giant and fractional giant Shapiro steps. As will be discussed in Chapter V, we attribute the difference between the two cases to the fact that all the junctions in the $[11]$ -oriented square-lattice array are directly injected with equal components of the macroscopic current (as is not the case for the $[10]$ -oriented square-lattice array). This results in the entire array behaving like a set of coupled one-dimensional arrays.

Since we believed that the suppression of fractional giant Shapiro steps in square-lattice arrays occurs gradually over a range of current angles with respect to the $[10]$ orientation, we have also measured square-lattice arrays in which the macroscopic current



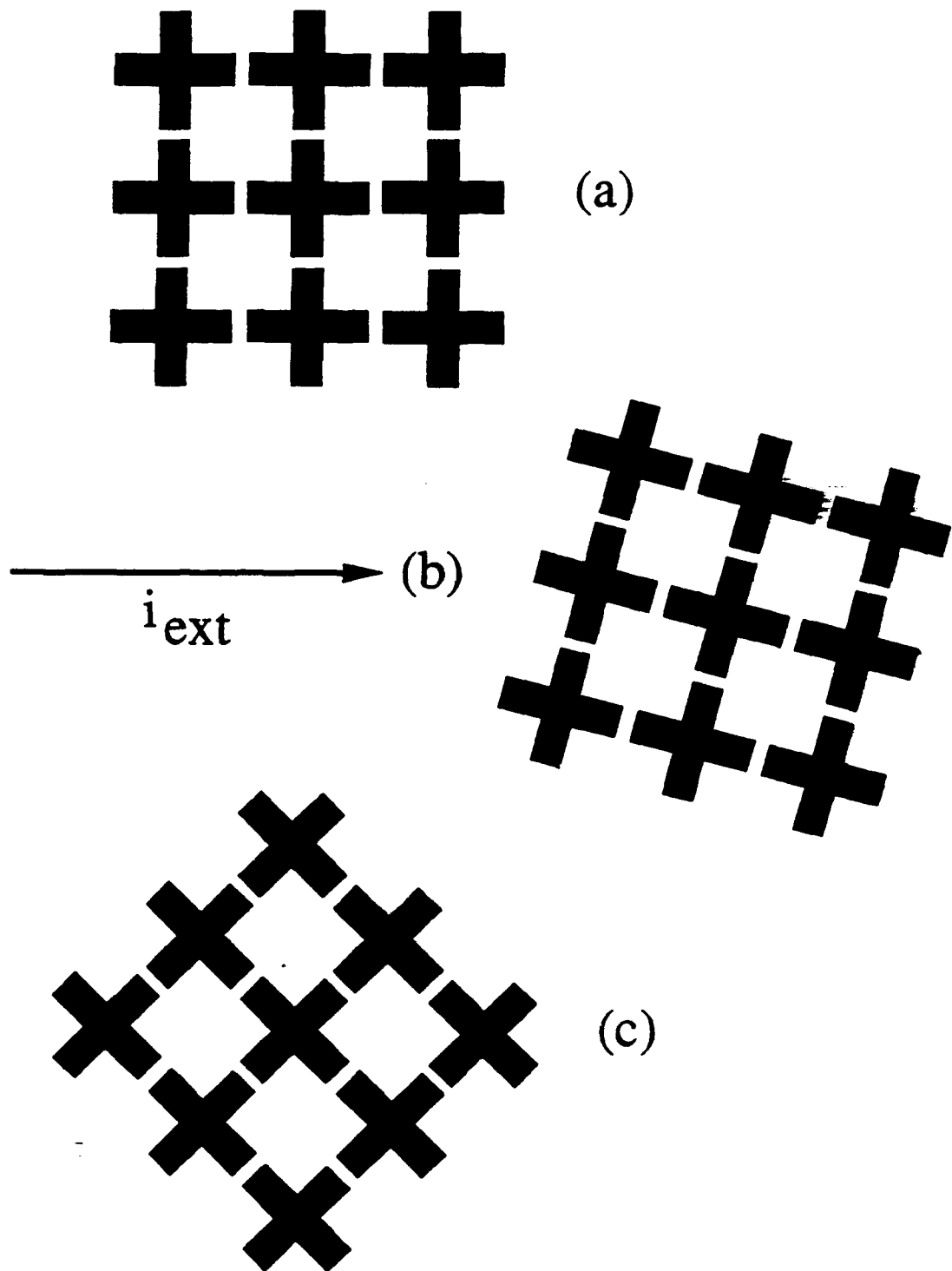


Fig. 2.1. Sections of the (a) [10], (b) 15°, and (c) [11] square-lattice arrays. The black crosses are Nb islands and the direction of the external current, i_{ext} , is as shown.

is injected at 15° with respect to the $[10]$ direction (Fig. 2.1b). Our measurements show that 15° arrays also exhibit fractional giant Shapiro steps, albeit small ones.

In addition to the square-lattice arrays, we have also studied triangular-lattice arrays, arrays in which each superconducting island is surrounded by six nearest neighbors in a close-packed geometry. These particular arrays are of special interest since they are a better model than the square-lattice geometry for naturally occurring grains in samples of granular superconductor. By changing the direction of the applied macroscopic current with respect to the array we were again able to affect the presence or absence of the fractional giant Shapiro steps in the array. In particular, we found that arrays in which the current is injected in the $[10\bar{1}]$ direction (Fig. 2.2a) exhibit *both* integer giant and fractional giant Shapiro steps. These arrays, like the $[10]$ -oriented square-lattice ones, have junctions which are perpendicular to the transport current and hence do not carry any component of the external current. Arrays in which the current is injected in the $[2\bar{1}\bar{1}]$ direction (Fig. 2.2b) exhibit *only* integer giant Shapiro steps. All the junctions in these arrays, like those of the $[11]$ -oriented square-lattice ones, are directly injected with the transport current. Based upon our results of both the square- and triangular-lattice arrays, we argue that if the Lorentz force, produced by the transport current, is directed towards the island barrier, then the array will behave like a set of coupled one-dimensional arrays and produce only integer giant Shapiro steps. If, however, the Lorentz force is directed towards any other direction, the array will produce *both* integer giant and fractional giant Shapiro steps.

In this chapter, we describe our method of fabricating the different geometric proximity-effect arrays we have just mentioned and our means of measuring them. We then follow with a presentation of our experimental results in Chapter III. To further understand these results, we have performed several different types of numerical simulations of the arrays we have experimentally studied. We describe these simulations and present their results in Chapter IV. In Chapter V, we discuss both our experimental and numerical results and draw our conclusions.

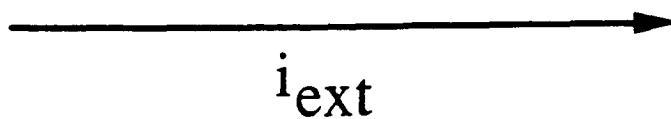
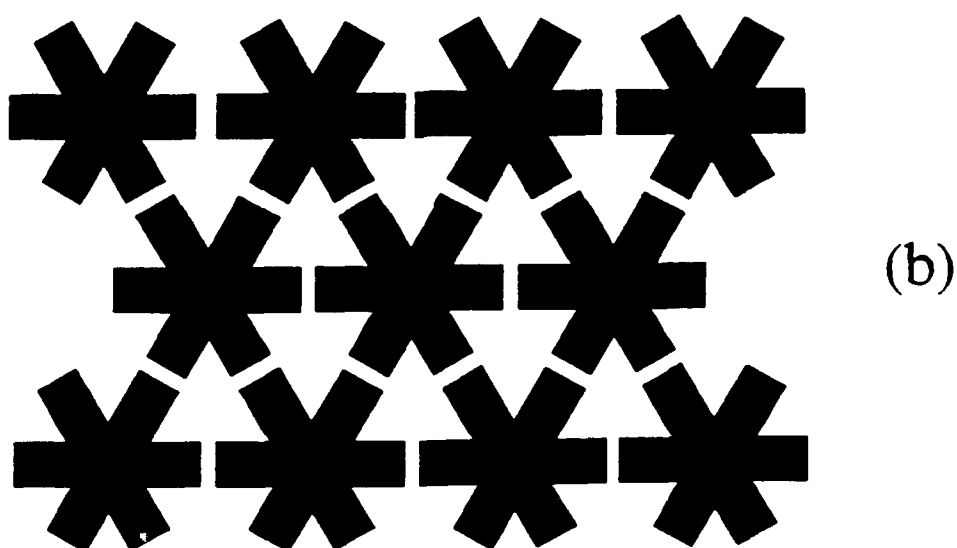
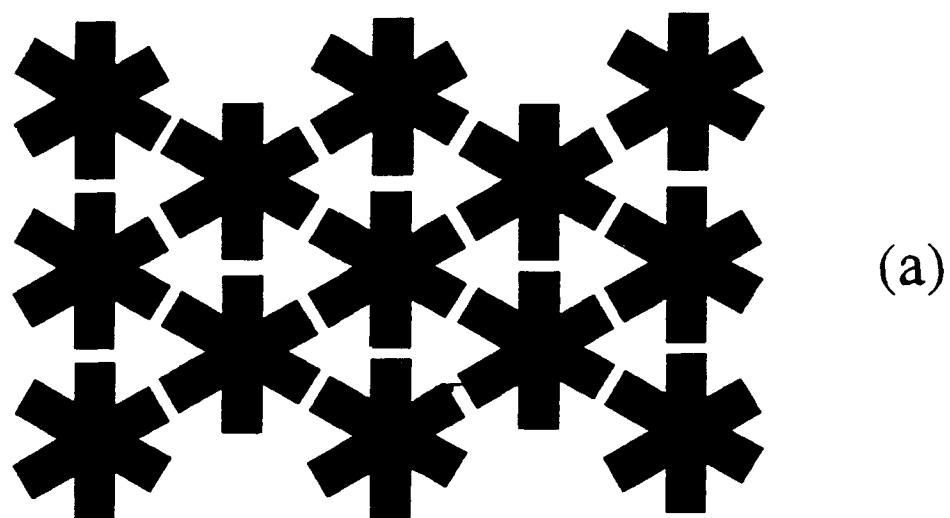


Fig. 2.2. Sections of the (a) $[10\bar{1}]$ and (b) $[2\bar{1}\bar{1}]$ triangular-lattice arrays. The black asterisks are Nb islands and the direction of the external current, i_{ext} , is as shown.

2.2 Fabrication

2.2.1 History

The very first proximity-effect arrays produced by this group were made by evaporating lead (Pb) through a fine metal mesh on top of a thin copper (Cu) film [Abraham, 1983]. The resulting SNS arrays were large (lattice constant, 75 μm) and the islands were *square*-shaped. Although much important work resulted from studying these arrays, including the identification of the Kosterlitz-Thouless phase transition in proximity-effect arrays, it soon became apparent that alternative methods for fabricating arrays were necessary since array nonuniformity and irreproducibility were ever-present problems in the fabrication process.

With recent advances in microfabrication technology, particularly in the area of photolithography, these particular obstacles were soon overcome, and in addition, the group gained greater flexibility in designing the microscopic geometry of the arrays. Arrays of *cross*-shaped Pb islands (lattice constant, 10 μm) on Cu film soon became the standard design for this group. Other geometries, including Sierpinski gaskets and arrays with deliberate positional disorder, were also designed and fabricated [Forrester, 1988]. Further improvements in SNS array fabrication included switching the superconducting material from Pb to niobium (Nb) [Benz, 1990]. The reasons for switching the superconducting material are threefold.¹ First, the refractory Nb is more robust than Pb and is recyclable. Second, Nb has a high superconducting transition temperature (9.2 K), therefore allowing for much higher and more easily accessible, Kosterlitz-Thouless transition temperatures. Third, the fabrication techniques associated with using Nb allow for greater flexibility, uniformity and control of the junction characteristics.

¹See Benz, thesis (1991) for specific details.

2.2.2 Array fabrication

The actual fabrication of two-dimensional square- and triangular-lattice SNS arrays is a multi-step process.² To create the Nb-Cu bilayer on which we will pattern the array, we first need to prepare a photoresist trilayer on a previously cleaned 1" x 1" x 0.025" polished sapphire substrate. The trilayer consists of an exposed layer of photoresist, a thin layer of aluminum (Al), and an additional layer of *unexposed* photoresist. We then expose the substrate to the "bilayer" mask using a 400 nm wavelength ultra-violet light from a Karl Suss (model MJB3) contact mask aligner.³ This mask defines not only the macroscopic geometry (10 mm x 1 mm and 10 mm x 3 mm) of the arrays but also the current and voltage pads. The sample is then developed and aluminum-etched to create an undercut (see Figure 2.3). The undercut is necessary to ensure nicely defined edges of the deposited metal bilayer.

After completing the above photolithography steps, we mount the sample onto a substrate holder in a thermal evaporator. We initially clean the substrate's surface with an rf argon (Ar) plasma in order to remove any water (H₂O) molecules that may have adhered to the surface and which would have prevented good adhesion of the Cu to the substrate's surface. Following the surface cleaning, we evaporate 0.35 μm of high purity Cu (99.999%) onto the substrate.

After thermal evaporation, we remove the substrate from the evaporator and mount it on a 50°F water-cooled substrate holder in a magnetron sputtering chamber. Since the Cu evaporation and Nb sputtering are not done *in situ*, it is necessary to clean the surface of the Cu using an rf Ar plasma. The Ar plasma removes the copper oxide (CuO₂) that formed

²For a detailed description of the fabrication process; see Appendix I.

³Bilayer masks were made using photolithography; see Appendix IV.

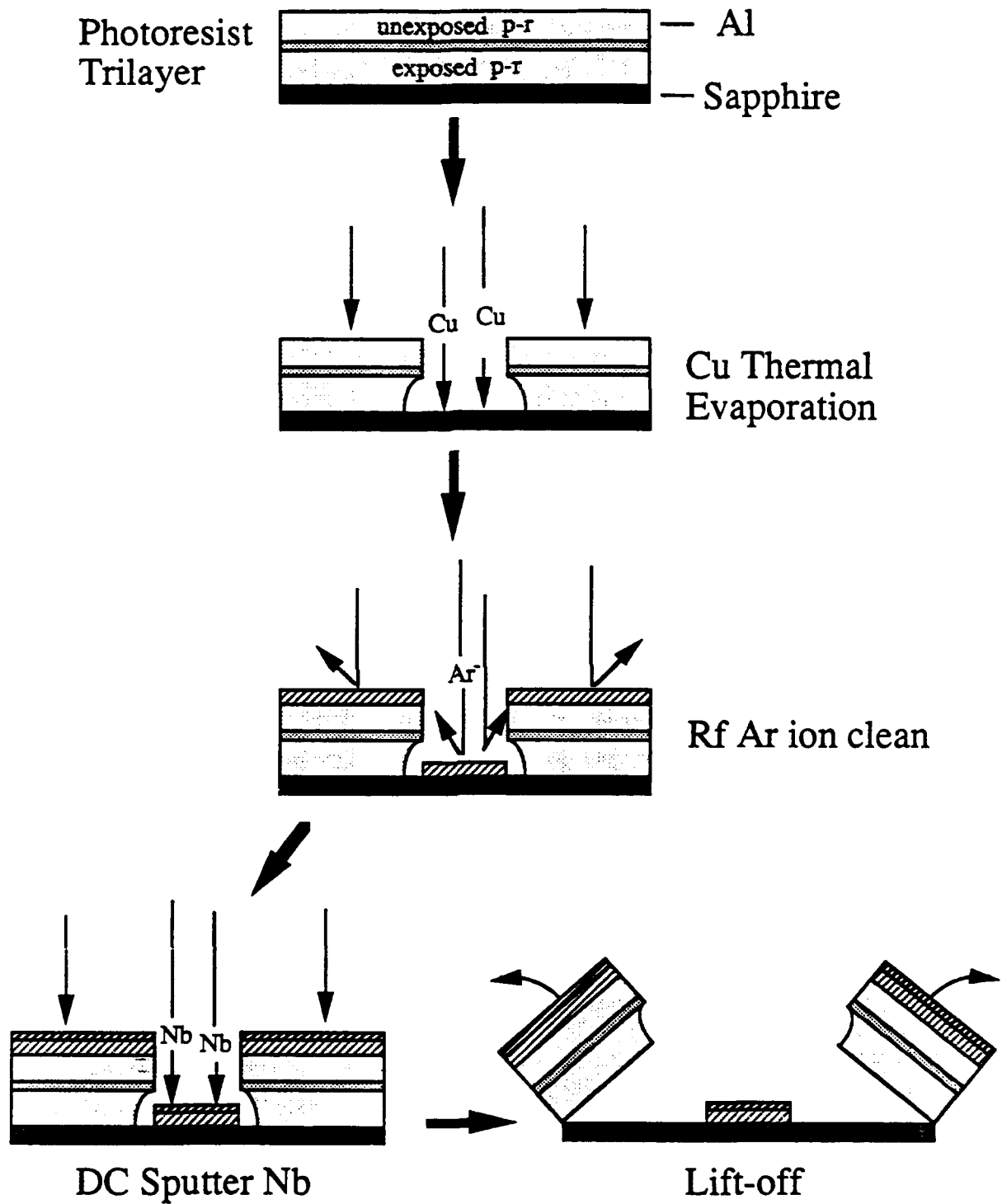


Fig. 2.3. Outline of the Nb-Cu bilayer fabrication process.

during the sample's exposure to air, thus ensuring a good interface between the Cu and the Nb. Approximately 50 nm of the CuO₂-Cu layer is removed using the rf Ar plasma and 0.2 μm of Nb (Nb purity, 99.9975%) is immediately (within 5 sec) sputtered onto the Cu surface. A simple liftoff of the photoresist using acetone, a photoresist solvent, is then done, leaving behind only the Cu-Nb bilayer on the substrate (see Fig. 2.3).

To pattern the junctions, we spin *inverting* photoresist (Hoechst AZ-5214E) onto the bilayer substrate.⁴ We use inverting photoresist, rather than the standard photoresist (Shipley 1400-27), because it is an ideal photoresist with which to perform reactive-ion etching. Arrays of junctions whose macroscopic current is injected along the [10] and [11] direction of the array unit cell are patterned merely by appropriately rotating the array mask⁵ with respect to the current pads and then exposing to UV light. This method is also used to pattern the 15° array. Once developed, the islands are formed using SF₆ reactive-ion-etching. We use SF₆ because the fluorine ions are selective only to Nb and not to Cu. Once the etching is completed, the photoresist is removed by placing the sample in a heated solution of photoresist stripper (see Fig. 2.4). The lattice constant for the square-lattice arrays is 10 μm and the junction length is 2 μm (see Fig. 2.5). The completed [10] oriented arrays contain 1000 x 100 junctions, the [11] arrays 1414 x 141, and the 15° array, 967 x 97. A SEM picture of the [10] oriented array is shown in Fig. 2.6.

The triangular-lattice arrays we measured are similarly made. Nb six-sided asterisk islands, whose lattice constant is 14 μm and junction length 2 μm (see Fig. 2.7),⁶ are patterned (and again, formed using SF₆ reactive-ion-etching) such that the macroscopic

⁴With inverting photoresist, only the unexposed areas will develop.

⁵Array masks were made by Advanced Reproductions, Andover MA.

⁶It would have been preferable to use a lattice constant of 10 μm in order to better compare the results of the measured triangular-lattice arrays with those of the square-lattice ones. However, had we in fact used this lattice constant and kept the junction length to 2 μm , the asterisk islands would be much too compact for us to easily fabricate the arrays. Hence, this is the reason we chose a lattice constant of 14 μm for our triangular-lattice arrays.

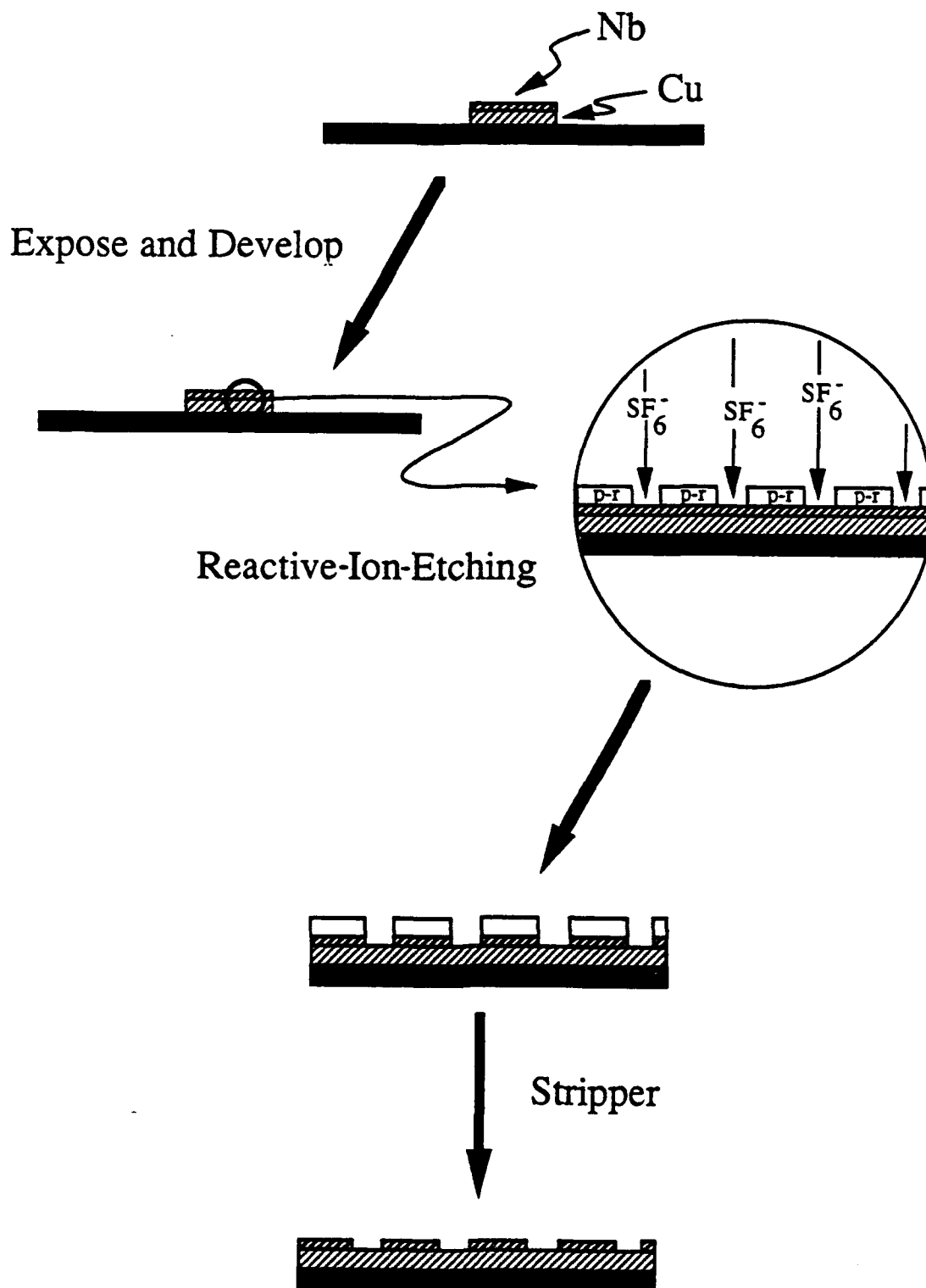


Fig. 2.4. Outline of array patterning and processing.

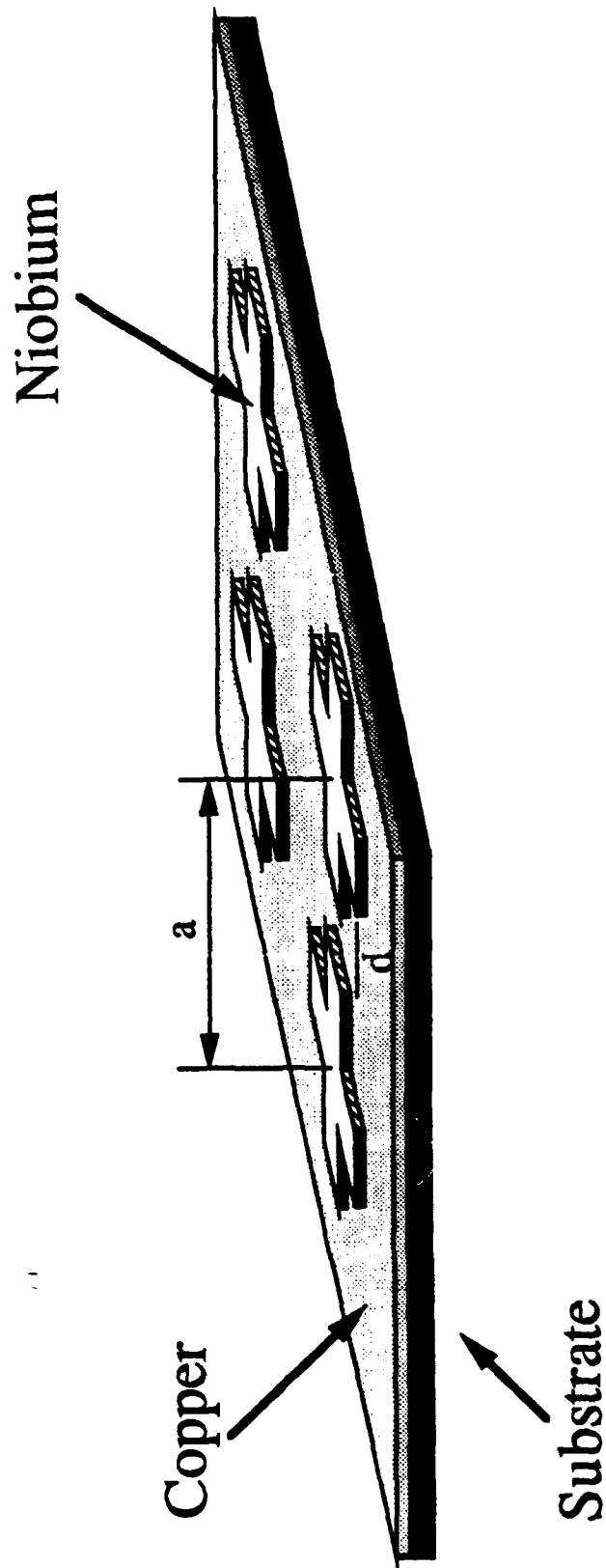


Fig. 2.5. 3- d schematic diagram showing a region of a completed square-lattice array. The junction region lies between the tips of the crosses, having length $d=2\text{ }\mu\text{m}$. The lattice constant is $a=10\text{ }\mu\text{m}$. Film thicknesses are $0.2\text{ }\mu\text{m}$ of Nb and $0.3\text{ }\mu\text{m}$ of Cu. The sapphire substrate is $0.025''$ thick.

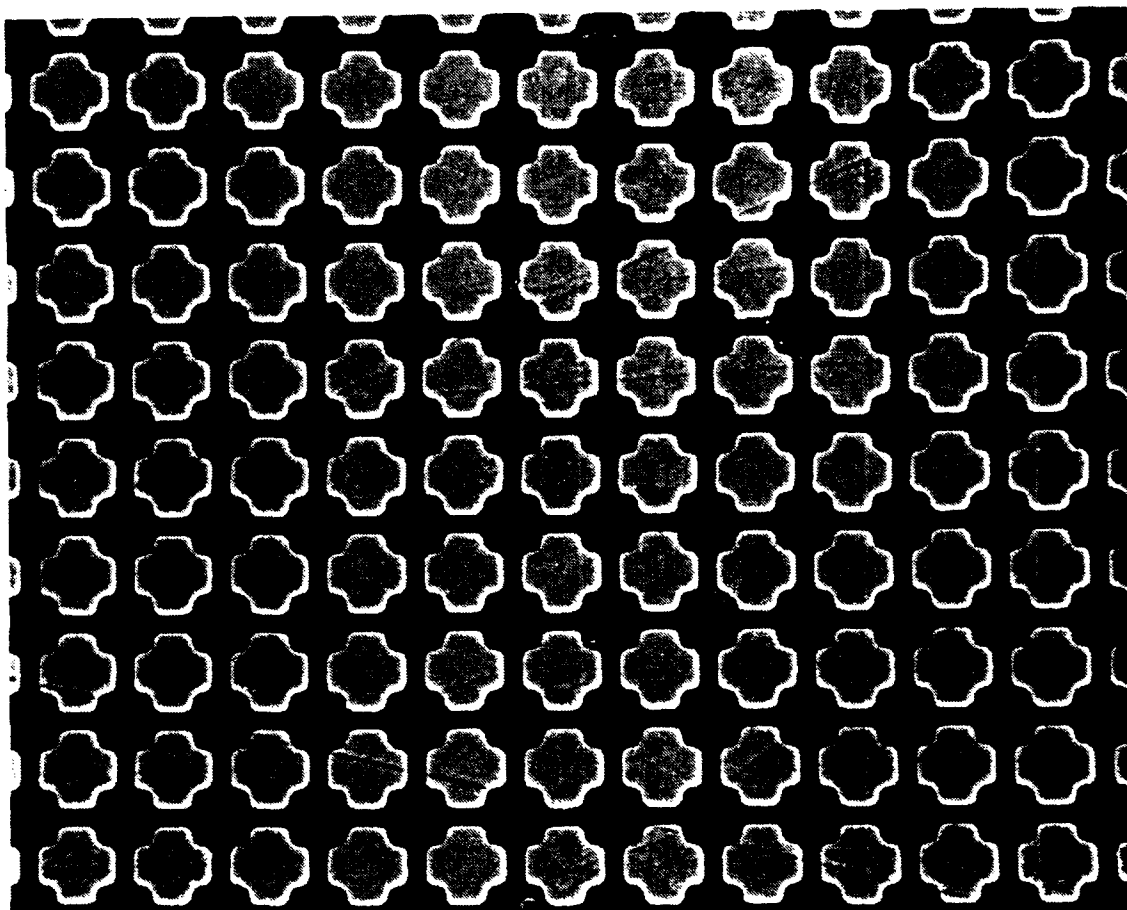


Fig. 2.6. SEM picture of an actual square-lattice array. The lattice constant is $10\text{ }\mu\text{m}$ and the junction length is $2\text{ }\mu\text{m}$.

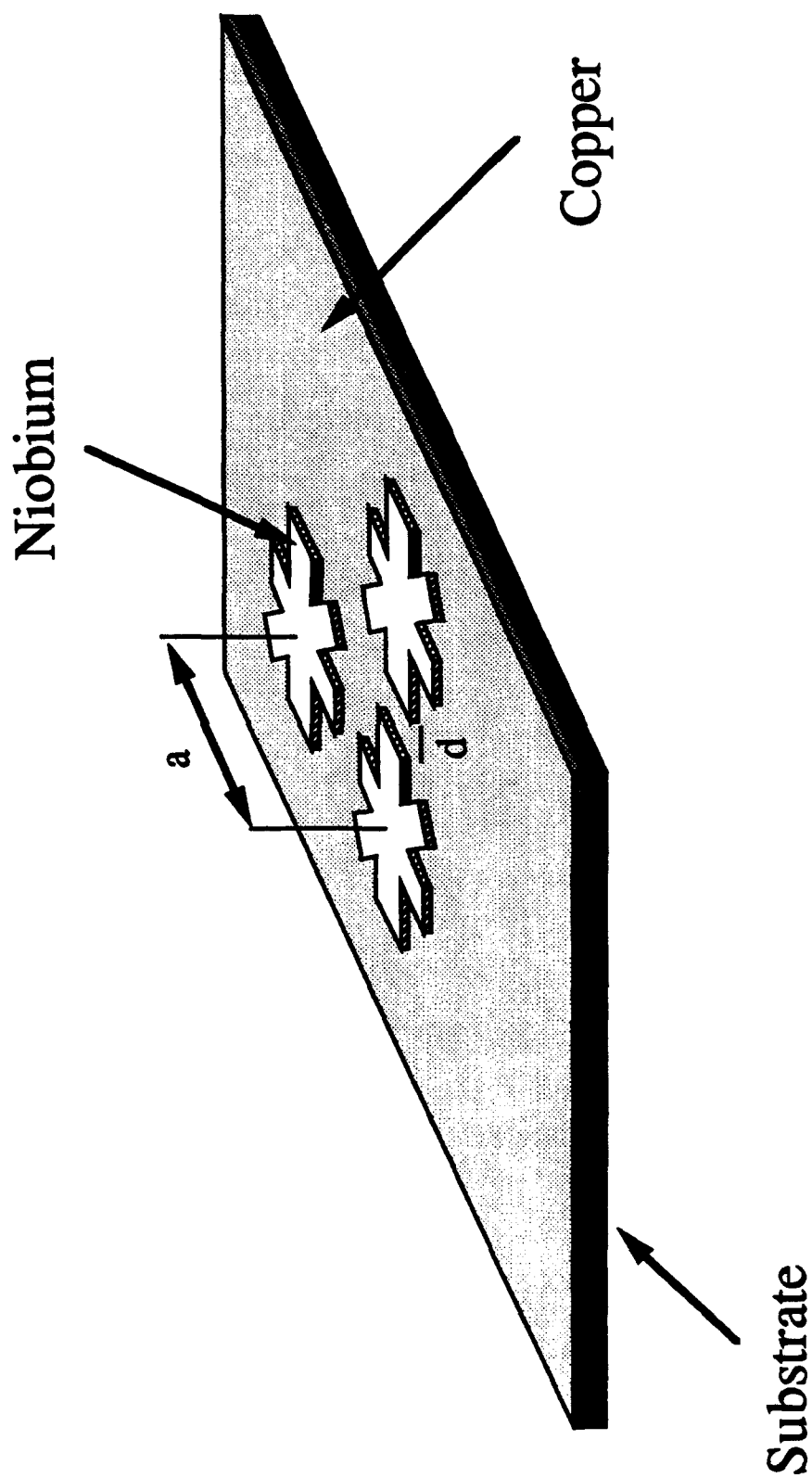


Fig. 2.7. 3- d schematic diagram showing a region of a completed triangular-lattice array. The junction region lies between the tips of the crosses, having length $d=2\text{ }\mu\text{m}$. The lattice constant is $a=14\text{ }\mu\text{m}$. Film thicknesses are $0.2\text{ }\mu\text{m}$ of Nb and $0.3\text{ }\mu\text{m}$ of Cu. The sapphire substrate is $0.025''$ thick.

current is injected along the $[10\bar{1}]$ and $[2\bar{1}\bar{1}]$ direction of the array unit cell. Again, the differently oriented arrays are patterned by simply changing the orientation of the mask with respect to the current injection pads and then exposing to UV light. While the $[10\bar{1}]$ triangular-lattice array contains 722×188 junctions, the $[2\bar{1}\bar{1}]$ array contains 625×217 junctions. A SEM picture of the $[10\bar{1}]$ oriented array is shown in Fig. 2.8.

All of the Josephson-junction arrays we fabricated have normal metal pads. The reason for this is that we wanted to avoid field-screening effects from large superconducting areas and thus improve the uniformity of the applied magnetic field in the array. The current pads are chosen to be normal also because we wanted the array to be evenly injected with the bias current. The excess islands on the current pads (as shown in Fig. 2.9) on some of the arrays are unimportant since the bias current still has time to spread itself uniformly before actually reaching the $N \times M$ array.

2.3 Measurement Apparatus

The measurement rig used to make the four-point measurements on the SNS arrays is one which was originally designed and built by D. Abraham (1983) and modified by M. Forrester (1988). Since a detailed description and diagram of the rig can be found in the thesis of Abraham (1983), we will only review its main features here. The rig has a temperature-controlled Cu substrate block inside a Pb-free "Naval Brass" vacuum can. It has been modified over the years to reduce the number of solder joints near the sample block, thus minimizing the field non-uniformity caused by the superconducting solder. On the outside of the vacuum can is a 10 cm long, 5.5 cm diameter copper solenoid. This solenoid can produce a uniform magnetic field (~ 13 mA/Gauss) perpendicular to the sample inside. The current and voltage leads have been rewired by us and consist of twisted pairs of 36 gauge copper wire. The wires are wound with many turns onto two separate copper block stages at the bottom of the rig in order to improve the heat sinking of the leads and to

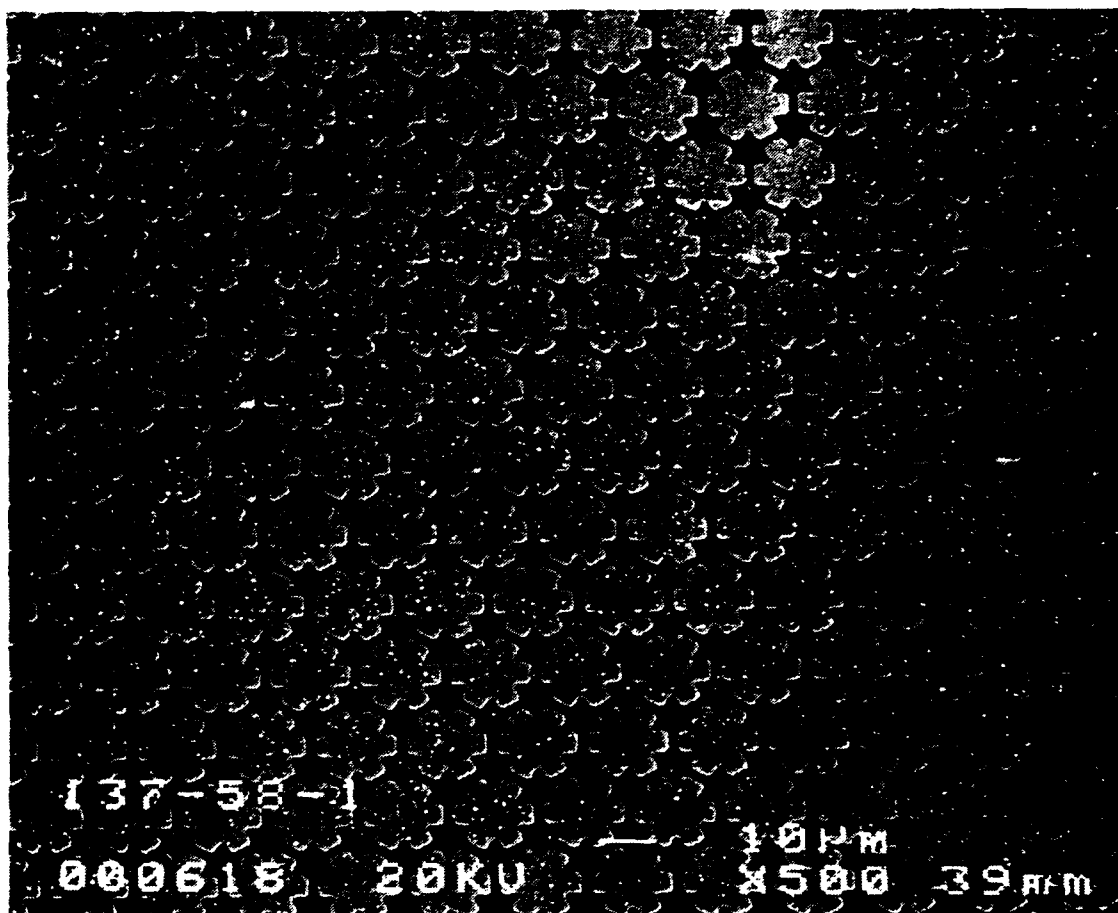


Fig. 2.8. SEM photograph of a triangular-lattice array. The lattice constant is $14\text{ }\mu\text{m}$ and the junction length is $2\text{ }\mu\text{m}$. The white nonconductive "spots" are of unknown origin.

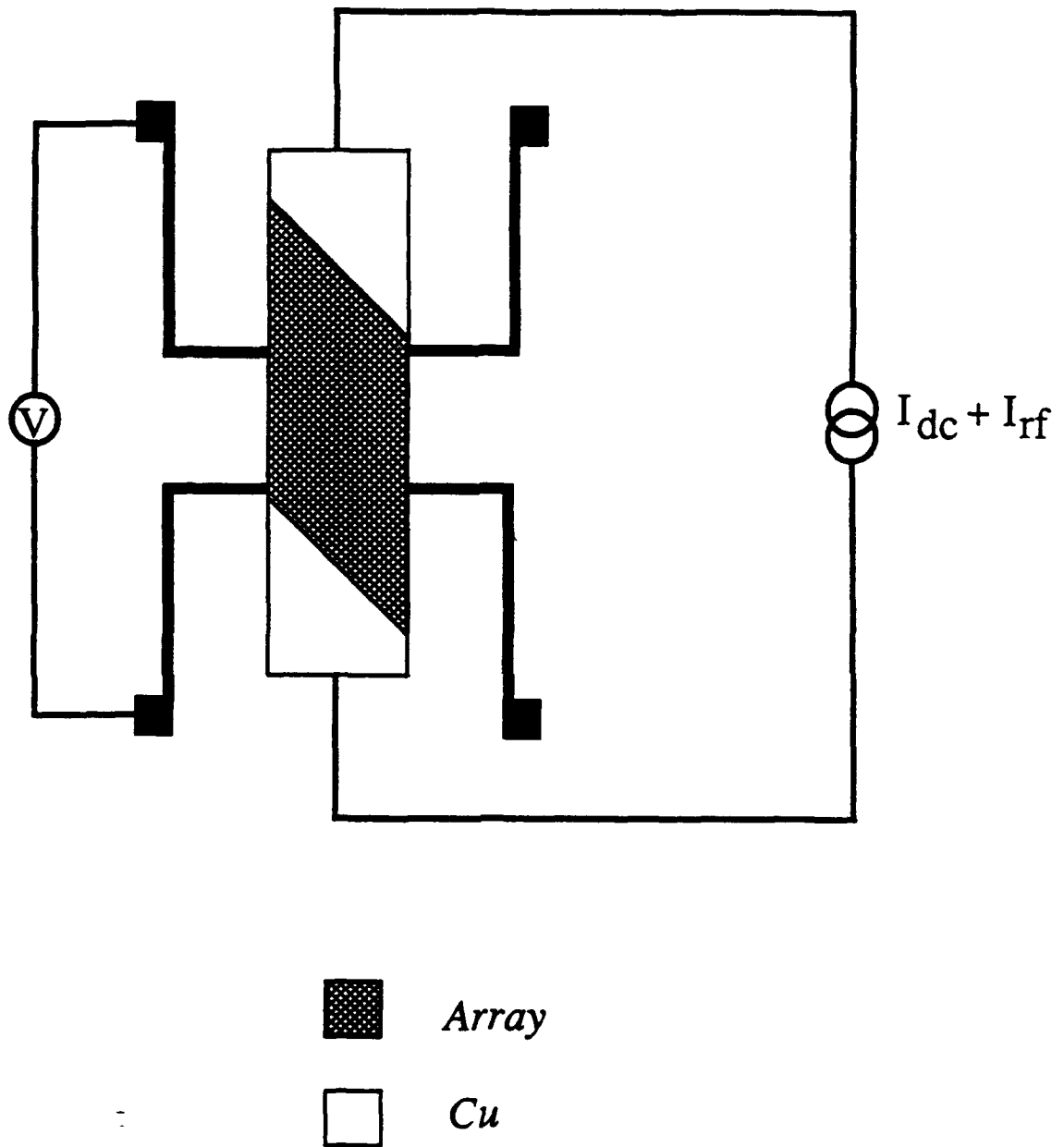


Fig. 2.9. Four-point probe measurement circuit for an array sample. In this case, the sample is a [11]-oriented square-lattice array.

reduce the effects of thermal emf's on the sample. The leads are connected to the sample's voltage and current pads using pressed indium-dot contacts. The four-point probe measurement circuit we used is shown in Fig. 2.9. With this circuit, we are able to perform several types of measurements, including current vs. voltage, dynamic resistance (dV/dI) vs. voltage, and dynamic resistance vs. perpendicular magnetic field curves.

Once the substrate is mounted onto the Cu block and the appropriate leads are connected to the sample, the vacuum can is slid over the sample and sealed with an indium o-ring. The rig is then placed in a μ -metal shielded ^4He cryostat. The μ -metal shields the rig from external magnetic fields, reducing them to ~ 0.1 mGauss [Benz, 1990]. The vacuum can is evacuated and a small amount of He exchange gas is placed into the can so that the sample block can be cooled by the liquid-He bath. A regulatable pumping system is used to control the temperature of the liquid-He bath. The lowest temperature which can be attained with this system is 1.25 K. The temperature of the Cu sample block is controlled with a Lake Shore Cryotronics Temperature Controller (model DRC-91C). A heating resistor can be used to heat the sample well above the temperature of the liquid-He bath, and a calibrated germanium thermometry resistor (Cryocal #4033, 1087Ω at 4.25 K), also mounted on the sample block, is used to measure the temperature.

A PAR 124A lock-in amplifier, with a PAR 116 preamplifier, is used for all of our measurements. In addition, a 1:100 transformer at the input is also included in order to improve the impedance match from the low-resistance of the array. The rms amplitude of the ac current through the sample is chosen to be at least 100 times smaller than the measured critical current of the array. Under these conditions, measurements with a sensitivity better than 1 nV could be obtained with lock-in time constants less than 1 sec [Benz, 1990]. An HP 8656B signal generator (frequency range of 0.1-990 MHz) is used for the rf source and a nanovoltmeter, Keithley Instruments model 148, for measuring the dc voltage (typically, 0.1-1.0 μV) across the array. Ground loops are broken by using a 1:1 transformer on the lock-in modulation signal output and 0.1 μF blocking capacitors on

the rf signal generator output. A homemade battery-powered supply is used as the dc current source (maximum current ≈ 100 mA) simply because of its low noise characteristics. This supply can be either hand or motor swept. To minimize electrical noise generation, all data are initially plotted on an HP 7045B analog XY recorder and then digitized for computer analysis.

2.4 Experiment

There is only a rather narrow temperature range in which we can optimally perform our measurements, for the following reasons.⁷ Because we want to avoid the effects of thermally excited vortices which are present at temperatures near or above the Kosterlitz-Thouless transition temperature, T_{KT} , we make our measurements well below the T_{KT} of our samples. However, we cannot measure our samples at too low a temperature because the critical current, $i_c(T)$, of a single junction in the array is an exponential function of temperature [De Gennes, 1964],

$$i_c(T) = i_c(0) \left(1 - \frac{T}{T_{co}}\right)^2 \exp\left(\frac{-d}{\xi_N(T)}\right)$$

where T_{co} is the superconductor transition temperature, ξ_N is the coherence length of the normal metal barrier and d is the effective separation between the islands. If $i_c(T)$ is large, the critical current of the array, $I_c = Mi_c$, where M is the number of junctions across the array, will be much larger; thus, the applied rf current drive will be too weak to have any effect on the array. At low temperatures, where $i_c(T)$ becomes larger, shielding effects, caused by large circulating currents around the perimeter of the array, and geometrical inductance effects can both dominate our measurements.

⁷Further details and explanations can be found in Benz, thesis (1990).

Hence, we see that we are very much limited to a set temperature range at which we can measure our arrays. In the following chapter, we will describe the results of our measurements.

CHAPTER III

SNS ARRAYS: EXPERIMENTAL RESULTS

3.1 Introduction

When a radio frequency (rf) current, $i_f \sin(2\pi\nu t)$, is applied to an $N \times M$ array of superconducting-normal-superconducting (SNS) Josephson junctions, *giant* Shapiro steps occur at dc voltages

$$V_n = n \left[\frac{N h \nu}{2e} \right], \quad n = 0, 1, 2, \dots \quad (3.1.1)$$

[Clark, 1973 and Leeman et al., 1984]. Here N is the number of junctions in series along the current direction. When a perpendicular magnetic field corresponding to a strongly commensurate number of flux quanta per unit cell, $f = p/q$ (where p and q are small integers), is also applied to the system, *fractional* giant Shapiro steps occur at voltages

$$V_n = n \left[\frac{N h \nu}{q 2e} \right], \quad n = 0, 1, 2, \dots \text{ and } q = 1, 2, 3, \dots \quad (3.1.2)$$

These steps are attributed to the driven motion, in a direction perpendicular to the macroscopic current, of a superlattice of *field-induced* vortices commensurate with the underlying array lattice [Benz et al., 1990; Free et al., 1990; K. H. Lee et al., 1990; and H. C. Lee et al., 1990]. The motion of *current-induced* vortices is thought to be responsible for *subharmonic* steps occurring at voltages

$$V_n = \frac{n}{m} \left[\frac{N\hbar v}{q2e} \right], \quad n = 0, 1, 2, \dots \text{ and } m = 1, 2, 3, \dots \quad (3.1.3)$$

in these arrays [K. H. Lee et al., 1991].

In this chapter, we will present the results of our experimental investigation of the effect of changing the macroscopic current direction with respect to the array unit cell on rf and dc current-biased overdamped Josephson-junction arrays. In particular, we focus on our discovery of the partial or complete *suppression* of fractional and subharmonic giant Shapiro steps in both square- and triangular-lattice arrays when the macroscopic transport current flows along certain directions with respect to the array unit cell.¹

3.2 Experimental Results

3.2.1 Magnetoresistance

As was stated previously, we fabricated and measured square- and triangular-lattice arrays whose macroscopic current flowed in various orientations with respect to the array. We first characterized these different arrays in terms of their magnetoresistance. Some of our data on the magnetoresistance of square- and triangular-lattice arrays are shown in Figures 3.1a and b. As had been found earlier through experiments by Brown and Garland (1986) and through simulations by Shih and Stroud (1984), the magnetoresistances of the two types of array lattices differ greatly. While the strongest resistance minimum (apart from $f=\text{integer}$) for both the square- and triangular-lattice arrays occurs at $f=1/2$, the next strongest minimum for the square-lattice array is at $f=1/3$; for the triangular lattice, it is at $f=1/4$. Such resistance minima indicate pinning of the vortex superlattice. We have found

¹Most of the results presented in this chapter have been published in Sohn et al., 1991 and 1992a.

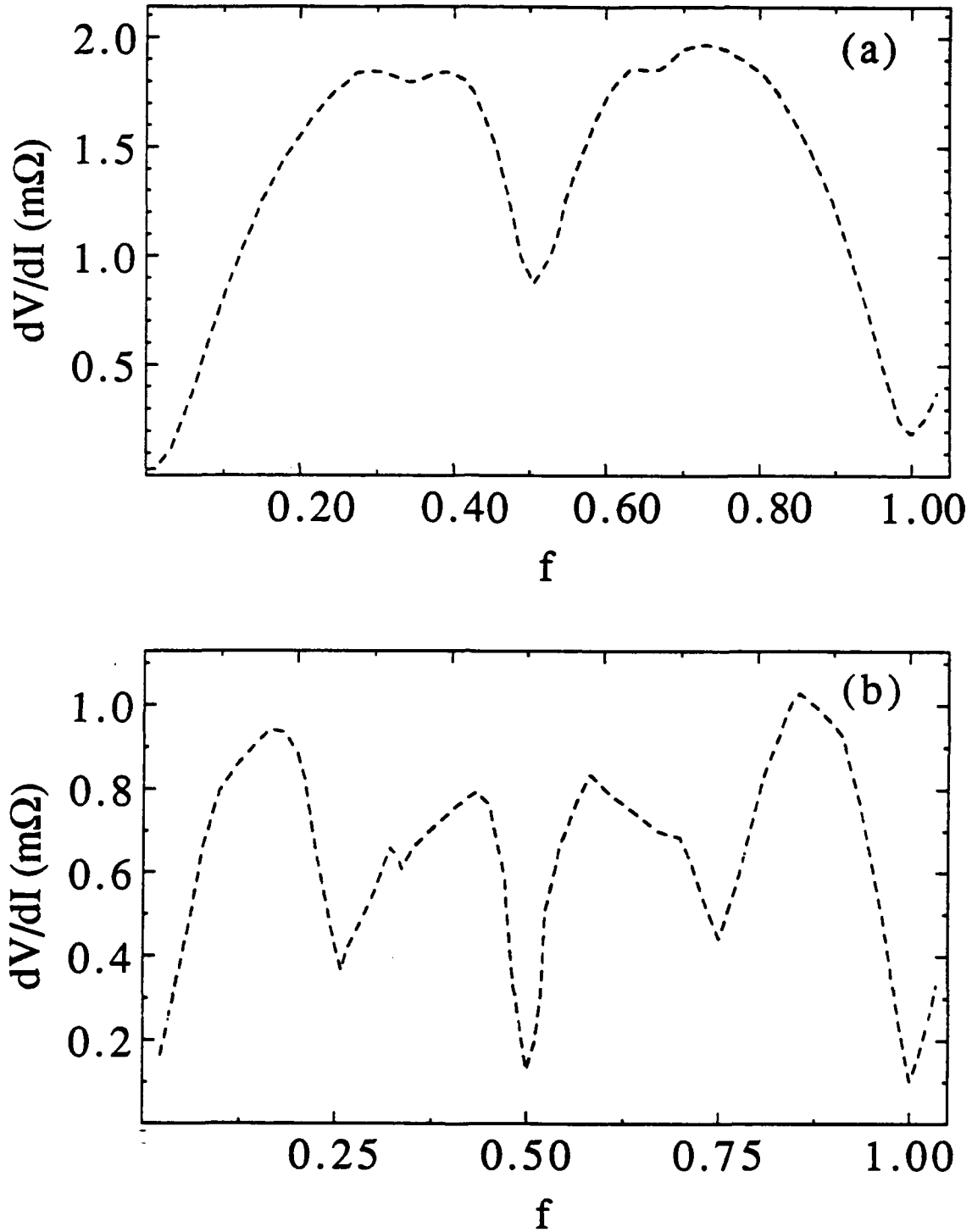


Fig. 3.1. Dynamic resistance versus number of flux quanta, f , per unit cell for the (a) square- and (b) triangular-lattice arrays. Data were taken at (a) $T=2.51$ K and (b) $T=3.97$ K. Both array lattices show strongest vortex pinning at $f=1/2$; however, the next strongest pinning for the square-lattice array is at $f=1/3$ and $2/3$, for the triangular lattice, $f=1/4$ and $3/4$.

that although the main features of the low-current magnetoresistance are *dependent* on the fundamental lattice of the array, these features are entirely *independent* of the orientation of the array with respect to the transport current.²

3.2.2 Giant Shapiro steps

A. Square-lattice arrays

For the [10]-oriented square-lattice arrays in zero field, we see integer giant Shapiro steps which are not flat, but show up as sharp minima in the differential resistance, as shown in Fig. 3.2, at voltages which agree with Eq. (3.1.1). The steps are not flat because of thermal fluctuations, noise, and inhomogeneities in the array.³ As expected, in the presence of a strongly commensurate field, i.e. $f=1/2$ or $1/3$, both integer giant and fractional giant Shapiro steps are observable at voltages agreeing with Eqs. (3.1.1) and (3.1.2), respectively. In addition, weak subharmonic steps at voltages corresponding to Eq. (3.1.3), where $m=2$ or 3 , are present in the [10]-oriented arrays at $f=0$, $1/2$, and $1/3$. These subharmonic steps begin to disappear at low rf frequencies ($\Omega=N\hbar\nu/2eI_C R < 0.3$, where I_C is the critical current and R is the normal-state resistance of the entire array).

As stated previously in the introduction of this chapter, subharmonic steps are thought to be a result of the motion of current-induced vortices [Benz, 1990; H. C. Lee et al., 1991; and José and Dominguès, 1992]. Lee et al. (1991) were the first to experimentally determine that the dc bias current produces an inhomogeneous self-field along the edges of the array. This self-field produces vortices whose subsequent motion throughout the array lattice produces the subharmonic steps. To test whether or not this

²Similarities in magnetoresistance of [10]- and [11]-oriented square-lattice arrays of *underdamped* Josephson junctions have also been reported by van der Zant et al. (1990).

³This is the main reason we take dV/dI vs. V measurements of our arrays. A V vs. I measurement would show steps which are simply too rounded to make any quantitative statements.

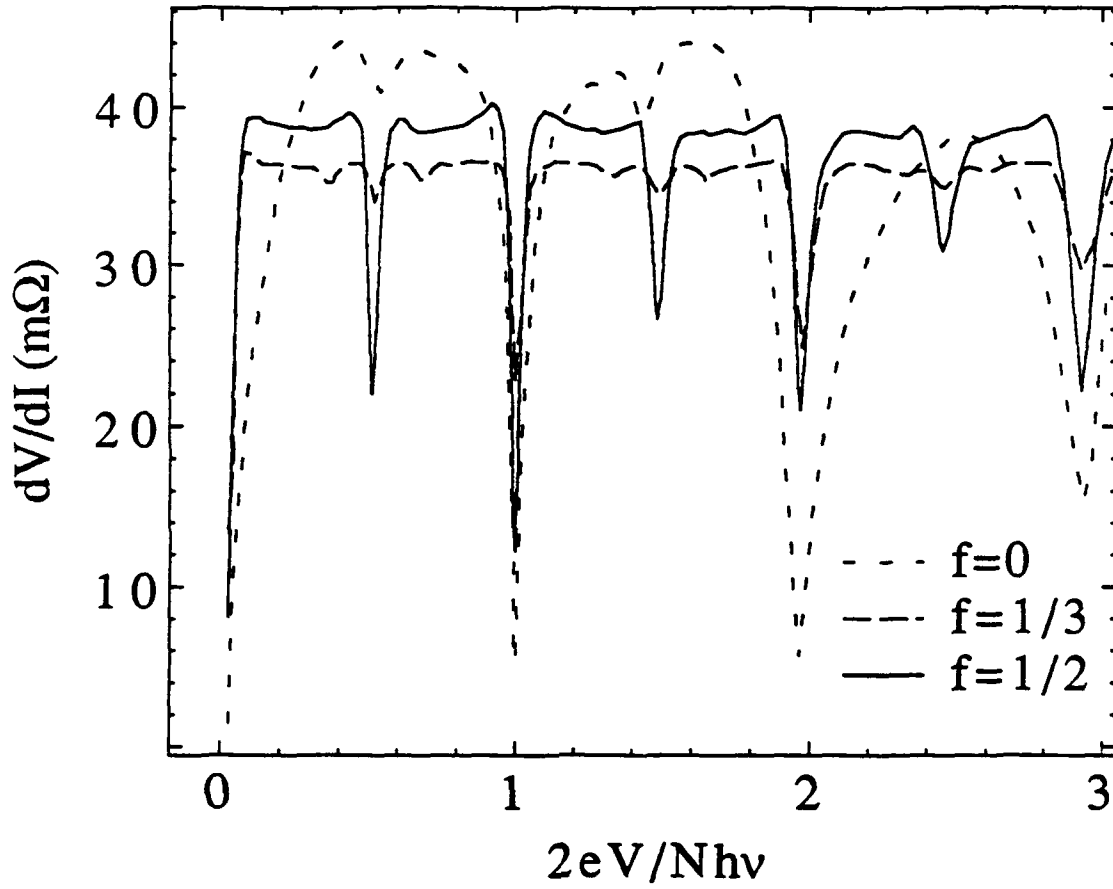


Fig. 3.2. Dynamic resistance vs. normalized voltage in the presence of perpendicular magnetic fields corresponding to $f=0$, $1/3$, and $1/2$ for the $[10]$ -oriented square-lattice array. Data were taken at $T=1.39$ K where $I_c=0.26$ mA, rf frequency $\nu=1.5$ MHz ($\Omega=N\hbar\nu/2eI_cR=0.45$). The rf drive current for $f=0$ was $2/3$ as large as for $f=1/2$ and $1/3$.

was the case for our samples, we followed Lee et al.'s work (1991) and placed a thin normal metal (Cu) film directly over our array and ran a current through the film in a direction directly opposite to the dc bias current. The sheet current produced entirely eliminated the perpendicular component of the self-field. Consequently, no vortices were produced and correspondingly, the subharmonic steps were suppressed [Rzchowski and Sohn, 1991]. This work further supports the belief that edge nucleation of vortices induced by the self-field of the array's dc bias current leads to subharmonic Shapiro steps.

In the [11]-oriented arrays (see Figure 3.3), we also see integer giant Shapiro steps whose voltages correspond to Eq. (3.1.1). More importantly, however, we do *not* observe fractional giant or subharmonic Shapiro steps at any transverse field strength ($f=0, 0.07, 0.18, 0.29, 0.33, 0.50$ were tried) in these arrays, apart from a small feature seen at the half-integer position. We tentatively attribute this small feature to the inflection point in the I - V curve midway between strong integer steps. These features often occur in single junctions as well, and in arrays, can occur at voltages corresponding to subharmonic steps. Changes in the rf frequency, such that Ω ranges from 0.18 to 0.73, have no effect on this complete suppression of fractional steps. Measurements made at different rf amplitudes and at different temperatures also consistently fail to show fractional giant or subharmonic Shapiro steps in [11]-oriented arrays.⁴

Because the surprising suppression of fractional giant Shapiro steps occurred for an extreme change in current direction, we also studied the dynamical properties of arrays in which the current was injected at only 15 degrees with respect to the [10] direction. Both integer and fractional giant Shapiro steps appear in this type of an array, but the fractional

⁴We note that our results are not in agreement with the theoretical predictions of Halsey (1990). Based on the assumption of low rf frequencies, the supercurrents flowing in a staircase pattern, and the array being *voltage*-biased, Halsey predicts that fractional giant and subharmonic Shapiro steps will be seen in [11]-oriented arrays. In addition, he predicts that subharmonic steps will also be observed in these arrays even when no field is present. Our simulations, which will be discussed in Chapter IV, confirm Halsey's assumption of staircase currents at low rf frequencies. However, our experimental, numerical, and analytical results—all of which are based on arrays which are *current*-biased—do not produce fractional or subharmonic steps. Halsey (1991) has suggested that this unanticipated difference might be due to the different bias choices in our two approaches.

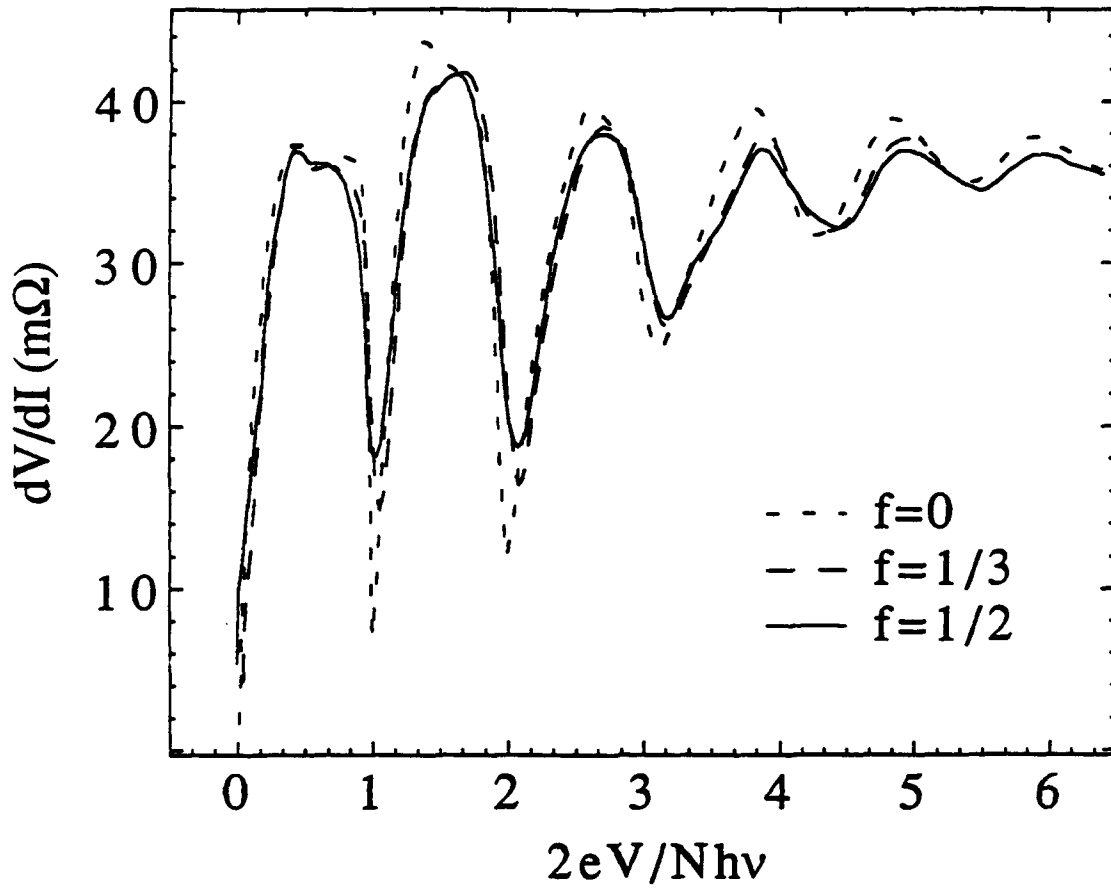


Fig. 3.3. Dynamic resistance vs. normalized voltage in the presence of perpendicular magnetic fields corresponding to $f=0$, $1/3$, and $1/2$ for the $[11]$ -oriented square-lattice array. Data were taken at $T=2.10$ K where $I_C=0.78$ mA, rf frequency $\nu=4.0$ MHz ($\Omega=N\hbar\nu/2eI_C R=0.58$). The rf amplitude was equal for all curves.

step, $n/q=1/2$, is quite weak, as determined by its minimum dynamic resistance; fractional giant Shapiro steps of $n/q > 3/2$ are nearly nonexistent (see Figure 3.4). This is in striking contrast to the [10]-oriented arrays, in which we observe strong fractional giant Shapiro steps for $n/q > 3/2$. Subharmonic steps, which are so prevalent in our [10]-oriented arrays at rf frequencies $\Omega > 3$, also appeared in the 15° array, albeit weakly, for $0.18 < \Omega < 1.24$.

B. Triangular-lattice arrays

The previous work on arrays in this group has been done mostly on square-lattice arrays. In this section, we present the results of our work on triangular-lattice arrays—arrays in which each superconducting island is surrounded by six nearest neighbors in a closed-packed geometry. Triangular-lattice arrays are of special interest since they are a better model than the square-lattice geometry for naturally occurring grains in samples of granular superconductor. By changing the direction of the applied macroscopic current with respect to the array, we found that we were again able to affect the presence or absence of the fractional giant Shapiro steps in the array.

The general dynamical properties of the triangular-lattice arrays have many parallels to those of the square-lattice ones. In Figure 3.5, we see that, as in the case of the [10]-oriented square-lattice arrays, the $[10\bar{1}]$ -oriented triangular-lattice arrays exhibit both integer and fractional giant Shapiro steps⁵ at voltages corresponding to Eq. (3.1.1) and (3.1.2). In Figure 3.6, we see that the $[2\bar{1}\bar{1}]$ -oriented triangular-lattice arrays, like the $[11]$ -oriented square-lattice arrays, show only integer giant Shapiro steps. One remarkable feature which is unique to the $[2\bar{1}\bar{1}]$ -oriented triangular-lattice arrays is that the even integer steps are much stronger than the odd ones. We have found that this unusual behavior is both field- and frequency-independent.

⁵H. C. Lee et al. (1990) have reported seeing integer and fractional giant Shapiro steps in triangular-lattice Pb-Au Josephson-junction arrays. The orientation of the arrays studied was $[10\bar{1}]$ [Newrock, 1991].

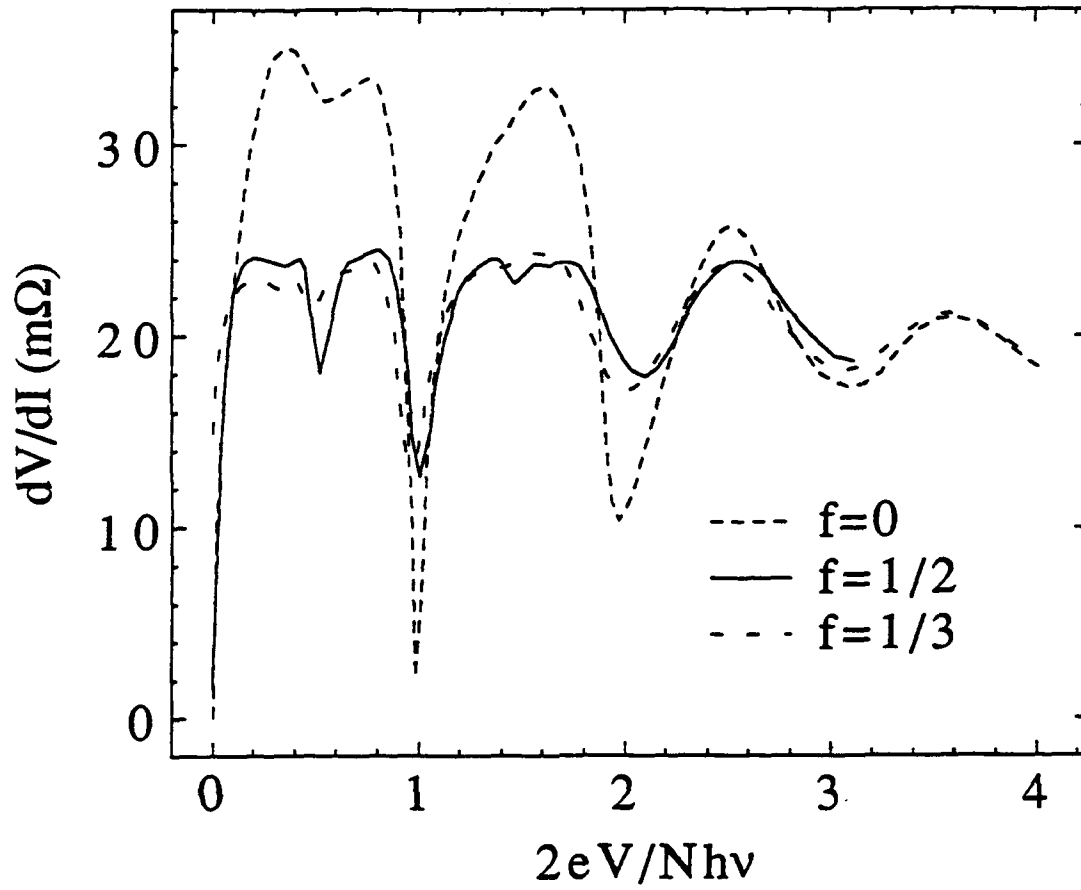


Fig. 3.4. Dynamic resistance versus normalized voltage for the 15° square-lattice array in the presence of perpendicular magnetic fields corresponding to $f=0$, $1/2$, and $1/3$. Data were taken at $T=2.52$ K and rf frequency $\nu=3.5$ MHz ($\Omega=N\hbar\nu/2eI_cR=0.41$).

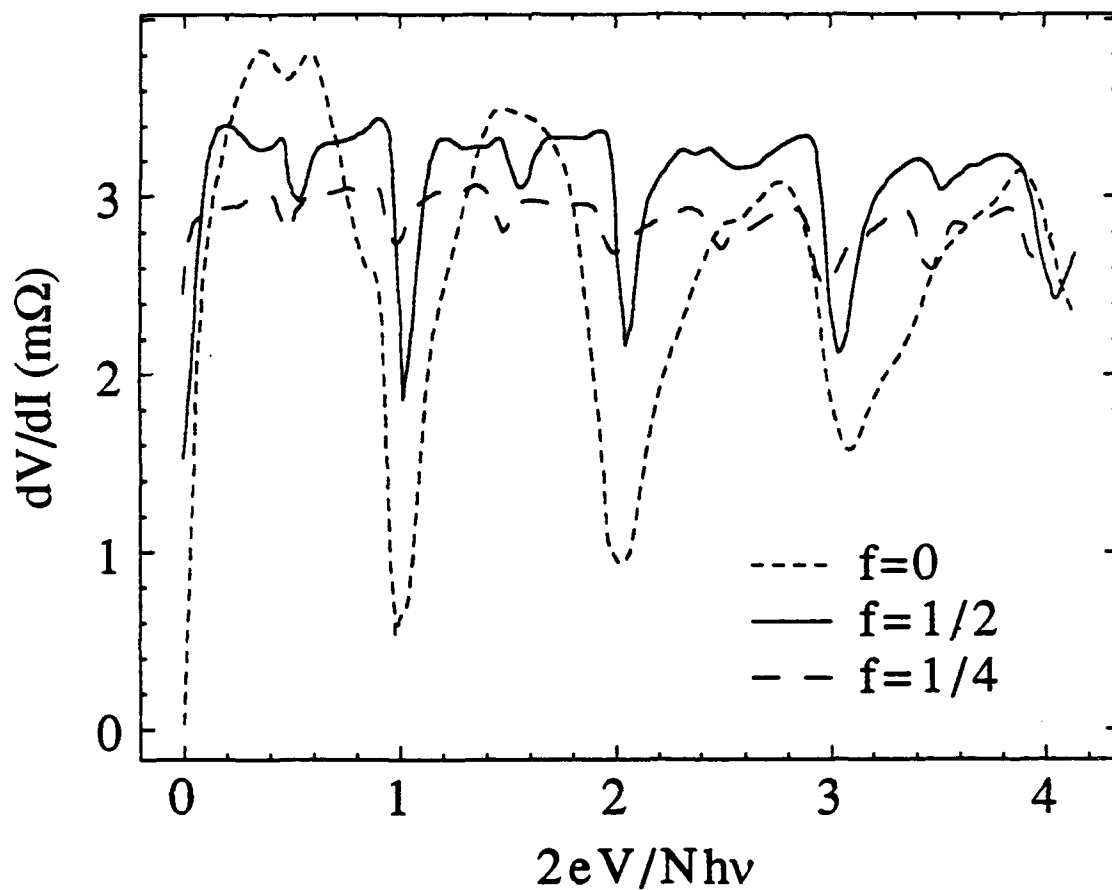


Fig. 3.5. Dynamic resistance versus normalized voltage for the $[10\bar{1}]$ -oriented triangular-lattice array in the presence of perpendicular magnetic fields corresponding to $f=0$, $1/2$, $1/3$, and $1/4$. Data were taken at $T=3.40$ K and rf frequency $\nu=0.90$ Mhz ($\Omega=N\hbar\nu/2eI_cR=0.33$).

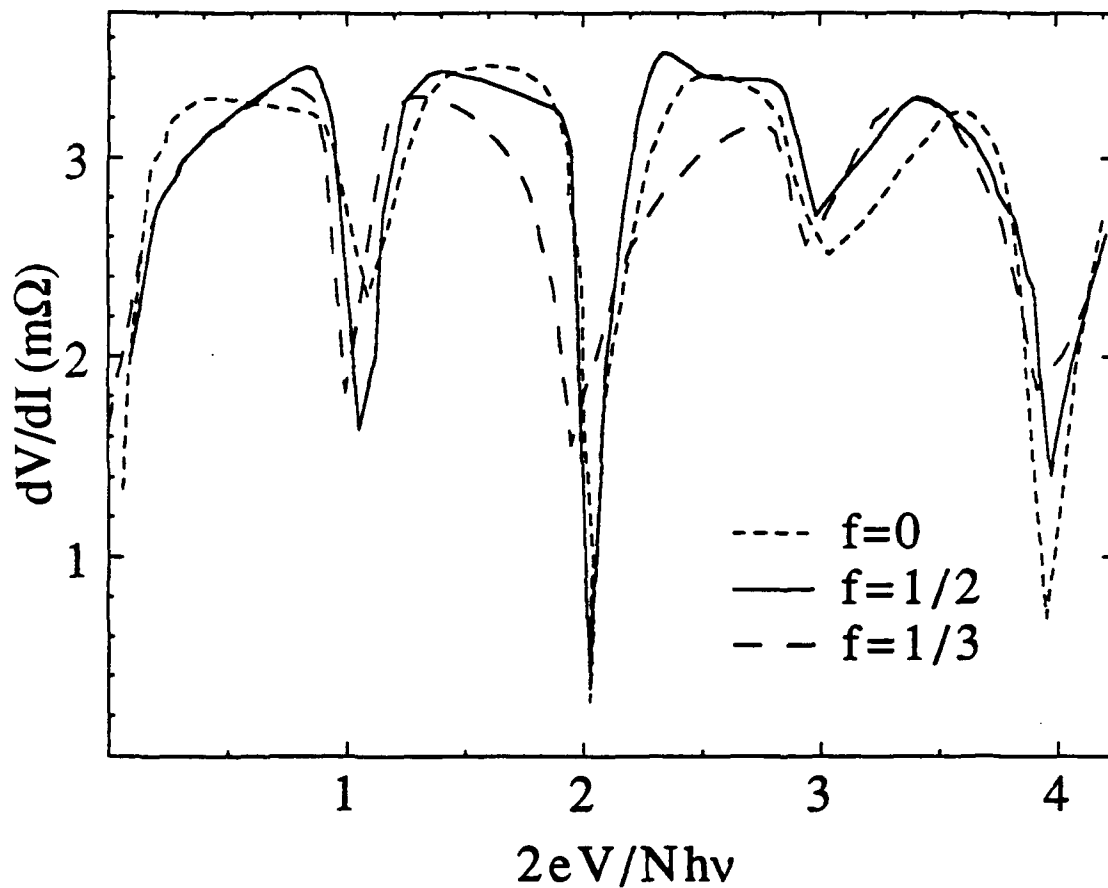
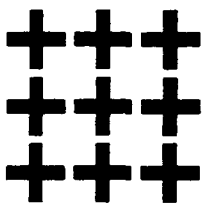
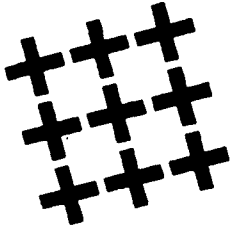
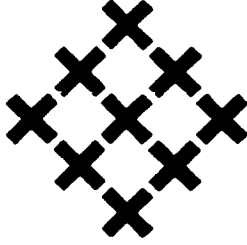
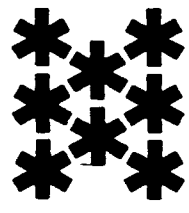
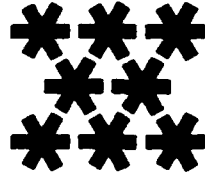


Fig. 3.6. Dynamic resistance versus normalized voltage for the $[2\bar{1}\bar{1}]$ triangular-lattice array in the presence of perpendicular magnetic fields corresponding to $f=0$, $1/2$, $1/3$, and $1/4$. Data were taken at $T=3.61$ K and rf frequency $\nu=0.7$ MHz ($\Omega=N\hbar\nu/2eI_C R=0.96$). Integer giant Shapiro steps in the $[2\bar{1}\bar{1}]$ case alternate in strength, the even steps being stronger than the odd ones.

Table 3.1. Strengths of fractional giant Shapiro steps produced by various geometries of Josephson-junction arrays. The black crosses and asterisks are Nb islands. The applied macroscopic current flows horizontally and "geometry" indicates the direction of the current with respect to the array unit cell. All array types showed integer giant Shapiro steps.

Array	Geometry	Fractional Steps
	[10]	Strong
	15°	Weak
	[11]	Absent
	$[10\bar{1}]$	Weak
	$[2\bar{1}\bar{1}]$	Absent

3.3 Summary of Results

A summary of our results can be found in Table 3.1. Briefly, we have found that the $[10]$ -oriented and 15° square- and $[10\bar{1}]$ -oriented triangular-lattice arrays produce both integer and fractional giant Shapiro steps. The $[11]$ -oriented square- and $[2\bar{1}\bar{1}]$ -oriented triangular-lattice arrays, however, produce only integer giant Shapiro steps.

CHAPTER IV

SNS ARRAYS: NUMERICAL SIMULATIONS

4.1 Introduction

The RCSJ model [W. Stewart, 1968 and D. McCumber, 1968] is often used to describe rf current-biased single Josephson junctions [P. J. Russer, 1972]. As stated in Chapter I, this model assumes that a Josephson junction is a parallel combination of a resistor r_n , a capacitor C , and a nonlinear Josephson element with critical current i_c . When current biased, this circuit can be described by the following equation of motion,

$$\frac{\hbar C}{2e} \frac{d^2 \gamma}{dt^2} + \frac{\hbar}{2er_n} \frac{d\gamma}{dt} + i_c \sin \gamma = i_{dc} + i_{rf} \sin(\omega t) \quad (4.1.1)$$

where $\gamma = \phi_j - \phi_i - \psi_{ij}$ is the gauge-invariant phase difference between the two superconducting islands, i and j , that make up the junction, $\psi_{ij} = \frac{2\pi}{\Phi_0} \int_i^j \vec{A} \cdot d\vec{l}$, with \vec{A} equal to the vector potential, i_{dc} and i_{rf} are the applied dc and rf current per junction, and i_c is the critical current of the junction. In the overdamped limit $\beta_C = (2ei_c r_n^2 C / \hbar) \ll 1$, Eq. (4.1.1) reduces to a first-order differential equation.

We have performed several types of numerical simulations—all based on the RCSJ model—of the various SNS arrays we have experimentally studied. In Sec. 4.2, we present the results of our large scale simulations of an $N \times N$ [11]-oriented square-lattice array.¹ These rather involved simulations consist of solving $\sim N^2$ coupled, nonlinear, first-order differential equations, which are derived from applying current conservation

¹Most of the results presented in this chapter have been published in Sohn et al., 1991 and 1992a.

laws to each node of the array. In addition to these large scale simulations, we have also simulated the basic unit cells of both square- and triangular-lattice arrays. As will be discussed in Sec. 4.3, these simulations, although simpler and therefore far less time consuming than the large-scale simulations, provide much detailed information on the dynamics of SNS arrays.

4.2 Large Scale Simulations of [11]-Oriented Square-Lattice Arrays

4.2.1 Algorithm

The numerical simulations of [11]-oriented square-lattice arrays we have performed are identical to those performed by Free et al. (1990) with the obvious exception that the macroscopic current in the array flows in the [11], and not the [10], direction. Using the RCSJ model described in Section 4.1, we can easily show that the current, i_{ij} , flowing through an individual junction in an $N \times N$ array is given by

$$i_{ij} = i_c \sin \gamma_{ij} + \frac{v_{ij}}{r_n} \quad (4.2.1)$$

where r_n is, again, the junction resistance, v_{ij} , the voltage drop across the junction, and γ_{ij} is the gauge-invariant phase difference across the junction,

$$\gamma_{ij} = \varphi_j - \varphi_i - \frac{2\pi}{\Phi_0} \int_i^j \vec{A} \cdot d\vec{l} \quad (4.2.2)$$

For our purposes, we choose the Landau gauge to be $\vec{A} = Hx\hat{y}$. Using the Josephson voltage relation [Josephson, 1962], we can relate v_{ij} to γ_{ij} with the following,

$$v_{ij} = \frac{\hbar}{2e} \frac{d\gamma_{ij}}{dt} \quad (4.2.3)$$

Current conservation at each array node places the constraint

$$\sum_j i_{ij} = i_i^{ext} \quad (4.2.4)$$

As in Free et al.'s simulations (1991), in our simulations, $i_i^{ext} = 0$ except at the boundaries, where $i_i^{ext} = \pm [i_{dc} + i_{rf} \sin(2\pi\nu t)]$; (+) indicates current being injected and (-) indicates current being extracted (see Figure 4.1). We choose periodic boundaries perpendicular to the transport current direction in order to avoid boundary effects arising from simulating small-sized arrays [Free et al., 1990 and Chung et al., 1990].

In order to solve the coupled first-order differential equations, Eqs. (4.2.1)-(4.2.4), we employ a fourth-order Runge-Kutta method with uniform time steps. Each array node is assigned an initial phase which will be used to integrate the equations.² I - V curves are calculated by ramping the current from zero to some current, I_{dc} . The individual phases are allowed to relax 400 rf periods before time averaging the voltage for an additional 400 rf periods. Because the amount of cpu time needed to solve the coupled first-order equations is enormous, we limit the size of the array to $N \times N$ where $N=2, 4, 6, 8$, and 16. All simulations were performed on a Sun 4, a Sun Sparc station SLC, and a Convex machine.³

²Initially, we chose $\phi_i=0$. Ideally, however, one would like to start with the zero-temperature ground-state configuration in order to avoid boundary-related metastable states due to finite array size.

³The use of a SUN 4 was provided by the Robotics Laboratory, Harvard University and the use of a Convex machine, by the Laboratory for Computational Physics at the Naval Research Laboratory, Washington, D.C.

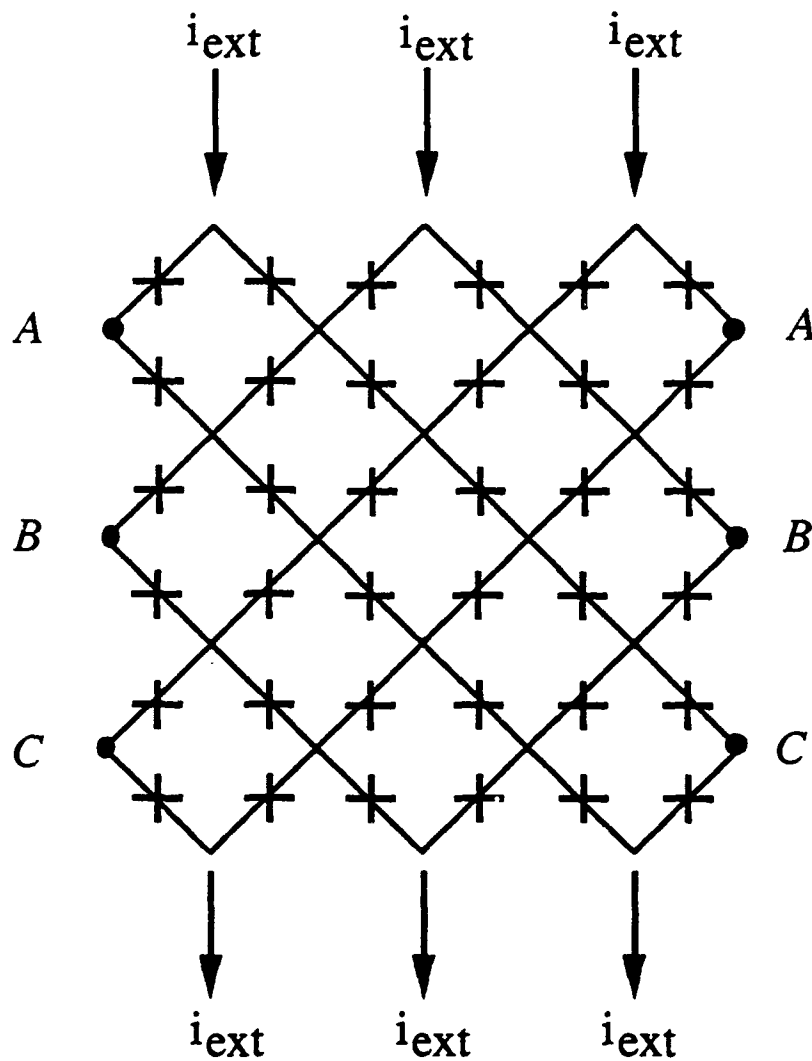


Fig. 4.1. Schematic drawing of a simulated 6 x 6 junction [11]-oriented square-lattice array with periodic boundaries in the direction perpendicular to the applied current, i_{ext} . Nodes A, B, C are the same for either side of the array in order to complete the periodic boundary conditions we imposed on our simulations.

4.2.2 The results

For a wide range of rf frequencies ($0.1 < \Omega < 1.5$) and amplitudes, we found that the resulting I - V curves for the 2×2 , 4×4 , 8×8 , and 16×16 [11]-oriented arrays at $f=1/2$ and for the 6×6 arrays at $f=1/3$ show only giant Shapiro steps whose widths varied with rf amplitude (see Figure 4.2). Nowhere do we see fractional giant or subharmonic Shapiro steps in any of the computed curves.

When we study the time evolution of the phases and the supercurrents of the simulated 8×8 or 4×4 junction [11]-oriented square lattice array on the first giant Shapiro step at low rf frequencies (i.e. $\Omega < 0.6$) and at $f=1/2$, we find that the supercurrents flow in a sequence of staircase patterns throughout an rf cycle (see Figure 4.3). At the beginning of an rf cycle, when $i_f \sin \omega t = 0$, the phases in the array resemble the $f=1/2$ ground state, i.e. staircase currents of alternating sign form a checkerboard pattern of clockwise and counterclockwise vortices within the array (see Fig. 4.3a). Motion of this superlattice of vortices was successfully used to describe phase coherence in [10]-oriented arrays [Free et al., 1990; Benz et al., 1990; and K. H. Lee et al., 1990]. In the [10] case, the Lorentz force drives the vortices straight through the weak links between the Nb islands. In contrast, in the [11] case, the Lorentz force drives the vortices toward the high energy barrier of the Nb islands. One might imagine that half of the vortices move around an island on one side, and half on the other side. If incoherent, such a motion of the vortex lattice across the array might be thought to explain the absence of fractional giant and subharmonic steps in diagonal arrays. In our simulations, however, the actual vortex motion does not follow this scenario. We found that as the rf drive advances in its cycle, only staircases of supercurrents flowing in the same direction as the drive current exist in the array, and the aforementioned vortices completely disappear (see Figure 4.3b). At the peak of the rf drive cycle, at which time the transport current is carried largely as normal current with an accompanying pulse of voltage, the pattern, however, quickly disappears

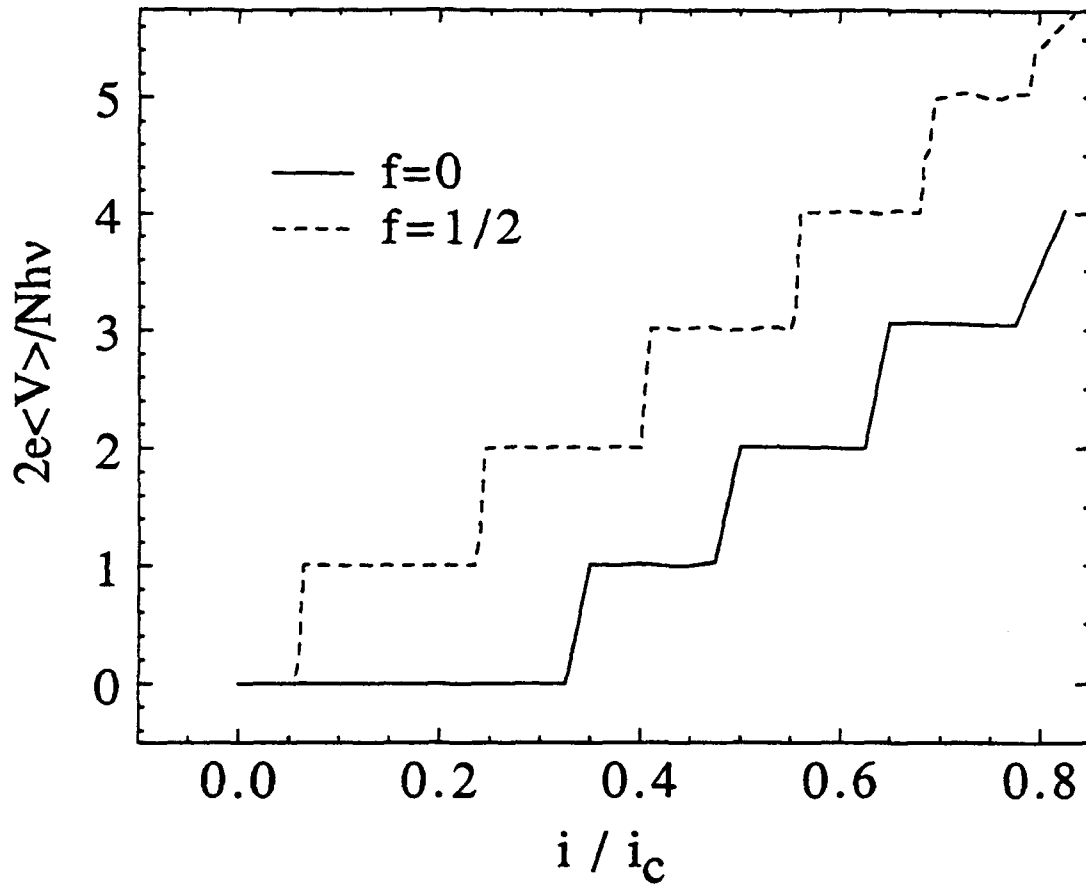


Fig. 4.2. I - V curves of a simulated 8×8 junction $[11]$ -oriented square-lattice array at magnetic-field strengths corresponding to $f=0$ and $1/2$ (solid and dashed lines, respectively). $\Omega=0.1$ and $i_T/i_c=0.75$ for both these curves. Increments of i/i_c were 0.025 for $f=0$ and 0.005 for $f=1/2$.

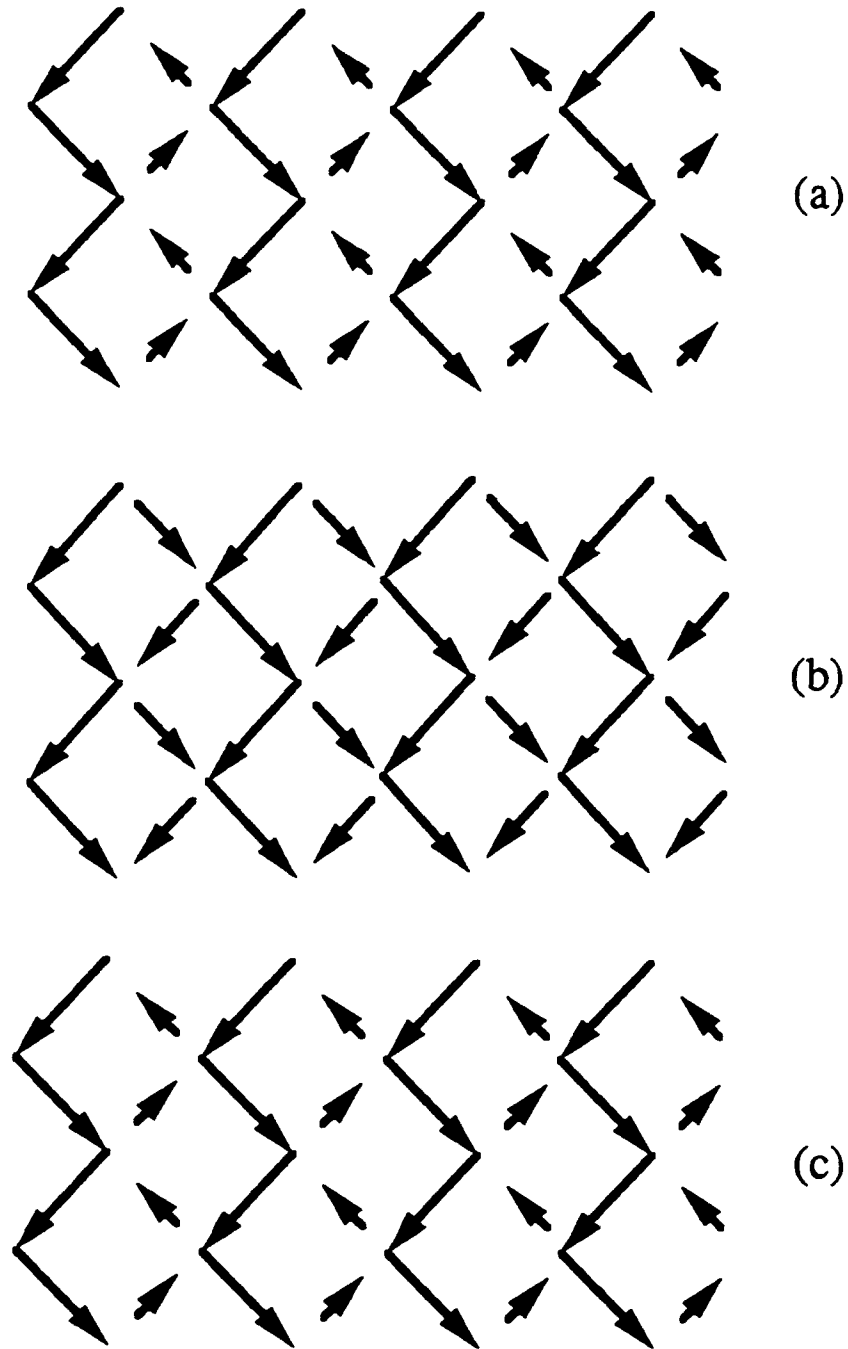


Fig. 4.3. Time evolution of the supercurrents in a simulated [11]-oriented square-lattice array on the first giant Shapiro step at $\Omega=0.1$ and $f=1/2$. Transport current flows from top to bottom. (a) At the beginning of an rf cycle, the supercurrents form a checkerboard pattern of clockwise and counterclockwise vortices within the array. (b) As the rf drive advances in its cycle, only staircases of supercurrents flowing in the same direction as the drive current exist and the aforementioned vortices completely disappear. (c) At the peak of the rf drive cycle, the previous state reappears, remaining until the end of the rf cycle.

and subsequently the previous state reappears, remaining until the end of the rf cycle (see Figure 4.3c). The motion described above corresponds to a $2\pi N$ phase slip of the array per rf cycle. Because the vortices disappear and reappear, their motion cannot be traced continuously in a simple way and a more general model than that used for the [10]-oriented arrays must be adopted.

In more detail, our simulations show that on a giant step at $f=1/2$ and low rf frequencies ($\Omega < 0.6$) all the time derivatives of the gauge-invariant phases, $d\gamma/dt$ (and hence all normal currents), in a plaquette are equal throughout an rf cycle (a typical wave form is shown in Figure 4.4). Thus, normal currents and supercurrents are separately conserved at each node. Supercurrent conservation is accomplished by having the supercurrents always flowing in a staircase pattern with $\gamma_1 = \gamma_2$ and $\gamma_3 = \gamma_4$. If we also require that the fluxoid in each plaquette must equal $2\pi f = \pi$ since $f=1/2$ in this case, we find that $2\gamma_1 - 2\gamma_4 = \pi \pmod{2\pi}$. Using these relationships, we see that the net supercurrents I_S and normal currents I_N per node are

$$I_S = i_C (\sin \gamma_1 + \sin \gamma_4) \quad (4.2.5)$$

$$I_N = \frac{\hbar}{e r} \frac{d\gamma_1}{dt} \quad (4.2.6)$$

If we set the total current through the cell equal to the applied transport current, we find that

$$\frac{\hbar}{2e i_C r} \frac{d\gamma}{dt} + \frac{1}{\sqrt{2}} \sin \gamma = i_{dc} + i_{rf} \sin(\omega t) \quad (4.2.7)$$

where $\gamma = \gamma_1 - \pi/4 = \gamma_4 + \pi/4$, and $i_{dc} = I_{dc}/2$ and $i_{rf} = I_{rf}/2$ are the applied dc and rf current per junction, respectively, in units of i_C . From Eq. (4.2.7), we see that the phase constraints in this regime cause all junctions in the array to have the same equation of motion as an

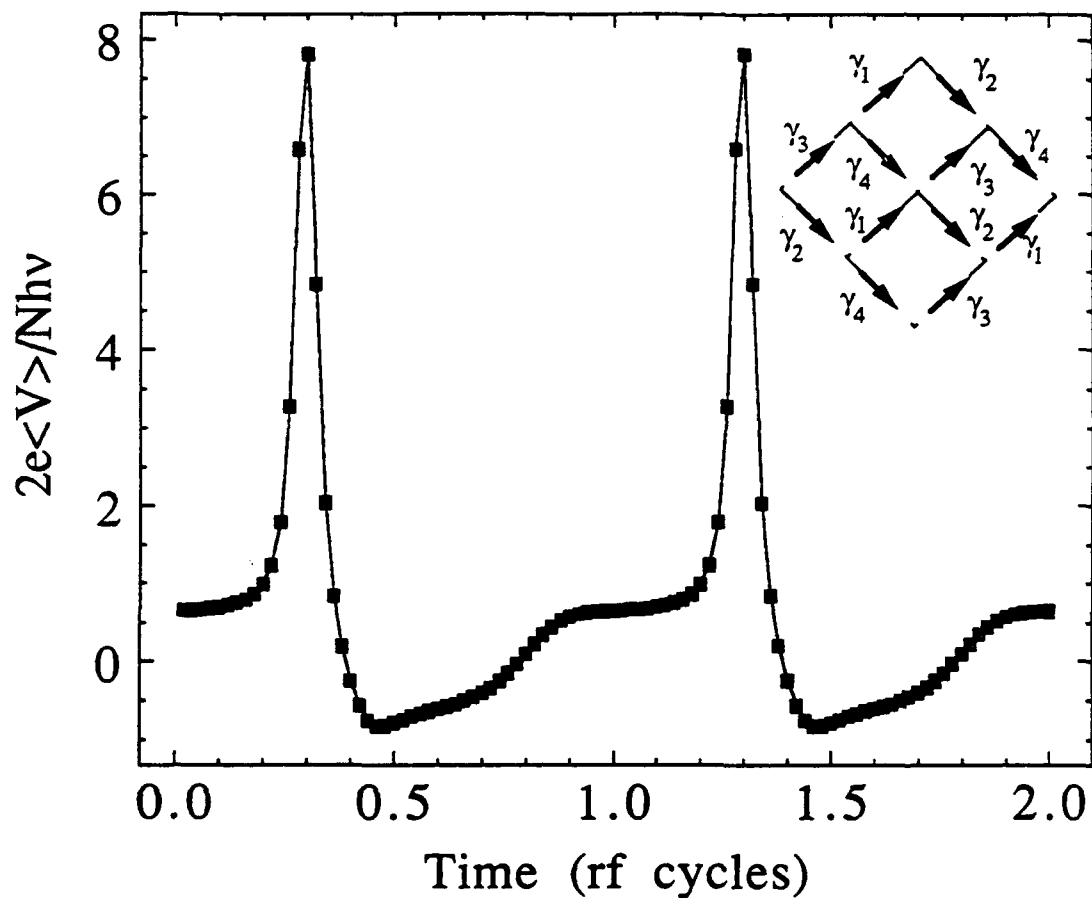


Fig. 4.4. Normalized instantaneous voltage vs. time (in rf cycles) across each junction in a plaquette of the simulated 8×8 junction [11]-oriented square-lattice array on the first giant Shapiro step at $i/i_c=0.15$ under the drive conditions in Fig. 4.2. Data points representing all junctions lie on top of each other and therefore cannot be distinguished in this figure. Inset: 2×2 section of the [11]-oriented array where the γ 's are the gauge-invariant phase differences of the corresponding junctions.

isolated single Josephson junction with critical current equal to $i_c/\sqrt{2}$ and resistance equal to r in the RSJ approximation. Renne and Polder (1974) have shown that single overdamped Josephson junctions produce only integer Shapiro steps.⁴ It follows then that the [11]-oriented arrays cannot support fractional giant or subharmonic Shapiro steps in the fully frustrated case, at least at frequencies low enough for the constraints derived from the simulations to apply.

4.2.3 Possible evidence of spatial period doubling

We emphasize that our numerical analysis discussed in the previous section is valid only for *low* rf frequencies (i.e. for $\Omega < 0.6$) where the time derivatives of the gauge-invariant phases, $d\gamma/dt$, in a plaquette are equal throughout an rf cycle and the supercurrents flow in a staircase pattern with $\gamma_1 = \gamma_2$ and $\gamma_3 = \gamma_4$ (see Fig. 4.4). We cannot use the same analysis for higher frequencies ($\Omega \geq 0.6$) because the $d\gamma/dt$'s are no longer equal to each other throughout an entire rf cycle, as shown in Fig. 4.5. In addition, although the supercurrents still flow in a staircase pattern, now only $\gamma_1 = \gamma_2$; $\gamma_3 \neq \gamma_4$.

The breakup in the symmetry of the gauge-invariant phases at high frequencies can be better described by pictorially displaying the flow of the supercurrents through the array during an rf cycle on an integer step. When we do this, we observe that when we increase the frequency above $\Omega = 0.6$, the supercurrents form, quite suddenly, unusual flow patterns. Figure 4.6a shows the rather simple and regular supercurrent flow pattern that exists when $\Omega < 0.6$. As a consequence of the supercurrents flowing in this manner, the entire array can be described as a periodically repeated 2×2 unit cell (shown as the shaded squares in the figure). At higher frequencies, i.e. $\Omega \geq 0.6$, the flow pattern of the supercurrent changes rather suddenly, as shown in Fig. 4.6b. Although the pattern is still

⁴Similar results and conclusions were also obtained by H. Eikmans and J. E. van Himbergen (1991) using a stability analysis.

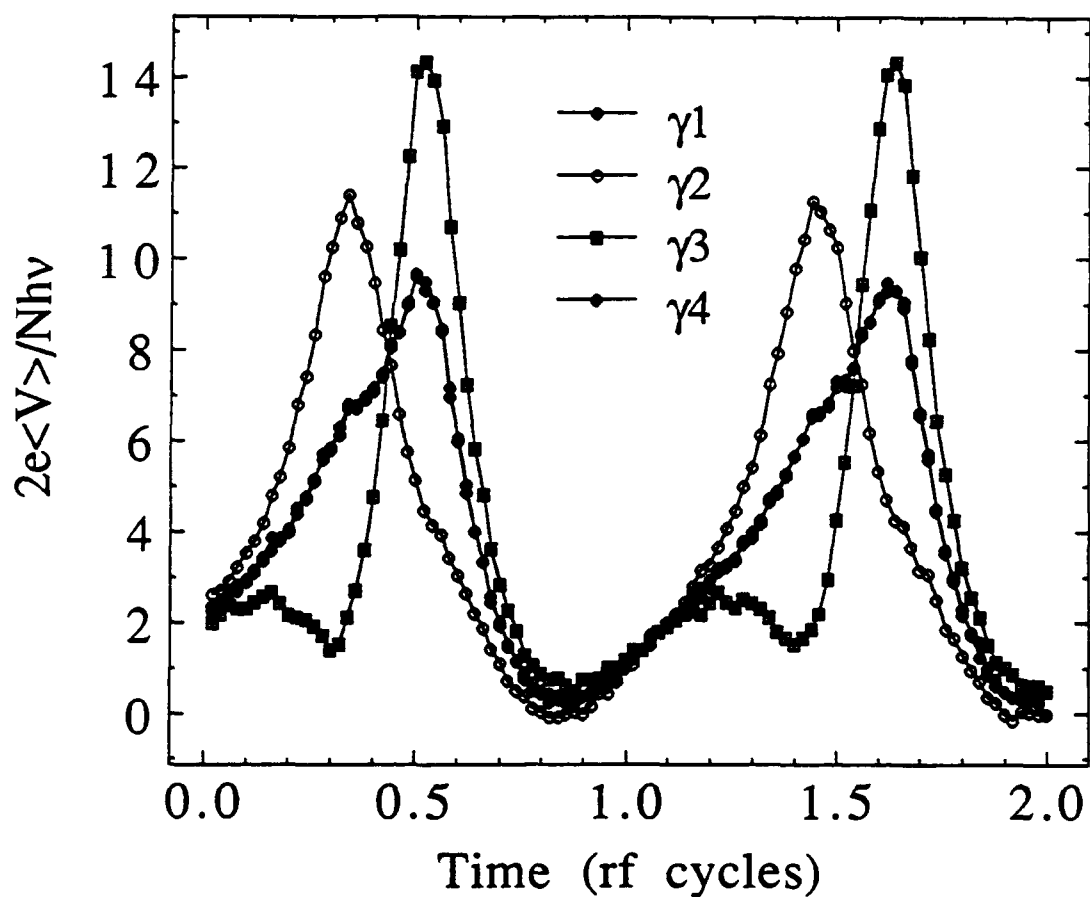
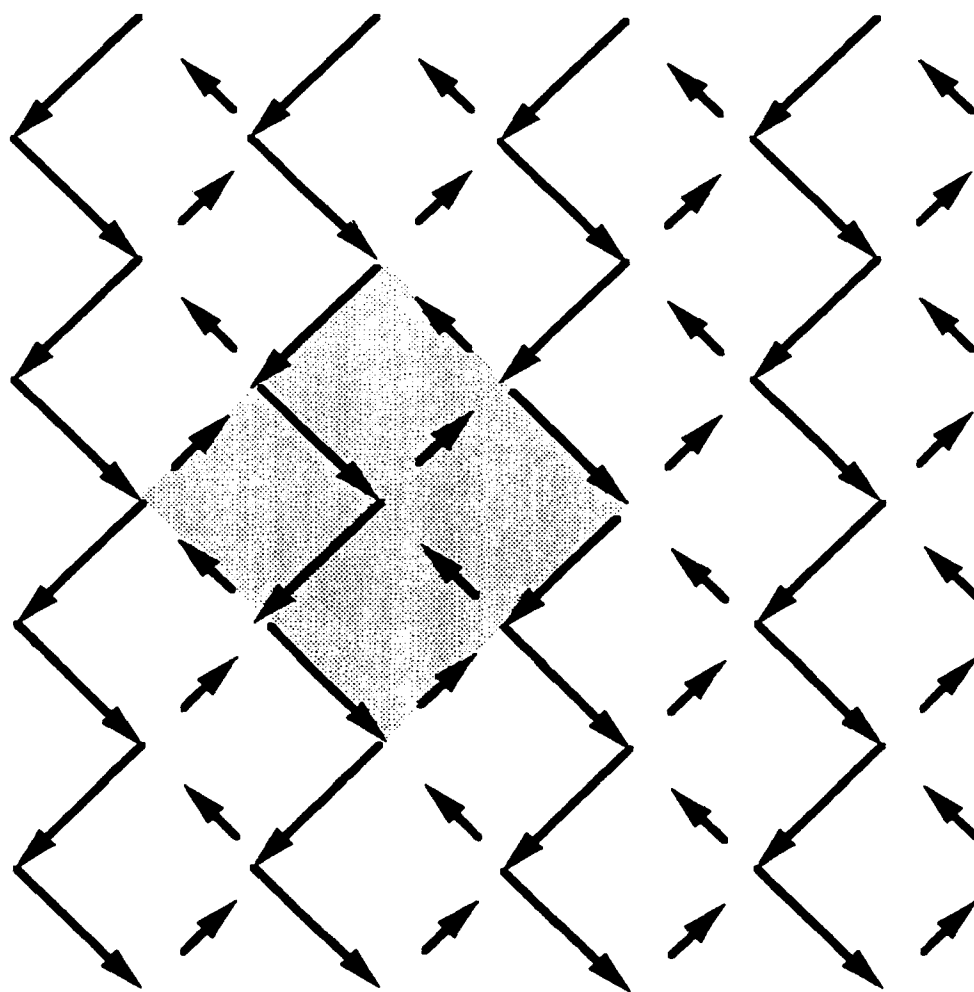
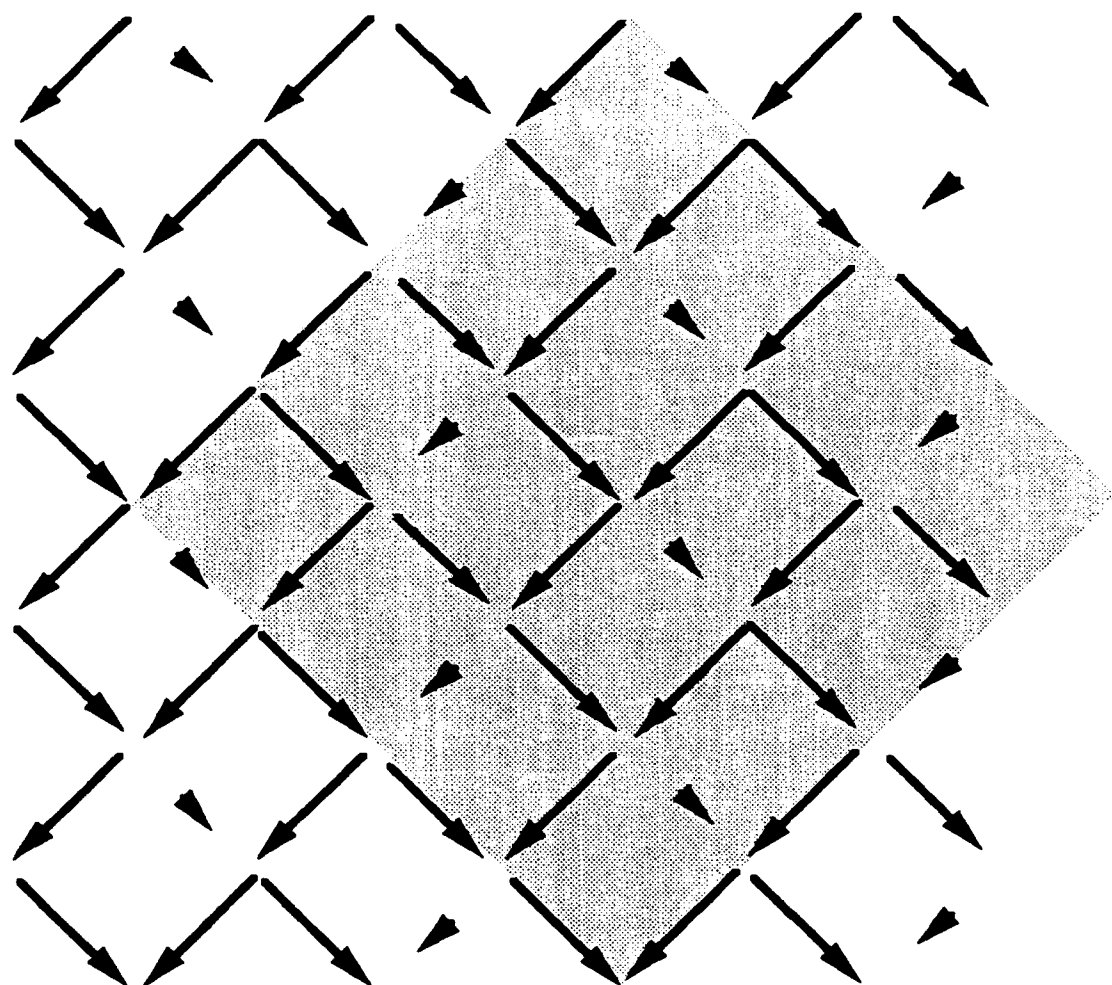


Fig. 4.5. Normalized instantaneous voltage vs. time (in rf cycles) across each junction in a plaquette of the simulated 8×8 junction [11]-oriented square-lattice array on the first giant shapiro step at $\Omega=0.6$ and $i_{rf}i_c=0.875$. γ_1 , γ_2 , γ_3 , and γ_4 are the same gauge-invariant phases differences shown in the inset of Fig. 4.4.



(a)

Fig. 4.6. (a) Supercurrent flow pattern throughout an 8×8 junction $[11]$ -oriented square-lattice array at $\Omega=0.1$ and $f=1/2$. Note that the entire array can be described as a periodically repeated 2×2 unit cell [one of which is shaded in the array]. (b, next page) Supercurrent flow pattern throughout the same array at $f=1/2$. Now, however, $\Omega=1.0$. Note that the supercurrent pattern has expanded to a periodically repeated 4×4 unit cell [shaded region]. In each figure, the transport current flows from top to bottom.



(b)

regular, it is no longer simple. Indeed, with the supercurrents flowing as they are, the array is now a periodically repeated 4 x 4 unit cell (shown as the shaded squares in the figure). If we increase only the drive current amplitude and keep Ω constant (where, again, $\Omega \geq 0.6$), the supercurrent flow, and subsequently, the spatial pattern of the array, changes again such that the array consists of periodically repeated 8 x 8 unit cells.⁵ Such *spatial period doubling* has never been reported in a system of *overdamped* Josephson-junction arrays and is quite surprising since the equation of motion of the system consists of only first-order differential equations.^{6,7} We have tried to investigate this further using parallel processors—a Connection Machine and a Maspar computer—since it is possible to simulate extremely large arrays with far less cpu time than when using a conventional serial computer (Sohn and Fitzgerald, 1991).⁸ However, due to the limited cpu time available to period doubling versus rf frequency or drive current.⁹

⁵Spatial period doubling of this kind is very similar to that found in the patterned flow of water between two rotating cylinders [Gollub and Swinney, 1974]. In the latter case, spatial period doubling leads to the onset of *turbulence*.

⁶Evidence of spatial and temporal period doubling has been found in single *underdamped* Josephson junctions and arrays where the equation of motion consist of second-order differential equations [see Octavio and Guerrero, 1990; Octavio, 1984; Kautz and Monaco, 1985; and Hadley, thesis, 1988].

⁷Although spatial or temporal period doubling is usually not found in systems whose equation of motion is a first-order differential equation; such effects leading to chaotic behavior *do* occur in systems which consist of *coupled* first-order differential equations. One example of this is the Lorenz system which models weather patterns [Lorenz, 1963]. The equations describing this system are given by

$$\begin{aligned} dx/dt &= \sigma(y-x) \\ dy/dt &= rx-y-xz \\ dz/dt &= xy-bz \end{aligned}$$

where σ , r , and b are constants. The solutions to the Lorenz system are highly sensitive to the initial conditions and are complicated for a wide range of σ , r , and b [Holden, 1986]. If we map out the trajectories of the solutions, we produce what is known as the "Butterfly Effect." Our own system consist of $\sim N^2$ coupled first-order differential equations; it should therefore *not* be surprising that we have found evidence of spatial period doubling in our arrays.

⁸Use of a Maspar was provided by the Robotics Laboratory at Harvard University and use of the Connection Machine, by Thinking Machines Corporation, Cambridge, MA.

⁹Because we are dealing with *spatial* and not temporal period doubling, we do not have any means of *experimentally* investigating the just described phenomenon in our SNS arrays.

4.3 Microscopic Model

In the following sections, we study both square- and triangular-lattice arrays of overdamped Josephson junctions on a more microscopic level. Rzchowski et al. (1991) have shown that the dynamics of an entire [10]-oriented square-lattice array at $f=1/2$ can be modeled with a 2×2 unit cell of the array. Their analysis centers on the detailed response of the gauge-invariant phase difference across each junction in the 2×2 cell. In Sec. 4.3.1, we present our own analysis of a 2×2 unit cell of the [11]-oriented square-lattice array at $f=1/2$. In Secs. 4.3.2 and 4.3.3, we extend this "microscopic" model to the unit cells of the $[10\bar{1}]$ - and $[2\bar{1}\bar{1}]$ -oriented triangular-lattice arrays, respectively, and describe our results.

4.3.1 The 2×2 unit cell of the [11]-oriented array

As has been previously discussed, the [11]-oriented square-lattice array at $f=1/2$ can be described as a 2×2 unit cell. Following Rzchowski et al. (1991), we demand that the superlattice unit cell carry a net current equal to the external drive current. For the [11] geometry, we model this as equal current flows of $(I_{tot}/2)=(i_{dc} + i_{rf}\sin\omega t)$, where I_{tot} is the applied current per node (normalized to the single-junction, i_c), in the orthogonal [10] and [01] directions in the cell. If we satisfy fluxoid quantization and total current conservation at the central node, we can write the following equations,

$$\alpha + \gamma + \beta' + \beta = \pi \quad (\text{mod } 2\pi) \quad (4.3.1.a)$$

$$\frac{d\beta'}{d\tau} + \sin\beta' - \frac{d\beta}{d\tau} - \sin\beta = \frac{I_{tot}}{2} \quad (4.3.1.b)$$

$$\frac{d\gamma}{d\tau} + \sin \gamma - \frac{d\alpha}{d\tau} - \sin \alpha = \frac{I_{tot}}{2} \quad (4.3.1.c)$$

$$\frac{d\gamma}{d\tau} + \frac{d\alpha}{d\tau} + \sin \gamma + \sin \alpha - \frac{d\beta}{d\tau} - \frac{d\beta'}{d\tau} - \sin \beta - \sin \beta' = 0 \quad (4.3.1.d)$$

where α , β , β' , and γ are the gauge-invariant phase differences as denoted in Fig. 4.7, $\tau = (2eicr_n/\hbar)t$, and $I_{tot} = I_{dc} + I_{rf} \sin(\omega t)$ is the applied dc and rf current per node. Making the following substitutions, $x = (\gamma - \alpha)/2$, $y = (\gamma + \alpha)/2$, $u = (\beta - \beta')/2$, and $v = (\beta + \beta')/2$, the above equations become

$$\frac{dx}{d\tau} + \cos y \sin x = \frac{I_{tot}}{4} \quad (4.3.2.a)$$

$$-\frac{du}{d\tau} - \sin y \sin u = \frac{I_{tot}}{4} \quad (4.3.2.b)$$

$$2 \frac{dy}{d\tau} + \sin y \cos x - \cos y \cos u = 0 \quad (4.3.2.c)$$

If we numerically solve Eq. (4.3.2), we obtain I - V curves which show only integer giant Shapiro steps. In addition, we learn that $dy/d\tau = 0$. Using this fact, we find that we can reproduce the equation derived from our simulations in the previous section, namely

$$\frac{d\zeta}{d\tau} + \frac{1}{\sqrt{2}} \sin \zeta = \frac{I_{tot}}{2} \quad (4.3.3)$$

where $\zeta = \gamma - \pi/4$. In order to derive Eq. (4.3.3), we had previously assumed that the voltages across the junctions in a plaquette were equal to one another. The numerical solution to Eq. (4.3.2) shows us that this assumption is correct.

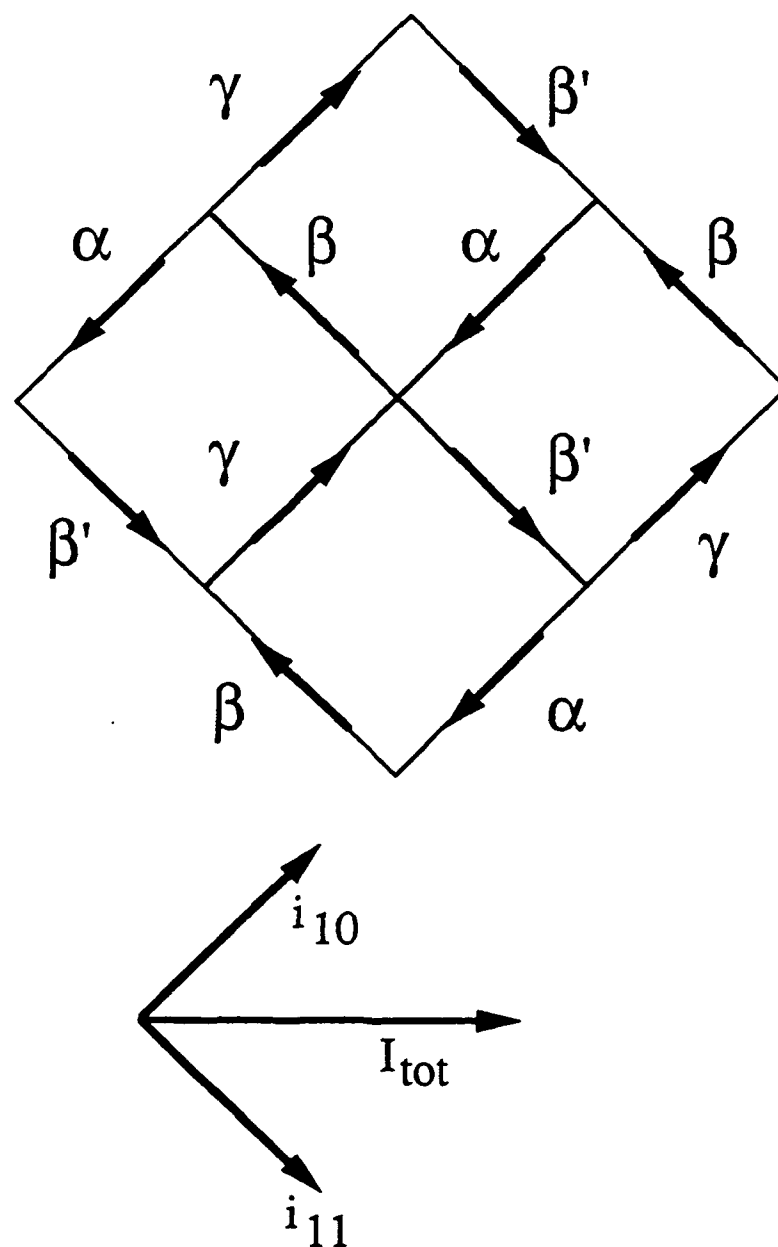


Fig. 4.7. 2×2 unit cell of the [11]-oriented square-lattice array. The gauge-invariant phase differences of the individual junctions are as indicated. I_{tot} is the applied current per node while i_{10} and i_{11} are the components of I_{tot} in the [10] and [11] array lattice direction. Both i_{10} and i_{11} are assumed to be $I_{tot}/2$.

We comment again that Eq. (4.3.3) is equivalent to an equation of motion for a single overdamped Josephson junction. Renne and Polder (1974) have analytically shown that these junctions produce only integer Shapiro steps. It follows then that [11]-oriented arrays produce only integer steps as well.

4.3.2 $[10\bar{1}]$ -oriented triangular-lattice array

Like the [10]-oriented square-lattice array, the $[10\bar{1}]$ -oriented triangular-lattice array produces both integer and fractional giant Shapiro steps. Satisfying fluxoid quantization, current conservation and net current flow, we can write the following equations for the $[10\bar{1}]$ array unit cell when $f=1/2$

$$\alpha + \beta + \gamma = \pi \quad (4.3.4.a)$$

$$\frac{d\gamma}{d\tau} - \frac{d\alpha}{d\tau} + \sin \gamma - \sin \alpha = I_{tot} \quad (4.3.4.b)$$

$$\frac{d\gamma}{d\tau} + \frac{d\alpha}{d\tau} + \sin \gamma + \sin \alpha - \frac{d\beta}{d\tau} - \sin \beta = 0 \quad (4.3.4.c)$$

where α , β , and γ are the gauge-invariant phase differences denoted in Fig. 4.8. If we let $x=(\gamma-\alpha)/2$ and $y=(\gamma+\alpha)/2$, Eq. (4.3.4) becomes

$$2 \frac{dx}{d\tau} + 2 \cos y \sin x = I_{tot} \quad (4.3.5.a)$$

$$2 \frac{dy}{d\tau} + \frac{1}{2} \sin 2y + \sin y \cos x = 0 \quad (4.3.5.b)$$

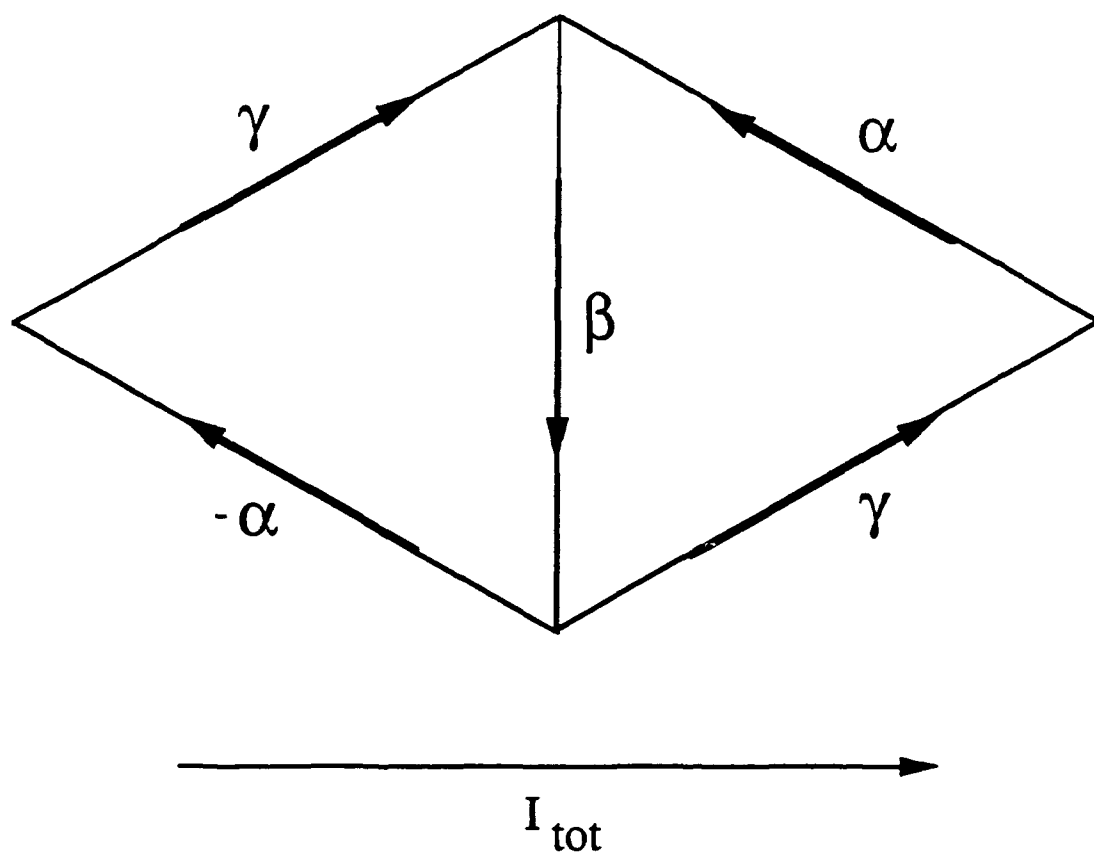


Fig. 4.8. Diagram of the unit cell in the $[10\bar{1}]$ -oriented triangular-lattice array. The gauge-invariant phase differences of the individual junctions are as indicated. I_{tot} is again the applied current per node.

Numerically solving Eq. (4.3.5) for a variety of rf powers, we obtain I - V curves which show both integer and fractional giant Shapiro steps. A plot of the stepwidth vs. rf power is shown in Fig. 4.9. The general features of Fig. 4.9, namely an oscillatory behavior similar to that of a single junction and a decrease in stepwidth with an increase in step number, are similar to those found in the stepwidth vs. rf power of the [10]-oriented square-lattice array.

4.3.3 $[2\bar{1}\bar{1}]$ -oriented triangular-lattice array

We have simulated a $[2\bar{1}\bar{1}]$ -oriented triangular-lattice unit cell, such as the one shown in Fig. 4.10. Based on our knowledge of the phase evolution of the junctions in the $[11]$ -oriented square-lattice array on an integer step at $f=1/2$ and at low rf frequencies, we make the assumption that the phase differences of the diagonal junctions, denoted as γ in Fig. 4.10, are equal. Because the sum of the total current is conserved at each node and because fluxoid quantization requires $2\gamma - \alpha = 2\pi f$, then, for $f=0$, we obtain the equation

$$2\frac{d\alpha}{d\tau} + 2\sin\frac{\alpha}{2} + \sin\alpha = I_{tot} \quad (4.3.6.a)$$

If $f=1/2$, Eq. (4.3.6.a) is replaced by

$$2\frac{d\alpha}{d\tau} + 2\cos\frac{\alpha}{2} + \sin\alpha = I_{tot} \quad (4.3.6.b)$$

Numerically solving Eq. (4.3.6.a), we obtain I - V curves which show only integer giant Shapiro steps. Interestingly, identical I - V curves are obtained when solving Eq. (4.3.6.b). Using the obtained I - V curves, we plot the stepwidth vs. rf power. Fig. 4.11 shows such a plot for $f=0$ and $\Omega=0.5$. Here we see that, as in our experimental results, the odd steps

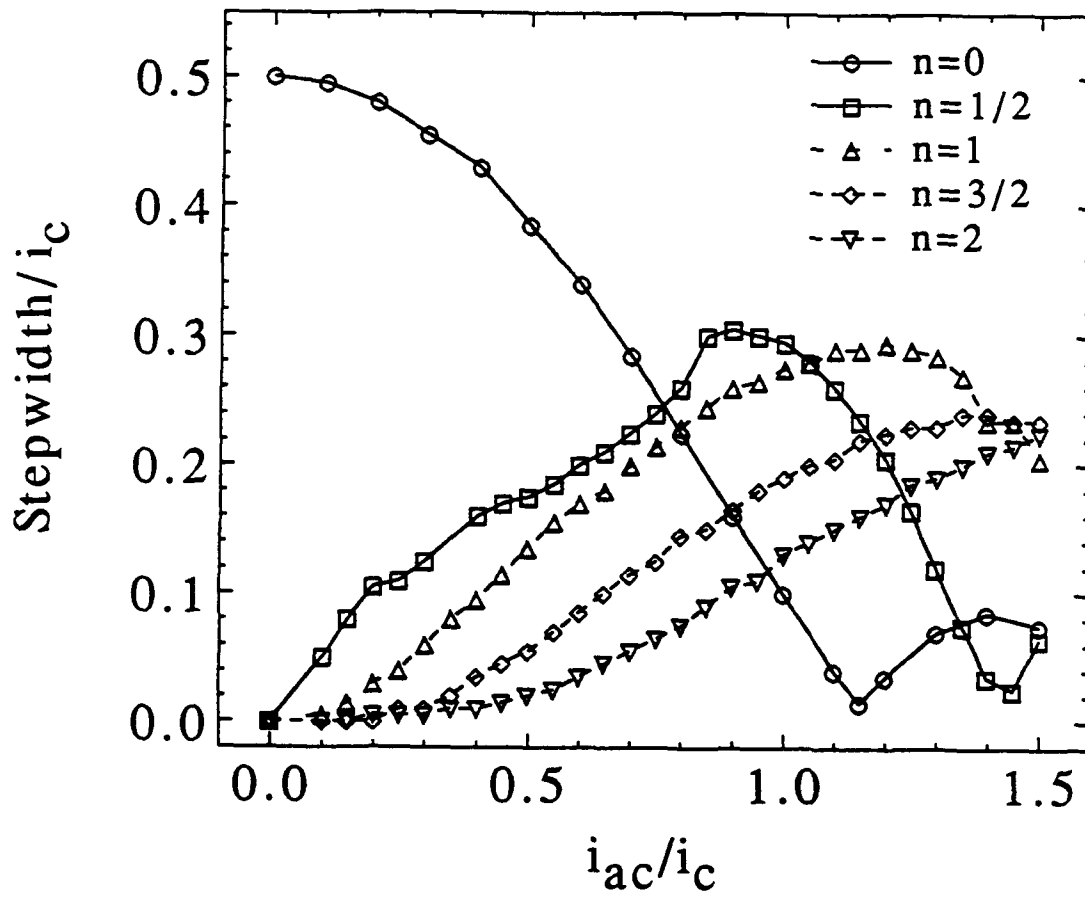


Fig. 4.9. Simulated stepwidth vs. rf power for the $[10\bar{1}]$ -oriented triangular lattice array at $f=1/2$. Oscillatory behavior and a decrease in stepwidth with an increase in step number are similar to single junction behavior.

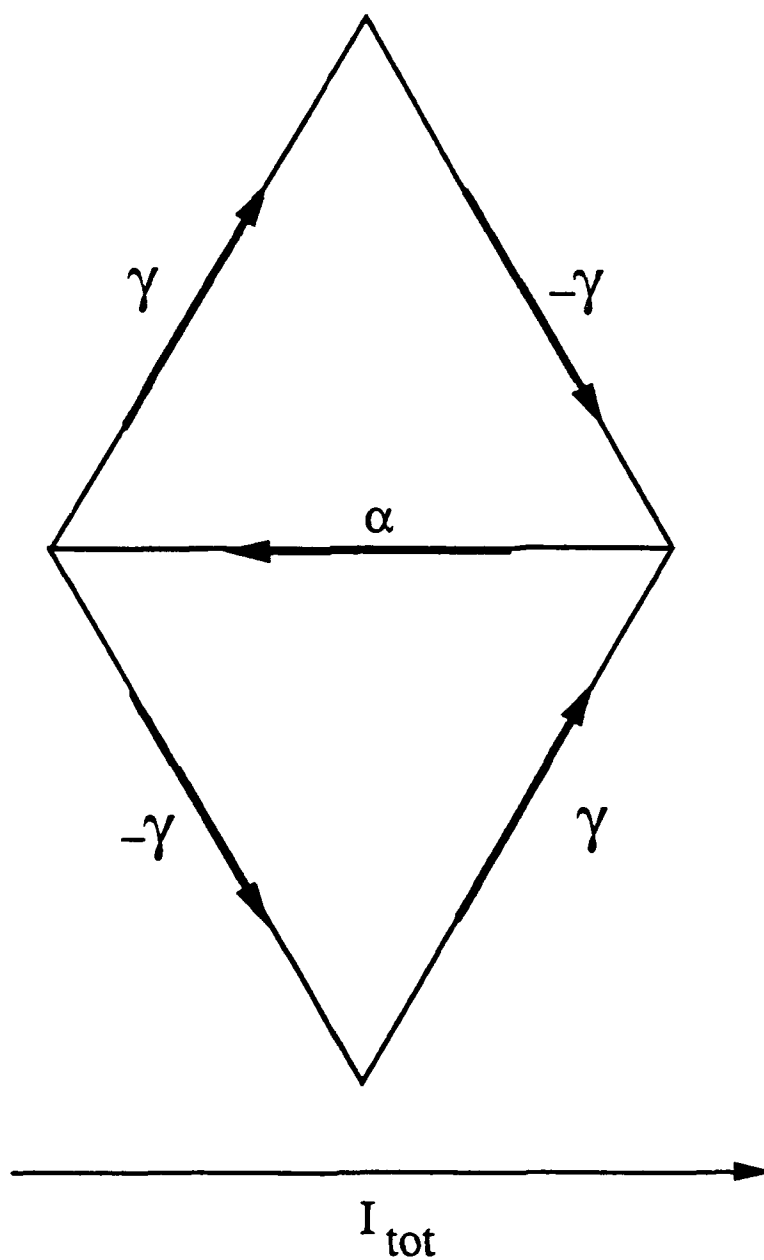


Fig. 4.10. Diagram of the unit cell in the $[2\bar{1}\bar{1}]$ -oriented triangular-lattice array. The gauge-invariant phase differences of the individual junctions are as indicated. Again, I_{tot} is the applied current per node.

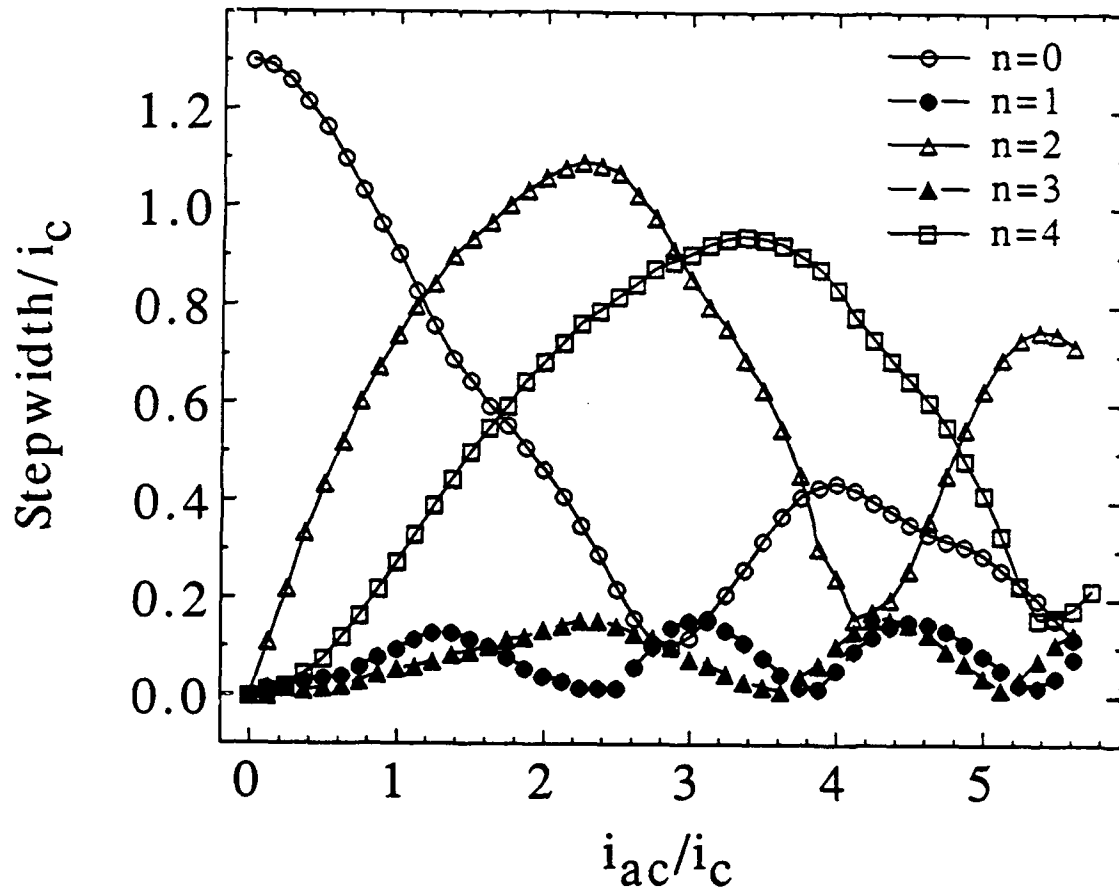


Fig. 4.11. Simulated stepwidth vs. rf power for the $[2\bar{1}\bar{1}]$ -oriented triangular-lattice array at $f=0$. Odd steps are smaller than even steps, agreeing with experimental results. Even steps never go to zero.

are indeed smaller than the even ones. Interestingly, the widths of the even steps never go to zero for any rf power.

4.4 Conclusion

The analysis we have just outlined can be used only for cases in which the array can be broken down into a periodically repeated cell. For the square-lattice array, we saw that we could describe the array as a periodically repeated 2×2 unit cell. For the triangular-lattice array, we saw that we could describe it as single unit cell. The size of the superlattice cell in the presence of a drive current at $f=1/2$ for intermediate angle arrays, such as the 15° array we experimentally studied, is not known at this time. Large scale simulations, such as those discussed in Section 4.2, are needed to determine this and to understand the finer details of these intermediate arrays. The spatial period doubling that was found in the $[11]$ -oriented square-lattice arrays using the large scale simulations cannot be investigated using our microscopic model since this model constrains the evolution of the gauge-invariant phase differences.

CHAPTER V

SNS ARRAYS: DISCUSSION

5.1 Introduction

Our experimental results show that the macroscopic transport current direction plays an important role in the observed step structure of square- and triangular-lattice arrays. In the systems we have studied, we found that the $[10]$ -oriented square- and $[10\bar{1}]$ -oriented triangular lattice arrays produce strong fractional giant Shapiro steps. These arrays have junctions which are perpendicular to the transport current and hence do not carry any component of the external current. In addition, the Lorentz force created by the macroscopic transport current is directed towards the *junction* sites. In contrast, we found that the $[11]$ -oriented square- and $[2\bar{1}\bar{1}]$ -oriented triangular-lattice arrays produce only integer giant Shapiro steps. All the junctions in these arrays carry some component of the external current. More importantly, however, the Lorentz force in these arrays is directed towards the *island* sites. This results in the arrays being mathematically reducible to a single junction for $f=1/2$. The 15° array is an intermediate case, as we have found that this array produces weak fractional giant Shapiro steps. Like the $[11]$ -oriented square- and $[2\bar{1}\bar{1}]$ -oriented triangular-lattice arrays, all of the 15° array's junctions carry some component of the external current; however, unlike the $[11]$ -oriented and $[2\bar{1}\bar{1}]$ -oriented arrays, the Lorentz force is directed (albeit somewhat obliquely) toward the junction sites.

In the following sections, we present two very different models which describe the dynamical properties of proximity-effect Josephson-junction arrays.¹ The two models, together, provide us with a better understanding of the arrays we have studied.

¹Much of what is presented in this chapter has been published in Sohn et al., 1992a.

5.2 The Moving Vortex Model

The behavior of [10]-oriented square-lattice proximity-effect Josephson-junction arrays has been described in terms of the driven motion of a superlattice of field-induced vortices commensurate with the underlying array lattice [Benz et al., 1990; Free et al., 1990; K. H. Lee et al., 1990; and H. C. Lee et al., 1990]. For example, when $f=1/2$, the 2×2 vortex superlattice moves one array unit cell in a direction perpendicular to the transport current after one rf cycle (see Figure 5.1). This motion leads to each junction in the array having an average phase slip of π per rf cycle. From the Josephson voltage relationship [Josephson, 1962],

$$V = \frac{\hbar}{2e} \frac{d\gamma}{dt} \quad (5.2.1)$$

it follows that the average voltage across the entire array is

$$\langle V \rangle = N \frac{\hbar v}{2e} \pi = \frac{N}{2} \frac{\hbar v}{2e} \quad (5.2.2)$$

which is Eq. (3.1.2) with $n=1$ and $q=2$.

There is some ambiguity involved, however, in using the vortex model when $f=1/2$. This happens because every plaquette is occupied by a circulating current, so it is not completely clear whether to count clockwise currents, counterclockwise currents, or both as "vortices." Nonetheless, we have found that the vortex model is a useful *phenomenological* description. The basic assumptions are that the overall macroscopic motion of the vortices is perpendicular to the external current direction, and that each junction will undergo a phase slip of 2π in the time it takes for the driven vortices to return

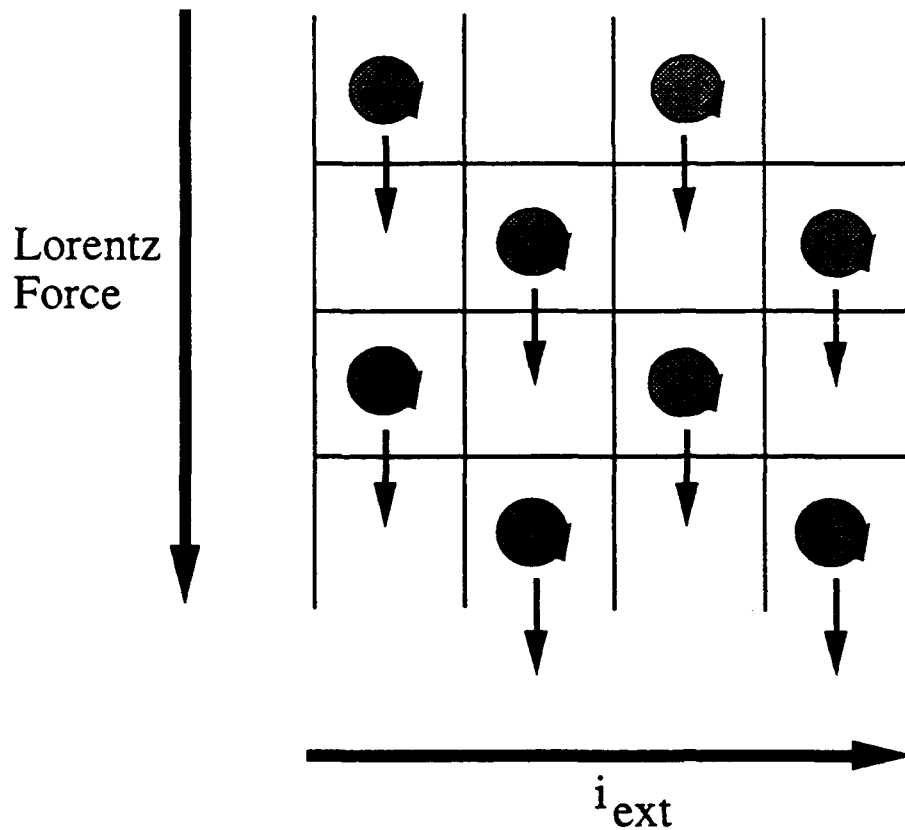


Fig. 5.1. Vortex configuration in the [10]-oriented square-lattice array at $f=1/2$. Large vertical arrow indicates the direction of the Lorentz force resulting from i_{ext} . Small arrows indicate macroscopic motion of vortices during one rf cycle on the $n/q=1/2$ step.

to their original configuration. (A more precise, but less intuitive, model [Octavio et al., 1991] is presented in the following section.)

Consider next the $[11]$ -oriented square-lattice arrays in the presence of a general field $f=p/q$. In this case, the Lorentz force directs the vortices toward the high energy barriers of the island sites (see Fig. 5.2 for the $f=1/2$ example). As we stated previously in Sec. 4.2.2, vortices cannot move through such a barrier; they can only move through the low energy barrier [Lobb et al., 1983] of the egg-carton potential. Based upon this, we can only conclude that *no* vortex-superlattice motion can occur in the $[11]$ -oriented square-lattice arrays. Consequently, these arrays behave like a set of coupled series arrays which produce only integer giant Shapiro steps.

Unlike in the $[11]$ -oriented arrays but very much like in the $[10]$ -oriented arrays, vortex-superlattice motion *can* occur in the 15° square-lattice array. The Lorentz force, in this orientation, directs the vortices, albeit obliquely, through the low energy barrier of the egg-carton potential of the array and into the nearest-neighbor plaquette. Consequently, fractional giant Shapiro steps can be produced by the 15° array, but less strongly than in the $[10]$ -oriented arrays, where the Lorentz force is directed exactly towards the lowest barrier position.

As we have stated previously, the experimental results we have obtained for the square- and triangular-lattice arrays are very similar. Like the $[10]$ -oriented square-lattice array, the $[10\bar{1}]$ -oriented triangular-lattice array exhibits fractional steps at voltages corresponding to Eq. (3.1.2). In Figure 5.3 we have drawn the $f=1/2$ state of the $[10\bar{1}]$ -oriented array. Here we see that the macroscopic motion of the vortices is through the low energy barrier of the egg-carton potential and toward the nearest-neighbor plaquette. Thus, the junctions in the array can slip $2\pi/q$ per rf cycle and correspondingly produce fractional giant Shapiro steps.

The $[2\bar{1}\bar{1}]$ -oriented triangular-lattice array is the most interesting of all the arrays we have studied. In Fig. 5.4 we have drawn the $f=1/2$ state of this array and have

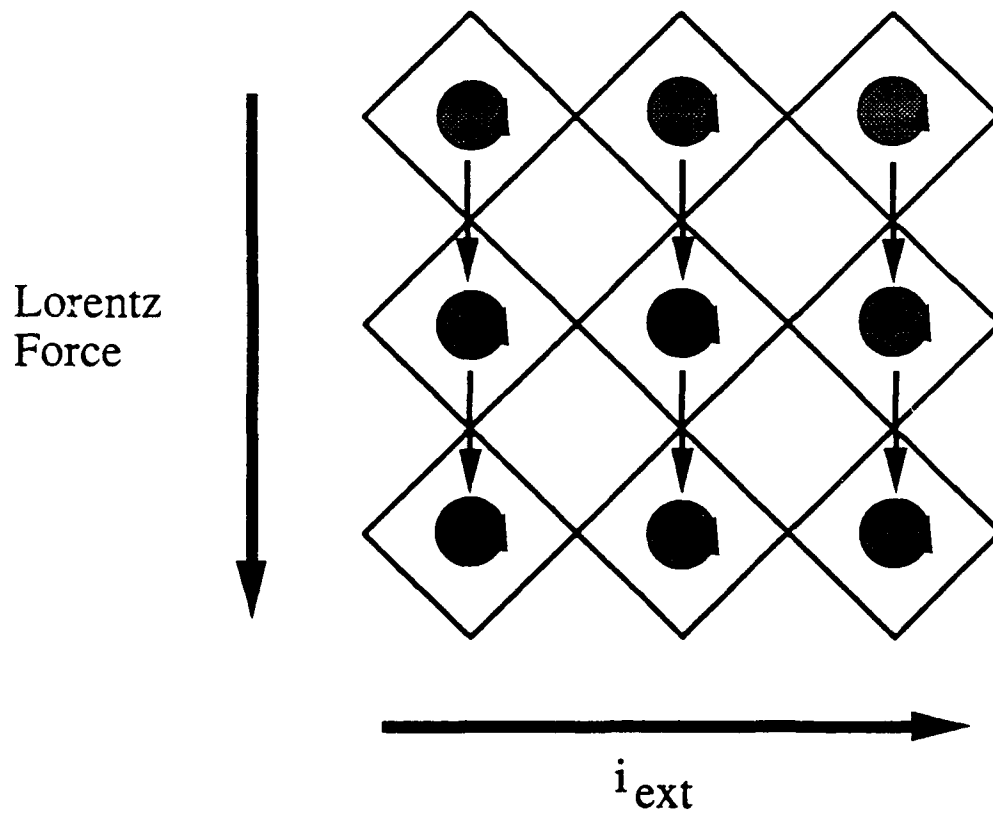


Fig. 5.2. Vortex configuration in the [11]-oriented square-lattice array at $f=1/2$. Large vertical arrow indicates the direction of the Lorentz force resulting from i_{ext} . Small arrows indicate macroscopic motion of vortices during one rf cycle on the $n/q=1$ step.

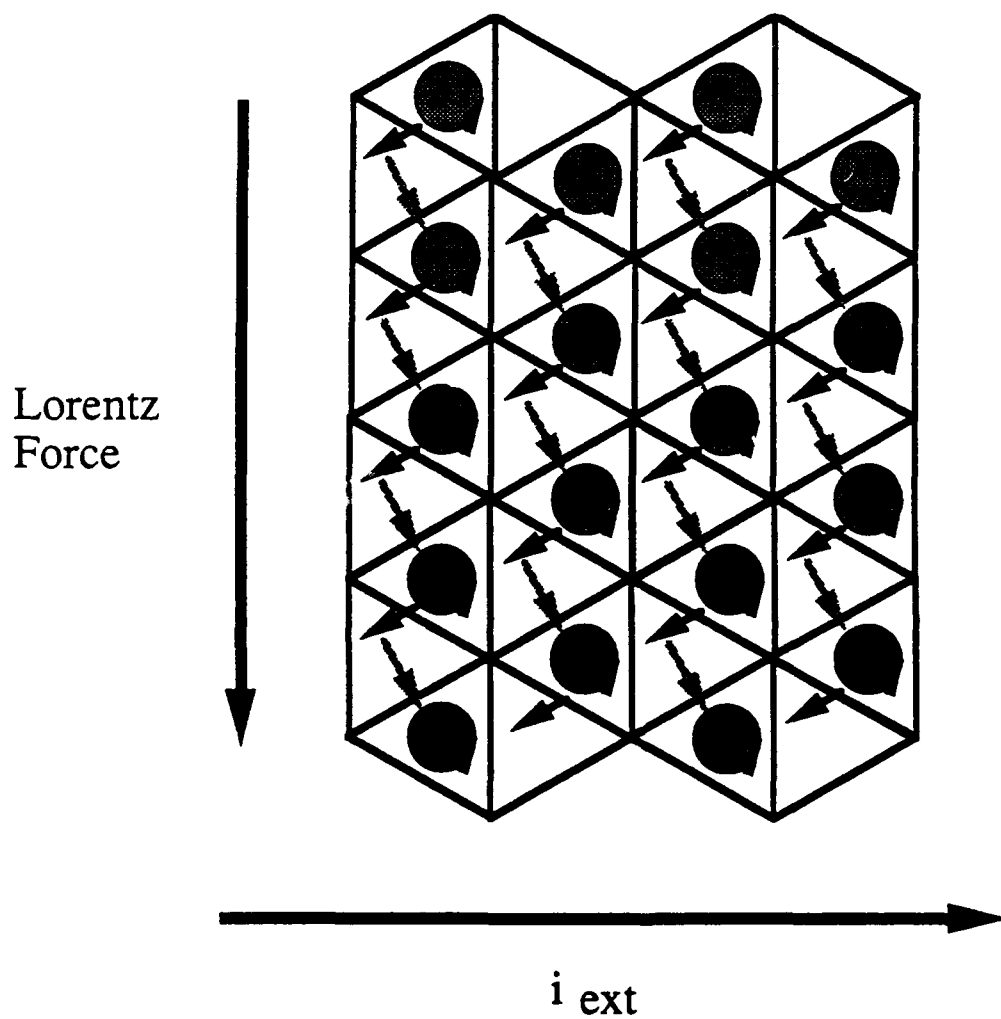


Fig. 5.3. Vortex configuration in the $[10\bar{1}]$ -oriented triangular-lattice array at $f=1/2$. Large vertical arrow indicates the direction of the Lorentz force resulting from i_{ext} . Arrows indicate macroscopic motion of vortices during 2 subsequent rf cycles on the $n/q=1/2$ step. While the light arrows indicate vortex motion during one rf cycle, the dark arrows indicate vortex motion during a subsequent rf cycle.

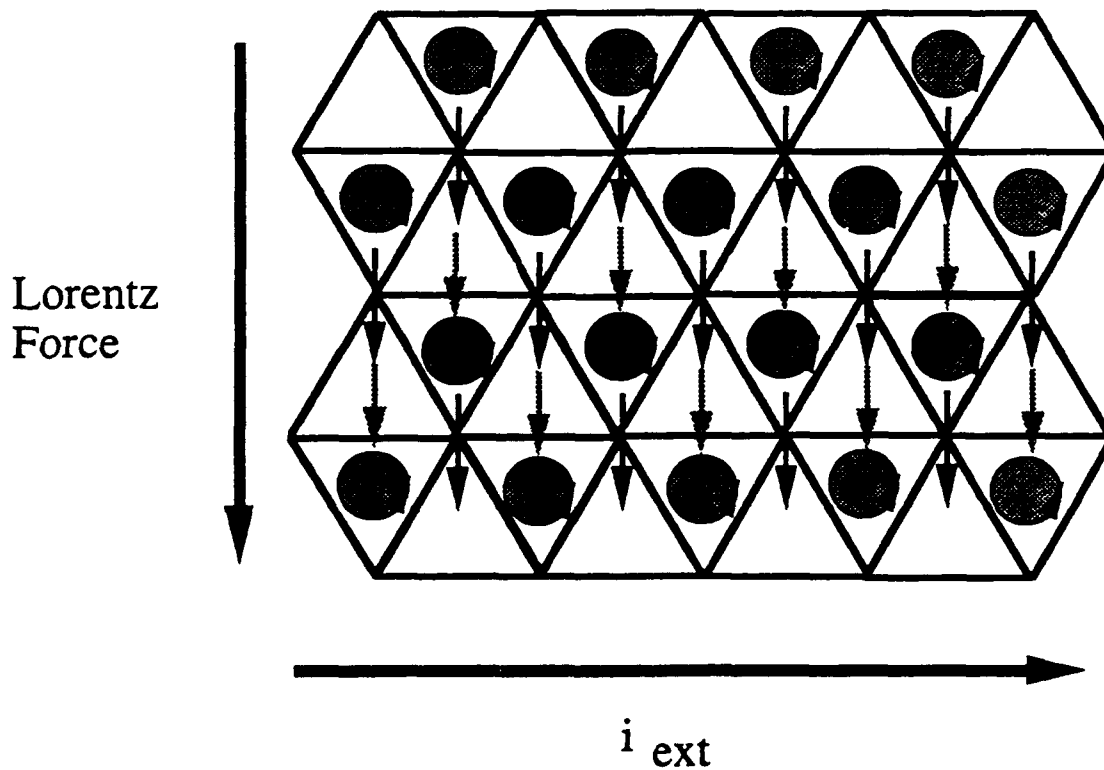


Fig. 5.4. Vortex configuration in the $[2\bar{1}\bar{1}]$ -oriented triangular-lattice at $f=1/2$. Again, large vertical arrow indicates the direction of the Lorentz force resulting from i_{ext} . The light arrows show that some of the vortices are directed toward the low energy barrier of the egg-carton potential. The dark arrows show that the remaining vortices are directed toward the *high* energy barrier. Because vortices cannot go through this barrier, no vortex-superlattice motion is possible. Fractional giant Shapiro steps are therefore not produced.

indicated by arrows the direction in which the vortices should move under the influence of the Lorentz force. The light arrows in the figure show that some of the vortices are directed toward the low energy barrier of the egg-carton potential and through the nearest-neighbor plaquette. The dark arrows show that the remaining vortices are directed toward the *high* energy barrier of the egg-carton potential. Since, as we have stated previously, vortices cannot go through the high energy barrier, we assert that no vortex-superlattice motion occurs in the array. Thus, as in the $[11]$ -oriented square-lattice array, the $[2\bar{1}\bar{1}]$ -oriented triangular-lattice array behaves as though it were a coupled series array which produces only integer giant Shapiro steps.

As we have stated previously, changing the macroscopic current direction does not affect the general features of the linear magnetoresistance of square- and triangular-lattice arrays, although it does affect the non-linear rf response of the individual arrays. The field modulation in a magnetoresistance measurement comes from the fact that the resistance, R , is a function of $T/T_c(f)$, which in turn is a function of field, *not* current. When we apply a small current, regardless of its direction with respect to the array, the wells in the egg-carton potential tilt slightly. Thermal fluctuations lead to the unpinning of the vortices and to the subsequent creation of a small voltage across the array. In an rf experiment, we are driving the system very hard, literally dragging the vortices from well to well. Therefore, current direction should and does play an important role in the outcome of these types of experiments.

The moving vortex model is only a phenomenological model which explains in general terms why fractional giant Shapiro steps can or cannot exist in certain oriented arrays. As we have just shown, when the Lorentz force in an array directs the vortices toward the high energy barrier of the island sites, no vortex-superlattice motion is

possible,² since the vortices cannot go through the islands. Consequently, the array behaves as though it were a set of coupled series arrays in zero field and produces only integer giant Shapiro steps. Since the moving vortex model is unable to predict the widths of the giant Shapiro steps, we take an entirely different approach towards explaining the presence or absence of fractional giant Shapiro steps in Josephson-junction arrays. In the section below, we undertake this task by examining the individual junctions in an array unit cell and applying Kirchoff's voltage law.

5.3 The Pendulum Model

The equation of motion for a single Josephson-junction [Eq. (4.1.1)] is identical to that of a damped driven pendulum with mass $\propto C$, damping $\propto 1/R$, and with constant and ac applied torques. In an array, the equations are coupled, via Kirchoff's laws, and the array becomes equivalent to a network of coupled pendula. Thus, representing the gauge-invariant phase differences, γ_{ij} , where i and j are the i th and j th island in the array as pendula, is a pictorial and quantitative description of the dynamical properties of the array [Octavio et al., 1991].

When driven by an rf current with frequency ν , a single junction can phase-lock to the rf current. When the junction is overdamped, γ swings around a total of $2\pi n$ in one rf cycle. If $\langle d\gamma/dt \rangle$ equals $2\pi n \nu$ as we have indicated, Eq. (5.2.1) transforms into the equation of an integer Shapiro step [Eq. (1.2.4)].

The above model has been successfully applied to the [10]-oriented square-lattice array [Octavio et al., 1991]. For $f=0$, the junctions parallel to the direction of the transport

²Simulations with periodic boundary conditions were done on 4×4 , 6×6 , and 8×8 junction [11]-oriented square-lattice arrays. These simulations showed that the vortices disappeared and reappeared in the next-nearest neighbor cells during one rf cycle. See Chapter IV for more details.

current act like isolated Josephson junctions and the perpendicular junctions play no role in the array. Eq. (3.1.1) is obtained by considering N γ 's swinging $2\pi n$ times per rf cycle.

For the $f=1/2$ state, the pendulum model must be applied to a 2×2 unit cell [Octavio et al., 1991]. In Figs. 5.5a and b, we have drawn two alternative versions of the $f=1/2$ ground state of such a cell. We take the phase differences, denoted as γ_A and γ_B , of the junctions parallel to the external current to be equal to $\pm\pi/4$ (the array's ground state at $f=1/2$ [Teitel et al., 1983a]) at the beginning of the rf cycle. When i_{ext} is applied in the direction shown in the figure, it winds γ_A and γ_B counterclockwise, γ_A by $3\pi/2$ and γ_B by $\pi/2$ [Free et al., 1990], in one rf cycle (see Fig. 5.5c) such that the cell is now in the other $f=1/2$ ground state shown in Fig. 5.5b. In the following rf cycle, the external current, i_{ext} , again winds γ_A and γ_B counterclockwise: this time γ_A by $\pi/2$ and γ_B by $3\pi/2$. Since half of the junctions in the array act like junction A and the other half act like junction B, we obtain an average phase-slip of π per rf cycle per junction. Eq. (3.1.2) is thus obtained.

For the [11]-oriented square-lattice array in the $f=0$ case, every junction is directly and equally injected with the transport current. Thus, all junctions in the array act like a single Josephson junction and will correspondingly phase-slip $2\pi n$ per rf cycle. Again, we see that we have obtained Eq. (3.2.2).

For $f=1/2$, we look at a particular plaquette in the array. Fig. 5.6a shows a plaquette with the direction of the transport current as indicated. We see in this figure that there are two different paths by which current travels across the [11]-oriented array. By Kirchoff's voltage law, $V_A + V_B = V_C + V_D$. This additional constraint forces $\gamma_A + \gamma_B$ to rotate rigidly with $\gamma_D + \gamma_C$ by 2π per junction per rf cycle as shown in Fig. 5.6b.³ (Our simulations show that at low rf frequencies the array remains in the staircase state. By definition this means that $\gamma_A = \gamma_B$ and is $\pi/2$ out of phase with $\gamma_D = \gamma_C$).

³The absence of fractional giant steps in the [11]-oriented square-lattice array at $f=1/3$ can also be explained by using Kirchoff's voltage law. As opposed to the two we found in the $f=1/2$ state, there are actually three different types of staircases in the array at $f=1/3$. By Kirchoff's voltage law, the voltage across each staircase must be the same. We again deduce that the only periodic solution which satisfies this requirement is one in which every junction must phase-slip $2\pi n$ per rf cycle.

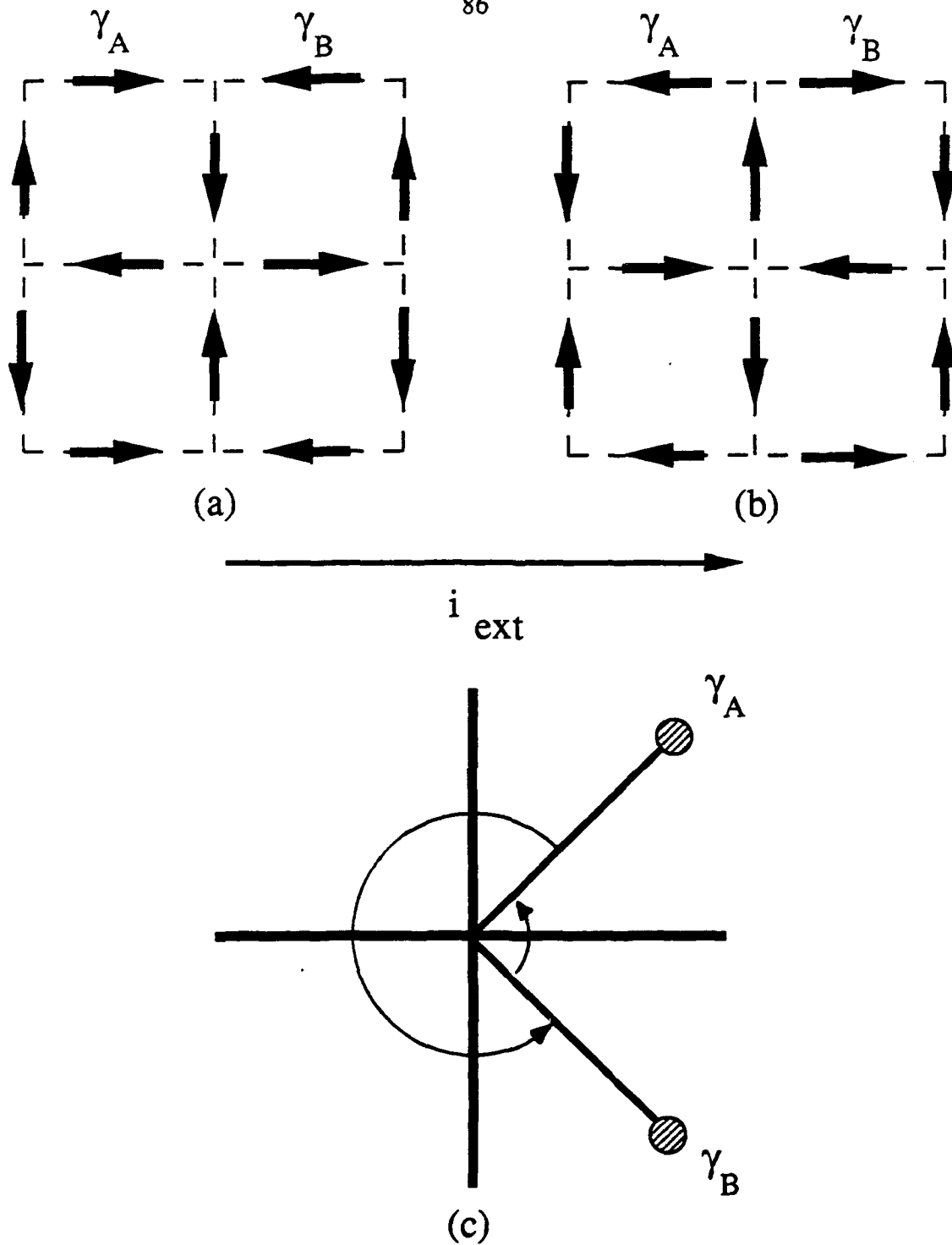
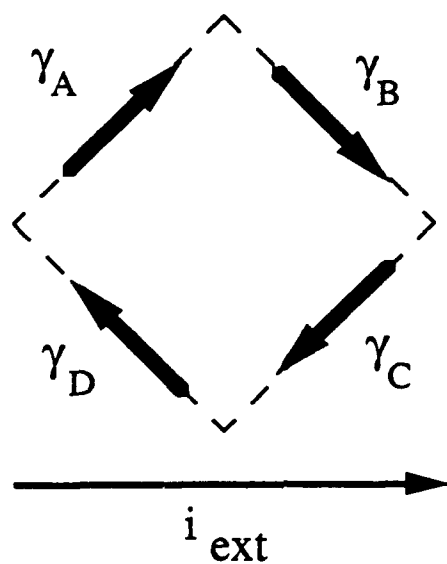
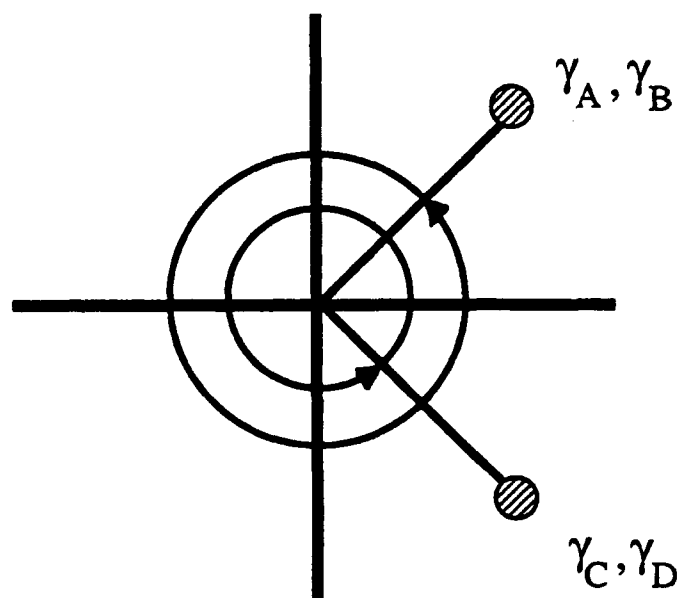


Fig. 5.5. Gauge-invariant phase differences, γ , for junctions in a 2×2 unit cell on the $n/q=1/2$ step at the (a) beginning and (b) end of an rf cycle in the $[10]$ -oriented array at $f=1/2$. Arrows indicate the direction of the supercurrents. The motion of γ_A and γ_B over the same time period is shown in the "pendulum" diagram (c). At the end of one rf cycle, the pendula have interchanged positions; γ_A has advanced $3\pi/2$ while γ_B has advanced by $\pi/2$.



(a)



(b)

Fig. 5.6. (a) Gauge-invariant phase differences, γ , for junctions in a unit cell on the $n=1$ step in the $[11]$ -oriented square-lattice array at $f=1/2$. Arrows indicate direction of the supercurrent. (b) The motion of γ_A and γ_B over the same time is shown in the "pendulum" diagram (c). Unlike in the $[10]$ -oriented case, in the $[11]$ -oriented case, each pendulum has advanced by 2π at the end of one rf cycle.

The results we have obtained from studying the triangular-lattice array can also be explained using the pendulum model. As in the $[10]$ -oriented square-lattice case, in the $[10\bar{1}]$ -oriented triangular-lattice, we find that the gauge-invariant phases are not forced to be locked together and move at some fixed rate per rf cycle in order to satisfy Kirchoff's voltage law. The perpendicular junctions allow the other junctions to rotate more freely. Therefore, the phases can evolve such that fractional steps can exist in this type of an array.

In the $[2\bar{1}\bar{1}]$ -oriented triangular-lattice array, we see that the array really has two types of junctions: straight-feed-through junctions, A , and diagonal ones, B and C , as shown in Fig. 5.7a. By Kirchoff's voltage law, we see that γ_A must move *twice* as fast as γ_B and γ_C per rf cycle. Thus, while junctions B and C are on their first giant Shapiro step, junction A is already on its second step (see Fig. 5.7b). Based on our analysis of the $[11]$ -oriented square-lattice case, we propose that Kirchoff's voltage law and the absence of perpendicular junctions again constrain the evolution of the gauge-invariant phase differences per rf cycle such that the only periodic solution is one in which the phases of the junctions rotate in multiples of 2π per rf cycle. Thus, only integer giant Shapiro steps are produced by the $[2\bar{1}\bar{1}]$ -oriented triangular-lattice array.

The alternating step widths produced by the $[2\bar{1}\bar{1}]$ -oriented triangular-lattice array can be accounted for by examining Eq. (4.3.6). In this equation, we see that the $\sin(\alpha/2)$ term, the term describing the diagonal junctions, contributes to *only* the even harmonics of the time-dependent voltage since its fundamental period is $4\pi n$. The term describing the straight-feed-through junctions, $\sin(\alpha)$, contributes to *both* the even *and* odd harmonics of the time-dependent voltage as its fundamental period is $2\pi n$.⁴ When the array is on an odd step, only the straight-feed-through junctions are on the step; the diagonal ones still have not locked to the rf frequency and are therefore not on a step. When the array is on an even

⁴We have simulated junctions whose current-phase relationship has been modified to $\sin(k\alpha) + \sin(m\alpha)$. We obtain I - V curves which show subharmonic steps corresponding to $(n/q)=1/k$ and $(n/q)=1/m$. It follows then that the $\sin(k\alpha)$ term contributes to the $2\pi/k$ harmonic of the time-dependent voltage and the $\sin(m\alpha)$ term, to the $2\pi/m$ harmonic.

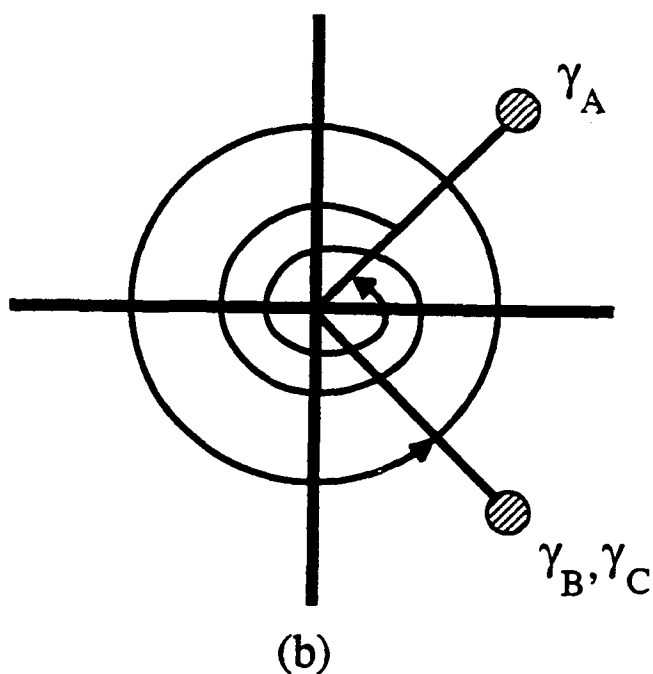
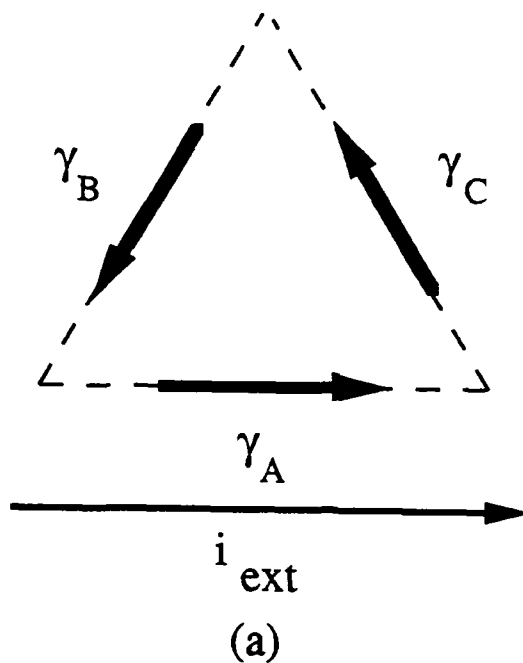


Fig. 5.7. (a) Gauge-invariant phase differences, γ , for a plaquette in the $[21\bar{1}]$ -oriented triangular-lattice array at $f=1/2$. Arrows again indicate the direction of the supercurrent. (b) By Kirchoff's voltage law, $V_A=V_B+V_C$ and accordingly, γ_A must rotate $4\pi n$ per rf cycle while γ_B and γ_C each rotate $2\pi n$ per rf cycle on the n th giant Shapiro step.

step, however, *all* the junctions are on a step, although *not* on the *same* step. As a result, the even steps are much wider than the odd ones, and do not go to zero width because the two steps go to zero for different power levels.

We stress that because of the perpendicular junctions in the $[10]$ -oriented square- and $[10\bar{1}]$ -oriented triangular-lattice arrays, the phase differences of the other junctions are *not* tightly locked together and therefore do not have to rotate at the same rate each rf cycle. Consequently, fractional giant Shapiro steps can be produced by the array. Contrast this to the $[11]$ -oriented square- and $[2\bar{1}\bar{1}]$ -oriented triangular-lattice arrays in which there are no perpendicular junctions. In this case, the phase differences of the junctions are locked together and must phase slip at the same rate each rf cycle, so that the only periodic solution is one in which integer giant Shapiro steps are produced.

5.4 Conclusion

In the course of our study, we have seen the importance of current direction on the dynamics of proximity-effect Josephson-junction arrays. When the Lorentz force, created by the transport current acting on the vortices, is directed toward the island sites, *only* integer giant Shapiro steps [Eq. (3.1.1)] are produced. The Lorentz force in the $[11]$ -oriented square- and $[2\bar{1}\bar{1}]$ -oriented triangular-lattice arrays we studied directed the vortices toward the island sites, and indeed, these arrays produced only integer giant Shapiro steps. If, however, the Lorentz force produced is directed (even somewhat obliquely) toward the junction sites, *both* integer giant [Eq. (3.1.1)] and fractional giant [Eq. (3.1.2)] Shapiro steps are produced. The Lorentz force satisfied this condition in the $[10]$ -oriented and 15° square- and $[10\bar{1}]$ -oriented triangular-lattice arrays. These arrays produced integer and fractional giant Shapiro steps.

The exact relationship between decreasing fractional giant Shapiro stepwidth and current orientation is presently unknown since rounding of the steps due to thermal

fluctuations, noise, and inhomogeneities in the array makes it difficult to experimentally measure the actual stepwidths. This prevents us from making a *quantitative* comparison between the results of our experiments and those of theory; only a *qualitative* comparison can be made. Based on our study of the square-lattice arrays, however, we hypothesize that this relationship might be $\cos(2\theta)$ or $\cos^2(2\theta)$, where θ is the angle off the [10] orientation.

In this chapter, we have presented two very different models under which we can interpret our experimental and numerical results. The moving vortex model provides a phenomenological explanation of why fractional giant Shapiro steps can or cannot occur in the various types of arrays studied. As was stated previously, in the cases where the Lorentz force directs the vortices toward the high energy barrier of the island sites, no vortex-superlattice motion is possible and the array behaves as though it were a set of coupled series arrays in zero field. The pendulum model gives a detailed description of how the gauge-invariant phase differences of the individual junctions evolve per rf cycle. In this model, we see that Kirchoff's voltage law *constrains* the evolution of the phase differences so that for the [11]-oriented square- and $[2\bar{1}\bar{1}]$ -oriented triangular-lattice cases, the only periodic solution allowed is one which corresponds to integer giant Shapiro steps. The perpendicular junctions in the [10]-oriented square- and $[10\bar{1}]$ -oriented triangular-lattice arrays, however, allow the phase differences of the other junctions in the array to evolve more freely per rf cycle. As a result, the allowed periodic solutions correspond to both fractional and integer giant Shapiro steps.

**PART B: ARRAYS WITH LONG-RANGE
INTERACTION**

**CHAPTER VI
MEAN FIELD THEORY**

6.1 Introduction

Two-dimensional arrays of Josephson junctions with short-range interaction are excellent models for exploring two-dimensional phase transitions,¹ flux pinning [Rzchowski et al., 1990], and glassy behavior [Pannetier et al., 1983 and 1984]. These arrays consist of superconducting *islands* which are arranged in a geometric lattice (usually triangular or square) and are Josephson-coupled to their nearest-neighbors.² In this chapter and the following, we present a theoretical and numerical investigation of a novel type of Josephson-junction array whose interesting properties in the disordered limit have already been theoretically noted by Vinokur et al. (1987).³ The arrays we examine differ from conventional Josephson-junction arrays in that they consist of two orthogonal sets of N parallel superconducting *wires* which are coupled to each other by a Josephson junction at every point of crossing (see Fig. 6.1). Because each vertical (horizontal) wire in the array is directly Josephson-coupled to every horizontal (vertical) wire, we describe these novel arrays as having *long-range* interaction.

¹See for instance, Kosterlitz and Thouless (1973); Lobb et al. (1983); Lobb (1984); and Mooij (1983a).

²See for instance, Brown and Garland (1986); and Sohn et al. (1992a).

³Much of what is written in this chapter has been submitted for publication [Sohn et al., 1992b].

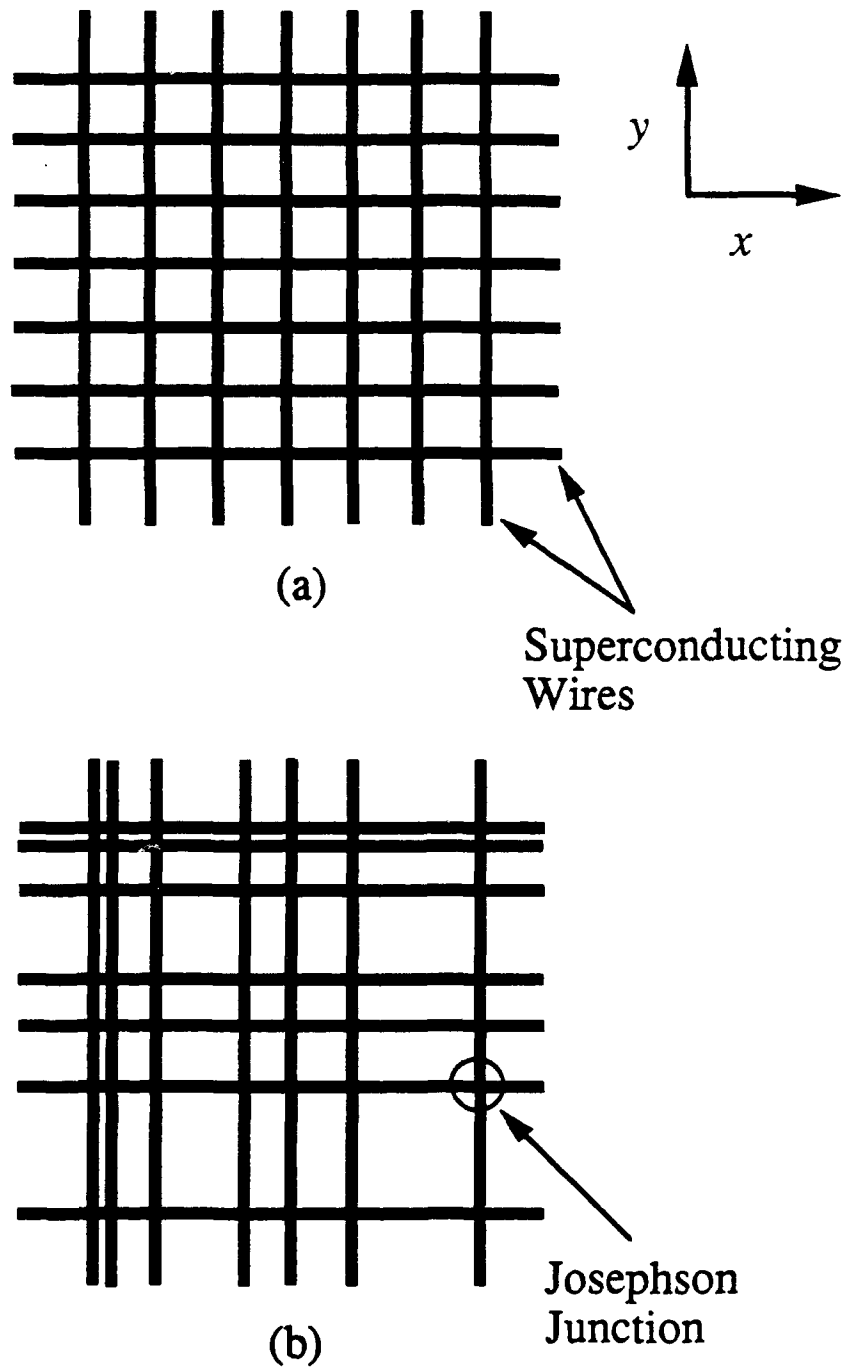


Fig. 6.1. Schematic drawing of an (a) ordered and (b) disordered Josephson-junction array with long-range interaction. The black lines, as indicated above, are superconducting wires which are coupled together through Josephson junctions.

For the system we have examined, it is assumed that the Josephson inductance ($\hbar/2ei_C$) of each junction is infinitely greater than both the kinetic and electromagnetic inductance of the wires connecting adjacent junctions. Consequently, for any circulating current flowing through the array of Josephson junctions, one can assume that the phase gradient along any wire in the array arises *only* from the presence of an external magnetic field. [In fact, this condition is hard to satisfy experimentally, except in small arrays, because of the N junctions in parallel coupled to a single wire.⁴] The Hamiltonian of the system is thus given by the sum of individual Josephson junction energies,

$$H = -\text{Re } E_J \sum_{i=1}^N \sum_{j=1}^N e^{i(\varphi_i^h - \varphi_j^v - A_{ij})} \quad (6.1.1)$$

Here, φ_i^h is the superconducting phase at $x=0$ of the i^{th} horizontal wire, φ_j^v is the phase at $y=0$ of the j^{th} vertical wire, N is the number of wires in each direction or set, E_J is the

Josephson-coupling energy which we take to be constant, and $A_{ij} = \frac{2\pi}{\Phi_0} \int_j^i \mathbf{A} \cdot d\mathbf{l}$ where

$\mathbf{A} = H \times \hat{y}$, and Φ_0 is one flux quantum.

Using the Thouless-Anderson-Palmer (TAP) equation [Thouless et al., 1977], Vinokur et al. (1987) showed that in the presence of a strong transverse magnetic field, disordered arrays with long-range interaction, i.e. those arrays in which the wires of each orthogonal set are randomly displaced, model a *spin glass*, and they investigated the glassy dynamics of such a system. To be more specific, they showed that these arrays undergo a phase transition at a temperature,

⁴See Chapters VIII and IX for further details.

$$T_c = \frac{E_J N^{1/2}}{2^{3/2} k_B} \left[1 + \frac{2H_0}{H} + \left(1 + \frac{8H_0}{H} \right)^{1/2} \right]^{1/2} \quad (6.1.2)$$

where H_0 is the field required to generate a flux quantum through the average-sized *strip* between two adjacent wires and H is the applied field [Vinokur et al., 1987]. Below this temperature, the random phases of the individual wires, φ_i , freeze into a macroscopically phase-coherent state such that,

$$\langle e^{i\varphi_i} \rangle \neq 0$$

without any long-range periodic order in their values. From (6.1.2), we see that for $H \gg H_0$, T_c approaches, to lowest order in H_0/H , the limiting form,

$$T_c = \frac{E_J N^{1/2}}{2k_B} \quad (6.1.3)$$

and for $H \ll H_0$,

$$T_c = \frac{E_J N^{1/2}}{2k_B} \left(\frac{H_0}{H} \right)^{1/2} \quad (6.1.4)$$

We have further studied these novel arrays, in both the *ordered* and *disordered* limit, by using the more simple mean-field approximation and Monte Carlo (MC) simulations. Despite general agreement between our results for the disordered arrays and those of Vinokur et al. (1987), some quantitative discrepancies do exist, which may stem from finite-size effects and the limited amount of disorder present in our arrays.

In this chapter, we describe our mean field analysis⁵ of ordered and disordered arrays with long-range interaction. We will present the results of our MC simulations in the following chapter and show that they are in good agreement with our mean field analysis. In addition to our theoretical and numerical work, we have fabricated these novel arrays and have performed both ac susceptibility and dc transport measurements on them. Our experimental procedure and results will be presented in Chapter VIII. Finally, in Chapter IX, we will discuss our experimental results.

6.2 Mean Field Theory

6.2.1 Ordered arrays

To perform a mean field analysis of ordered arrays with long-range interaction, we follow closely Shih and Stroud's mean field analysis of conventional Josephson-junction arrays [Shih and Stroud, 1983]. Shih and Stroud (1983) obtained the thermodynamic properties of conventional arrays by treating the phases of the individual array islands, ϕ_i , as classical thermodynamic variables within the canonical ensemble. Because of the long-range interactions in the arrays we now study (in contrast to the arrays previously studied), we are able to find analytical expressions for both the temperature-dependent order parameter of the system and the field-dependent transition temperature.

If we treat the phases of the individual wires in our arrays also as classical thermodynamic variables, we can calculate the order parameter of our system, $\eta_i^h = \langle \exp(i\phi_i^h) \rangle$, using the following

⁵The mean field analysis was performed by M. S. Rzchowski (1992).

$$\eta_i^h \equiv \left\langle e^{i\varphi_i^h} \right\rangle = \frac{1}{Z_i} \int d\varphi_i^h e^{i\varphi_i^h} e^{-\beta H_i^{MF}} \quad (6.2.1)$$

Here, H_i^{MF} is the contribution of the i th wire to the total mean-field Hamiltonian and is given by

$$H_i^{MF} = -E_J \sum_{j=1}^N \left[\cos \varphi_i^h \left\langle \cos(\varphi_j^v + A_{ij}) \right\rangle + \sin \varphi_i^h \left\langle \sin(\varphi_j^v + A_{ij}) \right\rangle \right] \quad (6.2.2)$$

where φ_j^v are the phases of the vertical wires which are directly coupled to the horizontal wire of phase φ_i^h . Z_i is the partition function,

$$Z_i = \int d\varphi_i e^{-\beta H_i^{MF}} \quad (6.2.3)$$

and $\beta = (1/k_B T)$. The expectation values in Eq. (6.2.2) are solved self-consistently from equations of the form of Eq. (6.2.1).

In zero field, $\eta_i^h = \eta_j^v \equiv \eta$, and consequently, Eq. (6.2.1) can be rewritten after some reduction as

$$|\eta| = \frac{I_1(NE_J \beta |\eta|)}{I_0(NE_J \beta |\eta|)} \quad (6.2.4)$$

where I_1 and I_0 are Bessel functions of the second kind. Fig. 6.2 shows a numerical solution of $|\eta|$ as a function of $2k_B T/NE_J$ in zero field. Near the array's transition

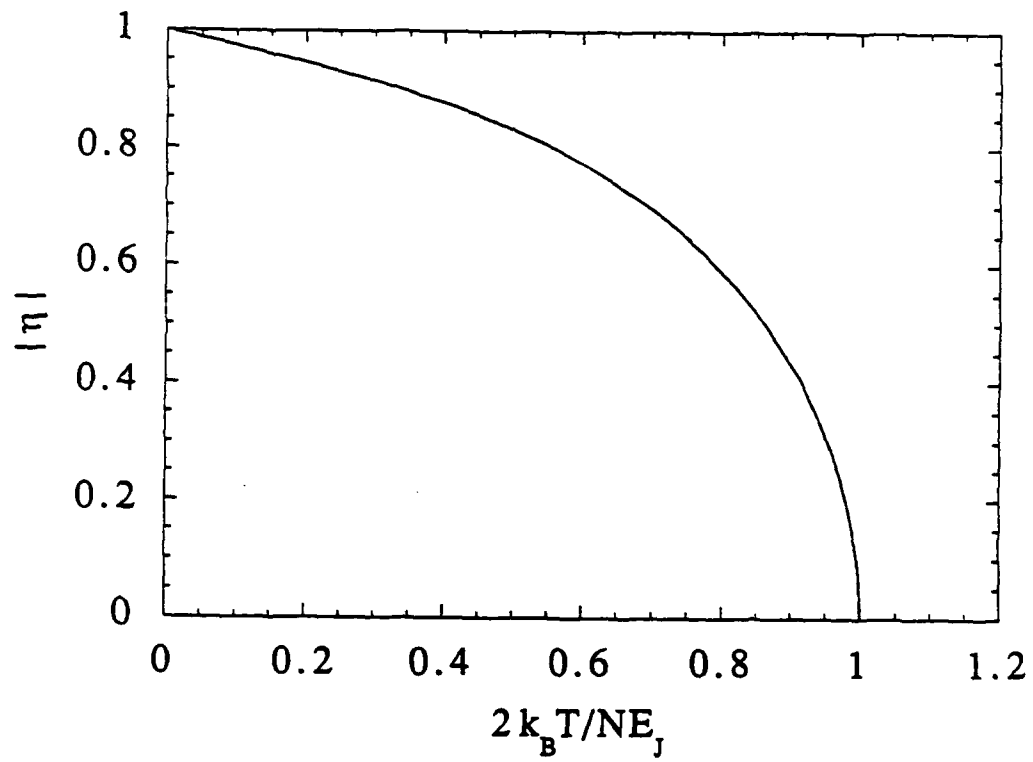


Fig. 6.2. Numerical solution for the magnitude of the order parameter, η , as a function of $2k_B T / NE_J$.

temperature, all the η 's are small, and correspondingly, so are the expectation values in Eq. (6.2.2). Eq. (6.2.4) can therefore be expanded for small argument to obtain,

$$T_c = \frac{NE_J}{2k_B} \quad (6.2.5)$$

The direct proportionality of the transition temperature to the number of horizontal or vertical wires in the array can be readily understood by recognizing the fact that in order for the system to enter the phase-coherent state, the energy per wire available for fluctuation ($k_B T$) must be on the order of NE_J , the total coupling energy between that wire and the wires orthogonal to it.

The mean energy per wire of the system in zero field can be derived from Eq. (6.2.2) and summing it over i . Doing this, we obtain the mean-field Hamiltonian,

$$H_{MF} = -\text{Re} E_J \sum_{i=1}^N e^{i\phi_i^h} \sum_{j=1}^N \eta_j^{v*} \quad (6.2.6)$$

The average of H_{MF} is thus

$$\langle H_{MF} \rangle = -\text{Re} E_J \sum_{i,j=1}^N \eta_i^h \eta_j^{v*} \quad (6.2.7)$$

Since, as we have stated above, $\eta_i^h = \eta_j^v \equiv \eta$ in zero field, Eq. (6.2.7) becomes

$$\langle H_{MF} \rangle = -E_J \sum_{i,j=1}^N |\eta|^2 = -N^2 |\eta|^2 E_J \quad (6.2.8)$$

For $2N$ wires, this means that the energy per wire is $-N\eta^2 E_J/2$. Taking the derivative of Eq. (6.2.8) with respect to temperature, we can obtain the heat capacity, C_V , of the system. Fig. 6.3 shows the plot of heat capacity per wire (in units of k_B), $C_V/2Nk_B$, vs. temperature. The data show typical mean field behavior, as well as the classical equipartition value of $(1/2)k_B$ per degree of freedom (wire) at low temperature.

We draw attention to the important fact that the derived thermodynamic properties of our arrays are all directly *dependent* on N , the array size. As N grows, so does the number of nearest-neighbors in the array, and consequently, the system becomes more mean field-like. This behavior is quite unlike that of conventional Josephson-junction arrays in which the number of nearest-neighbors remains constant despite the overall array size. The properties of conventional arrays are *size independent*.

In the presence of a magnetic field, corresponding to a commensurate number of flux quanta per unit cell, $f=p/q$ (where p and q are small integers), we expect the ground state phase and corresponding current configuration to be spatially periodic. Fig. 6.4 shows ground state configurations for $f=1/2$ and $f=1/3$. Values at the intersection of wires in this figure indicate the gauge-invariant phase difference $(\varphi_i^h - \varphi_j^v - \frac{2\pi}{\Phi_0} \int_i^j \vec{A} \cdot d\vec{l})$ across the junction at that position. The sum of the gauge-invariant phase differences (keeping track of the appropriate minus signs) around any closed loop is constrained by

$$\sum \gamma = 2\pi(n - f) \quad n = \dots -2, -1, 0, 1, 2, \dots$$

where n in the ground state is typically either zero or one. We employ bold plus signs in Fig. 6.4 to denote the centers of the smallest positive circulating current loops. If we view the ground states in terms of these positive circulating currents, we find that the states appear very similar to the ground states of conventional four-nearest-neighbor arrays, *despite* the fact that their properties are very different.

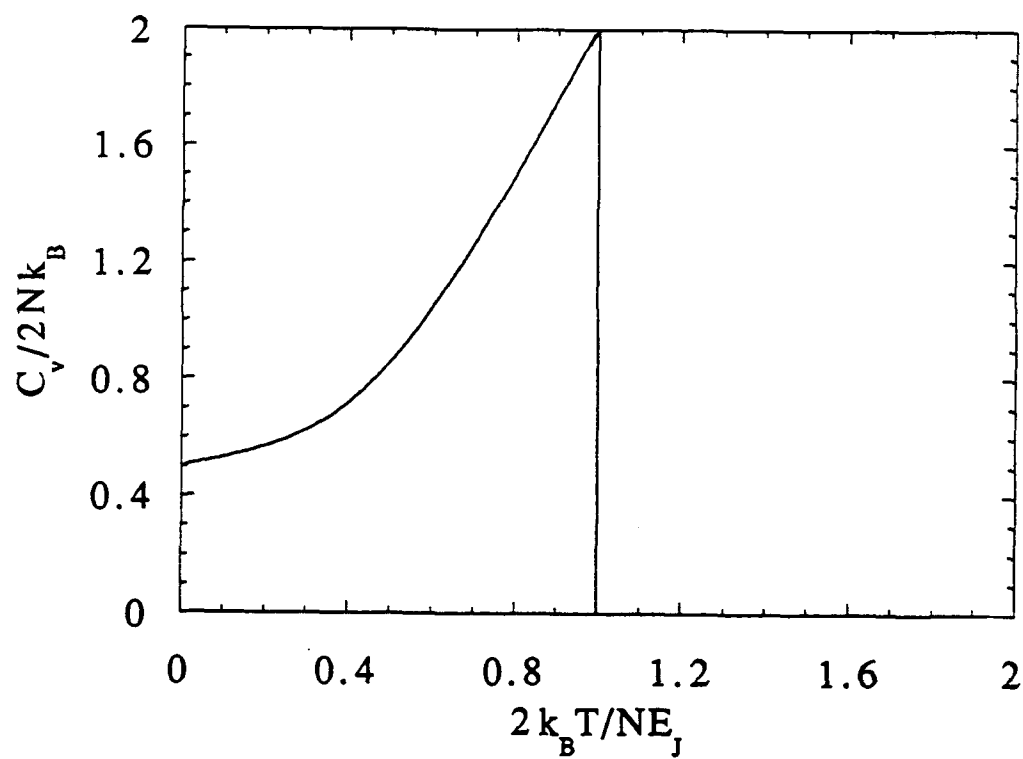


Fig. 6.3. Heat capacity per wire, $C_v/2Nk_B$, vs. normalized temperature, $2k_B T/NE_J$, as calculated by our mean field approximation.

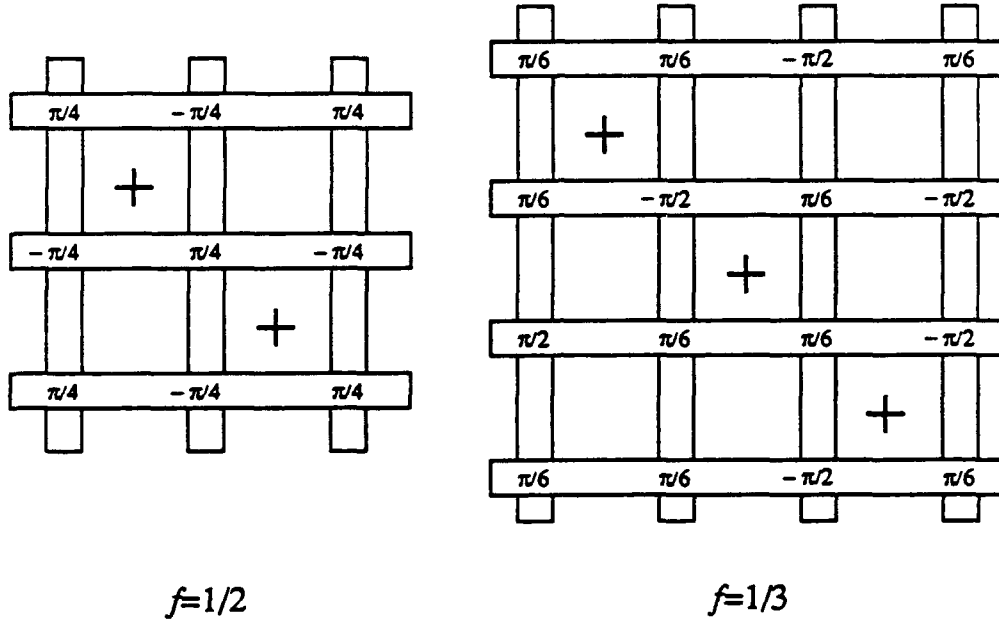


Fig. 6.4. Ground state configurations for $f=1/2$ and $1/3$. The values at the intersection of the wires are the gauge-invariant phase difference,

$\varphi_i^h - \varphi_j^v - \frac{2\pi}{\Phi_0} \int_i^j \vec{A} \cdot d\vec{l}$, across the junction at that position. The bold-face plus signs denote the centers of the smallest positive circulating current loops.

To calculate the array's transition temperature in the presence of a magnetic field, we again assume the order parameter, η , is small. Using the method of Shih and Stroud (1987), the self-consistency equation [Eq. (6.2.1)] can be expanded to read

$$\eta_j^h = \frac{1}{2}\beta E_J \sum_{k=0}^{N-1} \eta_k^v e^{i(2\pi fjk)} \quad (6.2.9)$$

Equivalently, we can write

$$\eta_k^v = \frac{1}{2}\beta E_J \sum_{j=0}^{N-1} \eta_j^h e^{-i(2\pi fjk)} \quad (6.2.10)$$

Substituting Eq. (6.2.10) into Eq. (6.2.9), we find that

$$\eta_j^h = \frac{1}{4}(\beta E_J)^2 \sum_{j'=0}^{N-1} \eta_{j'}^h \sum_{k=0}^{N-1} e^{i(j-j')(2\pi fk)} \quad (6.2.11)$$

If $f = p/q$, where p and q have no common factors and $q < N$, we can sum over k in Eq. (6.2.11) to obtain

$$\eta_j^h = \frac{1}{4}(\beta E_J)^2 \sum_{j'=0}^{N-1} \eta_{j'}^h N \delta_{j-j', qm} \quad m = 0, 1, 2, \dots \quad (6.2.12)$$

Since the delta-function is satisfied N/q times in a field of p/q , and $\eta_n = \eta_{n+q}$, we have

$$\eta_j^h = \left(\frac{N\beta E_J}{2} \right)^2 \frac{1}{q} \eta_j^h \quad (6.2.13)$$

which directly results in a mean-field transition temperature

$$T_c = \frac{NE_J}{2k_B\sqrt{q}} \quad (6.2.14)$$

in a field of $f = p/q$.

Summarizing, we have found the mean-field temperature for a transition to the ordered ground states described above in a field of $f=p/q$ to be $T_c(q) = \frac{NE_J}{2k_B\sqrt{q}}$ for an $N \times N$ array with $q < N$. Since two numerically close values of f can have very different values for their denominator q , $T_c(q)$ is a very discontinuous function in the case of an infinite array (see Fig. 6.5). These discontinuities are of course not present in the case of a *finite* array. By employing a finite-size analysis, we can understand the process by which the discontinuities are smoothed. Combining our previous expressions Eq. (6.2.9) and Eq. (6.2.10) for the linearized self-consistency equations near T_c , we can write

$$\sum_{j'=0}^{N-1} \sum_{k=0}^{N-1} \left(\alpha_{jk} \alpha_{j'k}^* \eta_{j'}^h - \frac{4}{(\beta E_J)^2} \eta_j^h \right) = 0 \quad (6.2.15)$$

where $\alpha_{jk} = \exp(i2\pi fjk)$. This expression is equivalent to the eigenvalue problem derived by Vinokur et al. (1987) in the disordered case. We have explicitly diagonalized the above matrix equation for a finite 10×10 array, calculating the mean-field transition temperature from the largest eigenvalue. We find that the mean-field transition in this finite array is a continuous function of f (see Fig. 6.6), as it must be physically, and equal to the infinite-array mean-field value for commensurate applied fields. We suggest that this continuous change of T_c with applied field is associated with a corresponding continuous change in the ground state configuration of the finite array. In contrast, the ground states in the infinite

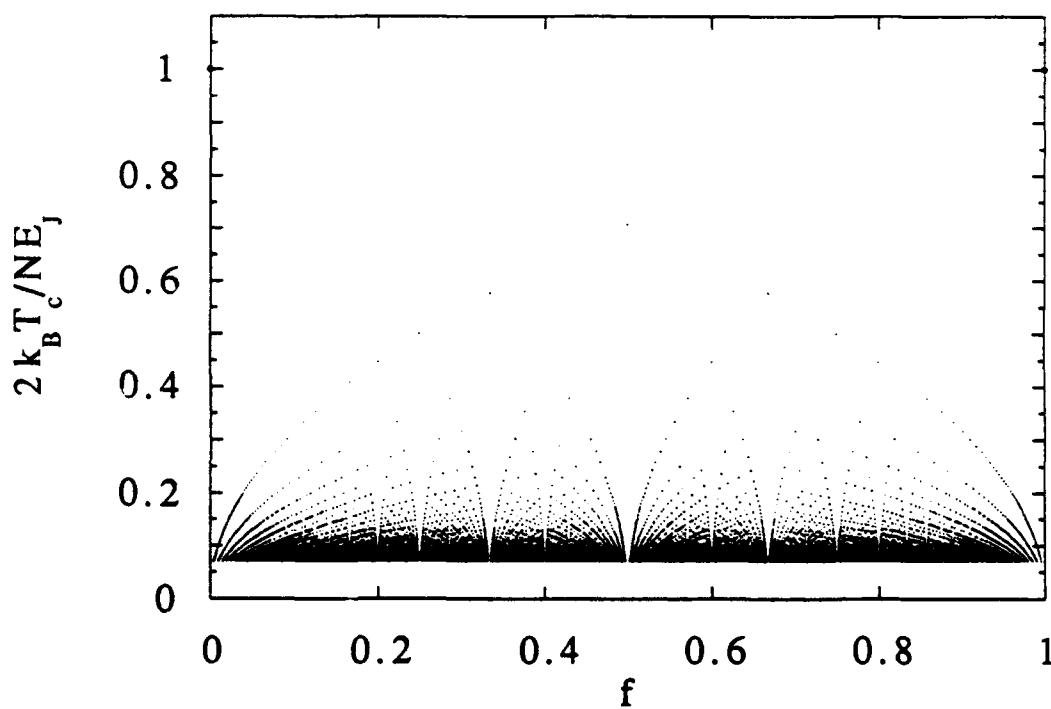


Fig. 6.5. Normalized transition temperature, $2k_B T_c / NE_J$, vs. number of flux quanta, f , per unit cell in an infinite-sized ordered array. The discontinuities found in this plot are not found in finite-sized ordered arrays (see Fig. 6.6).

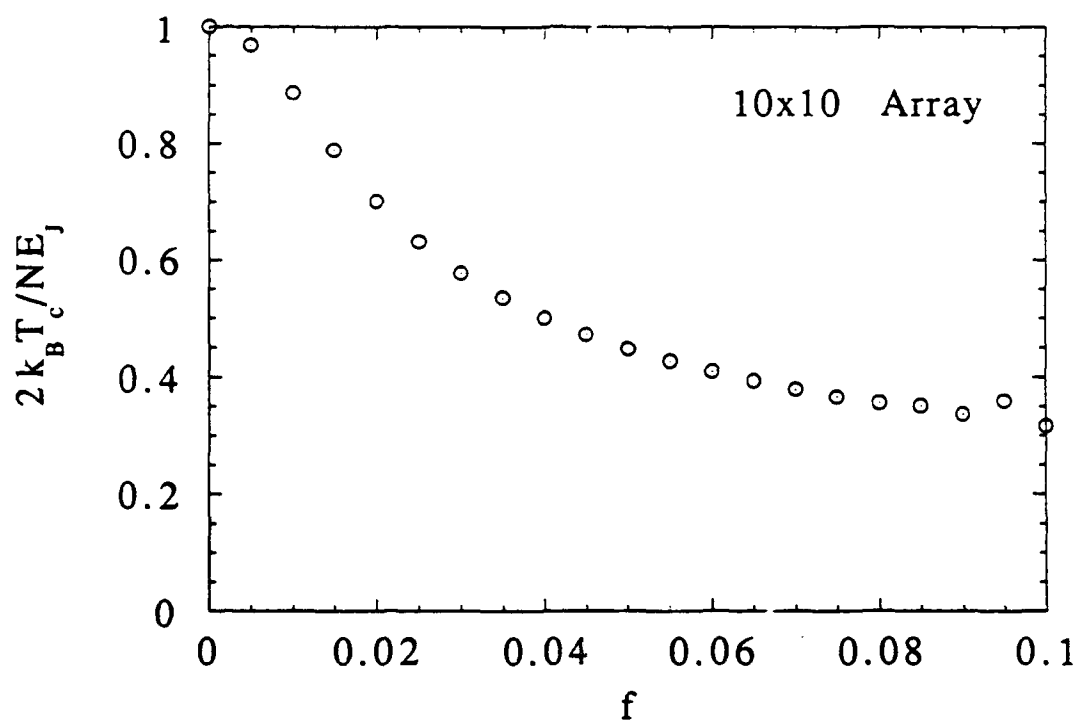


Fig. 6.6. Normalized transition temperature, $2k_B T_c / NE_J$, vs. number of flux quanta, f , per unit cell in a 10×10 array. Here, $f < 1/N$. Unlike in an infinite array, T_c is a smooth continuous function of f in a finite-sized array.

array have a $q \times q$ periodicity in a field of $f=p/q$, and hence the current distribution changes discontinuously with f .

Using current conservation in each wire as the equilibrium condition, we have calculated, to first order, states corresponding to f near a commensurate value in the finite array. We find these states to be made up of the commensurate ground states plus additional, small circulating currents analogous to a Meissner shielding state (except that these currents do not significantly shield the applied magnetic field because of the small i_c we have assumed). Near zero field, for example, we expect the ground state to be of this "Meissner" form until $f=1/N$ in an $N \times N$ array. In this regime, T_c drops smoothly from $NE_J/2k_B$ for $f=0$ to its low value of $T_c(f=0)/\sqrt{N}$ for $f=1/N$, the smallest commensurate field.

If one assumes the form $\eta_j = |\eta| e^{i\varphi_j}$ for the order parameter of the j^{th} wire, (where φ_j is the ground state phase of that wire), one can show that after substituting $T/T_c(q)$ for $NE_J\beta/2$ in Eq. (6.2.4), the mean-field thermodynamic properties derived in the zero field case and shown in Figs. 6.2 and 6.3 are in fact universal for all fields commensurate with the array.

6.2.2 Disordered arrays

We can also use matrix Eq. (6.2.15) to analyze the disordered mean-field T_c , as done by Vinokur et al. (1987), by replacing our previous expression for α_{jk} with $\exp[i2\pi f(j+\delta_j)(k+\delta_k)]$. Here δ_j and δ_k represent the deviations of the j^{th} and k^{th} wires from their ordered positions in units of the lattice constant. Fig. 6.7 shows the T_c (identified with the largest eigenvalue) of a 10×10 array averaged over an ensemble of ten systems. Each of these systems has spacings between the parallel wires which are uniformly distributed by up to $\pm 0.1\Delta x$, where Δx is the mean spacing.

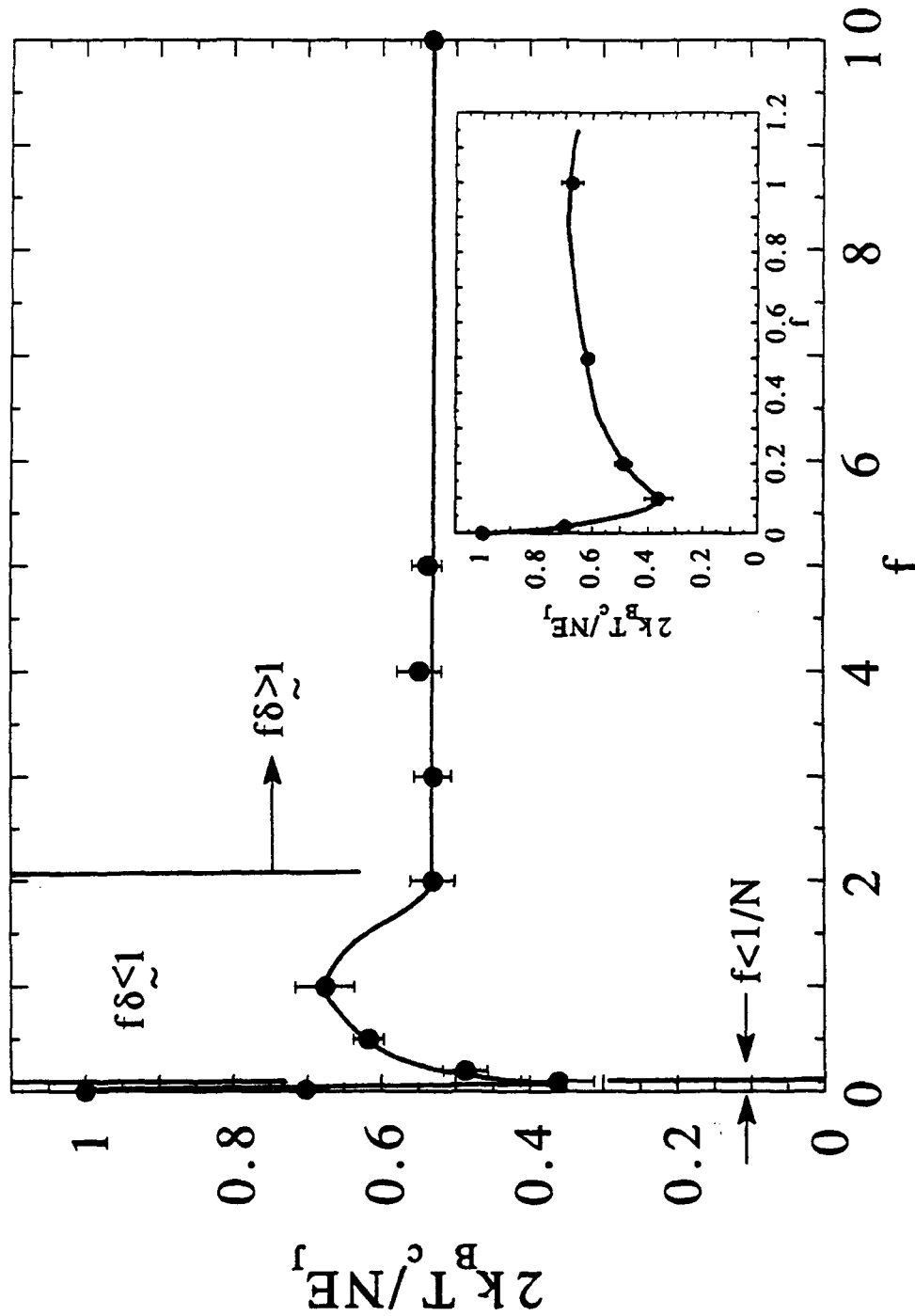


Fig. 6.7. Normalized mean-field transition temperature, $2k_B T_c / NE_J$, vs. number of flux quanta, f , per average unit cell in an ensemble-averaged 10×10 disordered array. The solid black line through the data is a guide to the eye. δ refers to the maximum fractional displacement of a wire from its ordered position, i.e. the maximum displacement is $\delta \approx \Delta x$, and is equal to 0.1 here.

As shown in the figure, the behavior as a function of field can be divided into four general regions. For extremely small fields, $f < \frac{1}{N^2}$, T_C approaches the zero field limit, $T_C = NE_J/2k_B$, since the amount of flux entering the entire array is much smaller than one flux quantum. For small applied field, $\frac{1}{N^2} < f < \frac{1}{N}$, T_C decreases as f increases. We note that this region directly corresponds to the one where $H < H_0$ (where, again, H_0 is the field required to generate a flux quantum through the average-sized strip between two adjacent wires) in Vinokur et al.'s analysis (1987). In the intermediate region, $\frac{1}{N} \leq f < 1$, we observe complicated behavior which we ascribe to the similarity between the disordered and ordered arrays when f is small. When $f\delta j < 1$, we expect (from our disordered expression for α_{jk}) that the effect of the disorder will be small, and thus, the dependence of T_C on f should resemble that of the ordered case. This is seen in Fig. 6.7 for $\frac{1}{N} \leq f < 1$, where the T_C , like that in the ordered array, rises (although the exact form is unknown at this time). As f increases to values greater than 1, the effects of disorder become more apparent, and the behavior moves toward the field-independent behavior described by Vinokur et al. (1987) in Eq. (6.1.3). We note, however, that the high field asymptote of T_C ($\sim 0.85E_J\sqrt{N}/k_B$) predicted by our mean field analysis is significantly larger than that predicted by Vinokur et al. (1987) ($E_J\sqrt{N}/2k_B$) for the same sized array. We will comment on this discrepancy in the next chapter.

6.3 Discussion

The size effects we have discussed in arrays with long-range interaction are unlike those found in conventional Josephson-junction arrays. Conventional arrays undergo a Kosterlitz-Thouless (K - T) phase transition in which thermally activated vortex-antivortex pairs become bound below a certain temperature, T_{KT} , which is *independent* of the actual

size of the array. T_{KT} is determined by the vortex core energy which does not change with array size for $N \rightarrow \infty$, and hence neither does T_{KT} .

Finite-array size, however, does affect the *nature* of the K - T transition in conventional arrays. The resistive behavior of these arrays can be described by the relationship, $V \propto I^a(T)$. In the ideal case, i.e. an infinite array, the exponent, $a(T)$, is predicted to jump from 3 just below T_{KT} to 1 just above [Nelson and Kosterlitz, 1977]. This sharp jump, known as the universal jump in the superfluid density, indicates the unbinding/binding of the vortex-antivortex pairs at T_{KT} . Finite-array size leads to deviations from this theoretical prediction. In particular, it causes a smearing of the jump in $a(T)$, in part due to nucleation of free vortices at all temperatures, $T > 0$ [Kadin et al., 1983], and to the logarithmic spatial interaction of vortices [Abraham, 1983]. The overall effect is a less pronounced KT transition in a finite array.

In the case of arrays with long-range interaction, we find that the transition to the macroscopically phase-coherent state occurs at a temperature, T_C , which is very much *dependent* on the actual size of the array. This dependence on size occurs because the number of nearest-neighbors in the array continually grows with increasing array size. Indeed, even in the limit of $N \rightarrow \infty$, these novel arrays cannot be considered as models of 2-dimensional systems [Nelson, 1991]. Because T_C is size dependent and does not depend on any type of vortex-antivortex interaction, we describe arrays with long-range interaction as truly mean-field like.

CHAPTER VII

MONTE CARLO SIMULATIONS

7.1 Introduction

We have performed Monte Carlo (MC) simulations of both *ordered* and *disordered* Josephson junction arrays with long-range interaction.¹ Implementing the well known Metropolis algorithm [Metropolis et al., 1953], we simulated free-boundary arrays of size $N \times N$, where $N=8, 20, 30$, and 50 . Using our MC simulations, we calculated various thermodynamic quantities such as the heat capacity, C_V , and phase-coherence modulus, M . M is a measure of long-range coherence of the phases, ϕ_j , of the individual wires.

This chapter is organized as follows. In Sec. 7.2, we motivate the reasons for implementing the Metropolis algorithm in our MC simulations, and in Sec. 7.3, we outline the actual algorithm we used. We then present our results in Sec. 7.4 and compare them with those derived from Vinokur et al.'s analysis (1987) and from our mean field theory [Sohn et al., 1992b].

7.2 Metropolis Algorithm²

If we have a system of N particles, each having a single degree of freedom, that can be described by the Hamiltonian, H_N , we can calculate the thermodynamic average of an observable, A , with the following

¹ The results presented in this chapter have been submitted for publication [Sohn et al., 1992b].

² Much of what is written in this section can be found in Forrester, thesis (1988). For a more thorough review of MC methods, see Binder (1986).

$$\langle A \rangle = \frac{\int_{\Omega} dx A(\mathbf{x}) \exp(-H_N(\mathbf{x})/k_B T)}{\int_{\Omega} dx \exp(-H_N(\mathbf{x})/k_B T)} \quad (7.2.1)$$

where $dx = dx_1 dx_2 \dots dx_i$ (with x_i describing the state of the i^{th} particle) and the integration is over the entire phase-space volume, Ω . In order to calculate Eq. (7.2.1), we can approximate the integrals as discrete sums,

$$\int f(x) dx \rightarrow \sum_v f(x_v) \Delta x_v$$

where x_v is a point on a regular grid. Because the system's phase space has a dimension of N , where $N \sim 10 \cdot 10^{23}$, the above approach is completely impractical. A better approach in solving Eq. (7.2.1) would be to choose M phase-space points at *random* rather than from a regular grid [Forrester, 1988]. Here, M would be some manageable number. Unfortunately, this process is highly inefficient since many of the M sampled points might be "unimportant" (in the sense that the Boltzmann factor, $\exp(-H_N/k_B T)$, would be much less than one).

To solve our problem, we employ the Metropolis method [Metropolis et al., 1953]. The Metropolis method is based on the idea of "importance sampling" where we choose phase-space points according to some probability $P(\mathbf{x})$ rather than choosing them at random [Forrester, 1988]. As a result, Eq. (7.2.1) now becomes,

$$\langle A \rangle = \bar{A} = \frac{\sum_{v=1}^M A(\mathbf{x}_v) P^{-1}(\mathbf{x}_v) \exp(-H_N(\mathbf{x}_v)/k_B T)}{\sum_{v=1}^M P^{-1}(\mathbf{x}_v) \exp(-H_N(\mathbf{x}_v)/k_B T)} \quad (7.2.2)$$

If we choose the probability function $P(\mathbf{x}_v)$ to be equal to the thermal distribution, $P_{eq}(\mathbf{x}_v) \propto \exp(-H_N(\mathbf{x}_v)/k_B T)$, Eq. (7.2.2) then becomes

$$\bar{A} = \frac{1}{M} \sum_{v=1}^M A(\mathbf{x}_v) \quad (7.2.3)$$

The above is no more than a computation of arithmetic averages, but at a set of phase-space points consistent with the “biasing” distribution.

We choose the phase-space points consistent with $P_{eq}(\mathbf{x}_v)$ in the limit of $M \rightarrow \infty$ by executing a random walk in phase-space, with the transition probability, $W(\mathbf{x}_v \rightarrow \mathbf{x}_{v'})$ (per unit time) for a step from \mathbf{x}_v to $\mathbf{x}_{v'}$ [Forrester, 1988]. We obey the detailed balance condition

$$P_{eq}(\mathbf{x}_v)W(\mathbf{x}_v \rightarrow \mathbf{x}_{v'}) = P_{eq}(\mathbf{x}_{v'})W(\mathbf{x}_{v'} \rightarrow \mathbf{x}_v)$$

so that the ratio of transition probabilities for $\mathbf{x}_v \rightarrow \mathbf{x}_{v'}$ and $\mathbf{x}_{v'} \rightarrow \mathbf{x}_v$ depends only on the energy change, $\delta H = H(\mathbf{x}_{v'}) - H(\mathbf{x}_v)$

$$\frac{W(\mathbf{x}_v \rightarrow \mathbf{x}_{v'})}{W(\mathbf{x}_{v'} \rightarrow \mathbf{x}_v)} = \exp(-\delta H/k_B T) \quad (7.2.4)$$

A choice of W consistent with Eq. (7.2.4) is

$$W(\mathbf{x}_v \rightarrow \mathbf{x}_{v'}) = \begin{cases} \exp(-\delta H/k_B T) & \delta H > 0 \\ 1 & \text{otherwise} \end{cases} \quad (7.2.5)$$

If $\delta H \leq 0$ for a given step, the step to x_V' is made, and a term $A(x_V')$ is added to the sum in Eq. (7.2.3). If, however, $\delta H \geq 0$, we first compare W to z —a random variable uniformly distributed on the interval $[0,1]$. If $W > z$, the move to x_V' is made and $A(x_V')$ is added to the sum in Eq. (7.2.3). If $W < z$, the move is not made and $A(x_V)$ is once again added to Eq. (7.2.3).

The values of the observable A are not computed after every step; rather they are computed after a set number of steps. This is done in order to avoid subsequent terms in the sum of Eq. (7.2.3) from being highly correlated. In addition, the values computed during some initial interval—the time during which the system thermally equilibrates and the biasing function $P(x)$ approaches $P_{eq}(x)$ —are discarded.

7.3 Implementation of Metropolis Algorithm

As stated in the previous chapter, the Hamiltonian of our system is

$$H = -\text{Re } E_J \sum_{i=1}^N \sum_{j=1}^N e^{i(\phi_i^h - \phi_j^v - A_{ij})} \quad (7.3.1)$$

Using Eq. (7.3.1), we proceed on a random walk through the phase-space of our system. This consists of making “passes” through the lattice of wires, i.e. going one-by-one over all wires in the array, and adjusting the phase of each wire once every pass according to the Metropolis algorithm. A “Monte Carlo step” is the adjustment of the phase of a single wire in the lattice. Because we want to reduce the correlations in the state of the system from one step to the next [Binder, 1986], we use a random number generator for every pass to generate a random order of stepping through the lattice.

As summarized by Forrester (1988), the Metropolis algorithm executed for each pass on every phase is the following

1. Select a phase, n , and change its phase by a random amount $\delta\theta_n$, from θ_n to $\theta_n + \delta\theta_n$. The choice of $\delta\theta_n$ will be discussed below.
2. Compute δH using Eq. (7.3.1), and $W = \exp(-\delta H/k_B T)$.
3. (a) If $\delta H < 0$, accept the move. If desired, compute the new value of each observable and add to corresponding sums in Eq. (7.2.3).
 (b) If $\delta H > 0$, generate a random number, z , where $0 < z < 1$.
 If $W > z$ accept move. Again, if desired, compute the new value of each observable and add to the corresponding sums, Eq. (7.2.3).
4. Go to Step 1.

During each pass, we select a phase and change its angle θ_n by some $\delta\theta_n$ as described in Step 1. We choose $\delta\theta_n$ by the following. Before we begin any part of the simulation, we choose a maximum phase change, $\delta\theta_{max}$. We then choose $\delta\theta_n$ randomly from the interval $[-\delta\theta_{max}, \delta\theta_{max}]$ by computing a random number γ , from a random variable distributed uniformly on $[-1, 1]$, and setting $\delta\theta_n = \gamma\delta\theta_{max}$. The value of $\delta\theta_{max}$ is adjusted throughout the early stages of the random walk (usually the first 30-40 passes) so that the acceptance rate for "uphill" moves (moves with $\delta H > 0$) is approximately one half, i.e.

$$\text{Acceptance rate} = \frac{\text{Number of uphill successes}}{\text{Number of uphill attempts}} = \frac{1}{2} \quad (7.3.2)$$

The above is necessary in order to discourage the consideration of "unlikely" moves and, therefore, promote efficiency [Binder, 1986].³

³In other words, we discourage our system from settling into a local minimum by accepting, half of the time, high energy moves which would "knock" the system out of a local minimum and perhaps toward a global minimum.

Initially, we discard the first 10,000-20,000 passes (stepping through the MC steps without calculating the thermodynamic observables). This is done in order to allow the system to equilibrate and to avoid correlations with the initial state of the system from occurring.⁴ After the equilibration period, we execute 20,000-30,000 averaging passes. We calculate the thermodynamic variables after each *pass* rather than after each MC step in order to reduce correlations between subsequent values of $A(x_V)$.

The calculation of the variables in which we are interested is fairly straightforward. We calculate all quantities as a function of temperature, in which we start at a high temperature and then anneal the system, i.e. we gradually cool the system.⁵ For the highest temperature, we choose a random phase configuration as the initial condition, while for each successive lower temperature, we use the final configuration from the previous temperature as the input. For each temperature, we use the $\delta\theta_{max}$ from the previous temperature as an initial guess for the maximum phase change. Thus, at each temperature, we execute 10,000-20,000 equilibration passes and 20,000-30,000 averaging passes. All MC simulations were performed on a Convex machine.⁶

7.4 Monte Carlo Results

7.4.1 Heat capacity, C_V

To calculate the heat capacity per wire, we used the well-known relation [Reif, 1965, p. 242],

⁴Forrester chose to execute 5,000-10,000 equilibration passes. These numbers are based on work by Tobochnik and Chester (1979), Teitel and Jayaprakash (1983a), and Fernandez et al. (1986).

⁵At temperatures well above the transition temperature, T_c , we cooled the system with temperature steps, $\delta T = 5E_J/k_B$. Just above the T_c , we chose $\delta T = E_J/k_B$. For $T \leq T_c$, we chose $\delta T = 0.1E_J/k_B$.

⁶The use of a Convex machine was provided by the Laboratory for Computational Physics at the Naval Research Laboratory, Washington, D.C.

$$C_V = \frac{\langle E^2 \rangle - \langle E \rangle^2}{2Nk_B T^2} \quad (7.4.1)$$

where E is the calculated energy of the system.⁷ Our calculations for both the ordered and disordered arrays, which will be presented in Secs. A and B, respectively, show that T_C is very much dependent on the size of the array and the strength of the applied magnetic field.

A. Ordered arrays

Fig. 7.1 shows the heat capacity per wire (again, in units of k_B), $C_V/2Nk_B$, of the different-sized arrays we simulated in zero field. As can be seen in the figure, $C_V/2Nk_B$ has a pronounced peak, indicating a phase transition, at a temperature, T_C . This peak sharpens and increases in height as we increase the size of the simulated array—a clear indication that the system is mean-field-like as opposed to Kosterlitz-Thouless-like.⁸ Comparing the simulated heat capacity curves with those derived from mean field theory, we find that the simulated curves approach the mean-field form as N is increased (see Fig. 7.1). Since the part of the heat capacity curve which has the steepest slope (usually where C_V is approximately half-maximum) corresponds to the discontinuous jump at T_C on the mean-field theory curve, we take the temperature at which this occurs to be T_C . From our MC simulations, we were able to confirm that T_C does indeed scale with N , as was

⁷This particular method of calculating C_V is strongly dependent on how many passes are included in the computation. The reason for this is that the method relies on subtracting two large fluctuating quantities and thus, the resulting C_V depends strongly on what fluctuations are included. These fluctuations are strongest near T_C , thus making computation difficult near this temperature. One way of avoiding this problem is to calculate C_V by differentiating the energy with respect to temperature, i.e. $C_V = dE/dT$ [Tobochnik and Chester, 1979].

⁸The behavior of C_V shows only a broad, size-independent peak in Kosterlitz-Thouless systems. See Shih and Stroud (1984); Tobochnik and Chester (1979); and Forrester (1988).

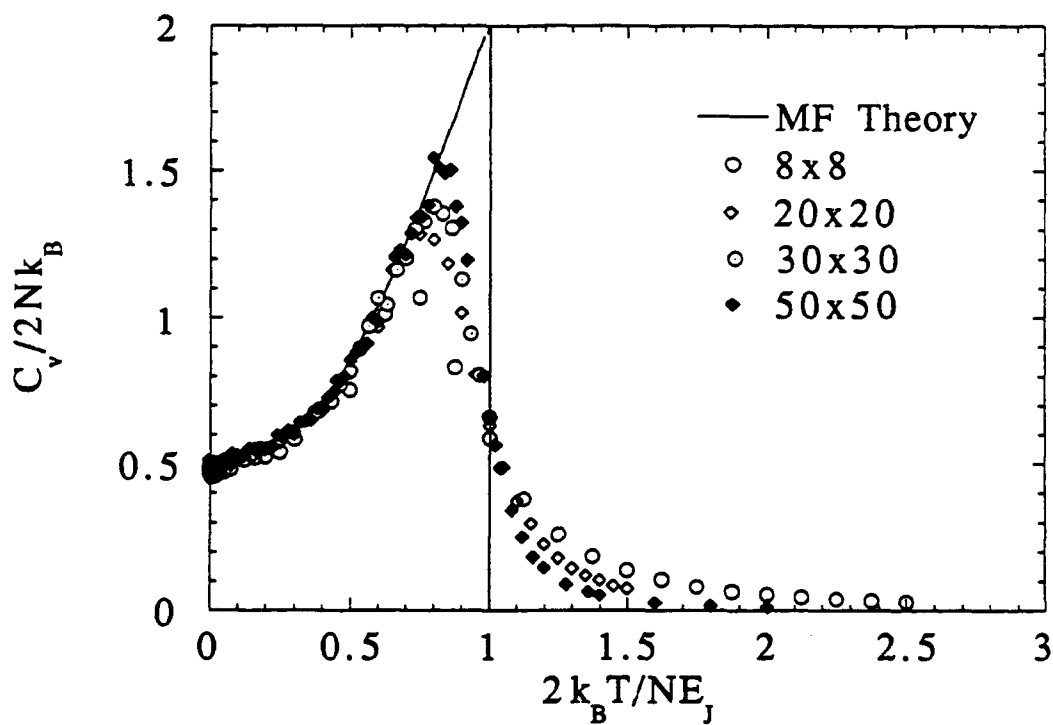


Fig. 7.1. Heat Capacity per wire, $C_v/2Nk_B$, vs. normalized temperature, $2k_B T/NE_J$, for the ordered array with long-range interaction in zero field as calculated by Monte Carlo simulations and mean field theory. The size of the simulated array is $N \times N$, where $N=8, 20, 30$, and 50 . The transition temperature in the simulations is taken to be the temperature at which the heat capacity curve has the steepest slope—usually where $C_v/2Nk_B$ is half-maximum.

predicted by our MF calculations.⁹ When a field, $f=p/q$, is present in the ordered array system, we found that $T_C = NE_J/2k_B \sqrt{q}$ (see Figs. 7.2a and b), again agreeing with our MF calculations.

B. Disordered arrays

To simulate *disordered* arrays, we have introduced disorder into our system by randomly varying the distance, Δx , between the parallel wires of each orthogonal set. Specifically, we have uniformly distributed the spacings by up to $\pm 0.1\Delta x$ in the arrays we refer to as having 10% disorder, and by up to $\pm 0.5\Delta x$ in arrays we refer to as having 50% disorder. Because the disorder introduced into the system is purely geometric¹⁰ and therefore only affects the A_{ij} term in the Hamiltonian [Eq. (7.3.1)], disordered and ordered arrays show *identical* behavior in zero field.

Figs. 7.3 and 7.4 show T_C vs. f for the 10% and 50% disordered arrays, respectively.¹¹ As a basis for comparison, T_C vs. f , as derived from Vinokur et al.'s analysis [Eq. (6.1.2)], is also shown on the same plots. As before, we can define T_C for

four different regions. For $f < \frac{1}{N^2}$, $T_C = NE_J/2k_B$. For $\frac{1}{N^2} \leq f < \frac{1}{N}$, $T_C = \frac{E_J}{2k_B \sqrt{f}}$.

This relationship is in agreement with our mean field theory analysis and with Vinokur et al.'s first order approximation of T_C for extremely small fields, Eq. (6.1.4), using the relationship $H/H_0 = fN$. We note, however, that, as shown in Figs. 7.3 and 7.4,

⁹In a real physical system, an upper bound of T_C does exist, i.e. $T_C < T_{C0}$, the superconducting transition temperature of the individual wires, above which $E_J = 0$.

¹⁰Another way of introducing disorder would be to vary the Josephson coupling strength, E_J , of each junction in the array. We instead choose to vary the distance between the wires and keep E_J constant, as this was originally proposed by Vinokur et al. (1987).

¹¹The results of the disordered arrays we present in this chapter are an average of 5 MC runs (each a different realization of a disordered array) since we found the results of the individual simulations to be very noisy.

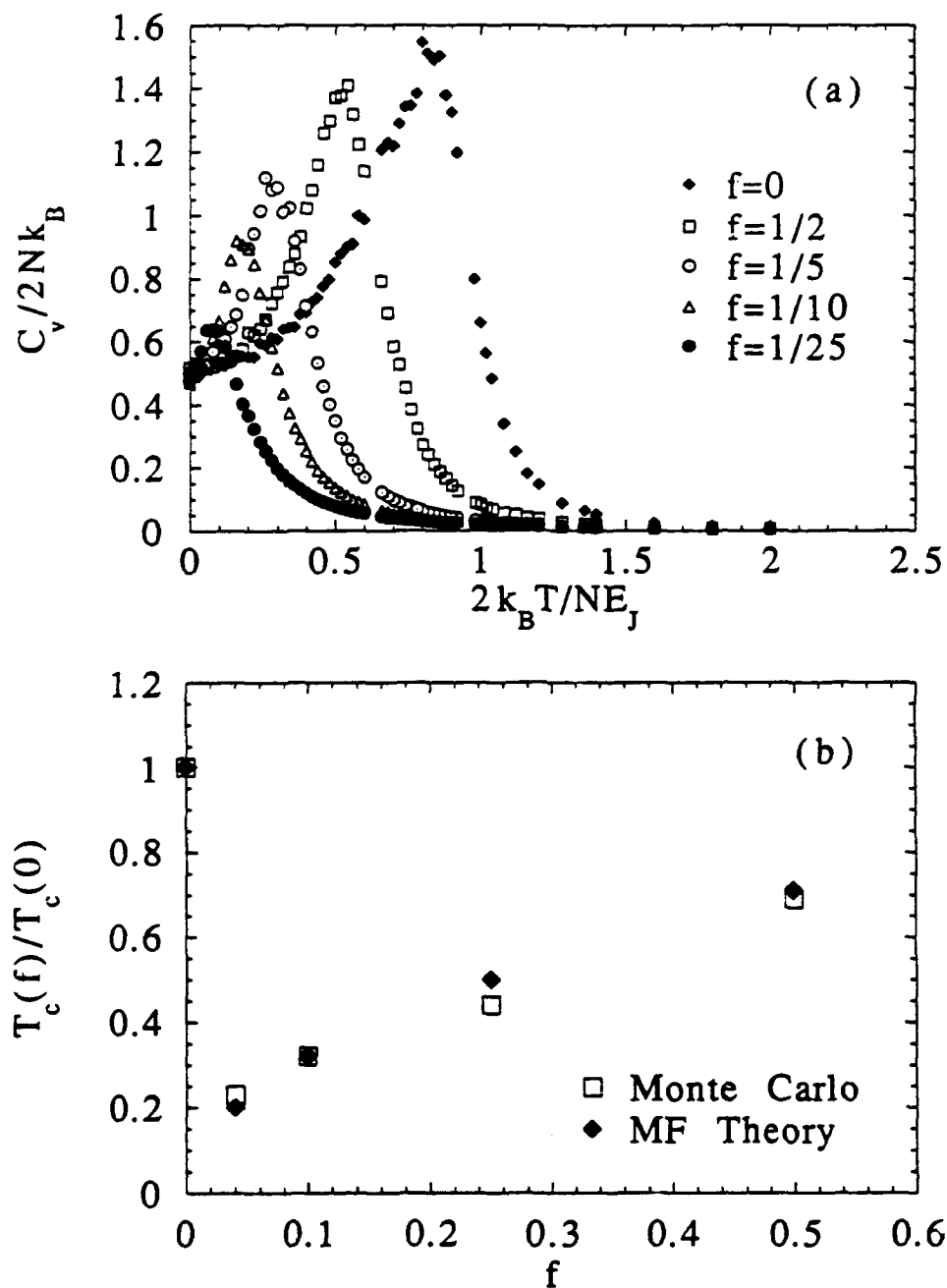


Fig. 7.2. (a) Heat Capacity per wire, $C_v/2Nk_B$, vs. normalized temperature, $2k_B T/NE_J$, for a simulated 50×50 ordered array in the presence of magnetic fields, $f=0, 1/2, 1/5, 1/10$, and $1/25$. (b) Comparison of $T_c(f)/T_c(0)$ vs. f between mean field theory and Monte Carlo simulations.

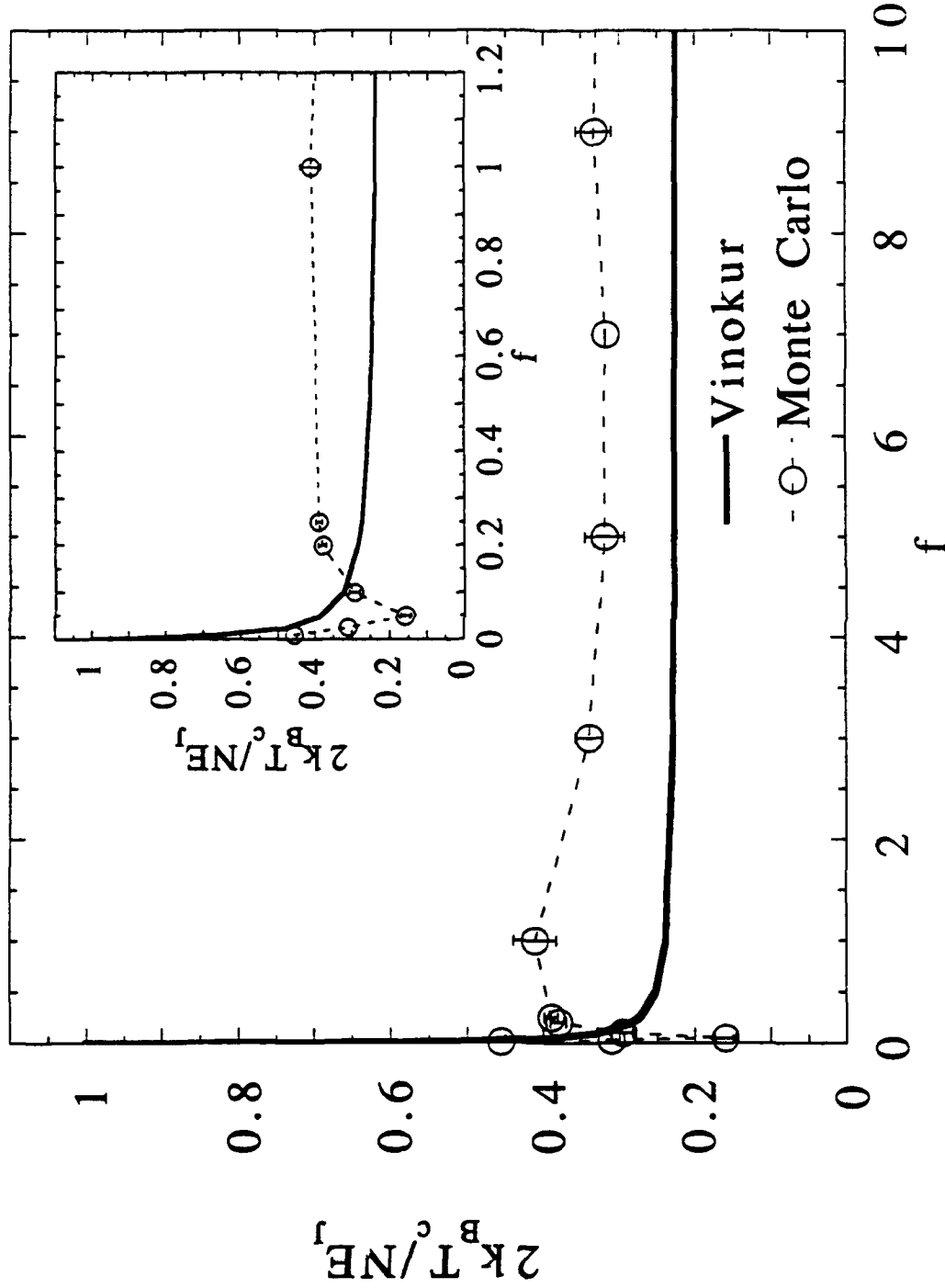


Fig. 7.3. Normalized transition temperature, $2k_B T_c / NE_J$, vs. field, f , for a simulated 10% disordered 20×20 array. All data shown are an average of 5 MC runs—all of different disordered arrays. For $f \gg 1$, T_c asymptotically approaches the value $\sim 0.75 E_J \sqrt{N} / k_B$. Inset: For $f < 1/N^2$, $T_c \sim NE_J / 2k_B$. For $1/N^2 < f < 1/N$, $T_c = E_J / 2k_B \sqrt{f}$; for $1/N \leq f < 1$, T_c rises with f , although the exact form is unknown. The peak at $f \sim 1$ can be attributed to the fact that the array is not fully disordered. For comparison, T_c derived from Vinokur et al.'s analysis [Eq. (6.1.2)] is also shown.

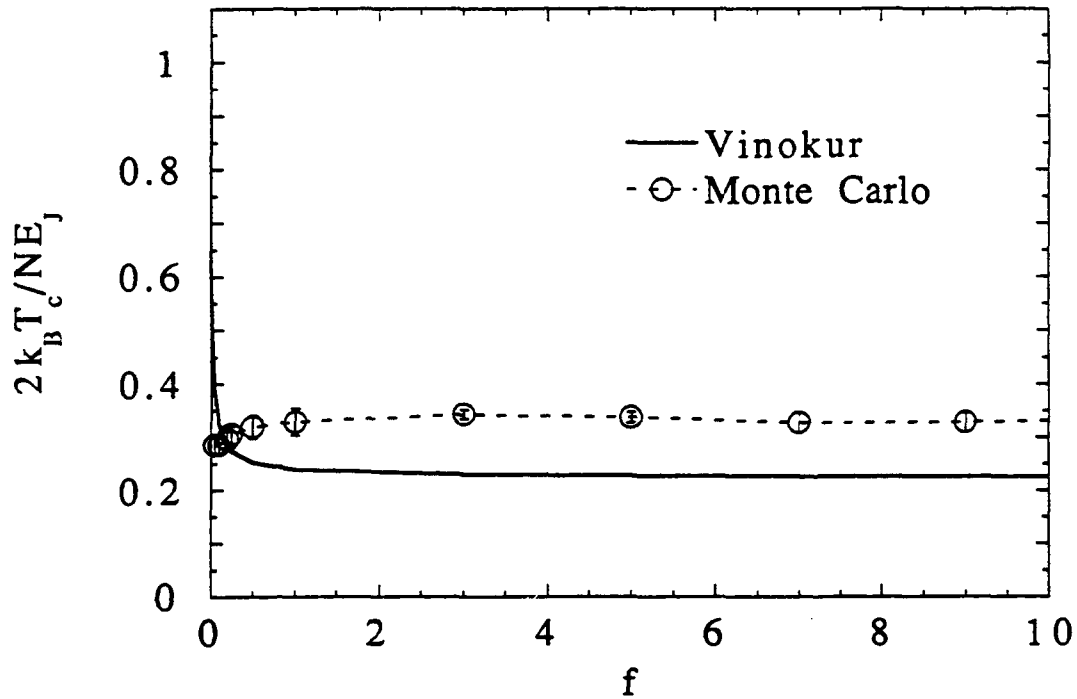


Fig. 7.4. Normalized transition temperature, $2k_B T_c / NE_J$, vs. field, f , for a simulated 50% disordered 20×20 array. All data shown are an average of 5 MC runs—all different disordered arrays. T_c scales with N and f in the same it does in the 10% disordered array. However, no peak in T_c at $f \sim 1$ occurs in the 50% disordered array. For comparison, T_c derived from Vinokur et al.'s analysis [Eq. (6.1.2)] is also shown.

it slightly differs from the exact form of T_C [Eq. (6.1.2)] predicted by Vinokur et al. (1987). For $\frac{1}{N} \leq f \leq 1$, we see that T_C rises with respect to f , very much as it does in ordered arrays for this region. This behavior was not predicted by Vinokur et al. (1987); the exact relationship between T_C and f in this regime is unknown at the present time.

The small peak in T_C at $f \sim 1$ is observable in only the 10%, and not the 50%, disordered array. We attribute this peak, which is also found in our mean field calculations with the same disorder (see Fig. 6.7), again to the fact that the array is not fully disordered. When $f \gg 1$, we find that T_C asymptotically approaches $\sim 0.75 E_J \sqrt{N}/k_B$, for both the 10% and 50% disordered arrays. Vinokur et al. (1987) predicted that T_C would asymptotically approach $(E_J \sqrt{N})/2k_B$. To see if the discrepancy between the two asymptotes was due to a size effect, we simulated 10% and 100% 50×50 disordered arrays to compare with the results on 20×20 arrays shown in Figs. 7.3 and 7.4. The asymptotic value of T_C of these arrays at high fields is still $\sim 0.75 E_J \sqrt{N}/k_B$, suggesting that size is not a crucial factor. The consistency of our results for 10% and 50% randomness suggests that the degree of randomness is not the source of the discrepancy. Thus, the discrepancy between the asymptote derived by our simulations and that by Vinokur et al. (1987) is presently of unknown origin.

7.4.2 Phase-coherence modulus, M

Using our MC simulations, we also calculated the phase-coherence modulus (known in other systems as the magnetization modulus [Shih and Stroud, 1983 and 1984; and Forrester, 1988]),

$$M = \left\langle \left| \sum_{j=1}^{2N} e^{i\varphi_j} \right| \right\rangle. \quad (7.4.2)$$

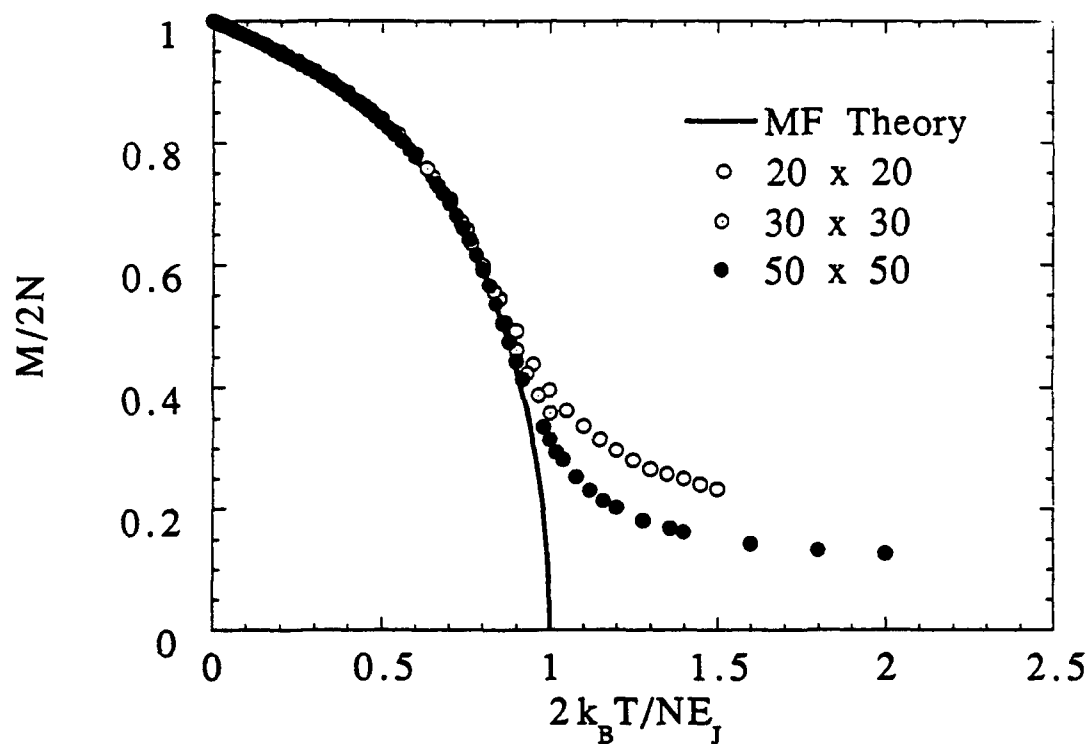


Fig. 7.5. Normalized phase-coherence modulus, $M/2N$, vs. normalized temperature, $2k_B T_c / NE_J$, for simulated arrays of size, 20×20 , 30×30 , and 50×50 , in zero field. For a comparison, the magnitude of η , originally shown in Fig. 6.1 and which is equivalent to the normalized phase-coherence modulus for an infinite array in zero field, is also plotted.

of our arrays. M is a measure of long-range coherence of the phases, ϕ_j , in the array. At temperatures well above T_c , $M=0$, indicating that the phases are completely random and not coherent at all. Closer to T_c , M begins to increase and continues to do so until $T=0$. At this temperature, $M=2N$ (in zero field), indicating that the phases have complete long-range coherence. Since it is not gauge-invariant, M is not a measurable quantity when a magnetic field is present in the system.

Fig. 7.5 shows the phase-coherence modulus, M , as a function of temperature for array sizes, $N = 20, 30$, and 50 . As can be seen in the figure, long-range phase coherence sets in gradually in these samples. This particular characteristic—the gradual onset of long-range phase coherence—is very similar to that of ordered conventional arrays [Forrester, 1988]. For $T > T_c$, M asymptotically approaches zero as shown in the figure. This approach to zero is slower for smaller arrays than for large ones. In the limit of $N \rightarrow \infty$, M would equal zero for $T \geq T_c$, as in the mean field plot, shown for comparison.

7.5. Summary

Through our Monte Carlo simulations, we have confirmed our mean field analysis which was presented in Chapter VI. We have shown that the transition temperature of arrays with long-range interaction is $T_c = NE_J/2k_B$ in zero field. Once a commensurate field, $f=p/q$, is present, $T_c = NE_J/2k_B \sqrt{q}$ in ordered arrays. In disordered arrays, T_c is defined for four different regions. For $f < \frac{1}{N^2}$, $T_c = NE_J/2k_B$, while for $\frac{1}{N^2} \leq f < \frac{1}{N}$, $T_c = \frac{E_J}{2k_B \sqrt{f}}$. For $\frac{1}{N} \leq f \leq 1$, T_c rises with f , although the exact form is presently unknown. Finally, for $f \gg 1$, T_c asymptotically approaches $\sim 0.75 E_J \sqrt{N}/k_B$.

CHAPTER VIII

EXPERIMENTAL DETAILS AND RESULTS

OF

ARRAYS WITH LONG-RANGE INTERACTION

8.1 Introduction

In this chapter, we present the first *experimental* investigation of arrays with long-range interaction.¹ Our arrays consist of Nb superconducting wires separated by an aluminum-oxide (Al_2O_3) barrier; the wires, therefore, are coupled to each other via tunnel junctions. We have performed both dc transport and ac susceptibility measurements on these arrays: the former, to make quantitative measurements on such non-linear properties as the critical currents of the system, and the latter, to detect the onset of long-range phase coherence. A description of our sample fabrication and measurement techniques can be found in Secs. 8.2 and 8.3 of this chapter, respectively. Our results, which are presented in Sec. 8.4, show that arrays with long-range interaction are far *less* simple than previous theoretical work [Vinokur et al., 1987 and Sohn et al., 1992] would suggest.

8.2. Fabrication

8.2.1 Array parameters

As we have noted in Chapters VI and VII, in zero field, the array's transition to the phase-coherent state is predicted to occur at a temperature, $T_c \approx NE_J/2k_B$, where $E_J = \hbar^2 J/2e$

¹Much of what is presented in this chapter has been submitted for publication [Sohn et al., 1992c].

and i_c is the critical current of a single junction in the array. In order to satisfy the condition, $T_c < T_{CO}$, the superconducting transition temperature of the individual wires, the product NE_J cannot be too large. For our fabricated arrays, N is chosen to be large (600 or 1000) so that: (1) the macroscopic size of the array would be large enough for us to conduct ac susceptibility measurements, and (2) slight defects and inhomogeneities would have less effect on the basic properties of the arrays.² Consequently, because of the inverse relationship of N and E_J stemming from the need for $T_c < T_{CO}$, i_c needs to be extremely small, $i_c < 0.6$ nA. One way of experimentally achieving this is to employ *tunnel* junctions, and in fact, we use Nb-Al₂O₃-Nb junctions. By controlling the thickness of the oxide layer in our junctions, we can in turn control the i_c in our arrays—the thicker the oxide, the smaller the i_c . We note, however, that the smallest i_c we have been able to achieve is ~ 1 μ A, approximately 1000 times larger than our theoretical target.

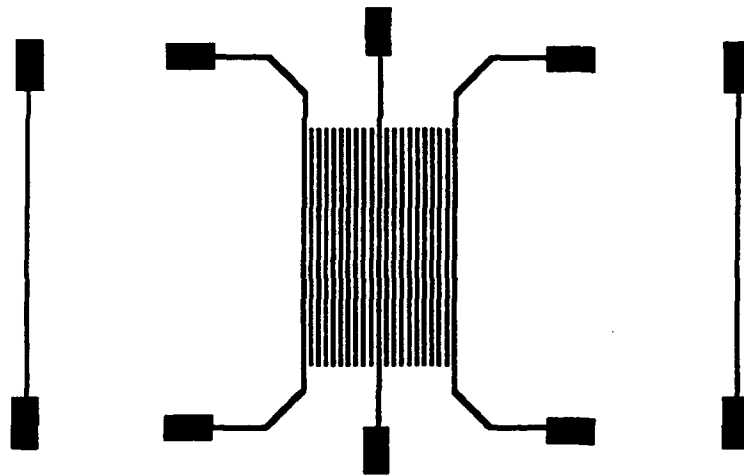
8.2.2 Mask design

The design and fabrication of arrays with long-range interaction are quite different from those of the SNS arrays we had previously discussed in Chapter II. For both the ordered and disordered arrays, we need two masks—each of which corresponds to one of the two orthogonal sets of wires in an array (see Fig. 8.1).^{3,4} The two *ordered* array masks each contain a set of N parallel lines, where $N=600$ or 1000. The lines are evenly

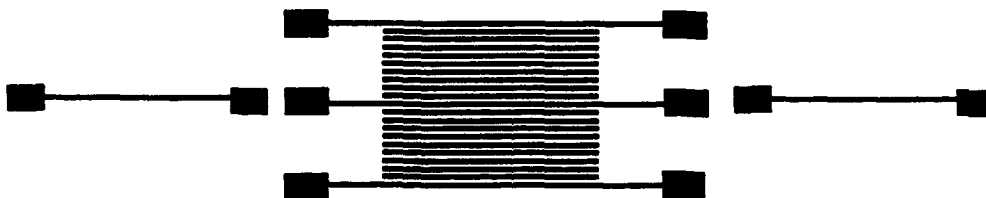
²Originally, our arrays were of size 10×10 , with a lattice constant of 10 μ m. To measure one of these arrays, we fabricated three 10×10 arrays—each of which consisted of the smaller 10×10 arrays with long-range interaction—very close to each other. The three “big” arrays were then large enough to fit under the coils we used for our ac susceptibility measurements. This design was abandoned for a more favorable one which will be described in the following section.

³All masks used were made by Micromask, Inc., Sunnyvale, CA.

⁴Although each mask contained only a set of parallel lines, the line widths in each are so narrow (2.5 μ m) that it is nearly impossible to use only one mask and simply rotate it ninety degrees with respect to itself without having appropriate alignment markers. Hence, we really need two different masks which are orthogonal to each other and have alignment markers.



(a)



(b)

Fig. 8.1. Schematic drawing of the two ordered array masks. Each mask, (a) and (b) contains $N=600$ or 1000 lines with each line being $2.5\text{ }\mu\text{m}$ wide. The lattice constant, Δx , is either $5.5\text{ }\mu\text{m}$ or $10\text{ }\mu\text{m}$. Some lines, as shown, are longer than the others and have pads attached to them. These wires serve as the current-feed and voltage electrodes of the array. The two masks, overlaid on top of one another, will form an array and two single junctions.

spaced with a lattice constant, Δx , of either $10\text{ }\mu\text{m}$ or $5.5\text{ }\mu\text{m}$, respectively. The corresponding macroscopic size of the ordered arrays is therefore either $6 \times 6\text{ mm}^2$ or $5.5 \times 5.5\text{ mm}^2$. The two *disordered* array masks each contained $N=600$ lines which are normally distributed with a mean spacing, $\Delta\bar{x}$, of $10\text{ }\mu\text{m}$ and a standard deviation, $\sigma_{\Delta x}$, of $2\text{ }\mu\text{m}$. Hence, the overall macroscopic size of these arrays is $6 \times 6\text{ mm}^2$. We have included two single lines, which are apart from the set of lines that will eventually become the array, in every mask. These lines, when crossed with their mates from the other masks, will form single junctions with which we will use to estimate i_c of the junctions in the array (to be discussed below). All lines are $2.5\text{ }\mu\text{m}$ wide, making the fabricated junctions of size, $2.5 \times 2.5\text{ }\mu\text{m}^2$.

Because of the novel array configuration, "busbar" electrodes on two opposing edges of the array to feed in a uniform bias current are not included in the overall design of the array, as they are in conventional arrays (see Chapter II). This is because such busbars would be shorted together by the superconducting wires of one set, and consequently, the N^2 individual junctions would not play any role in the dynamics of the system. Likewise, busbars on two perpendicular array edges are not included since each busbar would short the wires of its set, effectively transforming the entire array into one very large Josephson junction. Thus, in order to perform any kind of dc measurements on our fabricated arrays, we have made some of the lines in our mask much longer than the others and have attached pads to them. These particular wires serve as the current-feed and voltage electrodes of the array.

8.2.3 Sample fabrication

As stated in the introduction of this chapter, we chose to fabricate our arrays with SIS junctions in order to achieve very small critical currents. Originally, our arrays consisted of a set of Nb wires and a set of Pb wires. A native Nb oxide, NbO_x separated

the two orthogonal sets of wires, and thus, the wires were coupled by Nb-NbO_x-Pb junctions. We used Nb and Pb because the techniques by which we could fabricate Nb-NbO_x-Pb junctions were well-documented in the literature.⁵ We sputtered 2000 Å of Nb onto a previously patterned substrate (the actual method of patterning the substrates will be discussed below). We then oxidized the Nb layer by exposing the sample to air for 1/2 day. Following a lift-off and repatterning, we thermally evaporated a thin layer of Pb (500 Å) on to the sample. Pb, instead of Nb, was used because it is a soft metal and the process by which it can be deposited is very "gentle," i.e. thermal evaporation is far less harsh on a native oxide layer than is sputtering since relatively little heat is produced. Although this method of fabricating the arrays was extremely quick, it soon became apparent that another type of oxide-barrier and superconducting material, other than Pb, were needed. The reasons for this were the following. First, the arrays were not at all recyclable because of the Pb.⁶ Second, some Nb oxides are known to be conductive which can lead to especially "leaky" SIS junctions [Laibowitz, 1970]. By naturally oxidizing our Nb film, we had no way of controlling the type of oxide that would form on our sample. Third, by exposing the film directly to air, we introduced all different kinds of contaminants to the Nb film.

Nb-Al₂O₃-Nb SIS junctions were finally chosen to make up our arrays since they are known to be extremely robust and recyclable [Huggins and Gurvitch, 1985 and Morohashi et al., 1985 and 1987]. However, we are unable to fabricate ideally the Nb-Al₂O₃-Nb junctions in our arrays, i.e. by fabricating a Nb-Al₂O₃-Nb trilayer *in situ* and reactive-ion etching the Nb to create the junctions [Huggins and Gurvitch, 1985]. This is because our unique array geometry requires that the Josephson junctions interconnect all the array wires. Instead, we find that we must fabricate the junctions in several steps

⁵See for instance, Schwidtal (1972) and Basavaiah et al. (1976).

⁶We did attempt to coat our samples with G.E. varnish as Schwidtal (1972) had done to seal the sample from air; however, we simply did not find this to be a satisfactory process.

which are *not in situ*: this lowers the quality of the junctions that is achievable. We outline the specific fabrication steps below.⁷

Because the lines to be fabricated are so densely packed, a regular trilayer of photoresist-aluminum-photoresist⁸ cannot be used to create the usual undercut necessary for sharply defined edges of the deposited metal. The reason for this is that the developer does not *evenly* develop the exposed photoresist in this geometry. This uneven developing causes some lines to be much wider than others. To avoid this, we used a chlorobenzene technique to create the undercut (see Fig. 8.2). Following the protocol developed by Johnson (1990),⁹ we initially bake a layer of photoresist onto a polished oxidized silicon wafer. We then soak the substrate in chlorobenzene which "hardens" (actually, it polymerizes) the top layer of the photoresist so that the developer needs a longer time to develop this top layer than it does to develop the untouched bottom layer. We finally expose the substrate to the line mask using the Karl Suss Mask Aligner and develop it. The undercut that is created using this technique is barely visible under the highest magnification (660x) of a microscope.

After patterning, we mount the substrate in the magnetron sputtering chamber. After rf cleaning the substrate, we sputter 2000 Å of Nb onto the sample. The sample is then removed from the chamber and undergoes a liftoff and repatterning. Afterwards, the sample is once again mounted in the sputtering chamber. Because a thin layer of NbO_x inevitably forms on top of the Nb film when the sample is originally exposed to air, the sample is rf cleaned in order to remove this top layer of oxide. Once this is done, we sputter Al onto it. In our first attempts to form the aluminum-oxide layer, we

⁷For a detailed description of the fabrication process; see Appendix II.

⁸See Chapter II.

⁹See Appendix IV for a full outline of this protocol and another one which creates larger undercuts.

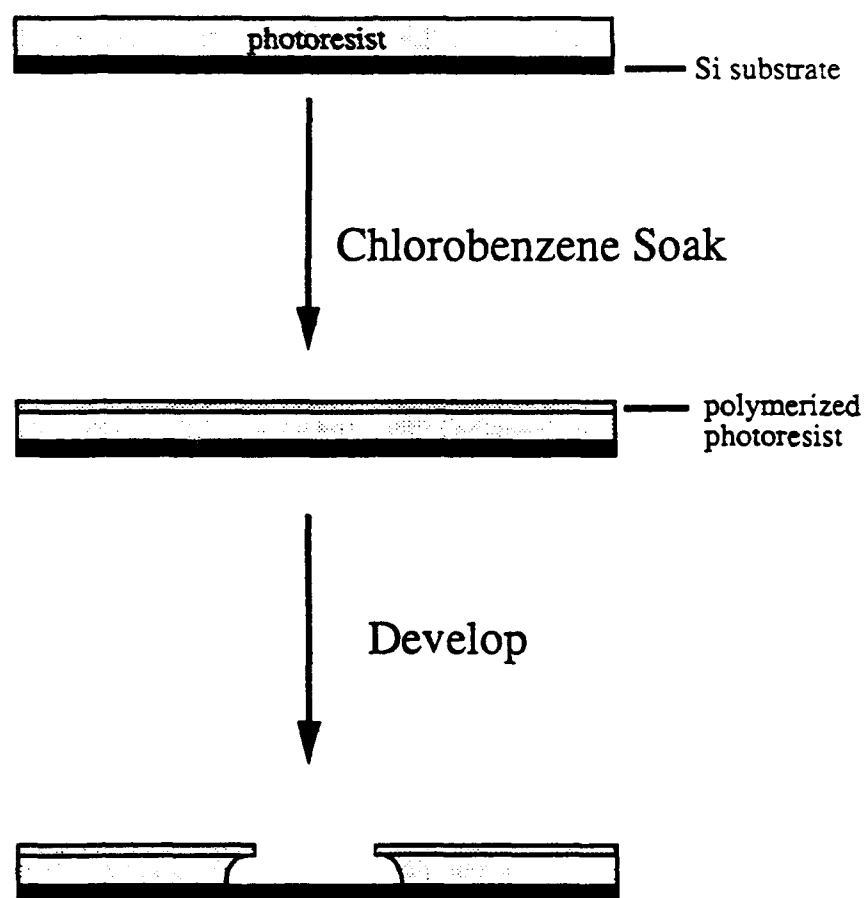


Fig. 8.2. Outline of the chlorobenzene process which is used to create small undercuts.

sputtered 46 Å of aluminum onto the substrate.¹⁰ We then oxidized the sample in a pure oxygen bath for various times and pressures.¹¹ Finally, we sputtered an additional 2000 Å Nb, *in situ*, onto the sample.

From our initial tests, we found that our fabricated junctions had extremely large critical currents (tens of microamperes) and were very leaky. We hypothesized that this was most likely due to some Al diffusing down into the Nb underlayer. Diffusion of this kind is caused by the sample overheating during the sputtering process [Huggins and Gurvitch, 1985 and Martinis and Ono, 1990]. Evidence that our own samples were overheating is that the Nb film often looked cloudy (an indication that the underlying photoresist burned) or cracked (an indication of heat stress with the underlying photoresist).

To improve the quality of our junctions, we altered the method by which we created the oxide-barrier. More importantly, however, we heat sunk the sample in the sputtering chamber better by sparingly applying Apiezon Thermal Grease H between the substrate and the water-cooled substrate holder. After rf cleaning the substrate, again to remove possible Nb oxides from the surface of the film, we sputter *only* 26 Å of Al and oxidize the sample at 500 mTorr for 10 minutes. An additional 26 Å of Al is then sputtered onto the oxide layer and oxidized at 500 mTorr for 35 minutes. This two step aluminum/oxidation process is necessary to ensure a much thicker oxide-barrier than the self-limiting barrier (10-15 Å) and hence junctions with smaller critical currents. In addition, the two step process prevents our sample from overheating. Following oxidation, we sputter, *in situ*, an additional layer (2000 Å) of Nb onto the sample to thus create our counterelectrodes. A simple lift-off is then performed and our sample is diced. A schematic drawing of the array

¹⁰Huggins and Gurvitch (1985) suggest working with an Al layer of thickness $d_A > 50$ Å since anything less would result in the oxide barrier containing possible Nb oxides. Higher leakage would therefore occur in the junction.

¹¹See Appendix III for a listing of critical current densities obtained from changing the O₂ pressure and oxidation times.

is shown in Fig. 8.3 and SEM photographs of both the ordered and disordered arrays are shown in Figs. 8.4 and 8.5.

8.3 Measurement Techniques

8.3.1 DC measurements

The rig we use to measure our samples is the very same one outlined in Chapter II. We have, however, made some modifications. Specifically, we have attached 1 k Ω resistors to the current and voltage leads. These resistors, nominally at the sample temperature, help to filter room temperature noise. With this modified rig, we perform two-point probe measurements, in the sense that separate voltage and current leads go down to the same pad, on our fabricated arrays.¹² (Four-point probe measurements, however, are performed on the single junctions). Two different lead configurations are tried on each of the arrays.¹³ In orientation A (Fig. 8.6a), the current is injected into one wire and extracted from another in the *same* set. In orientation B (Fig. 8.6b), the current is injected into one wire in one set and extracted from a wire in the *other* set. An HP 6177A DC power supply, rather than a Lake Shore Cryotronics Temperature Controller, is used to power the heater that controls the temperature in our dc measurements, since the latter can send noise down to our sample and "smear" the I - V curves. To minimize electrical noise generation, data, like those from the SNS arrays, are initially plotted on an HP 7045B analog XY recorder and then digitized for computer analysis. For reasons to be described

¹²We did attempt to perform four-point measurements on our arrays; however, we obtained some rather bizarre results. For example, when we measured the normal state resistances of some of our arrays below T_{CO} , we found that they were apparently negative! We attribute this phenomenon to defects which cause the currents in the array to flow along indirect paths, thereby reversing the sign of the potential between the two voltage pads we were measuring.

¹³As in the SNS arrays, the voltage and current leads of these arrays are attached using pressed indium dots.

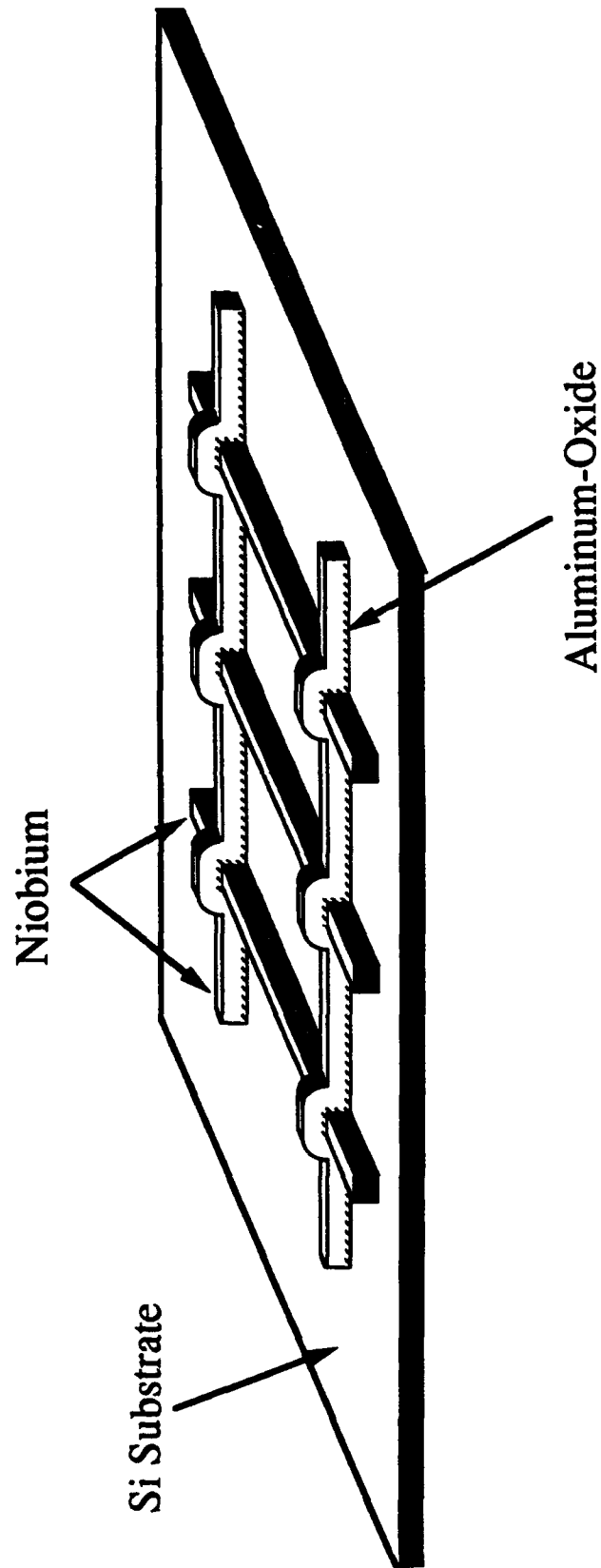


Fig. 8.3 Schematic drawing of a fabricated array with long-range interaction.

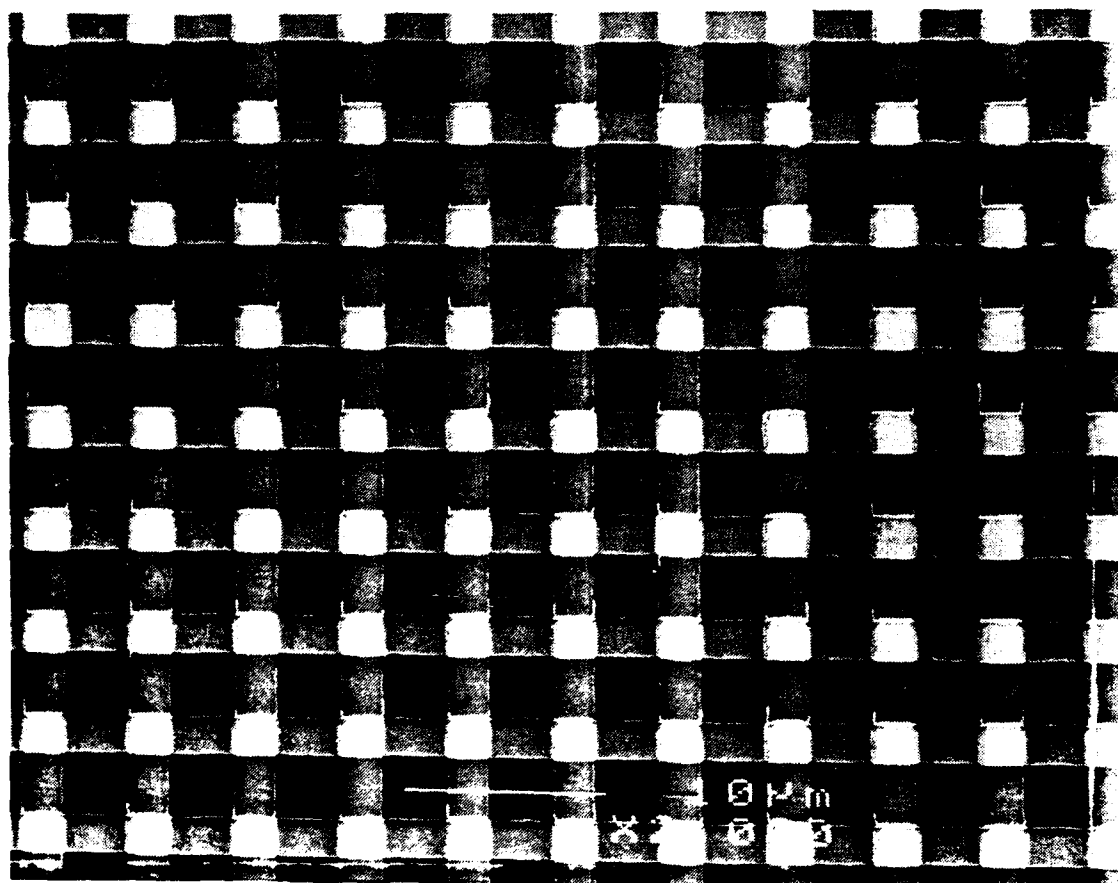


Fig. 8.4. SEM picture of an actual ordered array with long-range interaction. The lattice constant of the array is $5.5 \mu\text{m}$ and the junction size is $2.5 \times 2.5 \mu\text{m}^2$.

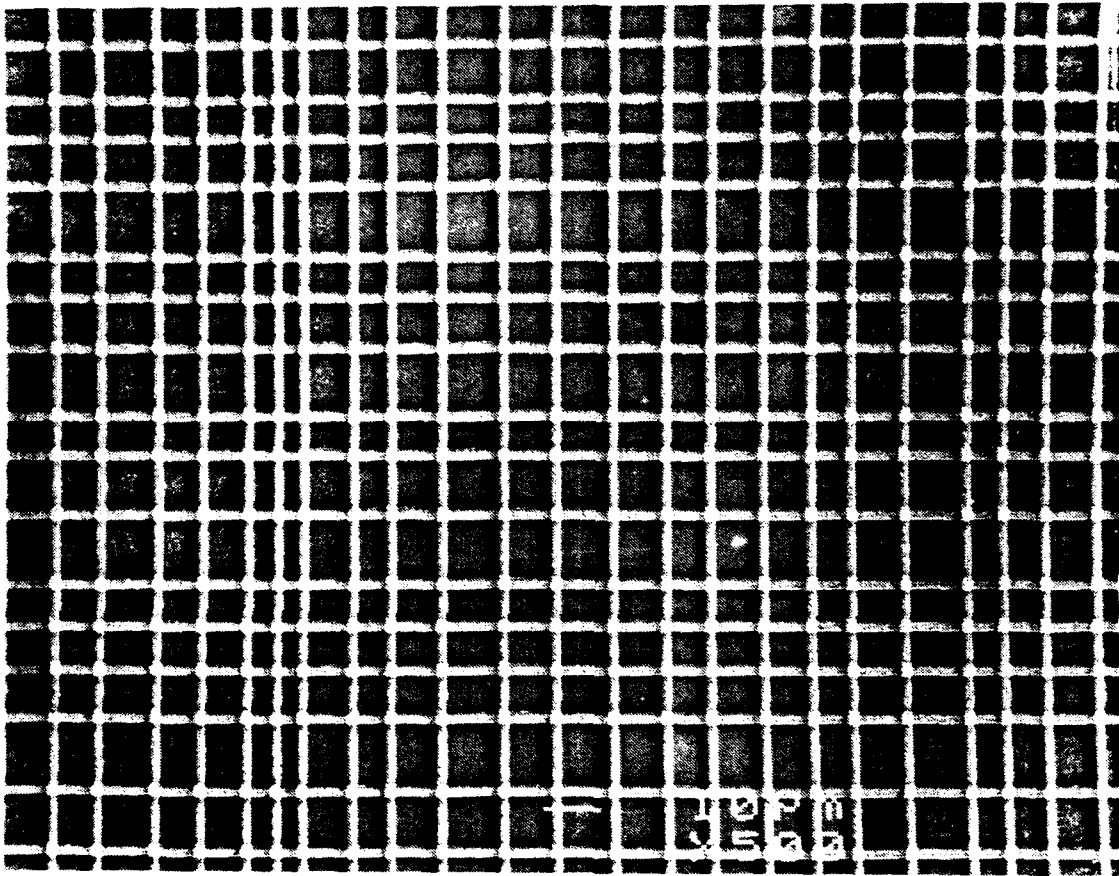
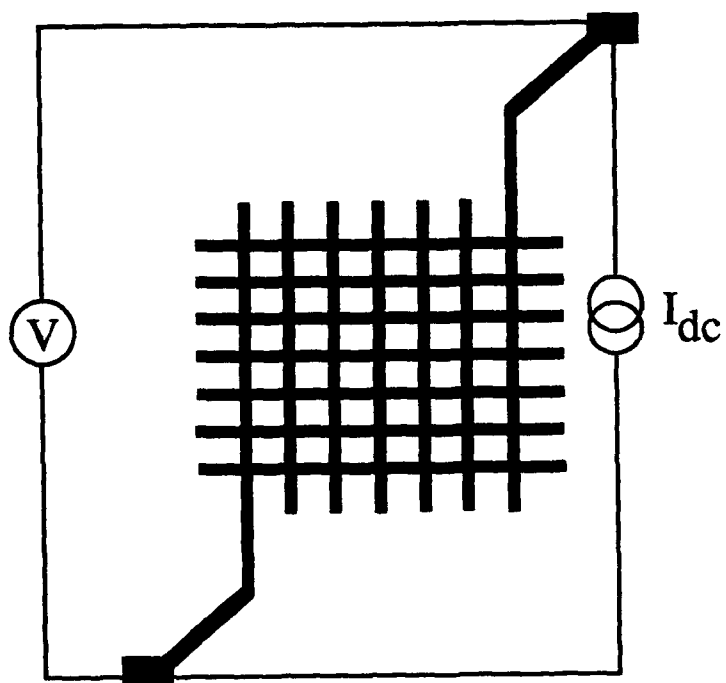
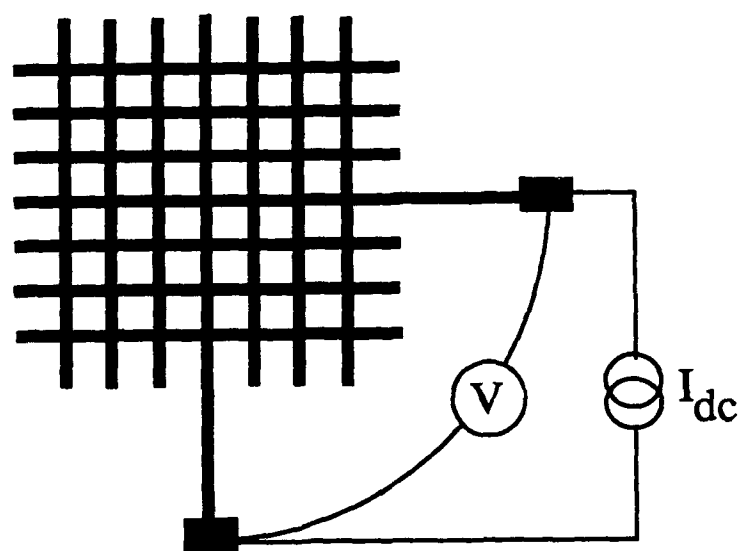


Fig. 8.5. SEM picture of an actual disordered array with long-range interaction. The wires are normally distributed with an average lattice constant of $10\text{ }\mu\text{m}$ and a standard deviation of $2\text{ }\mu\text{m}$. The junction size is $2.5 \times 2.5\text{ }\mu\text{m}^2$.



(a)



(b)

Fig. 8.6. The two different current-feed orientations we tried. (a) Current-feed orientation A: the current is injected into one wire of one set and extracted from another of the *same* set. (b) Current-feed orientation B: the current is injected into one wire of one set and extracted from a wire of the *other* set.

in Sec. 8.4.1, a Tektronix 2225 50 MHz oscilloscope is also used to record data from our arrays.

8.3.2 AC measurements

To conduct contactless ac measurements, we use a two-coil mutual-inductance technique similar to that outlined by Jeanneret et al. (1989). Our main measurement apparatus consists of a drive coil of radius $R_d=0.42$ cm and a pair of astatically wound receive coils of radius $R_r=0.24$ cm which is coaxially mounted within the drive coil (see Fig. 8.7).¹⁴ Using 40 gauge Cu wire, we carefully wound the coils such that all the turns in the coils are equally spaced. While the drive coil consists of a single layer of $N_d=23$ turns, the receive coils each consist of two layers of $N_r=15$ turns.¹⁵ The field produced by the drive coil at the sample is calculated to be ~ 45 $\mu\text{Gauss}/\mu\text{A}$. We balance the coils using a PAR 124A lock-in amplifier with a PAR 116 preamplifier at the input. Once the receive coils are balanced, we tighten the screw at the top of the drive coil to lock the two sets of coils together.

The two-coil apparatus is then placed in a teflon holder designed by M. S. Rzechowski of this group and mounted directly over the sample with a thin sheet of mylar (thickness=14 μm) separating the two (see Fig. 8.8). The mylar is used to prevent the sample from being scratched. We note that the entire apparatus is designed such that the coils are approximately 0.5 mm away from the sample. Ideally, one would like to have the receive coils to be as close to the sample as possible.¹⁶ The vacuum can, as described in Chapter II, is placed over the sample and the rig is placed in the temperature-controlled,

¹⁴The coil shafts were machined from the material, KEL-F.

¹⁵Two layers in each of the receive coils are used to increase the sensitivity of the coils.

¹⁶Jeanneret et al. (1989) state that the drive coil-sample distance in their apparatus was $\delta h_d=0.2$ mm, and the receive coil-sample distance $\delta h_r=30$ μm .

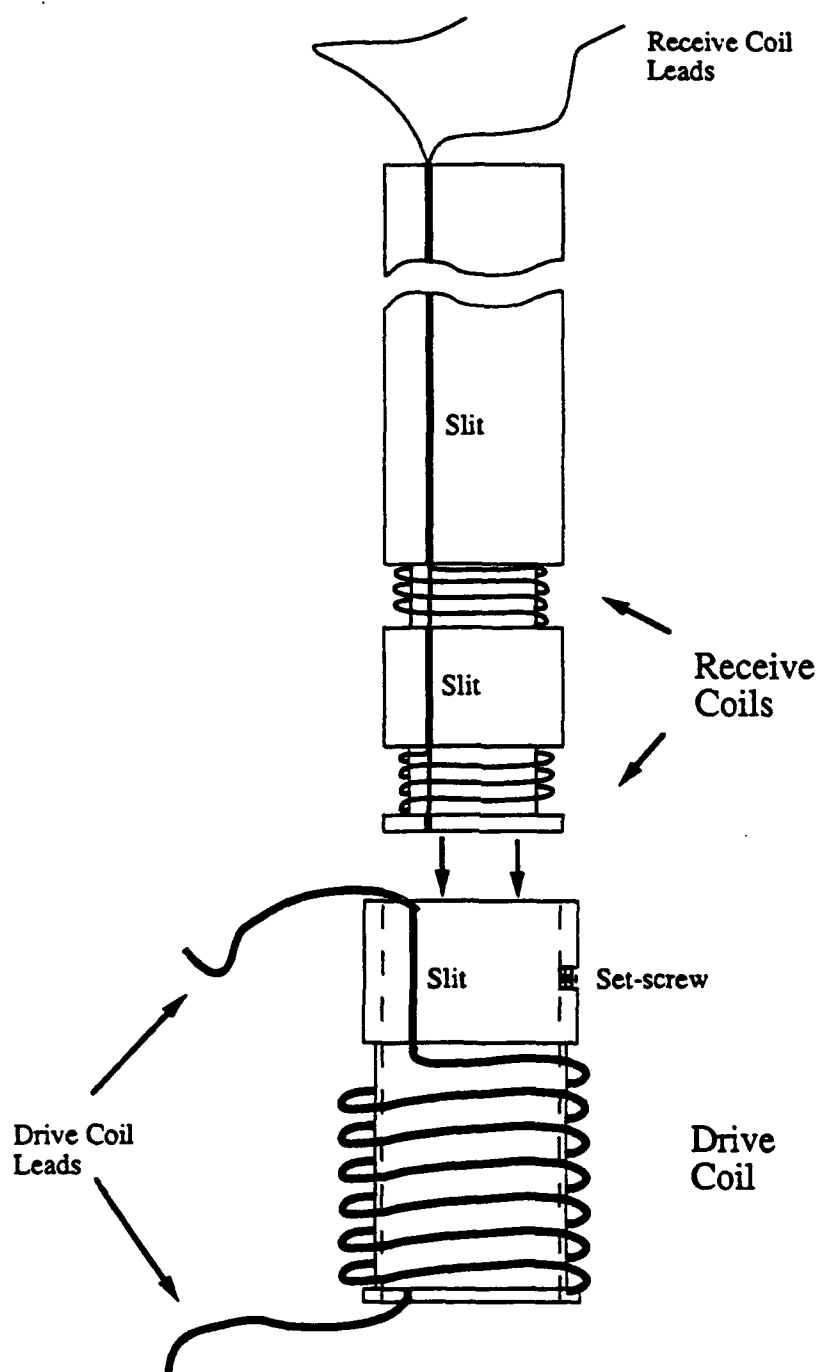


Fig. 8.7. Schematic drawing of the two-coil mutual-inductance apparatus we used to perform ac susceptibility measurements on our arrays. The pair of astatically wound receive coils is coaxially mounted within the drive coil as shown.

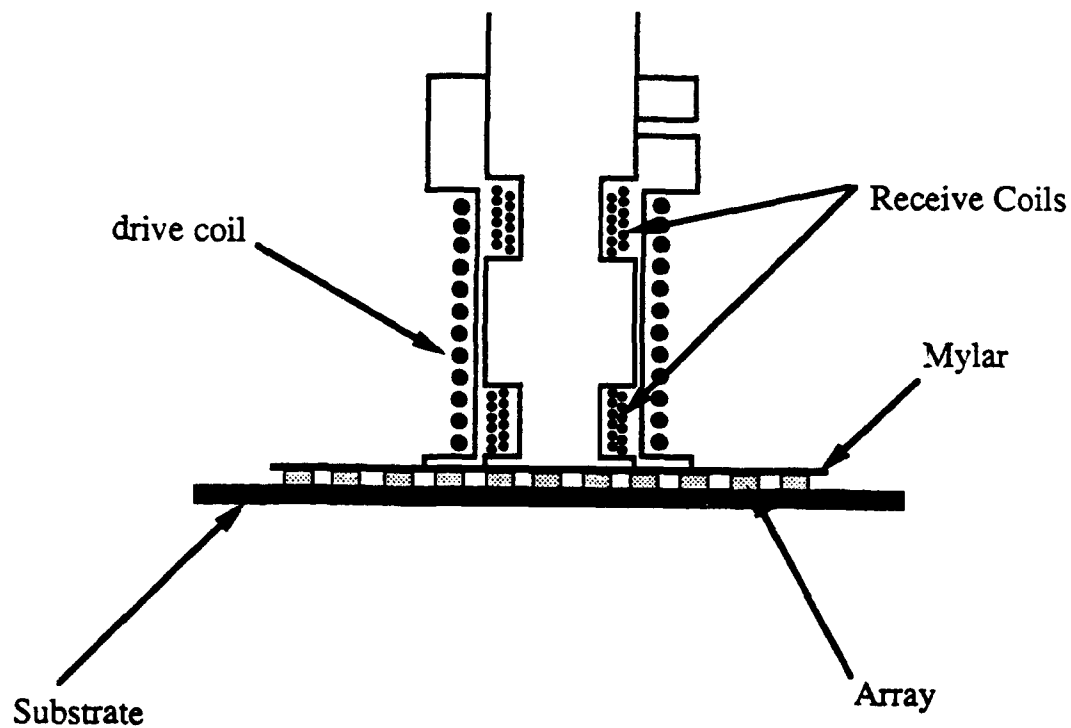


Fig. 8.8. Schematic drawing of the actual setup we use to perform our ac measurements. A thin mylar film is placed between the coils and the array so that the latter will not be scratched.

μ -metal shielded ^4He cryostat. The in-phase and out-phase components of the voltage, δV ,¹⁷ at the receive coil due to the screening current flowing through the sample in response to an ac current are detected by conventional lock-in techniques.

All of the ac measurement results we present in this chapter are from measurements taken in the frequency range of 80-100 kHz, since we achieved maximum signal output in this range. [However, we have conducted some of our ac measurements at frequencies as low as 10 kHz with similar results, but at lower signal/noise ratio.] Although such high frequencies are out of the range of ideal PAR 116 1:100 transformer performance, we nonetheless use the transformer for all our measurements in order to rid ourselves of ground-loops. While it increases the signal voltage by only a factor of ~ 3 , the transformer, at 100 kHz, does not distort our signals.¹⁸

8.4 Results

8.4.1 DC measurements

All the single junctions we fabricated concurrently with our arrays have normal state resistances, r_n , of approximately 670 Ω , and critical currents, i_c , ranging from 0.45 to 1.5 μA at $T=1.7$ K. (The $i_c r_n$ products of these junctions, therefore, range from 0.3 to 1.0 mV, compared to the ideal value of $i_{c0} r_n = \pi \Delta(T)/2e = 2.5$ mV where i_{c0} is the intrinsic

¹⁷The signal voltage, δV , can be written as

$$\delta V = i\omega I_d \omega \int_0^\infty dx \frac{M(x)}{1 + (2/\mu_0 h)(1/i\omega G)x}$$

where $x=hq_l$, with h equal to the sum of the distances the receive and drive coils are from the sample, and q_l being the in-plane component of the Fourier transform of r , the variable upon which the sample's sheet current density is dependent. $M(x)$ is the mutual-inductance distribution resulting from the geometry of the measuring system. See Jeanneret et al. (1989) for specific details on the derivation of this equation.

¹⁸We tested this by using a square-wave signal as our input signal. For a given high frequency, we found that the signal was not distorted.

critical current derived from microscopic theory, and $\Delta(T)$ is the temperature-dependent energy gap of the superconductor [Ambegaokar and Baratoff, 1963]). In addition, all the junctions appear to be resistively-shunted. Fig. 8.9 shows a representative I - V curve of one of the single junctions we measured; the junction is clearly non-hysteretic. Compare this I - V curve with those in Figs. 8.10a-c. These I - V curves are from test junctions we made while we were determining the appropriate fabrication recipe for our arrays. Fig. 8.10a is from a test junction which was fabricated using the recipe we have just outlined in the previous section. Figs. 8.10b and c are from test junctions which were fabricated using two other recipes.¹⁹ The I - V curves of these junctions show superconducting gaps, $2\Delta/e$, ranging from 0.85 to 2.5 mV, and $i_c r_n$ products ranging from 0.03-1.5 mV; one curve (Fig. 8.10c) even shows hysteresis. We note that the rather poor quality of the array junctions, as indicated by the single junctions fabricated concurrently with the arrays, should not drastically affect the arrays' properties since they are mainly determined by the *magnitude* of i_c . It is clear, however, that the i_c values obtained (even at $T=4$ K where we have measured i_c to be as small as 0.08 μ A) are ~ 100 -1000 times larger than the nA range required to conform to our theoretical target.

Upon measuring the arrays in current-feed orientation A, we find that the array critical currents, I_c , range from 11.5 to 33.0 μ A at $T=1.7$ K. In the current-feed orientation B, I_c ranges from 2 to 5 μ A. The range of I_c values we obtained for either current-feed orientation is far less than the $I_c=Ni_c \sim 1$ mA values we had anticipated from having N (≈ 1000) junctions, each with critical current i_c (≈ 1 μ A), in parallel. More striking is the fact that we found that both the ordered and disordered arrays show *hysteretic* behavior (Figs. 8.11a and b) even though they each consist of *non-hysteretic* junctions. Sweeping the dc current up and down, we observe that the arrays produce a

¹⁹ See Appendix III.

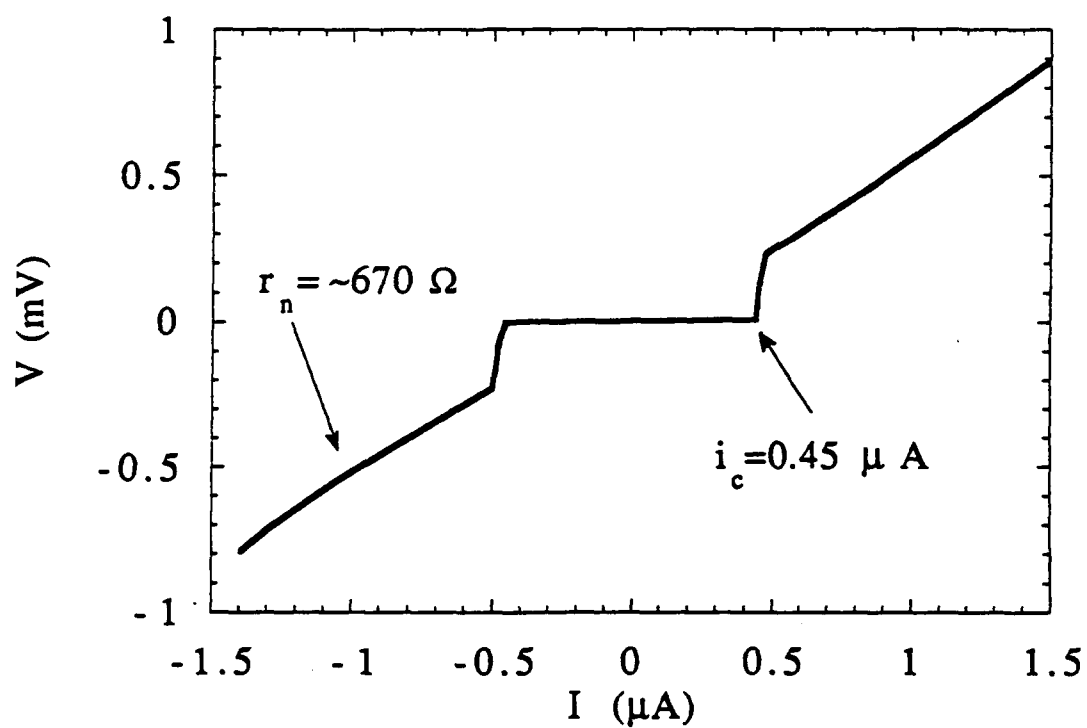


Fig. 8.9. Representative I - V curve obtained at $T=1.7$ K from one of our fabricated single junctions. The critical current, i_c , of the nonhysteretic junction is $0.45 \mu\text{A}$ and the normal state resistance, r_n , is 670Ω .

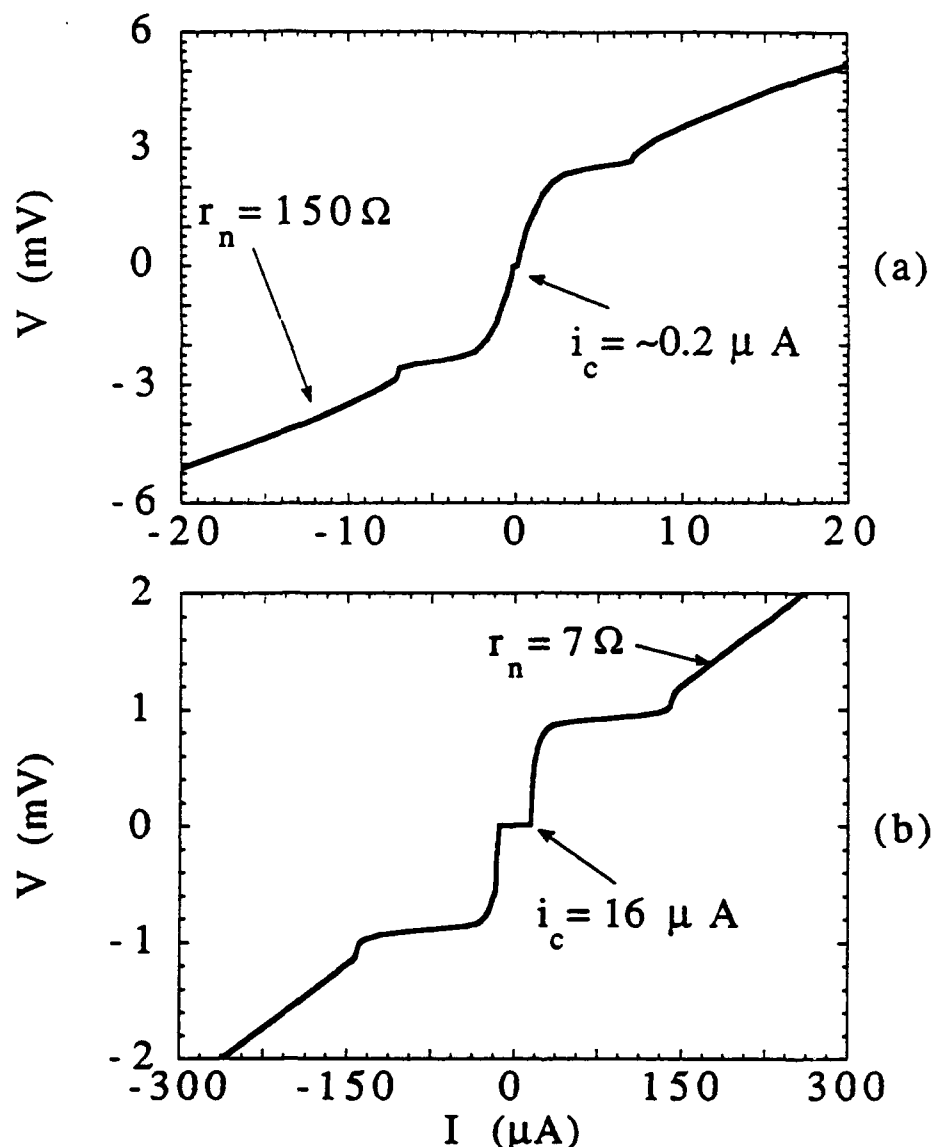
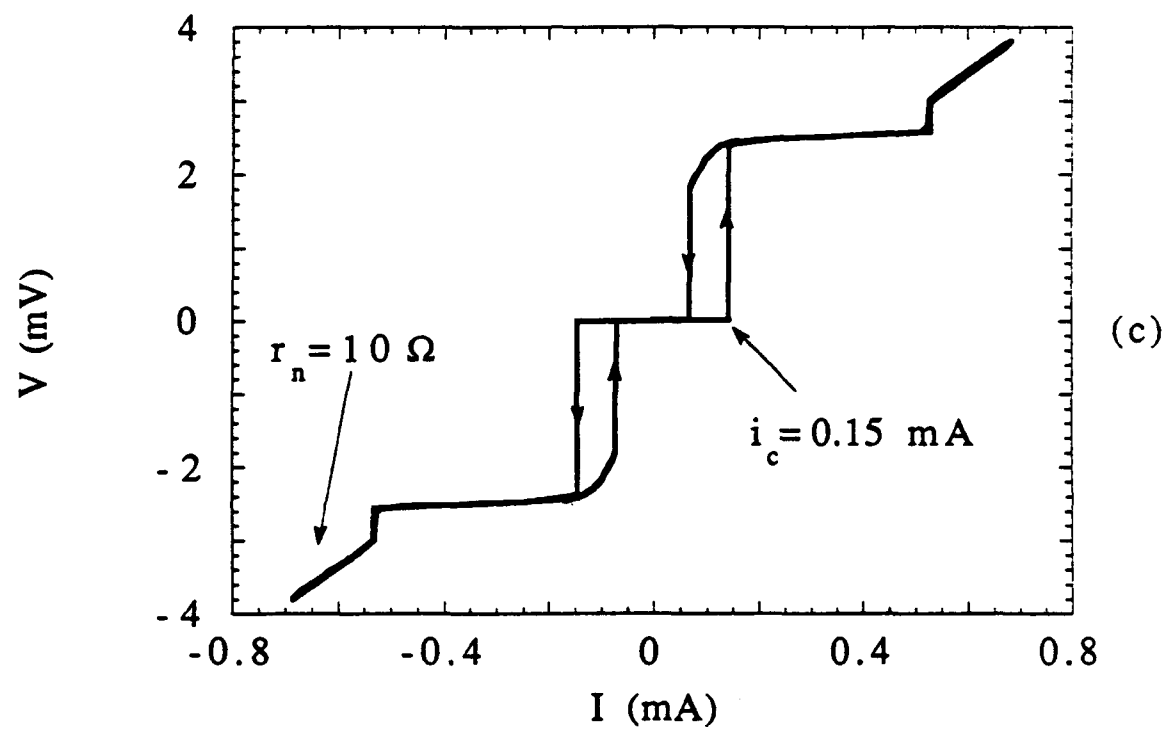


Fig. 8.10. Representative *I-V* curves obtained at *T* = 4.2 K from three differently fabricated single Nb-Al₂O₃-Nb junctions (size: 2.5 μm x 2.5 μm). (a) The non-hysteretic junction was fabricated in the same manner described in Section 8.2.2. The critical current, *i_c*, is approximately 0.2 μA, the normal state resistance, *r_n*, is 150 Ω, and the superconducting gap, 2Δ/*e*, is 2.5 mV. (b) The non-hysteretic junction was fabricated by oxidizing the Al layer at 1000 mTorr for 60 min (See Appendix III). For this junction, *i_c* = 16 μA, *r_n* = 7 Ω, and 2Δ/*e* = 0.9 mV. (c, next page) The hysteretic junction was fabricated by oxidizing the Al layer at 150 mTorr for 30 min (See Appendix III). For this junction, *i_c* = 0.15 mA, *r_n* = 10 Ω, and 2Δ/*e* = 2.5 mV. The "kink" in the *I-V* curves just above the superconducting gap is common to Nb-Al₂O₃-Nb and especially, to Nb-NbO_x-Pb junctions. It is due to a proximity effect of a normal layer on the niobium surface which consequently leads to the broadening of the density states of the two superconductors that make up the junction [see Paterno et al., 1975, and Nordman and Houck, 1978].



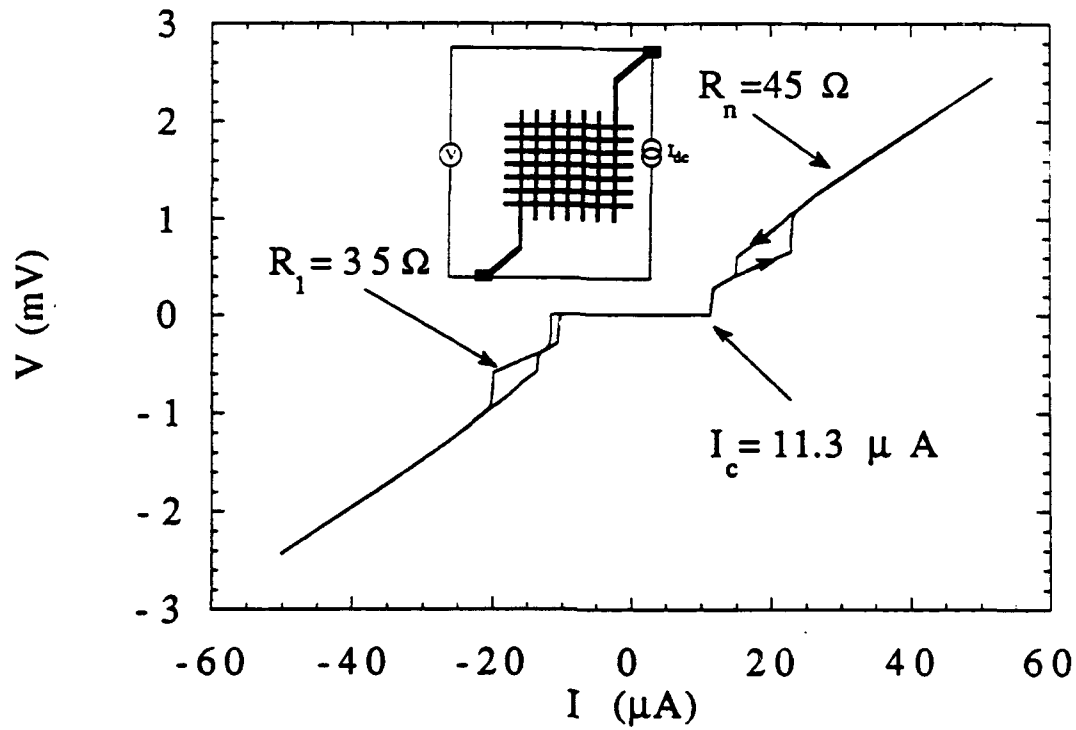
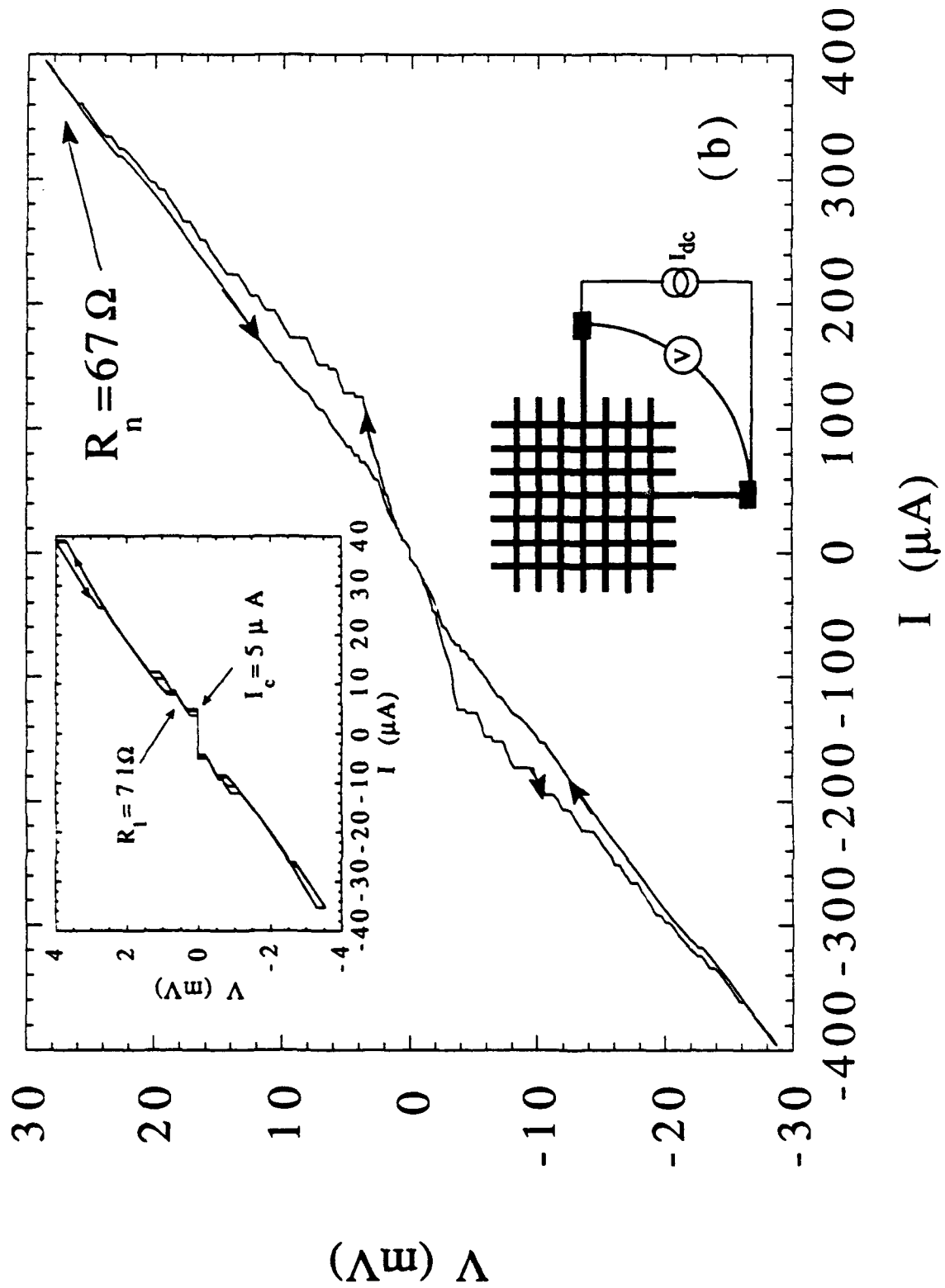


Fig. 8.11. I - V curves obtained at $T=1.7$ K from the two different current-feed orientations shown in Fig. 8.6. (a) I - V curve for current-feed orientation A. $I_c=11.3 \mu\text{A}$ and $R_I=35 \Omega$. (b, next page) I - V curve for current-feed orientation B. Inset: Magnification of the region near the origin. $I_c=5 \mu\text{A}$ and $R_I=71 \Omega$. All curves show hysteresis and step-like structure.



range of critical, I_C , and retrapping, I_r , currents (see inset to Fig. 8.11b).²⁰ This premature switching might be due to possible thermal activation processes [Fulton and Dunkleberger, 1974], though it is more likely due to trapped flux or noise, since none of the single junctions show any signs of premature switching.

The observation of voltage "steps" in both the critical- and retrapping-current portions of the array I - V curves is surprising. As shown in Fig. 8.11b, the steps along the upsweep portion of the curves are much more visible than those along the downsweep portion. Premature switching from one step to another is again observed (see inset to Fig. 8.11b). Comparing the I - V curves resulting from the two different current-feed orientations (Fig. 8.6a and b), we observe many more steps when current is fed in orientation B , i.e. where the current is injected in one wire of one set and extracted from a wire of the other set. However, curves derived from both current-feed orientations show a decrease in the number of steps as the temperature is increased. We note that the resistance, R_I , of the array after the first step is $35\ \Omega$ when the current is injected in and extracted from wires of the same set (Fig. 8.11a) and that it is $R_I=71\ \Omega$ when the current is injected in one wire of one set and extracted from a wire of the other set (Fig. 8.11b, inset). The reason for the 2:1 ratio of these R_I values is not well understood at present.

If we zero-field cool (ZFC) the ordered arrays in current-feed orientation B , we find that I_C is dramatically affected when a field is subsequently applied. For each ZFC run, we changed the field strength with the overall effect that I_C periodically oscillates with respect to field strength (see Fig. 8.12) and equals zero for $|f| \geq 0.27$. We note that the period of oscillation I_C undergoes corresponds to an area of $\sim 400\ \mu\text{m}^2$ —the significance of this will be discussed in Chapter IX. Unlike those of the ordered arrays, the critical currents of *disordered* arrays do not show any visible oscillation with varying field strengths; rather,

²⁰Because of this premature switching of I_C , we used an oscilloscope to take an average of I_C .

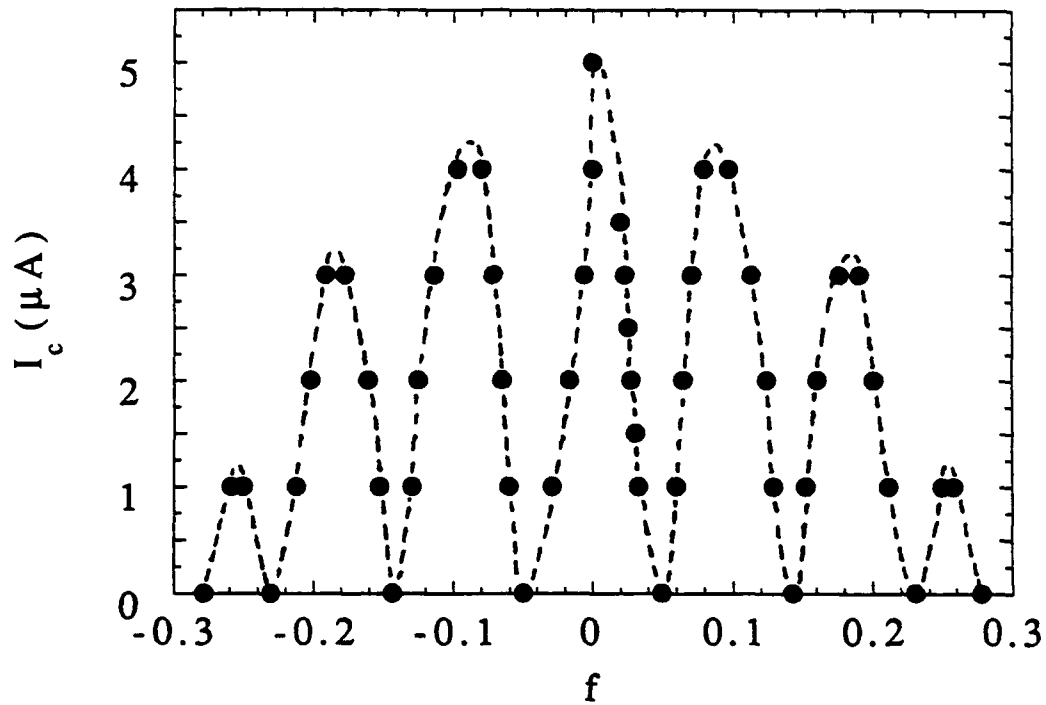


Fig. 8.12. Critical current, I_c , vs. field of an ordered 1000×1000 array with lattice constant of $5.5 \mu m$ and in current-feed orientation B . The critical current shows a periodic oscillation with decreasing amplitude when the magnetic field strength is varied. The period of oscillation corresponds to an area of $\sim 400 \mu m^2$. I_c is zero for $|f| \geq 0.27$. [The unusual distribution of data points results from measuring the values of f required to reduce I_c to successive integer values.]

they show a constant non-zero value with respect to the different field strengths we tried (from $f=0$ up to $f=5.75$).

8.4.2 AC measurements

As stated previously, the ac susceptibility results presented in this chapter were obtained by using a frequency range of 80-100 kHz. The ac current amplitude, $I_D\omega$, used was on the order of microamperes. [This translates to fields of 10-100 μ Gauss being produced at the sample. Such fields are small enough for the sample to give a linear response, in the sense that doubling the drive, $I_D\omega$, doubles the sample's response, $\delta V(\omega)$. We have confirmed this experimentally.]

In neither the ordered nor the disordered arrays, do we observe any feature at the superconducting transition of Nb (which, for our films occurs at ~ 8.8 K). The individual Nb wires give a negligible diamagnetic response to the ac field because of their very small dimensions. We do, however, observe a strong signal, corresponding to the array's broadened phase transition to a macroscopically phase-coherent state, at temperatures which range from 3 to 5 K, depending on the sample (see Fig. 8.13a and b).^{21, 22} A magnetic field ($f=1/q$, where $q=2, 3, 4, 5, 6$) applied to the ordered arrays leads to a marked effect on the transition temperature, T_C .²³ As shown in Fig. 8.14, small fields (i.e., large q) suppress T_C much more than do large fields (i.e., small q). This qualitative behavior corresponds well with that predicted by mean field theory [Sohn et al., 1992b] which is also plotted in Fig. 8.14, but the observed effect is only about a quarter as large as

²¹Because a measured array has a broadened transition (usually over 1 K-1.5 K), we define T_C as the temperature at which the slope of the transition signal is steepest.

²²We measured a T_C of 4 K for the 10 x 10 arrays described in Footnote (1). The critical current, i_c , of a single junction in these arrays was $\sim 7 \mu$ A.

²³We calibrate the fields by varying the magnetic field and measuring the array's ac response. This will be further discussed below.

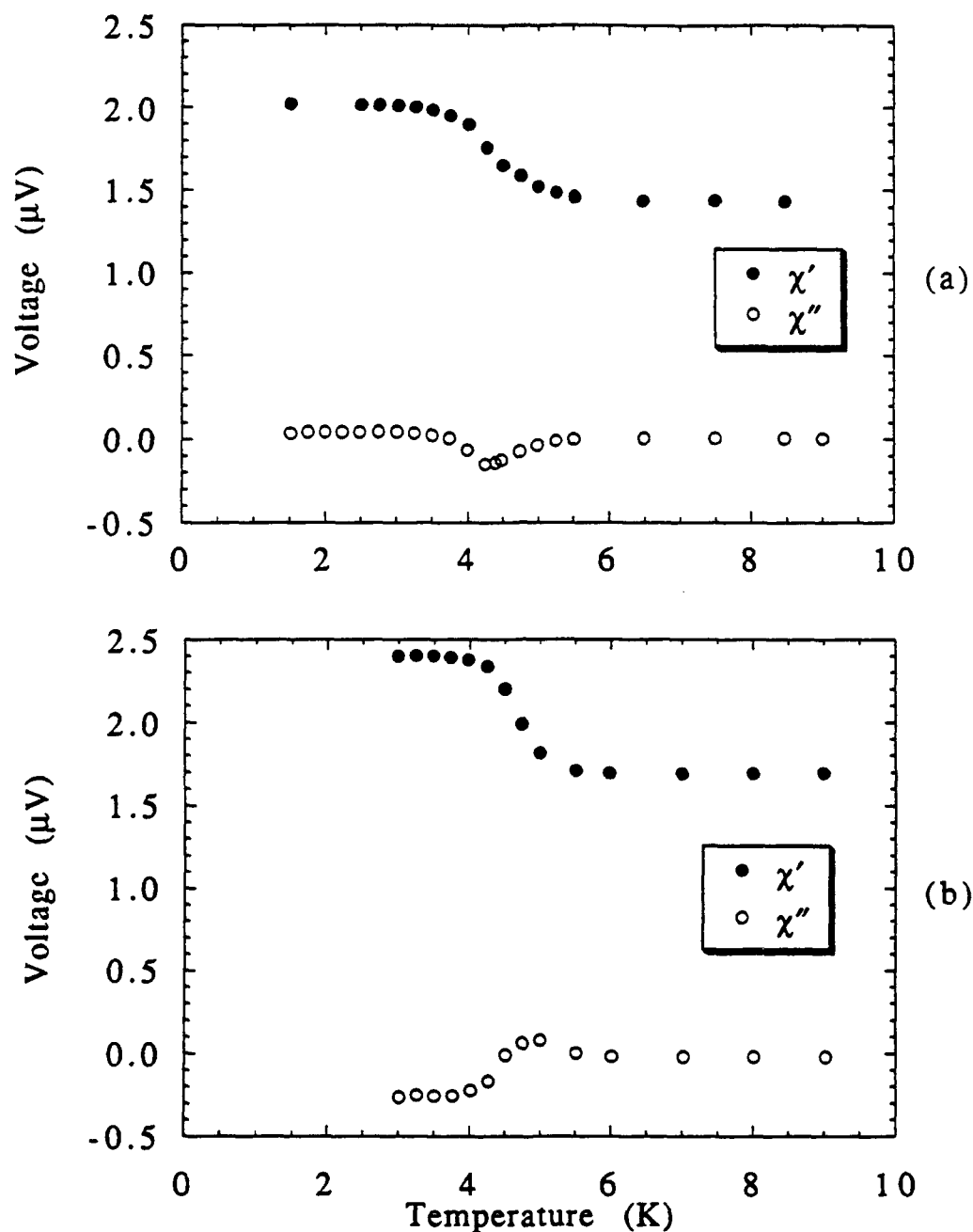


Fig. 8.13. AC response vs. temperature for the (a) 1000 x 1000 ordered and (b) 600 x 600 disordered array. χ' and χ'' are the components of the measured signal which are in- and out-of-phase relative to the reference phase (giving a pure in-phase signal in the normal state). The ac amplitude used to make the measurement was 0.5 μA for the ordered array and 0.25 μA for the disordered array; the frequency used was 100 kHz. The strong signal at $T \sim 4$ K in both arrays indicates the arrays' transition to the macroscopically phase-coherent state.

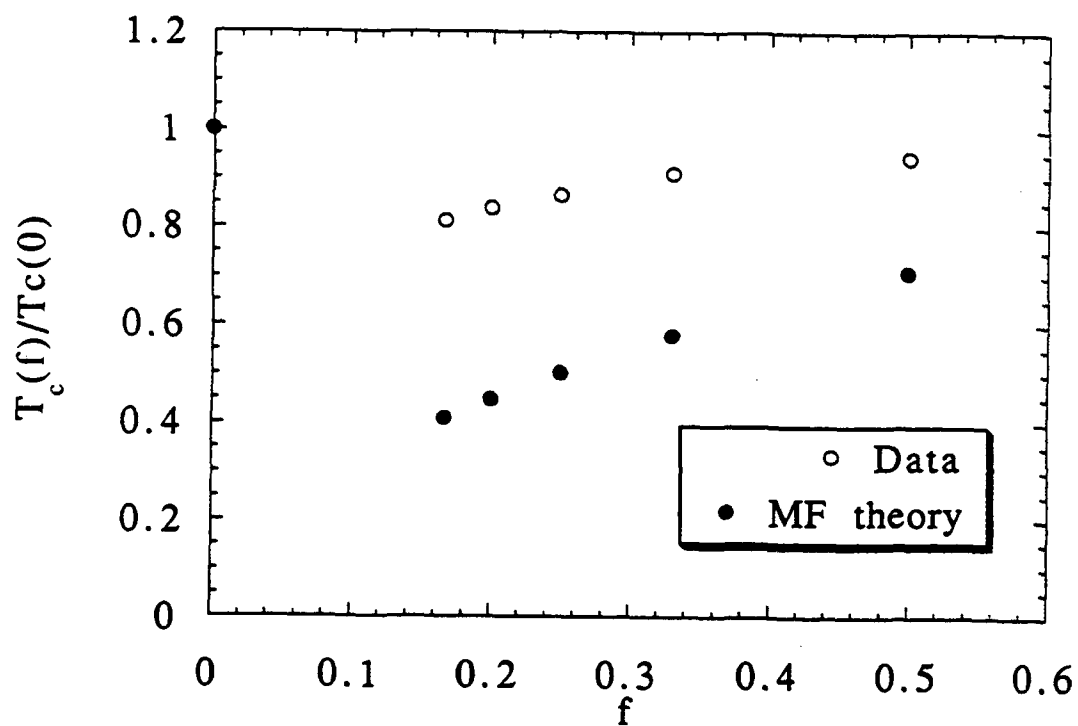


Fig. 8.14. Normalized transition temperature, $T_c(f)/T_c(0)$, vs. number of flux quanta, f , per unit cell for (a) our data obtained from a 1000×1000 ordered array and (b) our results from mean field theory. The data corresponds to fields $f=1/q$, where $q=2, 3, 4, 5, 6$.

the ideal prediction. Although we have not directly measured T_C for incommensurate fields, we expect that $T_C(f)$ is a continuous function with much substructure.

The T_C of *disordered* arrays, on the other hand, is not observed to be affected by a magnetic field, even between $H=0$ and $H\neq 0$, and whether zero-field-cooled (ZFC) or field-cooled (FC). This surprising observation is contrary to that theoretically predicted by Vinokur et al. (1987) and by us (Sohn et al., 1992b). One possible explanation is that, even in nominally zero field, an inhomogeneous stray field may be large enough to cause the array to be in the high field, constant T_C , regime of a disordered array. This regime, as defined by theory [Vinokur et al., 1987 and Sohn et al., 1992b], corresponds to $H > H_0$, where H_0 is again the field value giving one flux quantum through an average-sized strip between two adjacent wires, or $f=1/N$. For our disordered arrays, H_0 is only 0.3 mGauss! Thus, if an inhomogeneous stray field were present that could not be nulled everywhere to < 0.3 mGauss, the array would be in the high field, constant T_C , regime. This seems not implausible since an average stray field of up to 0.8 mGauss before nulling was observed.

If we vary the transverse magnetic field at temperatures near the transition, we find that the ac response, $\delta V(f)$, of the the ordered arrays, like that of conventional arrays [Martinoli et al., 1987], shows a complex oscillatory behavior. Figs. 8.15a-c show plots of the ac response vs. field. Here, we see that strong peaks in both the in-phase and out-phase components of the signal develop as we decrease the temperature from just above T_C to just below.²⁴ These peaks correspond to commensurate field strengths, $f=0, 1/2, 1/3, \dots, 1/8$. As shown in Fig. 8.16, only a single peak corresponding to $f=0$ appears in our disordered array data. The disordered arrays do *not* show any commensurability with the range of the applied fields we tried. This result is qualitatively consistent with the fact that the cell size in the lattice varies too much for any non-zero field to be commensurate with the array lattice.

²⁴The in-phase and out-phase components of our signal are with respect to the reference phase which gives a pure in-phase signal in the normal state. No corrections are made for any temperature dependence of the entire circuit.

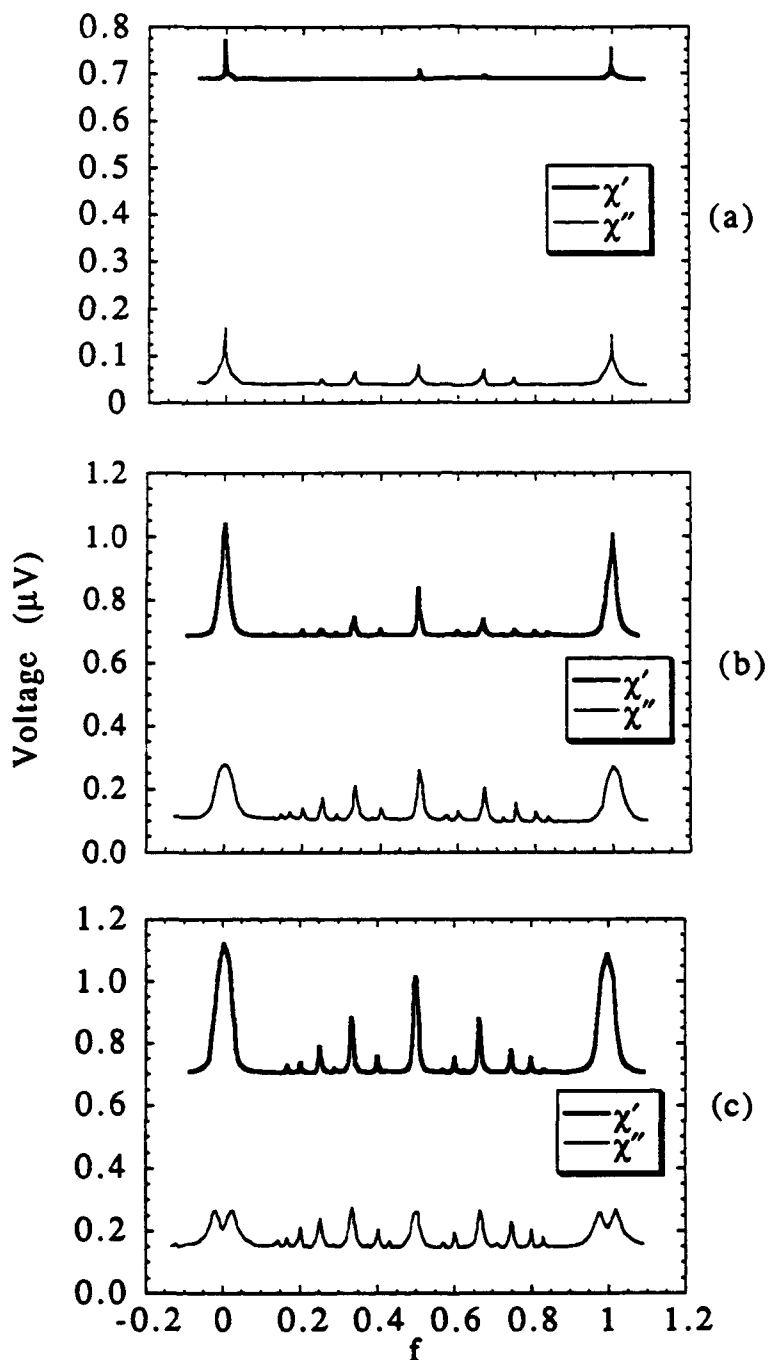


Fig. 8.15. Real and imaginary components of the complex ac response of a 1000×1000 ordered array to a varying magnetic field. The data were taken at (a) $T=4.25$ K, (b) $T=3.75$ K, (c) $T=3.5$ K. As temperature is decreased from just above T_C (which for this array is ~ 4 K) to well below T_C , the number of peaks increases. These peaks correspond to array commensurability with field strengths, $f=0, 1/2, 1/3, \dots, 1/8$. The frequency and excitation current used were 100 kHz and $2.1 \mu\text{A}$, respectively.

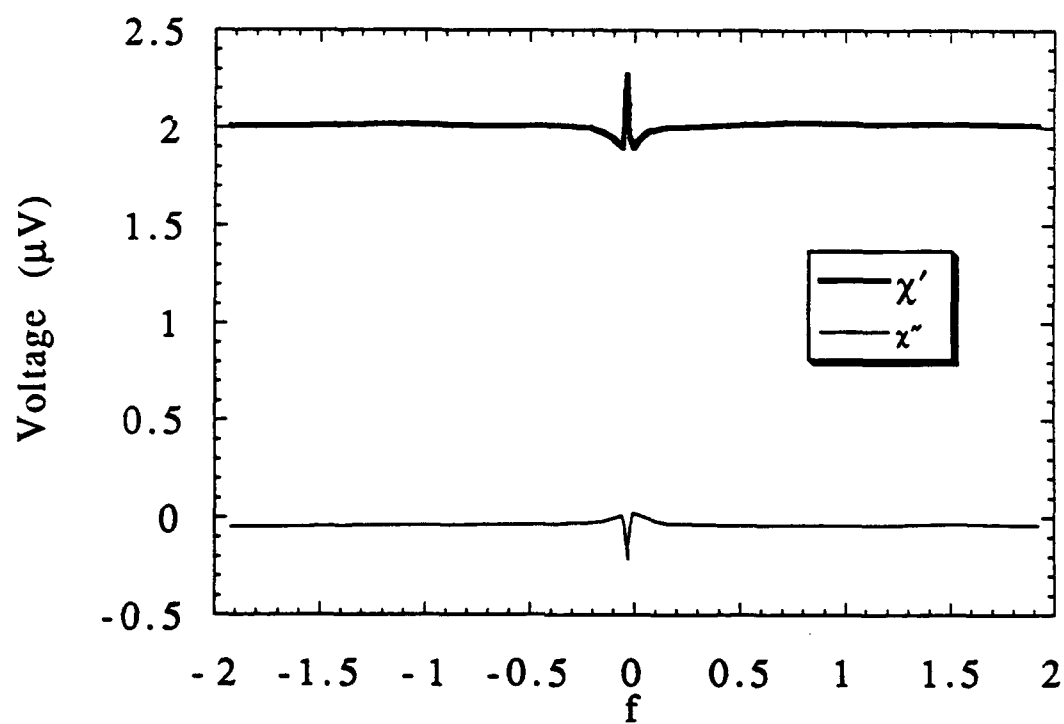


Fig. 8.16. Complex ac response of a 600 x 600 disordered array to a varying magnetic field. Only one peak, corresponding to $f=0$ is observed. The T_c of the array was 5.0 K and the data shown were taken at $T=4.75$ K. The frequency and excitation current used were 87.0 kHz and 0.5 μ A, respectively.

8.5 Summary

We have fabricated and measured both ordered and disordered arrays with long-range interaction using Nb filaments and an Al_2O_3 barrier. Our ac susceptibility measurements show a strong feature, corresponding to a transition to the macroscopically phase-coherent state, at $T \sim 4$ K. This feature is very much *field-sensitive* in ordered arrays, but, contrary to expectations, appears to be *field-insensitive* in disordered arrays. Our dc transport measurements reveal that these arrays have critical currents which are much *less* than the critical currents we expected from having N junctions in parallel in the array. In addition, they reveal that the arrays are *hysteretic* despite the fact that they consist of *non-hysteretic* junctions. Lastly, the dc measurements show that the arrays have voltage steps in their I - V curves. We discuss these results and their importance in the following chapter.

CHAPTER IX

DISCUSSION ON ARRAYS WITH LONG-RANGE INTERACTION

9.1 Introduction

Given our experimental results presented in Chapter VIII, it is evident that the properties of arrays with long-range interaction are not as straightforward as theoretical work had originally suggested [Vinokur et al., 1987 and Sohn et al., 1992b]. As was shown, the zero-field critical current, I_C , of the arrays is much less than the predicted value of Ni_C . [Again, this elementary prediction comes from the fact that there are N junctions in parallel which take current from the wire into which current is originally fed.] In addition, we observed our arrays undergoing the phase transition at $T_C \sim 4$ K, despite the fact the our i_C is ~ 100 times greater than that required to obtain that T_C from the theoretical model [Vinokur et al., 1987 and Sohn et al., 1992b]. Obviously, we must refine this theoretical model to account for these major discrepancies.

In this chapter,¹ we show that the electromagnetic inductance of an array wire is comparable to the Josephson inductance of the junctions. Consequently, there is a current-induced variation of the phase along any given wire in the array. We then discuss the many unusual dc properties our arrays have, including voltage steps in their I - V curves and hysteresis (despite the fact that they are composed of non-hysteretic junctions). Finally, we qualitatively explain our ac measurements.

¹Much of what is written in the chapter has been submitted for publication [Sohn et al., 1992c].

9.2 DC Measurements

Vinokur et al.'s (1987) and our [Sohn et al., 1992b] assumption was that the kinetic and electromagnetic inductance of the wires connecting adjacent junctions are negligible compared to the Josephson inductance ($\hbar/2eI_C$) of each junction in the array. Consequently, for any circulating current flowing through the array of weak Josephson junctions, the phase gradient along any wire in the array should arise *only* from the presence of an external magnetic field. The Hamiltonian describing this system is given by the sum of individual Josephson-junction energies,

$$H = -\text{Re } E_J \sum_{i=1}^N \sum_{j=1}^N \exp i(\varphi_i^h - \varphi_j^v - A_{ij}) \quad (9.2.1)$$

Here, again, φ_i^h is the superconducting phase at $x=0$ of the i^{th} horizontal wire, φ_j^v is the

phase at $y=0$ of the j^{th} vertical wire, and $A_{ij} = \frac{2\pi}{\Phi_0} \int_i^j \vec{A} \cdot d\vec{l}$ where $\vec{A} = Hx\hat{y}$ and Φ_0 is one

flux quantum. As will be shown below, this assumption—that the phase gradient along any wire in the array arises only from the the presence of a magnetic field—is incorrect when dealing with our experimental system.

9.2.1 Model for critical currents²

For the dc bias case, in which we are feeding current into one wire and out another of the same set (current-feed orientation A; see Fig. 8.6a), the action is dominated by the spreading of the current from the feed wire into $N \sim 1000$ cross wires. Since the current

²This model was developed by M. Tinkham (1992).

spreads so widely, thus causing much smaller phase gradients in the cross wires, we can get most of our results from only the phase along the current-fed wire, treating the cross wires as having the same zero phase. The phase difference between cross-wires n and $n+1$ along the current-fed wire in an array is $(2\pi I_n/\Phi_0)L_w$, where I_n is the current flowing through the wire at the n th junction site and L_w is the inductance (either kinetic or electromagnetic) of the wire segment in a cell defined by the cross wires, the current-fed wire and the wire parallel to it (see Fig. 9.1). In the simple case of a small number of extremely weak Josephson junctions in an array, I_n is small, because not much current is needed to reach the critical current of the junctions. Consequently, the phase gradient along the current-fed wire is small and $I_c \approx Ni_c$. However, in the case of a large number of stronger Josephson junctions, I_n can be quite large. This is because a huge current is needed to reach the critical current of all the junctions. As a result, the phase gradient along the current-fed wire can no longer be ignored. It is this current-induced phase shift along the wire which *limits* the effective number of junctions in parallel to some $N_{eff} < N$. This leads to $I_c = N_{eff}i_c$, and an explanation of why I_c is far less than we had expected.

We can estimate N_{eff} by ignoring the small phase gradients which result from the spreading of the current through the array everywhere except along the current-fed wire. From the above, we have,

$$\frac{d\phi_n}{dn} = \frac{2\pi I_n L_w}{\Phi_0} \quad (9.2.2)$$

Taking the derivative of Eq. (9.2.2), and noting that $dI_n/dn = I_c \sin \phi_n$ (if we can neglect the phase gradients in the cross wires) we obtain the Sine-Gordon Equation,

$$\frac{d^2 \phi_n}{dn^2} = \frac{1}{\lambda_n^2} \sin \phi_n \quad (9.2.3)$$

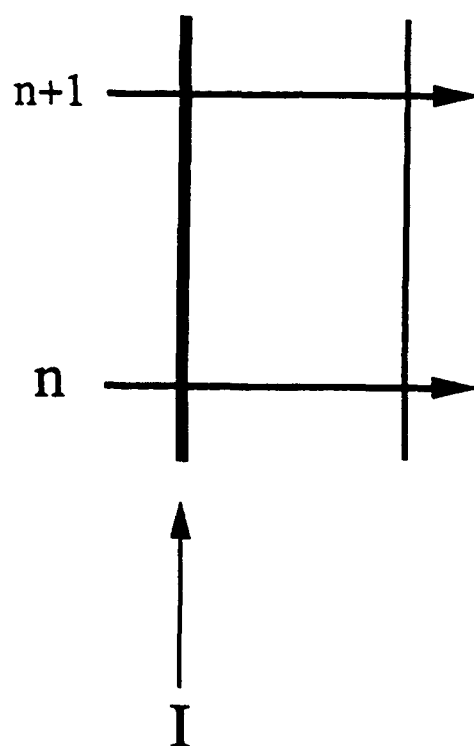


Fig. 9.1. Schematic drawing of a section of an array in which dc current is being fed into a wire.

where $(1/\lambda_n^2) = (2\pi L_w i_c / \Phi_0) \sim \beta_L$. Note that Eq. (9.2.3) has the same form as the familiar pendulum equation. For small phase differences, i.e. $I \ll I_c$, and $\varphi_n \ll 1$, we can linearize Eq. (9.2.3) to get

$$\frac{d^2 \varphi_n}{dn^2} = -\frac{\varphi_n}{\lambda_n^2} \quad (9.2.4)$$

This has the solution, $\varphi_n \sim e^{\pm n/\lambda_n}$. If $\lambda_n \ll N$, this implies that the current will leak off the current-fed wire before getting very far from the input. Then, if φ is the applied phase, we have $\varphi_n = \varphi e^{-n/\lambda_n}$ and total current

$$I = i_c \sum \sin \varphi_n \approx i_c \sum \varphi_n = i_c \varphi \lambda_n \quad (9.2.5)$$

The total phase difference, including the symmetric part of φ from the exit current wire, is $2\varphi = \varphi_{tot}$, so in the linear regime

$$\frac{dI}{d\varphi_{tot}} = \frac{1}{2} \lambda_n i_c \quad (9.2.6)$$

or

$$N_{eff} = \frac{\lambda_n}{2} = \frac{1}{2} \sqrt{\frac{\Phi_0}{2\pi L_w i_c}} \quad (9.2.7)$$

To find I_c of the array, we need to return to the nonlinear equation Eq. (9.2.3) since we want to consider the case where φ_n is no longer small. The maximum current corresponds to an applied $\varphi = \pi$ (not $\pi/2$). Drawing an analogy to a pendulum and the angular velocity it needs to move to an upward vertical position, we obtain for our system,

$$\left(\frac{d\varphi_n}{dn}\right)^2 \Big|_0 = \frac{2}{\lambda_n^2} (1 - \cos \varphi_{no}) \quad (9.2.9)$$

where φ_{no} is the initial phase. If we recall Eq. (9.2.2), $(d\varphi_n/dn) = (2\pi I_n L_w / \Phi_0)$, then it is easy to see that

$$I = \lambda_n i_c \sqrt{2(1 - \cos \varphi)} \quad (9.2.10)$$

For $\varphi_{tot} = 2\varphi$,

$$I(\varphi_{tot}) = \lambda_n i_c \sqrt{2\left(1 - \cos \frac{\varphi_{tot}}{2}\right)} \quad (9.2.11)$$

and

$$I_{\max} = I(2\pi) = 2\lambda_n i_c = 2\sqrt{\frac{\Phi_0 i_c}{2\pi L_w}} \quad (9.2.12)$$

As a check, if we let $\varphi_{tot} \ll 1$, Eq. (9.2.11) becomes Eq. (9.2.6). Note that by this criterion, $N_{eff} = 2\lambda_n$, as opposed to $(\lambda_n/2)$ found in Eq. (9.2.7).

To see how our calculation for I_c compares with our experimental data, we first calculate the total inductance, $L_w = L_{em} + L_{kin}$, of an array wire. We estimate the electromagnetic inductance, L_{em} , using the following

$$L_{em} \approx 2\ell \left[\ln \frac{4\ell}{p} + \frac{1}{2} + 0.1118 \frac{p}{\ell} \right] \times 10^{-7} \text{ H}$$

where ℓ is the length and p is the perimeter ($2d + 2w$, where d is the thickness and w is the width) of the given wire [Bleil, 1982, p. 5-29]. For our specific dimensions, $L_{em} \approx 2.2 \times 10^{-12}$ H. We estimate the kinetic inductance, L_{kin} , using the definition

$$L_{kin} = \mu_0 \lambda^2 \frac{\ell}{\sigma}$$

where λ is the penetration depth of Nb and σ is the cross sectional area of the wire [Kim, 1989]. For our wires, $L_{kin} \approx 2.1 \times 10^{-14}$ H. Since L_{em} greatly exceeds L_{kin} , $L_w \approx L_{em}$. We next insert L_w and the different measured i_c 's into Eq. (9.2.12). What we find is that the predicted I_c is a slight overestimate of our experimentally observed I_c . This overestimate may result from crudeness in the model, or it may be explained by a noting that in the parallel problem of H_{c1} in a long Josephson junction, the above solution actually describes a metastable state, with thermodynamic stability only up to a field $(2/\pi)$ times the corresponding value for H_{c1} [Tinkham, 1975, p. 201]. Applying that factor of $2/\pi$ here, we might expect to see "premature switching" becoming prominent at the lower value,

$$I_c = \frac{4}{\pi} \lambda_n i_c = \frac{4}{\pi} \sqrt{\frac{\Phi_0 i_c}{2\pi L_w}} \quad (9.2.13)$$

As shown in Fig. 9.2, the values for I_c obtained from Eq. (9.2.13) are in surprisingly good agreement with those observed from our arrays.

As stated earlier, the theoretical results obtained by Vinokur et al. (1987) and us [Sohn et al., 1992b], are for wires whose geometrical inductances are so small that, in zero field, there is no phase gradient along them. What we have just shown is that the electromagnetic inductance (10^{-12} H) is *not* completely negligible compared to the Josephson inductance ($\sim 10^{-9}$ H) of the junctions in the array. Consequently, to be realistic, a finite ratio of these two inductances *must* be included as an additional parameter

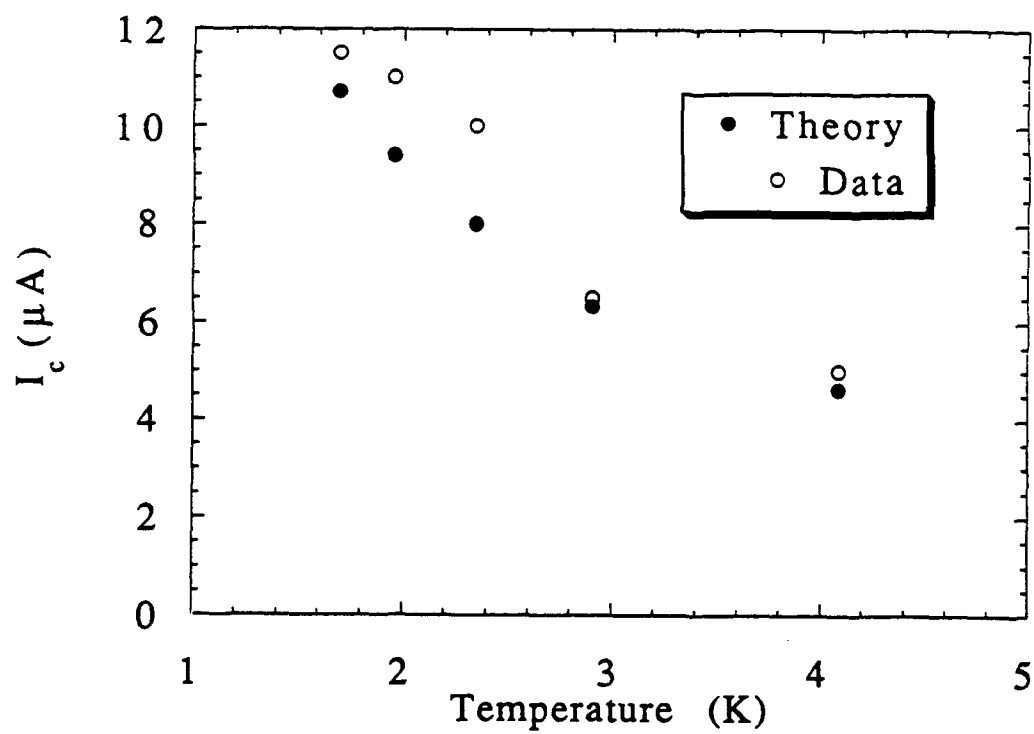


Fig. 9.2. Comparison between obtained data and our calculation of the critical current, I_c , of an array.

for the variation of the phase along a wire. Such an inclusion leads to a Sine-Gordon equation [Eq. (9.2.3)] that has a characteristic dimensionless length scale, λ_n , given by the square root of the inductance ratio. For our arrays, $\lambda_n \sim 46$ at T_C (where $i_C \sim 0.08 \mu\text{A}$) and ~ 20 at $T=1.7 \text{ K}$ (where $i_C \sim 0.45 \mu\text{A}$). Consequently, the effective number of junctions, N_{eff} , coupled to the current-fed wire, is not 1000; rather, it is [using Eq. (9.2.13)] $I_C/i_C = 4\lambda_n/\pi \sim 59$ at T_C and ~ 25 at $T=1.7 \text{ K}$. Our analytical result, that $N_{eff} = I_C/i_C = 4\lambda_n/\pi$, is further supported by the fact that the resistance of the first step, R_I , in Fig. 8.11a measured at 1.7 K corresponds to approximately 25 junctions—each with $r_n \sim 670 \Omega$ —in parallel.

The behavior of the array in the dc bias case in which current is injected into one wire of one set and extracted from a wire of the other set (current-feed configuration B) is much more complicated than the case we have just discussed. Suffice it to say, however, that the number of junctions in parallel which contribute to the critical current, I_C , of the array is also some effective number, $N'_{eff} \ll N$, where $N'_{eff} \neq N_{eff}$. As indicated in the inset of Fig. 8.11b, $I_C \sim 5 \mu\text{A}$ and $R_I \sim 71 \Omega$. These values correspond to approximately 11 junctions in parallel. This number for N'_{eff} can be related to the data we obtained by measuring I_C vs. field (see Fig. 8.12). As we have already noted, one period of oscillation in this figure corresponds to an area of $400 \mu\text{m}^2$ or an 11 unit cell x 1 unit cell "block." Thus, there is a reasonable degree of internal consistency in all of our dc measurements.

9.2.2 Voltage steps

The steps in the array I - V curves are thought to be a result of the unique geometry of the arrays. For the case of dc bias current being fed into one wire and out another of the same set (current-feed orientation A), the current mostly flows along the primary current-fed wire until the critical current, $I_C = 4i_C\lambda_n/\pi$, of N_{eff} parallel junctions is reached and they switch into the resistive state. The current then mostly spreads along the cross (with

respect to the primary current-fed wire) wires until at the critical current corresponding to the second step in the I - V curve, a second set of parallel junctions (which are in series with the N_{eff} normal junctions) is reached. [This second set could be those at the other feed wire.] The fact that the normal state resistance, R_N , of the array is larger than R_J , supports the idea the the second set of junctions are in series, and not in parallel, with the first set.

For the dc bias case where current is fed in orientation B , the current flows in a more complicated manner, since there are many more paths, corresponding to many different sets of parallel junctions, in which the current can flow. Therefore, it is not surprising that the resulting I - V curve has many more steps than those of current-feed orientation A .

Contrast the step behavior of our arrays to that of conventional arrays. Both van der Zant et al. (1988) and Tighe et al. (1991) report that the I - V curves of underdamped conventional arrays display steps in the I - V curves which correspond to the simultaneous switching of a single row of junctions across the width of the array into the resistive state. In their case, there are as many steps as there are rows in the array. In our case, there are as many steps as there are wires in the array through which the dc current can flow. As the temperature is lowered, the number of voltage steps increases. We attribute this to a breakdown in the array wires due to large currents flowing through them and to self-field effects that are created by these currents. The non-uniform step widths is most likely due to nonuniformities in the array.

9.2.3 Hysteresis

We attribute the curiously hysteretic behavior of the arrays to a collective phenomena occurring the array which we can only qualitatively explain. The initial condition of the array largely determines the paths along which the current flows in the array. When we begin to sweep the current up, the array is in a *static* state. When the we

begin to sweep the current down, the array is in a *dynamic* state. Since the two initial conditions are very different, this leads to the current flowing in different paths, thus producing hysteresis.

9.3 AC Measurements

The results of our ac measurements of T_C are the least well understood. We measure transition temperatures ranging from 3-5 K in both our ordered and disordered arrays. As stated earlier, the single junction critical current, $i_C(T_C)=0.08 \mu\text{A}$, we have measured is ~ 100 times larger than that required for Vinokur et al.'s analysis (1987) or our mean field approximation [Sohn et al., 1992b], i.e. $T_C=NE_J/2k_B$, to fit the T_C data. If the phase transition we measured in one of our arrays is indeed of the sort which is predicted, it would suggest that the array has effectively broken up into sets of smaller independent arrays, each of size $N'' \ll N$ (~ 1000). We note that $N'' \neq N_{eff}$ since our N_{eff} calculation is valid only for our dc measurements. For our arrays in zero field, N'' corresponds to ~ 4 . When a field is present, $N'' \sim 4$ for the ordered arrays, but ~ 22 for the disordered arrays (taking the \sqrt{N} dependence into account). This point of view—that the arrays act as if broken up into much smaller arrays—is supported by the fact that we have fabricated a sample which consists of four closely positioned 10×10 arrays whose individual elements each consist of 10×10 ordered long-range interaction arrays. This “array,” whose i_C , (measured from a single junction) is approximately $7 \mu\text{A}$, also exhibited a transition at $T_C \sim 4$ K, despite the fact that the arrays are physically 100 times smaller than the arrays we presented in this paper. Why our arrays, in zero field act like many smaller arrays may possibly be due to two different things. First, nonconstant stray fields, if sufficiently large, can affect the arrays by introducing phase gradients along the wires and forcing the disordered arrays into their high field, constant T_C , regime. Evidence that a stray field may have affected the ordered arrays can be found in Fig. 8.14, where we see that the measured

$T_c(f)/T_c(0)$ is much larger than that predicted by mean field theory [Sohn et al., 1992b]. A stray field could have depressed $T_c(0)$, thus making $T_c(f)/T_c(0)$ much larger than expected. Second, the fact that the electromagnetic inductance is no negligible compared to the Josephson inductance in the arrays may also contribute to the breaking up of the arrays. This is certainly a subject for future investigation.

When the ordered arrays are placed under a varying magnetic field, we see that they, like conventional arrays, display commensurability with certain fields. This means that the array wires have phase-gradients, caused by the magnetic fields, which leads to small circulating current loops. We have already shown in Chapter VI, that these circulating loops in a field, $f=p/q$, resemble those found in conventional arrays under the same field strength. The disordered arrays do not show any commensurability with any fields because, as stated previously, the cell size in the array varies too much for any field to be commensurate with the array lattice.

9.4 Summary

Thus, we see that the unique geometry of arrays with long-range interaction leads to the arrays having properties which are quite different from those of conventional arrays. As we have shown in this chapter, the wires in the arrays must be treated as "imperfect," i.e. there is a current-induced variation of the phase along any given wire in the array. This phase gradient is due to the fact that the geometrical inductance is *not* negligible compare to the Josephson inductance of the junctions. The ratio of these two inductances leads to a characteristic dimensionless length scale, λ_n , which consequently determines the effective size of the array at least in the dc bias case.

CHAPTER X

SUMMARY AND SUGGESTIONS FOR FUTURE RESEARCH

10.1 Summary

In part A of this thesis, we have seen the importance of current direction on the dynamical properties of proximity-effect Josephson-junction arrays. When the Lorentz force, created by the macroscopic transport current, directs the field-induced vortices of an array toward the high energy barrier of the island sites, *only* integer giant Shapiro steps are produced by the array. The reason for this is that the vortices cannot go through the islands, and thus no motion of the vortex superlattice, which would lead to fractional giant Shapiro steps, can occur. The Lorentz force in both the $[11]$ -oriented square- and $[2\bar{1}\bar{1}]$ -oriented triangular-lattice arrays we studied directs the vortices toward the islands, and indeed, these arrays produced only integer giant Shapiro steps. If, however, the Lorentz force directs the vortices toward any other direction, motion of the vortex superlattice can occur, and thus *both* integer giant and fractional giant Shapiro steps are produced. In our experiments, the bias current of the $[10]$ -oriented and 15° square- and $[10\bar{1}]$ -oriented triangular-lattice arrays produced such a force—these arrays produced integer and fractional giant Shapiro steps.

The moving vortex model we presented in part A provides a phenomenological explanation of why fractional giant Shapiro steps can or cannot occur in the various types of arrays studied. In addition to this model, we have also presented what we call the pendulum model. This particular model gives a detailed description of how the gauge-invariant phase differences of the individual junctions in an array evolve per rf cycle. What we have seen in this context is that the evolution of the phase differences are *constrained* by Kirchhoff's voltage law such that for the $[11]$ -oriented square- and $[2\bar{1}\bar{1}]$ -oriented

triangular-lattice cases, the only periodic solution allowed is one which corresponds to integer giant Shapiro steps. The perpendicular junctions in the [10]-oriented square- and $[10\bar{1}]$ -oriented triangular-lattice arrays, however, permit the phase differences of the other junctions in the array to evolve more freely per rf cycle. As a result, the allowed periodic solutions for these arrays correspond to both fractional and integer giant Shapiro steps.

In part B, we theoretically and experimentally investigated a system of ordered and disordered Josephson junction arrays with long-range interaction. Using Monte Carlo simulations and a mean field analysis, we showed that, in zero field, these novel arrays undergo a phase transition to a macroscopically phase-coherent state at a temperature, $T_C = NE_J/2k_B$. When a magnetic field, corresponding to a strongly commensurate number of flux quanta per unit cell, $f = p/q$, is introduced to the system, we find that $T_C = NE_J/2k_B \sqrt{q}$ in the ordered array case. In contrast, we find that the T_C for the disordered array case is defined for four regions of f . When $f < \frac{1}{N^2}$, T_C approximates the zero-field value. When

$\frac{1}{N^2} \leq f < \frac{1}{N}$, $T_C = \frac{E_J}{2k_B \sqrt{f}}$. However, when $\frac{1}{N} \leq f \leq 1$, T_C rises as a function of f

although the exact form is presently unknown. Finally, when $f \gg 1$, T_C asymptotically approaches $\sim 0.75 E_J \sqrt{N}/k_B$. We note that this asymptote is $\sim 50\%$ higher than the $E_J \sqrt{N}/2k_B$ asymptote predicted by Vinokur et al. (1987). As we stated in Chapter VII, the origin of this difference has not been identified.

Experimentally, we have shown that both the ordered and disordered arrays are extremely complicated compared to conventional Josephson-junction arrays. Through dc transport measurements, we have shown that the wires in the arrays must be treated as "imperfect", i.e. there is a variation of the phase along any given wire in the array if it carries current. This variation is due to the fact the electromagnetic inductance is *not* completely negligible compared to the Josephson inductance of the junctions. The ratio of these two inductances leads to a characteristic dimensionless length scale, λ_N , which

consequently determines the effective size of the array, N_{eff} . We have suggested that the voltage steps in the array I - V curves are due to currents flowing along different wires in the arrays. The hysteretic behavior of the arrays, despite the fact that they each consist of non-hysteretic junctions, appears to be due to a collective phenomenon.

Our ac measurements of arrays with long-range interaction show that the arrays do undergo a transition to a macroscopically phase-coherent state. The temperature at which this occurs suggests that the arrays act as if they were broken up into smaller sets of independent arrays. We say this because the single junction critical current, $i_c(T_c) \sim 0.1 \mu A$, we have measured is ~ 100 times larger than that required to account for the observed T_c , if indeed $T_c = NE_J/2k_B$, with $N \sim 1000$. Why the arrays in zero field would effectively break up into many smaller arrays is unknown, although it may possibly be the result of a stray field or the electromagnetic inductance being comparable to the Josephson inductance in the arrays, consequently leading to a phase-gradient along the wires induced by thermal noise currents.

10.2 Future Research

As we have stated in Chapter V, the exact relationship between decreasing fractional giant Shapiro stepwidth and angle of current injection is presently unknown. Since it is very difficult to directly measure stepwidths due to thermal fluctuations, noise, and inhomogeneities in the array, it might be more promising to simulate the differently-oriented rf current-biased arrays. By doing so, one could quantify the widths of the steps produced by these arrays and thereby determine exactly what function of θ , where θ is the angle off of the $[10]$ orientation, the stepwidths are.

The possibility of spatial period doubling in rf current-biased SNS Josephson junctions is truly an exciting prospect. As stated in part A of this thesis, such period doubling has not been seen in these types of arrays, and it certainly would be very difficult

to experimentally prove its existence since our present means of measuring the arrays is based on the temporal and not spatial periodicity of the arrays. However, as we had attempted to do, one could pursue this matter using computer simulations.

It is obvious that more work needs to be done to further understand arrays with long-range interaction; such work, however, has been beyond the scope of this thesis. As we have stated in Chapter IX and reiterated in our summary, our experimental evidence seems to indicate that the arrays effectively break up into smaller arrays, and it is the T_C of these smaller arrays that we are measuring. Fabricating and measuring different-sized arrays can directly test whether ours is a correct interpretation. Unfortunately, this is a rather involved project since better and more controlled techniques, other than the ones we used and outlined in this thesis, for fabricating small critical-current Nb-Al₂O₃-Nb tunnel junctions are needed. The question of why the disordered arrays, despite all predictions from theory [Vinokur et al., 1987 and Sohn et al., 1992b], never showed a field-dependent T_C is intriguing. As we have stated, a possible stray field down at the array may be an answer to this difficult question. Certainly, this is an important issue to be resolved.

In addition, our analytical model which predicts I_C and N_{eff} in our arrays is incomplete since: (1) it is valid only when the array is static—it does not describe the array when it is in the dissipative state and (2) the two ways of deriving N_{eff} , one directly using $dI/d\phi_n$ and the other using I_C/i_C , produce different results, the former a factor of four smaller than the latter. A variety of dynamical simulations could be performed to help strengthen and complete this model. In addition, these simulations could help us better understand the array voltage steps and hysteresis.

Finally, we note that since arrays with long-range interaction are so different from conventional Josephson-junction arrays, it would be extremely interesting to investigate their dynamical properties. By doing so, we should be able to obtain a better understanding of their collective effects, and for that matter, their properties as a whole.

REFERENCES

- Abraham, David W., unpublished doctoral thesis, Harvard University (1983).
- Ambegaokar, V., and A. Baratoff, *Phys. Rev. Lett.* **11**, 104 (1963).
- Barone, A., and G. Paterno, *Physics and Applications of the Josephson Effect* (Wiley and Sons, New York, 1982).
- Basavaiah, S., and J. H. Greiner, *J. Appl. Phys.* **47**, 4201 (1976).
- Benz, S. P., unpublished doctoral thesis, Harvard University (1990).
- Benz, S. P., M. S. Rzchowski, M. Tinkham, and C. J. Lobb, *Phys. Rev. Lett.* **64**, 693 (1990).
- Binder, K., *Monte Carlo Methods in Statistical Physics*, ed. by K. Binder (Springer-Verlag, New York, 1986), p. 1.
- Bleil, D. F., *American Institute of Physics Handbook*, ed. by D. E. Gray (McGraw-Hill, New York, 1982), p. 5-29.
- Brown, R. K., and J. C. Garland, *Phys. Rev. B* **33**, 7827 (1986).
- Chung, J. C., K. H. Lee, and D. Stroud, *Phys. Rev. B* **40**, 6570 (1989).
- Clark, T. D., *Phys. Rev. B* **8**, 137 (1973).
- De Gennes, P. G., *Rev. Mod. Phys.* **36**, 225 (1964).
- Ebner, C., and D. Stroud, *Phys. Rev. B* **25**, 5711 (1982).
- Eikmans, H., J. E. van Himbergen, 1991 (unpublished).
- Fernandez, J. F., M. F. Ferreira, and J. Stankiewicz, *Phys. Rev. B* **34**, 292 (1986).
- Forrester, M. G., unpublished doctoral thesis, Harvard University (1988).
- Free, J. U., S. P. Benz, M. S. Rzchowski, M. Tinkham, C. J. Lobb, and M. Octavio, *Phys. Rev. B* **41**, 7267 (1990).
- Fulton, T., and L. N. Dunkleberger, *Phys. Rev. B* **9**, 4760 (1974).
- Gollub, J. P., and H. L. Swinney, *Phys. Rev. Lett.* **35**, 927 (1975).
- Hadley, P., unpublished doctoral thesis, Stanford University (1989).
- Halsey, T. C., *Phys. Rev. B* **41**, 11634 (1990).
- Halsey, T. C., private communication (1991).
- Holden, Arun V., *Chaos* (Princeton University Press, New Jersey, 1986), p. 113.

- Huggins, H. A., and M. Gurvitch, *J. Appl. Phys.* **57**, 2103 (1985).
- Jeanneret, B., J. L. Gavilano, G. A. Racine, Ch. Leemann, and P. Martinoli, *Appl. Phys. Lett.* **55**, 2336 (1989).
- Johnson, A. T., unpublished doctoral thesis, Harvard University (1990).
- José, J., and D. Dominguéz, private communication (1992).
- Josephson, B. D., *Phys. Lett.* **1**, 251 (1962).
- Kadin, A. M., K. Epstein, and A. M. Goldman, *Phys. Rev. B* **27**, 6691 (1983).
- Kang, J. H., private communication (1991).
- Kautz, R. L., and R. Monaco, *J. Appl. Phys.* **57**, 875 (1985).
- Kim, D. H., unpublished doctoral thesis, University of Minnesota (1989).
- Kosterlitz, J. M., and D. J. Thouless, *J. Phys. C* **6**, 1181 (1973).
- Laibowitz, R. B., and J. J. Cuomo, *J. Appl. Phys.* **41**, 2749 (1970).
- Lee, H. C., D. B. Mast, R. S. Newrock, L. Bortner, K. Brown, F. P. Esposito, D. C. Harris, and J. C. Garland, *Physica B* **165 & 166**, 1571 (1990).
- Lee, H. C., R. S. Newrock, D. B. Mast, S. E. Hebboul, J. C. Garland, and C. J. Lobb, *Phys. Rev. B* **44**, 921 (1991).
- Lee, K. H., D. Stroud, and J. S. Chung, *Phys. Rev. Lett.* **64**, 962 (1990).
- Lee, K. H., and D. Stroud, *Phys. Rev. B* **43**, 5280 (1991).
- Leeman, Ch. , Ph. Lerch, and P. Martinoli, *Physica* **126B**, 475 (1984).
- Lobb, C. J., *Physica* **126B**, 319 (1984).
- Lobb, C. J., David W. Abraham, and M. Tinkham, *Phys. Rev. B* **27**, 150 (1983).
- Lorenz, E. N., *J. Atmos. Sci.* **20**, 130 (1963).
- Martinis, John M., and R. H. Ono, *Appl. Phys. Lett.* **57**, 629 (1990).
- Martinoli, P., Ph. Lerch, Ch. Leeman, H. Beck, *Proceedings of the 18th Int. Conf. on Low Temperature Physics, Kyoto, 1999* (1987).
- McCumber, D. E., *J. Appl. Phys.* **39**, 3113 (1968).
- Metropolis, N., A. W. Rosenbluth, M. N. Rosenbluth, A. H. Teller, and E. Teller, *J. Chem. Phys.* **21**, 1087 (1953).
- Mooij, J. E., in *NATO Advanced Study Institute on Advances in Superconductivity*, ed. by B. Deaver and J. Ruvalds (Plenum, New York, 1983a), p. 433.

- Mooij, J. E., in *Percolation, Localization, and Superconductivity*, ed. by A. M. Goldman and S. A. Wolf (Plenum, New York, 1983b), p. 325.
- Morohashi, Shin'ichi, Fugitoshi Shinoki, Akira Shoji, Masahiro Aoyagi, and Hisao Hayakawa, *Appl. Phys. Lett.* **46**, 1179 (1985).
- Nelson, David R., and J. M. Kosterlitz, *Phys. Rev. Lett.* **39**, 1201 (1977).
- Nelson, David R., private communication (1991).
- Newrock, R. S., private communication (1991).
- Nordman, J. E., and L. L. Houck, in *Future Trends in Superconductive Electronics*, ed. by B. S. Deaver, C. M. Falco, J. H. Harris, and S. A. Wolf (American Institute of Physics, New York, 1978), p. 354.
- Octavio, M., *Phys. Rev. B* **29**, 1231 (1984).
- Octavio, M., and L. E. Guerrero, *Phys. Rev. A* **42**, 4630 (1990).
- Octavio, M., J. U. Free, S. P. Benz, R. S. Newrock, D. B. Mast, and C. J. Lobb, *Phys. Rev. B* **44**, 4601 (1991).
- Pannetier, B., J. Chaussy, and R. Rammal, *J. Phys. (Paris), Lett.* **44**, L853 (1983).
- Pannetier, B., J. Chaussy, R. Rammal, J. C. Villegier, *Phys. Rev. Lett.* **53**, 1845 (1984).
- Paterno, G., P. Rissman, and R. Vaglio, *J. Appl. Phys.* **46**, 1419 (1975).
- Reif, F., *Fundamentals of Statistical and Thermal Physics* (McGraw Hill, New York, 1965).
- Renne, M. J., and D. Polder, *Rev. Phys. Appl.* **9**, 25 (1974).
- Russer, P. J., *J. Appl. Phys.* **43**, 2008 (1972).
- Rzchowski, M. S., S. P. Benz, M. Tinkham, and C. J. Lobb, *Phys. Rev. B* **42**, 2041 (1990).
- Rzchowski, M. S., L. L. Sohn, and M. Tinkham, *Phys. Rev. B* **43**, 8682 (1991).
- Rzchowski, M. S., and L. L. Sohn, 1991 (unpublished).
- Schwidtal, K., *J. Appl. Phys.* **43**, 202 (1972).
- Shapiro, S., *Phys. Rev. Lett.* **11**, 80 (1963).
- Shih, W. Y., and D. Stroud, *Phys. Rev. B* **28**, 6575 (1983).
- Shih, W. Y., and D. Stroud, *Phys. Rev. B* **30**, 6774 (1984).
- Shih, W. Y., and D. Stroud, *Phys. Rev. B* **32**, 158 (1985).

APPENDIX I

FABRICATION OF SNS NIOBIUM-COPPER-NIOBIUM ARRAYS

1. Ultrasonic clean 1" x 1" x 0.25" polished sapphire substrates with Trichloroethylene (TCE), Acetone (ACE), and Methanol (MeOH), 10 min each.

2. Photoresist-Aluminum-Photoresist trilayer

- a) Spin Shipley 1400-27 photoresist @4000 rpm for 30 s
- b) Bake for 30 min. @ 100°C
- c) Blanket expose entire substrate for 15 s in Karl Suss Mask Aligner, using soft contact mode
- d) Evaporate 500 Å of low purity aluminum (Al) in alumina boat, $P_b < 1 \times 10^{-6}$ Torr
- e) Spin Shipley 1400-27 photoresist @4400 rpm for 30 s
- f) Bake for 30 min @ 80-90°C

Note: If the trilayer procedure is not done step after step, the photoresist will absorb H₂O and wrinkle the Al layer. Consequently, the substrate will have a very "cloudy" look. This is ok.

- g) Expose bilayer mask for 4 s in Karl Suss (hard contact mode)
- h) Develop fully (~1 min) in 5:1 H₂O:Microposit 351 Developer. Rinse thoroughly and blow dry with dry N₂.
- i) Expose voltage pad mask for 4 s in Karl Suss (hard contact mode)
- j) Develop fully (~1 min), using fresh developer. [It is very important to use fresh developer every time, since the developer weakens considerably after initial use. Failure to do so will lead to bad metal-substrate adherence.] Rinse thoroughly and blow dry.
- k) Etch Al until completely gone (~2 min). Rinse thoroughly and blow dry.
- l) Form undercut using fresh developer (~30 s). Rinse and blow dry.
- m) Back-etch Al in undercut (~2 min), rinse and blow dry.

- Sohn, L. L., M. S. Rzchowski, J. U. Free, S. P. Benz, M. Tinkham, and C. J. Lobb, Phys. Rev. B **44**, 925 (1991).
- Sohn, L. L., and R. J. Fitzgerald, 1991 (unpublished).
- Sohn, L. L., M. S. Rzchowski, J. U. Free, M. Tinkham, and C. J. Lobb, Phys. Rev. B **45**, 3003 (1992)a.
- Sohn, L. L., M. S. Rzchowski, J. U. Free, and M. Tinkham, submitted to Phys. Rev. B (1992)b.
- Sohn, L. L., M. T. Tuominen, M. S. Rzchowski, J. U. Free, and M. Tinkham, submitted to Phys. Rev. B (1992)c.
- Stewart, W. C., Appl. Phys. Lett. **10**, 277 (1968).
- Teitel, S., and C. Jayaprakash, Phys. Rev. B **27**, 598 (1983)a.
- Teitel, S., and C. Jayaprakash, Phys. Rev. Lett. **51**, 1999 (1983)b.
- Thouless, D. J., P. W. Anderson, and R. G. Palmer, Phil. Mag. **35**, 593 (1977).
- Tighe, T. S., A. T. Johnson, and M. Tinkham, Phys. Rev. B **44**, 10286 (1991).
- Tinkham, M., *Introduction to Superconductivity* (McGraw-Hill, New York, 1975; reprinted by Krieger, Florida, 1980).
- Tinkham, M., *Josephson Effect and Macroscopic Quantum Phenomena*, 1991 (unpublished).
- Tobochnik, Jan, and G. V. Chester, Phys. Rev. B **20**, 3761 (1979).
- van der Zant, H. S. J., C. J. Muller, L. J. Geerligs, C. J. P. M. Harmans, and J. E. Mooij, Phys. Rev. B **38**, 5154 (1988).
- van der Zant, H. S. J., unpublished doctoral thesis, Delft University of Technology (1991).
- van der Zant, H. S. J., H. A. Rijken, and J. E. Mooij, J. Low Temp. Phys. **79**, 289 (1990).
- Van Duzer, T., and C. W. Turner, *Principles of Superconductive Devices and Circuits* (Elsevier North Holland, New York, 1981).
- Vinokur, V. M., L. B. Ioffe, A. I. Larkin, and M. V. Feigel'man, Sov. Phys. JETP **66**, 198 (1987).

3. Copper Evaporation

- a) Mount sample on evaporator sample block and install, using insulating teflon sheet and screws. [Always a good idea to clean teflon sheet before installing sample block. Use scotch-brite and rinse with either MeOH or EtOH. Towel dry.] Connect wire from sample block to high-voltage feedthrough for application of rf. Check continuity and grounding.
- b) Place high purity (99.999%) **copper** in large tungsten or molybdenum boat and mount in evaporator using the electrodes for copper.
- c) Pump chamber to $P_b < 2 \times 10^{-7}$ Torr (degas on).

Rf clean substrate:

- turn ion gauge off, $P_b < 1 \times 10^{-7}$ Torr
- adjust Ar pressure in chamber to 15 mTorr (100 mTorr foreline pressure)
- attach rf matchbox
- open shutter
- set forward power on rf supply to 12 W and tune loading inductor to minimize reflected power until it reads 0-1 W. The dc self-bias voltage on rf matchbox meter should read ~100 V. [Meter on matchbox is fairly unreliable. Place trust on the rf power supply reading.] Rf clean for 5-6 min and close shutter.

- d) Shut off Ar flow and pump chamber again to $P_b < 2 \times 10^{-7}$ Torr (degas on).

Evaporate:

- turn on thickness monitor and set density $\rho = 8.96 \text{ gm/cm}^3$.
- slowly increase current. Cu should melt ~8 Amps, if new. If previously melted, will melt 8-9.5 Amps.
- boil off impurities for > 2 min (>300 Å total)
- open shutter and zero thickness monitor simultaneously
- increase current up to 13.5 Amps. [Important not to go above 15 Amps as substrate will overheat, leading to burnt photoresist and Cu peeling.]
- evaporate ~3500 Å copper and immediately turn off power supply.
- cool down sample before opening up chamber. [Do not close the shutter while cooling. If shutter is closed, heat cannot escape and sample will overheat, leading to the Cu film peeling back.]

4. Nb sputtering

- a) Cover Al magnetron target with Aluminum foil. Using dry N₂, blow away any particulates that may have fallen onto the Nb target.
- b) Mount substrate using stainless steel substrate clamp with 1" square holder, making sure that the shield and substrate holder are not electrically shorted.

- c) Mount 1 5/8" diameter dark space shield. This should be ~0.25" from substrate and again, make sure shield and substrate holder are not electrically shorted.
- d) Pump chamber to $P_b < 1.5 \times 10^{-7}$ Torr (degas on). This usually takes 4-5 hrs.
- e) Once chamber has reach appropriate pressure, start Meissner shroud. Chamber pressure should go down to $P_b < 9 \times 10^{-8}$ Torr. Turn off ion gauge.
- f) Cooling water should be flowing through sample holder and appropriate magnetrons
- g) Rotate substrate above Al target position
- h) Start Ar flow (35 sccm), and adjust gate valve until chamber pressure reads ~6mTorr.
- i) Tune matchbox so that rf power source reads 23 W forward power and 0-1 W reflected power. If plasma does not ignite, close diffusion "pump" flap so that chamber pressure increases to 25-29 mTorr. Plasma should ignite at this pressure and have a dc self-bias voltage of 600 V; open flap and return chamber pressure to 6 mTorr. Turn off rf source.
- j) Increase rheostat until voltage reads 300 V. At this point, plasma should ignite. If it does not, close the flap until it does. Once ignited, open flap and increase voltage to 500 V; 150 mA.
- k) dc clean target for total of 15 min. After an initial 8 min, begin rf Ar ion etching substrate over Al target on and off at 1 min intervals for a total of 4 min. At 15 min mark, turn off rf power, and immediately rotate substrate niobium target, and put it to ground. This should all be done within 5 s. [Greater than 5 s will lead to a poor Cu-Nb interface and subsequently low Kosterlitz-Thouless transition temperatures.]
- l) Sputter Nb onto substrate for 10 min (200 Å/min).
- m) Let substrate warm up (5-6 hrs) before opening chamber.

5. Lift off in ACE, 10-30 min.

- Ultrasonic substrate 1 min in fresh ACE, 2 min. in MeOH
- Blow dry

6. Clean masks

Rinse masks with propylene glycol monomethyl ether acetate (PGMEA) and MEOH and blow dry. [Best to lightly wipe the chrome surface of masks with a PGMEA-soaked cloth first before rinsing. This wipes away any "large" and stubborn photoresist particulates sticking to the surface of the mask.]

7. Inverting photoresist

a) Spin **Hoechst AZ-5214E** photoresist @ <4000 rpm for 30 s (1.4 μm). [Shipley 1400 series photoresist is incompatible with Hoechst AZ photoresist. The solvent for the AZ resist is PGMEA, not ACE. AZ resist is also a noninverting resist, just skip inverting steps.]

b) Bake for 30 min @ 90°C

c) Expose array mask for 4 s in Karl Suss (hard contact mode). [Vacuum pressure mode in Karl Suss should be > 8 barr. If not, check for leaks as anything less than 8 barr will lead to unusually rounded islands and shorts.]

d) Inverting step:

- bake sapphire substrate in oven for 4 min @ 120°C
- blanket expose for 90 s in Karl Suss (soft contact mode)]
- develop 75 s with **Hoechst AZ-422 MIF** for inverting process (noninverting pr-3 min)
- rinse very thoroughly (+5 min) and blow dry.

8. Reactive ion etch

a) Turn on cooling water between sample holder and cathode

b) Pretune matchbox so that rf supply reads **44 W** forward power and **0-1 W** reflected power. Matchbox self-bias voltage should be ~ **30 V**.

c) After pumping and venting (with dry N_2) 3 times, vent chamber final time and mount sample using Si spacer between clips and substrates.

d) Pump chamber < 100 mTorr and vent 3 times

e) Set flow rate of SF_6 to 13 sccm (~250 mTorr chamber pressure). Flush chamber for 15 min.

f) RIE for 4-5 min (Nb etch rate ~750 $\text{\AA}/\text{min}$). [Don't worry if newly exposed Cu surface starts to darken. There is an additional chemical reaction between the plasma and the photoresist/pump oil going on in the chamber. The by-products of this reaction adhere to the Cu surface. This does not affect the properties of the array. The colder the cooling water and the better the pumping minimizes this effect, as well as minimizing the "cinnamon" odor that follows when opening up the chamber.]

g) Turn off rf and SF_6 gas flow

h) Vent and pump with dry N_2 three times and then vent to atmosphere.

i) Remove sample

9. Strip photoresist

- a) Soak substrate in heated Hoechst AZ-300T photoresist stripper (70-80°C, low setting)
- b) Strip for 25-30 min and then ultrasonic clean 1-2 min.
- c) Rinse with H₂O and blow dry.

- g) Rotate substrate above Al target position
- h) Start Ar flow (35 sccm) and adjust gate valve until chamber pressure reads ~6 mTorr.
- i) Tune matchbox so that rf power source reads 8 W forwards power and 0-1 W reflected power. The dc self-bias voltage should be 250 V. Turn off rf source.
- j) Start dc cleaning of niobium target (500 V; 150mA) for 15 min. At the 15 min mark, start rf cleaning of the the substrate.
- k) After 5 minutes, immediately turn off rf power, rotate substrate niobium target, and put it to ground.
- l) Sputter Nb onto substrate for 10 min (200 Å/min).
- m) Let substrate warm up (5-6 hrs) before opening chamber.

4. Liftoff in ACE, 30-40 min

- Ultrasonic substrate 20 min in fresh ACE, 5 min each in TCE, ACE, and MeOH
- Blow dry

5. Follow step 2 for repatterning

6). Al₂O₃-Nb deposition

- a) Again mount substrate in sputtering chamber and pump system down as outlined in 3a-d.
- b) Rotate substrate above Nb target
- c) Once chamber has reached appropriate pressure, start Ar flow (35 sccm, and adjust gate valve until chamber pressure reads ~6 mTorr. Tune matchbox so that rf power source reads 23 W forward power and 0-1 W reflected power. The dc self-bias voltage should be 600 V. Turn off rf source.
- d) dc clean Al target 6 min (500 V, 85 mA). At the 6 min mark, begin rf Ar ion etching substrate over Nb target on and off at 1 min intervals for a total of 5 min. At the 15 min mark, turn off rf power, immediately rotate substrate over Al target and put it to ground.
- e) Sputter Al onto substrate for 15 s (104 Å/min).
- f) Reduce Ar flow to zero and pump chamber out. Close gate valve and fill chamber with pure O₂ until chamber pressure reads 500 mT. Oxidize 10 min.

APPENDIX II

FABRICATION

OF

SIS NIOBIUM-ALUMINUM OXIDE-NIOBIUM ARRAYS

1. Ultrasonic clean 2.5" diameter polished silicon oxide wafer with TCE, ACE, and MeOH, 10 min each.
2. Photoresist trilayer
 - a) Spin Shipley 1400-27 photoresist @4800 rpm for 40 s
 - b) Bake for 25 min @ 70°C
 - c) Cool on vent and soak in chlorobenzene 10 min
 - d) Bake for 12 min @ 70°C
 - e) Expose pads, covering the array with black electrical tape, for ~2 min in the Karl Suss (hard contact mode)
 - f) Expose entire mask, including array section, for 3.5 s in Karl Suss (HC mode)
 - g) Develop fully (~15 s), using fresh 5:1 H₂O:Microposit 351 Developer. Rinse thoroughly and blow dry with dry N₂.
3. Nb sputtering
 - a) Using dry N₂, blow away any particulates that may have fallen onto the Nb target.
 - b) Apply sparingly Apiezon grease (H) onto substrate holder and mount substrate using stainless steel substrate clamp with 2.25" circular holder, making sure that the shield and substrate holder are not electrically shorted.
 - c) Mount 1.75" diameter dark space shield. This should be ~0.25" from substrate and again, make sure shield and substrate holder are not electrically shorted.
 - d) Pump chamber to P_b < 1.5x10⁻⁷ Torr (degas on).
 - e) Once chamber has reached appropriate pressure, start Meissner shroud. Chamber pressure should go down to P_b < 9x10⁻⁸ Torr. Turn off ion gauge.
 - f) Cooling water should be flowing through sample holder and appropriate magnetrons.

- g) Pump chamber until $P_b < 1 \times 10^{-7}$ Torr. Again adjust Ar flow and chamber pressure and begin dc cleaning of Al target (500 V, 85 mA) for 15 min. At 15 min mark, rotate substrate over Al target.
- h) Sputter Al onto substrate for 15 s (104 Å/min).
- i) Repeat step f. However, oxidize Al for 30 min.
- j) Pump chamber until $P_b < 1 \times 10^{-7}$ Torr (degas on). Start Meissner shroud and make sure substrate is over the Al target. Turn degas off and start Ar flow (35 sccm). Adjust gate valve until chamber pressure reads ~6 mTorr.
- k) dc clean Nb target for 20 min (500 V, 150 mA). At the 20 min mark, rotate substrate over Nb target.
- l) Sputter Nb onto substrate for 10 min (200 Å/min).
- m) Let substrate warm up (5-6 hrs) before opening chamber.

7. Liftoff--repeat step 4.

Note: The above protocol will produce junctions whose j_c 's are ~7 Amps/cm².

APPENDIX III

FABRICATION

OF

NIOBIUM-ALUMINUM OXIDE-NIOBIUM JUNCTIONS

1. Follow steps 1-5 in Appendix II.
2. Al_2O_3 -Nb deposition
 - a) Mount substrate in sputtering chamber and pump system down as outlined in steps 3 a-d in Appendix II.
 - b) Rotate substrate above Nb target
 - c) Once chamber has reached appropriate pressure, start Ar flow (35 sccm, and adjust gate valve until chamber pressure reads ~6 mTorr. Tune matchbox so that rf power source reads 23 W forward power and 0-1 W reflected power. The dc self-bias voltage should be 600 V. Turn off rf source.
 - d) dc clean Al target 6 min (500 V, 85 mA). At the 6 min mark, begin rf Ar ion etching substrate over Nb target on and off at 1 min intervals for a total of 5 min. At the 15 min mark, turn off the rf power, immediately rotate substrate over Al target and put it to ground.
 - e) Sputter Al onto substrate for 30 s (104 Å/min).
 - f) Reduce Ar flow to zero and pump chamber out. Close gate valve and fill chamber with pure O_2 until chamber reaches desired pressure (see Table AIII.1 at end of this appendix). Wait for a set amount of time.
 - g) Pump chamber until $P_b < 1 \times 10^{-7}$ Torr (degas on). Start Meissner shroud and make sure substrate is over the Al target. Turn degas off and start Ar flow (35 sccm). Adjust gate valve until chamber pressure reads ~6 mTorr.
 - h) dc clean Nb target for 20 min (500 V, 150 mA). At the 20 min mark, rotate substrate over the Nb target.
 - i) Sputter Nb onto substrate for 10 min (200 Å/min).
 - j) Let substrate warm up (5-6 hrs) before opening chamber.
3. Liftoff--repeat step 4 in Appendix II.

Table AIII.1. The various oxygen pressures and "wait" times needed to oxidize the Al layer to produce the given critical current densities. The critical current densities are reproducible to within 20%. The asterisk (*) denotes a recipe developed by J. H. Kang (1991).

Pressure (mTorr)	Time (min)	j_c (Amp/cm ²)	R_n (ohm)
1000	60	256	7
150*	30	2400	10
100	10	6800	1

APPENDIX IV

MICROFABRICATION PROTOCOLS

Fabricating Masks (Dark Field)

a) Design mask on a transparency sheet. Use black electrical tape to clearly define edges

b) Using the equation,

$$L = f\left(2 + M + \frac{1}{M}\right)$$

where L is the camera distance away from the drawing, f is the focal length of the camera, and M is the magnification, take photos of the drawing. The film used should be **Kodak Ektagraphic HC Slide Film**

c) Develop film according to manufacturer's instructions

d) Ultrasonic clean Chrome mask with **TCE**, **ACE**, and **MeOH**, 10 min each

e) Spin **Shipley 1400-27** photoresist on mask at 4000 rpm for 30 s

f) Bake 30 min at 90°C

g) Expose mask to negative 8-9 s

h) Develop in **5:1 351 Microposit Developer:H₂O** for 1 min

i) Etch chrome 2 min

j) Rinse with **H₂O** and blow dry

Cleaning Chrome Masks

a) Soak masks, chrome side up, in a **3:7 30% H₂O₂:H₂SO₄** bath until solution stops bubbling

b) Rinse thoroughly with distilled **H₂O**

c) Rinse with **ACE**, blow dry

d) Rinse with **MeOH**, blow dry

Recycling Sapphire Substrates [adapted from D. Abraham, 1983]

- a) Remove any photoresist by soaking substrates in heated **AZ-300T** photoresist stripper (70-80°C, low setting) for 25-30 min. Failure to do so will result in photoresist reacting with the various acid and base baths that follow. Rinse thoroughly.
- b) Soak substrates in a saturated solution of **KOH** until either the metal is visibly gone or the solution has stopped bubbling. Rinse thoroughly.
- c) Soak substrates in a **1:1 HCl:HNO₃** bath. Be sure not to have any metal attached to the teflon substrate holder or else the metal will dissolve and the residues will dirty the substrates.
- d) After rinsing substrates thoroughly with water, soak them in a boiling 5% soap (Liquinox) solution for 20-30 min.
- e) Rinse thoroughly and place in ultrasonic for 20 min. Blow dry.

Note: Substrates can for the most part be recycled up to two times. Further recycling, especially substrates used for fabricating SNS arrays, will lead to noticeable etching (from other procedures, especially reactive-ion-etching) of the polished surface.

Alternatives to Photoresist-Aluminum-Photoresist Trilayer—Chlorobenzene Techniques

I. For small undercuts (< 0.5 μm) [Adapted from A. T. Johnson, 1991]

- spin **Shipley 1400-27** photoresist at 4800 rpm for 40 s (1.2 μm).
- bake 25 min at 70°C
- soak in chlorobenzene 10 min
- bake 12 min at 70°C
- expose with mask 4-5 s
- develop in **5:1 351 Microposit Photoresist developer:H₂O** approximately 1-2 min

II. For large undercuts (> 0.5 μm)

- spin **Shipley 1450J** photoresist at 6000 rpm for 30 s
- bake 20 min at 65°C
- cool to room temperature
- soak in chlorobenzene 10 min
- bake for 10 min at 65°C
- expose with mask for ~15 s
- develop in **5:1 351 Microposit Photoresist developer:H₂O** approximately 1-2 min

Aluminum Etch

Mix: 84% phosphoric acid (H_3PO_4)
5% acetic acid (CH_3COOH)
5% nitric acid (HNO_3)
6% water (H_2O)

Chrome Etch

Mix: 396 ml H_2O
24 ml HNO_3
62 g ammonium cerium nitrate

ACKNOWLEDGEMENTS

There have been many people who share credit for this work and who made my stay at Harvard a memorable experience.

I am extremely fortunate to have had Prof. Michael Tinkham as my thesis advisor for the last three years. I have learned a great many things from him, including how to be a better scientist. His keen insights into a wide range of physics problems have always left me in awe and is something which I can only hope to have someday.

Prof. Christopher J. Lobb has been a continuous source of ideas and, especially, encouragement for me, ever since my days as an undergraduate here at Harvard. It is he who first introduced me to Josephson-junction arrays—I will always be grateful.

Prof. Mark S. Rzchowski, my main collaborator, has helped me in so many ways around the lab that it is impossible to list them all here. He has been extremely patient with me, answering all my questions, and has always helped me debug my computer codes. His encouragement through the roughest of times is very much appreciated.

There are three individuals whose cheerful outlook on research has greatly motivated me. Prof. John Free provided the “skeletons” for the two major computer codes used in this thesis. His laid-back attitude towards science and his moral support has carried me through a number of difficult times. Dr. Mark Tuominen, the postdoc in our group, is one of the most happy and intelligent persons I have ever met. His enthusiasm for science is extremely contagious, and I would like to thank him for all his help on getting the fabrication of the tunnel junctions discussed in this thesis underway. I hope that I can be a postdoc just like him. Prof. Miguel Octavio has given me much needed encouragement for my research on arrays, and I look forward to the building of our company, Emittive Arrays.

I would like to thank Dr. Donald Liebenberg of the Office for Naval Research and Drs. Jay Boris and Elaine Oran of the Laboratory for Computational Physics at the Naval Research Laboratory in Washington, D.C. for providing me with an unlimited amount of cpu time on their Convex machine. In addition, I would like to thank Prof. Roger Brockett and George Thomas of the Harvard Robotics Laboratory for allowing me to use not only their SUNs but also their newly acquired MASPAP parallel processor. Lastly, I would like to thank Thinking Machines Corp. in Cambridge, MA for providing me with free cpu time on their CM-2 machine.

The people in Gordon McKay Laboratory have helped me tremendously and the accomplishments of this thesis should be shared with them. I would like to thank all the current members of the Tinkham group—Tom Tighe, Ashraf Hanna, Rich Fitzgerald, Niraj Anand, and Jack Hergenrother—for helping me around the lab. Special thanks go to Tom Tighe and Rich Fitzgerald who never failed to get me out of a particular bind, whether in or out of the lab. More special thanks go to Tom Tighe and Jack Hergenrother who took the SEM photos found in this thesis. In addition, I would like to thank Dr. Sam Benz for first introducing me to the cleanroom and to David Carter for managing it so well over the last two years. Dr. Charlie Johnson has maintained an active interest in my work long after he left the group and has often provided me with much needed advice. I thank him very much for caring. The members of the Westervelt group, especially Dr. Charlie Marcus, Alex Rimberg, Raj Seshadri, and Fred Waugh, and those of the “first-floor” staff, Elizabeth Hemingway, Debbie LeBlanc, and Dr. Clive Hayzledon have all provided a source of outlet for me both in and out of the lab—I shall miss them all.

Finally, I would like to extend my gratitude to all those who have come before me; I wish much success to all those who will come after.

I dedicate this work to both my parents and my sister who have always provided me with unwavering support and love.

This research was supported in part by National Science Foundation Grant No. DMR-89-20490 and DMR-89-12927, Office of Naval Research Grant No. N00014-89-J-1565, and Joint Services Electronics Program Grant No. N00014-89-J-1023. I am grateful for an Office of Naval Research Fellowship during the first three years of my graduate study.